Electric Commuter Aircraft: Project ElectriFly

Final Report
Group 13

Alberto Aversa	5334918	Sam Broos	4992873
Vani Dadoo	5320461	Luca Dissel	5283388
Ada Fabrykiewicz	5049660	Malgorzata Gniadek	5209404
Vishwajeetsinh Jadhavrao	5281172	Thijs Savelberg	5041228
Bas van der Spek	4455851	Marta Vale de Almeida Norte	5218896

Delft University of Technology

TU Delft

This page is intentionally left blank.

Electric Commuter Aircraft: Project ElectriFly

Final Report
Group 13

by

Alberto Aversa	5334918	Sam Broos	4992873
Vani Dadoo	5320461	Luca Dissel	5283388
Ada Fabrykiewicz	5049660	Malgorzata Gniadek	5209404
Vishwajeetsinh Jadhavrao	5281172	Thijs Savelberg	5041228
Bas van der Spek	4455851	Marta Vale de Almeida Norte	5218896

Submitted to Tutor:

Nathan Eskue

and coaches:

Bruno Santos
Chiara Falsetti

on June 27, 2023

at Delft University of Technology

First Edition

TU Delft

Executive Overview

The emergence of electric aircraft creates a promising vision of cleaner and more sustainable aviation. The 2015 Paris Agreement is a legally binding agreement ratified by 195 countries[1]. By which all countries are obliged to reduce their greenhouse gas emissions. To reach this goal several national and international institutions decided on imposing emission taxes. This suggests that in the future, fuel-based aviation will need to be reduced. The exponential growth of the electric aviation world market [2], reflecting the increased interest described. However, one significant challenge that impedes the widespread adoption of electric aircraft is the limited range. With current technology, it is not possible to operate routes longer than 500 km. Not enough to cover a typical propeller flight length of 700-1000 km [3] and meet regional aviation needs. While battery technology is rapidly improving, it still significantly limits the distance an electric aircraft is able to fly. The mission needs statement is therefore given as:

> "To overcome range limitations intrinsic to electric aircraft to provide a sustainable and feasible alternative to short-haul fuel-based commercial aircraft"

ElectriFly is an electric aircraft operating in collaboration with a mid-flight recharging done *eCarus*, which can be a potential solution to the problem of range. This project aims to perform the preliminary design of an all-electric aircraft with a mid-flight recharging system. From this need, the project objective statement was described as:

> “Create a 6-8 passenger all-electric commuter aircraft with comparable performance characteristics of similar aircraft currently in operation, with the ability to interface with a digital twin and recharge mid-flight."

Based on which ElectriFly’s top-level requirements have been identified and described in Table 1.

Table 1: *Top-level requirements*

ID	Requirement
OPR-1	The aircraft shall fly at least 500 km in ideal ISA conditions without recharging
OPR-2	The aircraft shall have a takeoff distance of less than 1000m
OPR-3	The aircraft shall have a turnaround time of a maximum of 45 minutes
STR-1	The cabin shall fit at least 6-8 passengers
SAF-1	The reliability of the individual batteries shall be not less than 99%
RCH-1	The aircraft shall be in-flight rechargeable
COS-1	Operational cost per hour shall be less than 1400$/h
SCH-1	The aircraft shall be designed with the resource constrain of 10 students
SCH-2	The aircraft shall be designed in less than 10 weeks
SUS-1	At End-of-Life, the aircraft structure shall be not less than 80% reusable
SUS-2	At End-of-Life, the batteries shall be not less than 80% reusable
SUS-3	Emissions shall be fewer than 50% of conventional aircraft

Operations

Due to high environmental consciousness [4], advantageous grands and growing green energy grid Europe was chosen as the main operational region. An example case with Rotterdam Airport as the hub was investigated. Possible routes planned can be seen in Figure 1. Routes shorter than 500km are reachable with a mission profile without in-flight recharging. Another mission profile contains the use of the in-flight recharging system to reduce the demand for ground recharging. This allows for quick turnaround times, and operability to small airports with no or small on-ground recharging infrastructure. The last mission profile can reach destinations of up to 1400 km, by use of a single in-flight recharging procedure to maximize range. Further destinations could be reached with the use of consecutive in-flight recharging procedures.

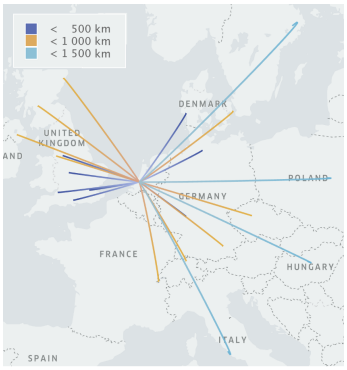

Figure 1: *Operational model of Rotterdam Airport*

[1] https://unfccc.int/process-and-meetings/the-paris-agreement [Accessed on 30.05.2023]
[2] https://www.statista.com/statistics/1337818/electric-aircraft-market-size-worldwide/ [Accessed on 23.05.2023]
[3] https://flyaeolus.com/blog/private-jet-versus-propeller-airplane/ [Accessed on 21.6.2023]
[4] https://epi.yale.edu/epi-results/2022/component/epi [Accessed on 21.6.2023]

Battery

At the beginning of this analysis, a preliminary weight estimation was used to find the required battery properties for design convergence and abidance with normal and commuter aircraft certification CS-23 [1] regulations, which is crucial for minimizing certification time and costs. The current battery density available of 265 Wh/kg was not sufficient for an optimized aircraft structure. However, the currently in-development solid-state batteries are expected to be available by 2035 when ElectriFly will get into service. This battery type was chosen, by identifying their advantages in terms of energy density (600 Wh/kg) [2] and safety. Moreover, their lifetime is high, estimated at 10 000 cycles [3]. The final battery properties used for the design are summarized in Table 2.

Table 2: *Battery Overview*

Parameter	Requirement	Battery Property
Energy Density [Wh/kg]	600	600
Power Density [W/kg]	400	500
Cycle Life	6 000	10 000

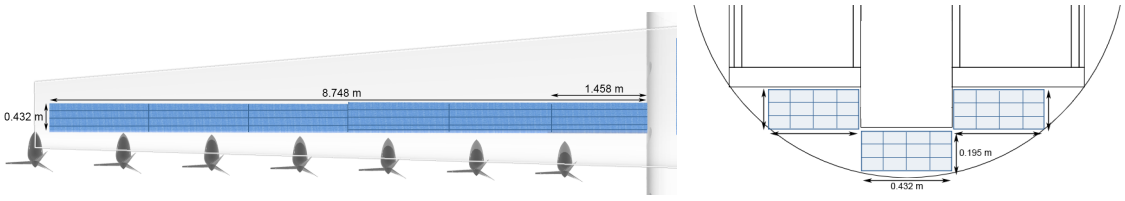

(a) *Wing* **(b)** *Fuselage*

Figure 2: *Battery and module placement*

Considering the cell structure, a lithium-metal anode with polymer coating combined with a sulphide-based electrolyte and NMC cathode is considered the most optimal configuration, due to its high ionic conductivity, high potential difference and low dendrite expansion [3]. Half of the battery weight is placed in the wing, while 25% in front and 25% end of the fuselage. A total of 4 battery packs is needed in the aircraft, where a single battery pack consists of 36 modules in series. These modules are made of 81 battery cells in parallel and 6 in series each. In the fuselage, the battery has been separated into 3 segments, each consisting of 12 modules. This configuration is visualized in Figure 2b. While the fuselage was optimized to occupy the full span with 4 modules chord-wise and 6 module-wise, pictured in Figure 2a.

Table 3: *Material properties for conductor material*

Parameter	Value
Cable length	20 m
Cable diameter	3.5 cm
Drogue diameter	35 cm
Weight cable	180 kg
Weight cable unit	200 kg
Cable efficiency	99.86%
Recharging rate	1.7 MW

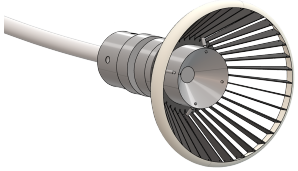

Figure 3: *CAD model of the drogue*

In cruise, the Electrifly will receive 1161 kWh from eCarus at a rate of 1.7 MW. Therefore, an interface has to be designed focused on delivering this high power in an efficient, safe, and reliable way. For this Electrifly is equipped with a cable-drogue-probe configuration inspired by military air-to-air refueling. The ElectriFly is equipped with the cable and droge as shown in **??**, and is stored in a circular drum inside the tail cone, while the recharging drone contains the probe. The design has an efficiency of 99.86% and a reliability of 99.9% and includes many sensors to ensure safety and aid the connection process. The recharging process induces the largest thermal restriction for the batteries. This heat is collected using a liquid cooling system. The final design parameters are given in Table 3.

Propulsion Analysis

Electric motors offer a lot of variability in terms of placement and size, as they are generally smaller and lighter. Distributed Electric Propulsion (DEP) system was chosen due to its enhanced lift generation and reduced cable connection loss due to the lower amperage required. After the lift, drag and efficient analysis the 14-engine configuration was chosen powered by Emrax208 motors[5]. The additional lift coefficient generated by DEP during the cruise is 0.3 and up to 0.7 using climb. With many propellers being present on the wing turbulence is induced, which in turn, considerably increases the drag. This could be partially mitigated with the use of plasma actuators, which create a secondary flow

[5]https://emrax.com/ [Accessed on 10.06.2023]

contrasting the induced vortices. These devices can also work to direct the flow over the control surfaces in regenerative mode. Their functioning, however, still needs to be thoroughly investigated.

The use of propellers opens up the possibility of making use of the concept of energy harvesting. This entails operating the propeller at high advance ratios and thus producing negative thrust and negative torque. The latter can be used to partially charge the batteries, although the potential that can be harvested from the flow is still fractional. The propeller is thus designed to work in both propulsive and regenerative phases.

Structural & Manufacturing Analysis

The structural design was performed for the most important aircraft parts – the wing and fuselage. The fuselage has a circular cross-section with a 2.2 m diameter, incorporating two business class seats per row. The fuselage is designed to accommodate 30kg of luggage per passenger. The top layout consists of the cockpit, door aisle, luggage holds, 4 rows of passenger seats and a lavatory at the back. The total length is 12.5m. The fuselage skin thickness was designed to be 1 mm and it is reinforced with 20 stringers of 300 mm2. The wingbox features 10 stringers and a skin thickness of 0.6mm. For both structures, Al7075 alloy was chosen for the skin and CFRP/PEEK(60% fibre) composite was chosen for the stiffeners due to the excellent mechanical properties of those materials for the corresponding loads. Most of the loads are concentrated at the wing-fuselage crossing, therefore, for further optimization, this section should be reinforced while other sections may be designed with less stiffness leading to further weight optimization.

ElectriFly's design utilizes digital thread – a dataset containing product components information from the beginning of the product life until the end of life. The thread starts at the manufacturing phase. Sensors and AI algorithms can be used to monitor the processes, detect failures and ensure quality control. The organizational process of line production will be optimized with data and machine learning algorithms. The aluminium sheet used for ElectriFly can be manufactured with traditional methods. Since the composites are thermoplastic different manufacturing processes must be used. The fibres must be pre-impregnated with melt impregnation or quasi-solution impregnation. Then, automatic lay-up must be used simultaneously with consolidation by a heated lay-up nozzle. Future alternatives are offered by additive manufacturing when the technology matures. The next step in the digital thread is the digital twin. Sensors are implemented in the ElectriFly structure to monitor pressure, force, temperature, and damage detection. To limit the weight of the sensors, only the critical structures with the highest loads will utilise them. The data shall be uploaded to a large digital twin that will then analyse it to ensure aircraft health and provide predictive maintenance capabilities. A lighter, less detailed pre-trained model shall be uploaded to the edge device present in ElectriFly that analyses real-life data for anomalies and notifies the crew about potential problems and lines of action. A significant reduction in reaction time and cost for maintenance can be achieved with the digital twin technology.

Aerodynamic & Stability Analysis

The aerodynamic analysis provided an assessment of ElectriFly's lifting capabilities and drag. The wing planform and its high-lift devices were designed to provide enough lift during the entire mission. However, the lift provided by the wing will be enhanced by the distributed propulsion system. This augmentation will allow for the reduction of wing size and eliminates the necessity of excessive high-lift devices. Moreover, the propellers that are placed on the wing tips, rotate opposite to the vortex generated at the wing tip. The contrary rotation will reduce the lift-induced drag, in turn reducing ElectriFly's power consumption.

To reduce down-wash and distributed propulsion propeller wake effect, a T-tail configuration has been chosen. The vertical tail volume was reduced by 20% from the vertical tail volume found in historical data, as the distributed propulsion system vectored thrust capabilities improve lateral stability, allowing for a smaller vertical tail area. Battery placement has a significant effect on the shift in the position of the centre of gravity. Therefore, their distribution has been used as a variable to optimize stability and horizontal tail sizing. The performance analysis aimed to show the feasibility of ElectriFly's mission with respect to its aerodynamic and propulsive capabilities. The ElectriFly is theoretically able to fly over 12 000 m in altitude and faster than 140 m/s. A significant change can be seen in the mission's cruise condition. Moreover, the range was assessed in greater detail, yielding a range of 640 km with maximal payload and 680 km with no payload. Since requirement OPR-1 is complied with by over 100 km, further reduction and optimisation are to be found in ElectriFly's energy usage.

Final Design Configuration

The final design has been described in Table 14.1. Due to the iterative nature of aircraft design, further improvement of the design is possible. The design team predicts further weight reduction due to adjusted wing size, thanks to the lift generation DEP system benefits, and possible battery range extension by adjusting flight altitude and speed to the new design.
The aircraft features a fly-by-wire cockpit, equipped with an automatic flight guidance system capable of providing autopilot functionality. While ElectriFly must perform standard communication, in addition a reliable link with

Table 4: *Overview of geometrical parameters*

Wing		Fuselage		Tail		Propeller	
S_W	35.13 m^2	Nose length	2.69 m	S_v	5.3 m^2	Blades/prop	3
b_W	20.53 m	Tailcone length	4.48 m	b_v	2.82 m	Propellers	14
A	12 -	Cockpit length	2.5 m	Λ_v	30 deg	Clearance	0.44 m
$\bar{c}$	1.79 m	Fuselage length	12.54 m	S_h	5.27 m^2	Diameter	0.88 m
λ_W	0.45 -	Outer diameter	2.24 m	b_h	4.87 m		
$\Lambda_{0.25c}$	0 deg			Λ_h	13 deg		
Airfoil	NACA 44018			Airfoil	NACA0012		

Recharging		HLD & Control Surfaces		Landing Gear		Motor	
Cable length	20 m	LE flaps span	85%	y_{mlg}	1.4m	Casing diameter	208 mm
Cable diameter	3.5 cm	TE flaps span	70%	l_{mlg}	6.39m	Axial Length	85 mm
Drogue diameter	35 cm	Ailerons span	15%	l_{ng}	1.15m		

recharging drone system is necessary. Three main types of communication have been identified: Air-to-space, air-to-air and air-to-ground. Digital twin sensors send data directly to its computer, which selects relevant information to the Flight Management System.

Through costs analysis, total non-recurring development costs are estimated to be $252 million. With manufacturing costs of $3.5 million per aircraft and unit price of $4.3 million, the break-even point found is 315 aircraft produced required for return on investment. Furthermore, operating costs with on-ground-charging were calculated to be $696 per hour of flight. With an additional $377 per flight to cover airport operations, insurance and additional maintenance. Mission model with mid-air recharging drone settles at operational costs of $1730 per flight hour. The total operational costs exceed requirement COS-1 chosen based on the current operational costs of fuel-based competition. However, the price exceeds the requirement by only 13%, which is reasonable for a newly developed technological solution at the beginning of its operation. The producer expects that in-line with European Union sustainability goals, through subsidies and taxation differences, fully electric aircraft with mid-air recharging capabilities will still offer competitive prices.

Figure 4: *ElectriFly*

Sustainability

In the final sustainability analysis, it was evaluated whether the ElectriFly complies with the most vital sustainability requirements that were set in the early development phase. In doing so, research was done on the carbon footprint of the ElectriFly compared to a non-electric commuter aircraft with the same mission profile. ElectriFly produces 3.5 times less CO_2 emissions than a conventional aircraft and therefore meets REQ-SUS-3. It is relevant to note that this method includes the carbon footprint of both the production and replacement of the battery. Additionally, an extensive analysis was performed on the possibility of recycling more than 80% of both the batteries and materials used in aircraft structures. The analysis showed that a combination of direct recycling and Hydrometallurgy will provide the most viable results. By applying these techniques along with an efficient recycling program, the 80% goal should be achievable. Furthermore, it was concluded that also the used materials can be meaningfully recycled up to 85% of the aircraft, by weight, in a way that is economically viable as well. The techniques that would have to be applied for this are dependent on the specific material. Overall, this means that also top-level requirements REQ-SUS-2 and REQ-SUS-1 are met. Finally, the chapter elaborates on the noise expectation of the ElectriFly. This research showed positive expectations regarding the overall noise impact of the aircraft. This is mainly due to the relatively silent electric motors and the concept of distributed propulsion. Furthermore, it is discussed how by applying mitigation methods such as the steep approach technique and the use of noise-absorbing materials, the noise could be further reduced.

Summary

The increasing pressure imposed by climate change on the future of humanity has brought sustainability to the forefront of public debate. Governmental authorities are therefore urged to introduce regulations that will mitigate the impact of human activities with a high rate of emissions. As aviation is responsible for more than 2% of global emissions, it is one of the main domains where change is expected. The goal is to reach zero-emissions aviation by 2050. This presents a huge challenge to the aviation industry as it implies finding suitable alternatives to jet fuel. The use of batteries in an attempt to electrify aviation is one of the alternatives considered. However, batteries impose high restrictions on flying distance, and while producing no emissions in operation, their emissions in production and at end-of-life, along with their potentially short lifetime, have to be taken into account.

This report aims to provide a potential solution to the restrictions on the range by incorporating a mid-flight recharging system into an all-electric passenger commuter aircraft, named ElectriFly. This plane is able to fly for 600 km at a speed of 110 m/s before recharging. Then, its range can be extended to reach a theoretical perpetual flight capability with the implementation of in-flight recharging. The aircraft is to be recharged by a drone developed by eCarus, that is, Group 10, by means of a drogue and probe system, similar to existing military mid-air refuelling technologies. This capability not only allows to increase range but also solves another problem common to electric vehicles, namely turnaround time. Indeed, the long recharge phase on the ground can be replaced by one in the air, allowing for short ground times. In order to make this possible, an extensive analysis was performed in the domains of propulsion, aerodynamics, performance, structures, stability and manufacturing.

The aircraft will be powered by 4 solid-state batteries, connected in parallel to comply with the energy requirement, with an energy density of 600 kWh/kg. These batteries drive a system of 14 propellers. The use of distributed propulsion, in possible combination with plasma actuators, provides advantages in terms of aerodynamic performance, as an additional lift is generated while the propeller-induced drag is minimised. Moreover, this technology allows for noise to be reduced and for the possibility of implementing the principle of regenerative braking. This relieves some of the energy stress put on the recharging drone. In addition, the aircraft structure is equipped with sensors that measure data in real-time, building a digital twin system which allows for predictive maintenance, along with the reduction of downtime by isolating issues to certain specific aircraft and further information on anomalies in flight to be given to pilots.

Each unit is expected to cost $4.3 million and has an operational cost of $781 per hour of flight with on-ground recharging, $1590 per hour of flight with mid-air recharging and an extra $377 per flight for other expenses. The aircraft is set to operate mainly in Europe due to the high focus on sustainability, but expansion to North America and South East Asia is possible.

Figure 5: *Front view of ElectriFly*

Figure 6: *Side view of ElectriFly*

Contents

1. Introduction

The introduction of electric aircraft creates a promising picture of greener and more sustainable aviation. Aircraft flying on sustainable aviation fuel (SAF) only show potential reductions of greenhouse gases (GHGs) of up to 70% [4], and hydrogen aircraft, while having the potential to decarbonise the industry, is itself "leak-prone gas with a potent warming effect" [1]. Moreover, the impact of SAF on land use and hydrogen production on the atmosphere (based on fossil fuels and producing methane emissions, a worse GHG), the overall environmental footprint still remains significant[2] [5].

A cleaner alternative is an all-electric aircraft, which has the potential to significantly reduce carbon emissions and noise pollution while also offering increased efficiency. However, one major challenge impedes electric aircraft from widespread adoption: range. The limited energy storage capacity of current batteries imposes constraints on the distance covered by electric aircraft. Nonetheless, the problem of range can be effectively addressed with a mid-flight recharging system. By integrating a sophisticated recharging mechanism in design and replenishing energy reserves in flight, electric flights can embark on longer, cleaner journeys.

This thesis examines the preliminary development of an all-electric aircraft, named ElectriFly, capable of mid-flight recharging and integrated with a digital twin interface. A holistic approach is utilised, covering all relevant technical and economic aspects. The scope of this project is defined as all-electric aircraft, therefore hybrid (turbo-electric) or electric aircraft involving hydrogen fuel cells are not examined. This research shall shed light on the upcoming battery technology and how that impacts the development of electric aircraft, as well as highlight the futuristic concepts that can be considered in the development of this aircraft for propulsion and structures. The work shall also generate fresh insight into the integration of this aircraft with a mid-flight recharging system, as well as a digital twin used for predictive health maintenance. The recharging system is developed in close collaboration with DSE group 10: Mid-flight recharging system, with a complete recharging hub network. Electric aircraft feature complex electrical circuits and require close monitoring of the battery during flight. Therefore, ElectriFly is designed with an integrated digital twin functionality, which can enable real-time monitoring, predictive maintenance and performance optimisation.

This final report described the design developed by 10 aerospace engineering undergraduates at the Delft University of Technology. The overall structure of the study takes the form of three parts. The first part of this paper shall examine the methodology in Chapter 2, identify the market gap in Chapter 3, and address the mission profiles and operations in Chapter 4. The second part of the paper shall address all the technical aspects of design, beginning with a division of the available budgets among the subsystems in Chapter 5, and then moving on to the battery analysis in Chapter 6, development of the recharging system in Chapter 7, followed by the aerodynamic, propulsive and structural analyses in Chapter 8, Chapter 9, Chapter 10. Consequently, the performance is analysed in Chapter 11, followed by the stability analysis in Chapter 12 and the aircraft systems in Chapter 13. The final design configuration is presented in Chapter 14, and the manufacturing and digital twin are developed in Chapter 15. The third part begins by elaborating on the risk analysis of ElectriFly in Chapter 16, followed by the sustainability and cost analyses in Chapter 17, Chapter 18 respectively. Finally, the product verification is done in the form of a compliance matrix in Chapter 19 and the project design and development logic is detailed in Chapter 20.

[1] https://www.edf.org/media/study-emissions-hydrogen-could-undermine-its-climate-benefits-warming-effects-are-two-six [Accessed on 20.6.2023]

[2] https://www.theguardian.com/environment/2023/mar/07/hydrogen-clean-fuel-climate-crisis-explainer [Accessed on 20.3.2023]

2. Methodology

This chapter shall describe the methodology used in this report and during the course of the project to develop the final design. First, the top-level requirements are detailed in Section 2.1. Then, an overview of the previous work is given in Section 2.2, and finally the methodology used in this study is given in Section 2.3.

2.1. Top-level Requirements

To define ElectriFly's mission and all its high-level capabilities, a set of 12 driving requirements is given in Table 2.1. These top-level requirements define the basic mission of ElectriFly: to fly 6-8 passengers over a range of 500 km with a turn-around time of less than 45 minutes. To ensure safety, the reliability of the individual batteries shall be at least 99%, and they shall be able to be recharged in flight. To make sure that the aircraft is sustainable in all aspects, there are three sustainability requirements: 80% reusability of the structure, 80% reusability of the batteries, and an environmental footprint of less than 50%. To be able to compete with other counterparts, the ticket prices need to be competitive, for which the operational costs need to be lesser than 1400$ per flight hour. Finally, this design shall be developed by 10 students in 10 weeks.

Table 2.1: *Top-level requirements*

Category	Identifier	Requirement
OPR	OPR-1	The aircraft shall fly at least 500 km in ideal ISA conditions without recharging
	OPR-2	The aircraft shall have a takeoff distance of less than 1000m
	OPR-3	The aircraft shall have a turnaround time of a maximum of 45 minutes
STR	STR-1	The cabin shall fit at least 6-8 passengers
SAF	SAF-1	The reliability of the individual batteries shall be not less than 99%
RCH	RCH-1	The aircraft shall be in-flight rechargeable
COS	COS-1	The operational cost per hour shall be less than 1400$/h
SCH	SCH-1	The aircraft shall be designed with the resource constrain of 10 students
	SCH-2	The aircraft shall be designed in less than 10 weeks
SUS	SUS-1	At End-of-Life, the aircraft structure shall be not less than 80% reusable
	SUS-2	At End-of-Life, the batteries shall be not less than 80% reusable
	SUS-3	Emissions shall be fewer than 50% of conventional aircraft

Regulations from CS-23: In addition to the top-level requirements, ElectriFly will adhere to EASA CS-23 requirements [1]. This classification is used to certify aircraft of the type 'normal' and 'commuter' for operations, which is applicable to ElectriFly and allows for simpler and cheaper certification compared to higher classes. CS-23 defines several requirements on the subject of loading, take-off, stall and landing conditions that need to be adhered to in the preliminary stage of design. These requirements have been presented for every technical section of the report.

2.2. Overview of Prior Results

This report is the final in a series of four reports developed over the course of this project. Initially, a project plan was developed to plan the different phases. Then a foundation for the technical aspects of the design was set up in the second baseline report. The third report is the mid-term report, where the conceptual design of the aircraft was performed.

The midterm report aimed to evaluate feasible aircraft configurations, for which it performed two trade-offs to arrive at the most optimal design. For the initial trade-off, 8 conceptual designs were qualitatively traded-off to yield the best 3 configurations: the conventional, blended wing body and twin-boom configuration, given in Figure 2.1.

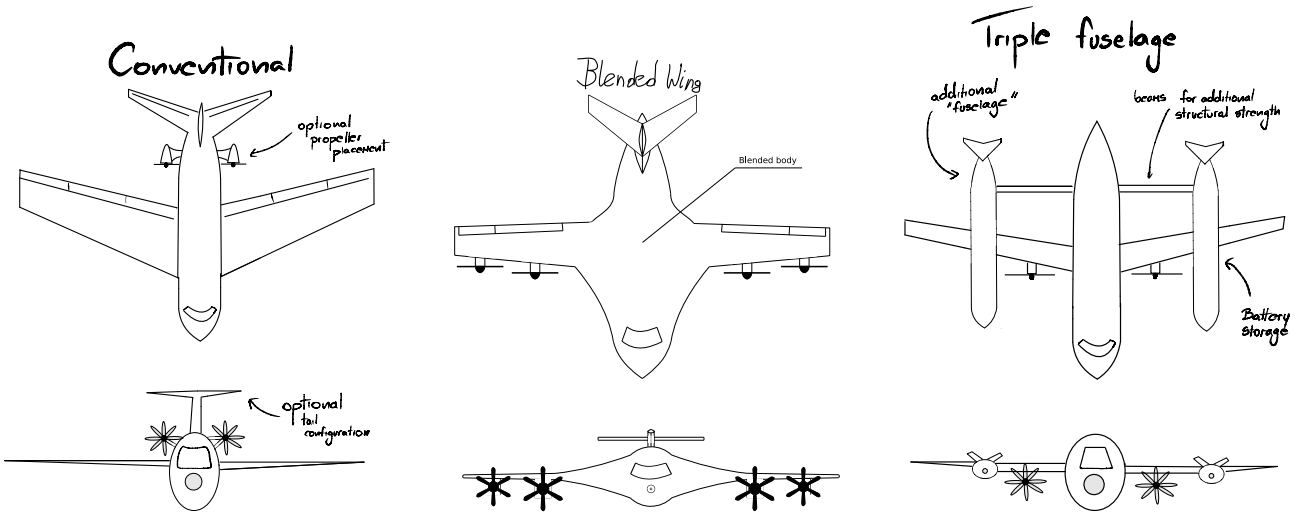

(a) *Design 1: Conventional Aircraft* **(b)** *Design 3: Blended Wing* **(c)** *Design 7: Triple Fuselage*

Figure 2.1: *Best three optimal configurations*

Subsequently, the 3 configurations were further analysed in terms of aerodynamics, structures, stability and propulsion. The iteration between Class I and Class II weight estimations were performed taking into account all geometrical parameters of the aircraft. The criteria for the final trade-off can be reflected in Table 2.2, where the OEW/MTOW ratio, L/D ratio, induced drag effect, pitch stability coefficient, vertical and horizontal area along with center of gravity range are compared.

Table 2.2: *Numerical results of subsystem analysis used for Final Trade-off.*

Design	OEW/ MTOW	MTOW[kg]	L/D	Induced drag effect [K]	Pitch Stability Coefficient	Vertical Tail Area [m^2]	Horizontal Tail Area [m^2]	c.g. range
CNV	0.36	7,350	16.6	0.038	-3.84	9.28	6.48	8.8%
BWB	0.64	14,400	29.3	0.072	-0.99	5.04	7.04	4%
TWN	0.45	9,000	15.7	0.038	-2.66	8.75	6.11	70%

Finally, the final trade-off, evaluated on the basis of aerodynamic and structural efficiency, propulsion and battery integration, recharging system compatibility, stability and operations, was performed. According to the scoring presented in Table 2.3, the best optimal design was found to be the conventional configuration. The report concluded with developed analyses of manufacturing technologies, cost, risk and sustainability of the selected configuration.

Table 2.3: *Final trade-off results*

Weight	**30%**	**20%**	**20%**	**15%**	**10%**	**5%**	
Criteria/Configuration	Structural efficiency	Aerodynamic performance	Propulsion & battery	Recharging system	Operations	Stability	Score
Conventional	5	4	4	4	5	4	4.4
Blended Wing Body	1	4	3	2	2	3	2.35
Twin-Boom Tail	4	3	5	3	5	4	3.95

The initial configuration of the aircraft, that is the initial parameter values that were developed in the mid-term report, are presented here in Table 2.4. This configuration shall serve as the starting point for the design in this report, as described in the following section.

Table 2.4: *General characteristics for the initial configuration*

Aircraft Parameters	Value
Take-off Length [m]	1000
Cruise Altitude [ft]	15000
Cruise Speed [m/s]	110
Range [km]	500

Weights [kg]	Value
MTOW	7358
OEW	2653
Battery Weight	3445
Payload	1260

Structures	Value
Wing Area [m2]	39.5
Wingspan [m]	21.78
Aspect Ratio	12
Length [m]	12.54

2.3. Technical Workflow

The methodology behind the technical aspect of this report is presented in Figure 2.2. Based on the preliminary design that was established in the midterm report, a battery system can be designed. The required performance of the battery is dependent on the characteristics of the initial design and the mission profile. Based on the energy and power requirements, it can be determined what type of battery is needed and how much weight the required battery will add to the MTOW. Also, the preliminary sizing and placement of the battery are performed.

Having established the 'heart' of the aircraft, the other subsystems can be designed. This is done mostly in parallel and should be well coordinated as the various subsystems have many common factors and overlapping areas. After having designed these subsystems, the aircraft will have changed significantly compared to the initial starting point. It is therefore of vital importance that the whole design process is iterated to converge to a final design. It can be that in this process, conflicts and difficulties arise involving multiple subsystems. In this case, extensive trade-offs will be performed to determine the most efficient design solution.

Additionally, all the specific design steps must be validated and verified. Furthermore, it needs to be securely checked whether the final design complies with the requirements that were set. This latter includes evaluating the technical performance of the aircraft as well as performing an extensive cost and sustainability analysis. In the cost analysis, comprehensive market research is done and estimates of the total costs are made. This way, a picture can be formed of how economically viable ElectriFly will be. The sustainability analysis mainly concerns end-of-life strategies for the battery and structures. Moreover, the carbon footprint is evaluated along with the expected noise impact.

In parallel to the conceptual design of the ElectriFly aircraft itself, the concept of a digital twin is assessed for its strategies, challenges and opportunities, and will allow for further development. The digital twin will display a digital life presentation of the ElectriFly and its subsystems, to provide a conceptual revolutionary addition to the ElectriFly aircraft. The specific features and details of this model will be discussed later in the report.

The computational design of the ElectriFly aircraft and its subsystems has been performed with the use of a collaborative coding model, which allowed for concurrent engineering. This was done using a modular system of Python code, capable of iterations. A central file of parameters was updated by the different subsystems and fed back. For example, if structural or aerodynamic parameters changed, the code model would automatically calculate the new required stability parameters and tail sizing.

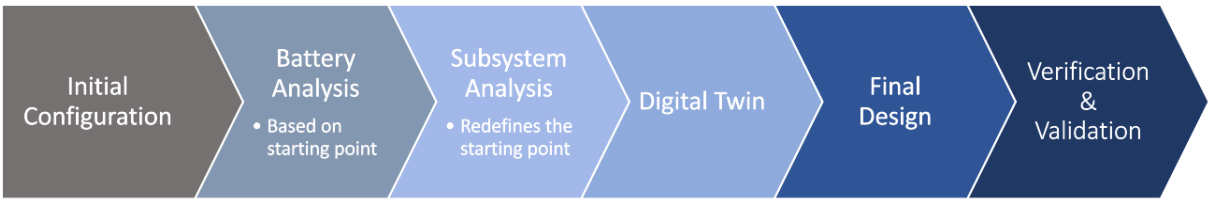

Figure 2.2: *Technical workflow*

3. Market Analysis

Aircraft exist because they have a consumer, therefore the objective of this chapter is to investigate business models for the fully electric ElectriFly aircraft, which in turn also finds potential customers. Section 3.1 explains the importance of growing aviation sustainably, Section 3.2 discusses regions where operations of ElectriFly are feasible, whilst Section 3.3 mentions potential customers in these regions.

3.1. Growth Through Sustainability

The Paris Agreement from 2015 is a legally binding agreement ratified by 195 countries, stating a limit in the rise of global temperature to a level below 1.5 deg by limiting emissions and eventually reaching net zero by 2050[1]. Greenhouse gases, such as CO_2, were especially addressed. To reach this goal, both national and international institutions are currently ratifying emission taxes, which directly affect airlines[2]. For this reason, the International Air Transport Association has set forth the same goal for all airlines in the world [3]. This calls for airlines and aircraft to become more and more sustainable, as current fuel-based aviation emits a considerable percentage CO_2.

Fuel is one of the main components of operational costs for airlines. Additionally, the prices of this resource can be volatile depending on the geopolitical situation at the time [4]. The preliminary cost analysis suggests that powering the aircraft with electricity is cheaper than with aviation fuel. The energy cost calculated for ElectriFly, using the price of 0.44$/kWh for the Netherlands, used as a representation of the European market, was $340 per flight hour. This result is lower compared to fuel-based twin-engine turboprop's fuel cost, averaging $933 per flight hour[5]. Therefore decreasing the fuel operational cost is an additional reason, besides sustainability, for airlines to move away from fuel-based aircraft.

One of the alternatives to fuel-based aviation is electric-based aviation since electricity can be produced sustainably. Therefore, this project's focus is to investigate and design the feasibility of fully electric aircraft and address its limitations. Since no combustion occurs on such an aircraft, it is overall quieter, and noise pollution is also limited as an effect, promoting sustainability. This was also used as a rationale for supporting electric aircraft in the conceptual design since it increases the quality of life for residents near the airport. A more in-depth analysis of noise will be presented in Section 17.4. The growth of the electric aviation market [6] indicates that it is likely that more investment will be made in this sector as time progresses, meaning that the aviation industry acknowledges the possibility of aviation becoming all-electric.

3.2. Investigating Feasible Operations Regions

In order to check the feasibility of the project, the competition analysis should not be limited to fuel-based aircraft but rather also extended to direct competition in the form of other fully-electric aircraft. From the latter category, electric vehicles like Alice, produced by Eviation [6], and Lilium Jet[7], currently in development, was considered as the main future competition. Although the sustainability objectives of the two companies are similar to the ones considered for ElectriFly, it should be noted that the range is their main limitation. Due to the limited energy density of the batteries available (kWh/kg), both Alice and Lilium are designed to perform ranges shorter than 500 km. The project design addressed this issue by developing a mid-flight recharging drone system in collaboration with recharging drone eCarus (DSE group 10). The solution allows the extension of the aircraft's range and significantly expands the choice of operational routes. Additionally, airlines can use the mid-flight recharging capability to minimise their turnaround time by charging the aircraft before landing so that the charging time on the ground is reduced. Both of these business models, that is, maximising range and minimising turnaround time will be assessed and discussed further in Chapter 4.

3.2.1. European Aviation Region

[1] https://www.un.org/en/climatechange/net-zero-coalition [Accessed on 02.05.2023]
[2] https://climate.ec.europa.eu/eu-action/european-green-deal/delivering-european-green-deal/aviation-and-eu-ets_en [Accessed on 02.05.2023]
[3] https://www.iata.org/en/programs/environment/flynetzero/ [Accessed on 02.05.2023]
[4] https://www.mckinsey.com/industries/travel-logistics-and-infrastructure/our-insights/why-rising-fuel-prices-might-not-be-as-bad-for-the-airline-sector-as-it-seems [Accessed on 02.05.2023]
[5] https://www.iaopa.eu/AOPAFuelPriceServl [Accessed on 02.05.2023]
[6] https://www.eviation.com [Accessed on 01.05.2023]

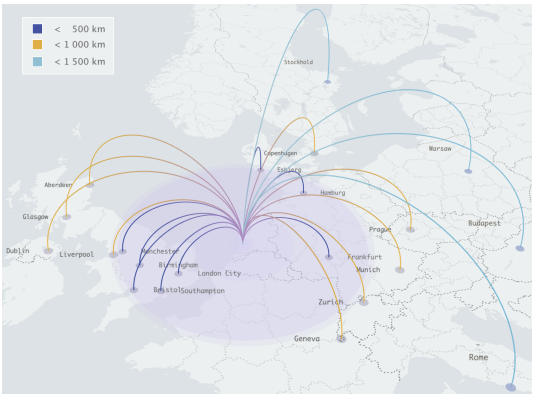

Figure 3.1: *Operations Model with Rotterdam Airport as the Main Hub*

After consultation with the mid-flight recharging team, it was concluded that both sides' market feasibility research points towards Europe as an operation region. Europe is one of the regions leading in sustainability [7], and its governments offer several subsidies to promote sustainable development. *European Green Deal* aims to reduce transport emissions by 90% by 2050 (compared to 1990). EU emission trading system since 2012 cover also aviation, therefore the companies are obliged to purchase tradeable allowances [8], which increases operational costs for conventional fuel-powered aircraft. Furthermore, past initiatives suggest that the EU is willing to offer additional funds and subsidies for Green-tech projects [9], which can be helpful in the development phase. Both teams are based in Europe, and as potential manufacturers, the teams have a greater chance of benefiting from the subsidies. Recognizing this, the ElectriFly team contacted D. Dijk[10] from the innovation department of Rotterdam Airport to discuss market possibilities of ElectriFly, and he gave Table 3.1 which shows a list of destinations where Rotterdam airport wants to expand toward in the business charter/commuter sector. The reason for interest in these destinations is primarily due to the large travel times allowed by either car or train, as compared to the high speed that can be achieved with an aircraft like ElectriFly. Additionally, Rotterdam airport had found that a majority of business passengers travelling from Amsterdam to Hamburg, originated from the Rotterdam region, giving more incentive to tap into this niche market. Rotterdam Airport covers the area of two large Dutch cities: Rotterdam and the Hague. The region has the largest seaport in Europe, a lot of business and trade activities. ElectriFly can meet the business charter demand. As seen in Table 3.1, the first 8 destinations with a radius of 500km were chosen and marked by the purple circle. As per D.Dijk, a majority of the business charter sector has flights in the range of 500km, making ElectriFly a viable competitor in this region. Additionally, the rest of the popular routes are less than 1000km away from Rotterdam, meaning these destinations can be accessed with a single mid-flight recharge. Therefore, the region outlined in Figure 3.1 becomes the strongest business model for ElectriFly thus far.

Table 3.1: *Rotterdam Airport Expansion Routes Expectations*

Destination	Distance (km)	Car Travel [hh:mm]	Train Travel [hh:mm]	ElectriFly [hh:mm]	Destination	Distance (km)	Car Travel [hh:mm]	Train Travel [hh:mm]	ElectriFly [hh:mm]
London City	320	06:18	04:48	00:49	Aberdeen	714	15:13	12:27	01:48
Manchester	483	08:51	07:55	01:13	München	666	08:43	09:01	01:41
Birmingham	437	07:30	05:49	01:06	Dublin	728	12:53	14:52	01:50
Hamburg	413	05:33	06:36	01:02	Zurich	582	08:44	09:01	01:28
Frankfurt	357	04:39	04:30	00:54	Geneva	645	09:58	08:09	01:38
Southampton	422	07:05	05:42	01:04	Copenhagen	687	09:46	11:54	01:44
Bristol	489	08:15	06:41	01:14	Liverpool	518	09:31	07:54	01:19
Esbjerg	473	08:04	14:30	01:11	Glasgow	712	12:47	09:11	01:48
					Prague	736	09:28	11:49	01:52

3.2.2. Asia-Pacific Aviation Region

The most intense growth in annual passenger air traffic seen in Asia [11] indicated the potential for expansion on Pacific Asia region. The area is well suited for electric turboprop aircraft due to the multitude of domestic flights and common short international flight routes. This claim can be supported by the analysis of the 5 top domestic and international routes in the region presented in Table 3.2. For most popular destinations, an average distance of 1150 km can be calculated. Furthermore, due to the area being a conglomerate of islands, aviation cannot be replaced by railways alternatives in any foreseeable future. This potential was noticed by ATR, a Europe-based turboprop aircraft manufacturer, which predicts that the highest turboprop aircraft demand in the next 20 years will be seen in Pacific Asia [12]. The route lengths considered emphasize the need for collaboration with the mid-air recharging company and the advantage of the ElectriFly over its competition. It should be considered that the aircraft will be designed universally, yet the primary focus in terms of routes and market needs will focus on this region.

[7] https://epi.yale.edu/epi-results/2022/component/epi [Accessed on 1.05.2023]
[8] https://climate.ec.europa.eu/eu-action/european-green-deal/delivering-european-green-deal/aviation-and-eu-ets_en [Accessed on 02.05.2023]
[9] https://ec.europa.eu/commission/presscorner/detail/en/ip_22_4402 [Accessed on 01.05.2023]
[10] Innovation department, Rotterdam Airport
[11] https://www.airlines.iata.org/news/passenger-numbers-to-hit-82bn-by-2037-iata-report [Accessed on 02.05.2023]
[12] https://www.atr-aircraft.com/wp-content/uploads/2022/07/ATR_Market-Forecast_2022_Digital_HD.pdf [Accessed on 31.05.2023]

Table 3.2: *Top South East Asian Routes in May 2023 \cite{AsianRoutes}*

Domestic				International			
From	**To**	**Distance [km]**	**Popularity**	**From**	**To**	**Distance [km]**	**Popularity**
HAN	SGN	1149	908	KUL	SIN	298	427
CGK	DPS	982	723	CGK	SIN	878	347
CGK	KNO	1383	541	BKK	SIN	1410	276
CGK	UPS	1433	530	DPS	SIN	1668	265
CGK	SUB	692	411	MNL	SIN	2372	230
Weighted Average		1139		**Weighted Average**		1171	

3.2.3. North America Aviation Region

North America and the Caribbean can be seen as the next expansion destination in line. This region shows a lot of potential as short-haul flights make up for almost half of the domestic flights market[13]. The most popular routes include Honolulu - Kahului (162 km), Atlanta - Orlando (720 km) and Las Vegas - Los Angeles (360 km)[14]. Therefore, the market application of ElectriFly is possible both with and without a mid-air recharging system, depending on the route choice. Furthermore, the lacking fast speed railway net in the region suggests that the market opportunities will be increasing[15].

3.3. Identifying Customers

Now that the demand and the feasible market gap have been identified, it is perhaps useful to assess the potential customers that may be interested in all-electric commuter short-haul aircraft, i.e. ElectriFly. The focus can be narrowed down to Europe and Southeast Asia, since these are the primary business model considered, in accordance with the recharging team.

3.3.1. European Airlines

The following show a few charter airlines in the European region that operate from Rotterdam or Amsterdam airport and may be interested in adding ElectriFly to their fleet. The first two are situated in Rotterdam and have frequent 4-8 passenger flights in around the 500km range. The third is another charter operator situated in Schiphol but has several propeller aircraft in its fleet, similar to BinAir, making them the most promising candidates. The fourth customer type is individuals wanting private luxury ownership.

1. **ASL-JetNetherlands Group [16]:** Large charter airline group operating in Rotterdam, also conducting short to medium-haul routes within Europe that fly 500km to 1000km. Although their current fleet is primarily jet aircraft, they have made contracts to purchase 6 all-electric Lilium eVTOL aircraft, a competitor to ElectriFly, showing ASL's efforts to pursue sustainable air mobility in the Benelux.

2. **BinAir [17]:** Headquarters are based in Germany, that primarily operate short to medium-hall routes within Europe. The Fleet consists of propeller and jet aircraft, used to fly a range of around 500km to 100km.

3. **Aerodynamics BV [18]:** A charter airline operating from Amsterdam Schiphol airport, with a large variety in the fleet from small propeller aircraft to Boeing 747s and helicopters. Their wide variety in fleet types including propeller aircraft, and their proximity make them a suitable customer to be interested in ElectriFly.

4. **Fly Aeolus** [19]: An European Air Taxi operator. Mainly covering door-to-door travel model. The company connects smaller and low traffic airport.

3.3.2. Southeast Asian Airlines

The following shows a few main potential customers that may be interested in ElectriFly, first three of whose primary fleet for Southeast Asian routes consists of small commuter propeller aircraft that fly short-haul routes for a low number of passengers. The fourth customer is individuals who are interested in private charter flights.

[13] https://theicct.org/aviation-rail-shift-lower-carbon-mar22/ [Accessed on 01.06.2023]
[14] https://www.oag.com/busiest-routes-right-now [Accessed on 01.06.2023]
[15] https://www.axios.com/2023/05/25/france-us-ban-short-haul-flights [Accessed in 01.06.2023]
[16] https://www.aslgroup.eu/nl [Accessed on 01.06.2023]
[17] https://aviapages.com/company/binair/ [Accessed on 01.06.2023]
[18] https://www.aerodynamics.nl/en/charter/ [Accessed on 01.06.2023]
[19] https://flyaeolus.com/rates/ [Accessed on 01.06.2023]

1. **Asian Aerospace Corporation [20]:** Conducts short-haul routes between the most popular Southeast Asian destinations such as Kuala Lumpur and Hong Kong, one of which was mentioned in Table 3.2. This is probably the strongest case for a potential customer.

2. **AirSWIFT [21]:** Philippine-based domestic commuter airline that operates short-haul routes to small airports and destinations. The main routes are between Manila and El Nido, two islands separated by water.

3. **Sunlught Air [22]:** Offers flights to Siargao islands, and is also a domestic Philippines based airline.

4. **Yugo Private Aviation [23]:** Provides private and charter flights to individuals interested in luxury, based in Singapore. Their fleet consists of similar-sized turbofan aircraft, including the Beechcraft Super King Air 350[24], which is a direct competition to ElectriFly. Since ElectriFly shall be designed to have better performance with respect to such competition, it would make sense to cater to companies like Yugo, who will be interested in improving their fleet.

[20] https://www.asianaerospace.com.ph/home/ [Accessed on 01.06.2023]
[21] https://www.air-swift.com/destination/ [Accessed on 01.06.2023]
[22] http://sunlightair.ph/ [Accessed on 01.06.2023]
[23] https://yugoplus.com/ [Accessed on 01.06.2023]
[24] https://news.yugoplus.com/top-turboprop-aircraft-to-charter/ [Accessed on 01.06.2023]

4. Operations and Mission Profiles

In this chapter, the operations of typical flight missions are given, linked to the market analysis of Chapter 3. First, the mission profiles of the aircraft are defined and overlayed with the Europe market in Section 4.1. Secondly, the operational aspect of in-flight recharging and ground turnaround are elaborated in Section 4.2 and Section 4.3 respectively. Lastly, in Section 4.4, the phases from the mission profiles are expanded in the functional flow and functional breakdown diagrams.

4.1. Mission Profiles

The flight mission profiles were established and will be elaborated in the following subsections. The profiles differentiate for the suitability of specific routes and missions, that is, the distance to the destination and the recharging capabilities at that destination. The following three flight profiles were established: flight without recharging (A), flight optimised for minimising on-ground charging time (B) and flight optimised for range (C). These have been translated into mission profiles as shown in Figure 4.2, 4.4, and 4.5 respectively. With knowledge from the Market analysis of Europe from Chapter 3, an example case of flight routes from Rotterdam Airport is shown inFigure 4.1. The circular range of 600 km shows routes that can be performed with flight profiles A and B, whereas routes outside of the circular range require flight profile C. It should be noted that in this chapter, the required battery capacity per phase is given in (relative) percentages, the exact content of the battery will be calculated as 1459 kWh in Figure 4.3.

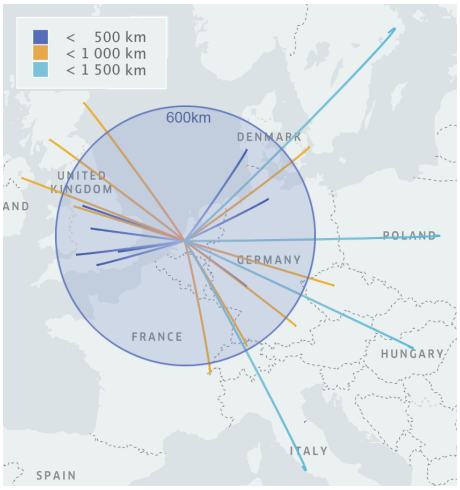

Figure 4.1: *Operations model of Rotterdam Airport*

Flight without recharging (A)

For normal flights, a cruising range of 500 km is set by requirements (REQ-OP-01). A cruising altitude of 15,000ft or FL150 was selected, which will further be elaborated on in Chapter 11. Additionally, a 50 km climb and descent range is assumed, totalling 600 km range in normal operations.
The maximum range of flight profile A requires a charging of 65% on the ground, equalling 1040 kWh. With a maximum turnaround time of 45 minutes, this would yield a charging rate of 1400 kW. Compared to state-of-the-art Tesla supercharging at 250 kW [1], the system required for ElectriFly is six times as powerful. Fast chargers of 1400 kW will thus be a demand onto the electrical infrastructure at regional and larger airports. With the current state of development of Megawatt Charging Systems (MCS) [8] [9], such sophisticated systems can be expected to be in an operational state towards 2035.

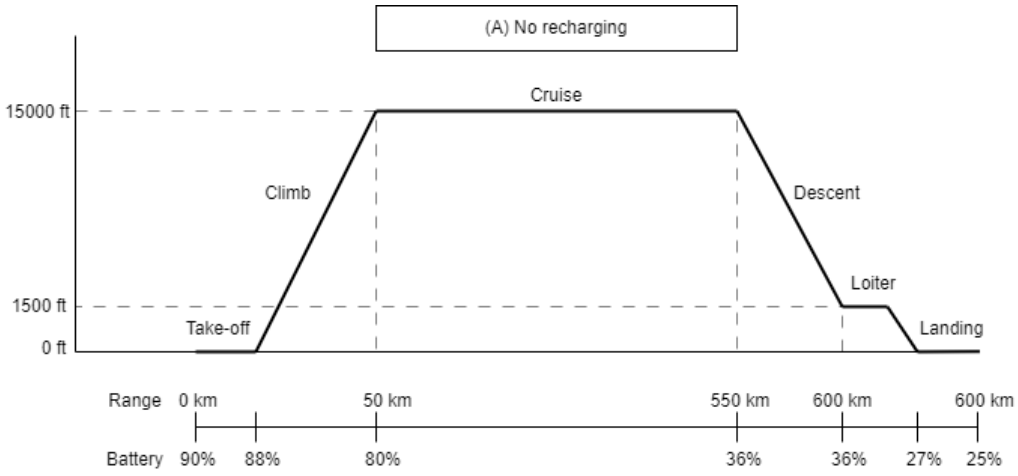

Figure 4.2: *Mission profile without recharging*

[1] https://www.tesla.com/blog/introducing-v3-supercharging [Accessed on 20.06.2023]

Figure 4.3 shows the percentages of battery charge reserved for the different flight phases of the mission profile. In normal operation, a total of 25% battery capacity will always remain available for emergencies. Of this, 10% is allocated for diversion, 5% a margin, and 10% as a depth of discharge margin. The battery includes depth of discharge margins to increase durability and achieve the estimated number of life cycles.

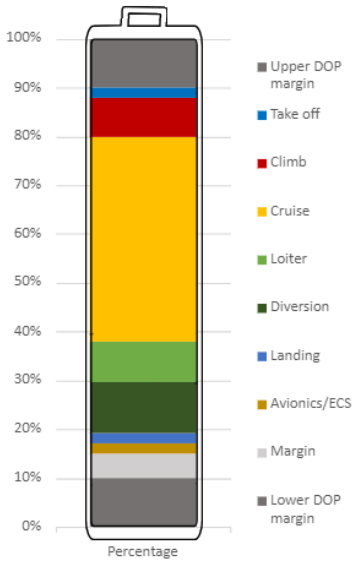

Figure 4.3: *Battery content*

Flight optimised for ground charging (B)

Flight profile B performs a flight with a similar range as flight profile A, but will reduce or remove the demand for the on-ground charging and its infrastructure, by utilising the in-flight charging operations prior to landing. This allows for reaching smaller regional airports lacking in ground recharging infrastructure. Additionally, the turnaround time can be minimized, as in-flight recharging is already performed prior to landing. The drone is capable of delivering 1160 kWh in 40 minutes at a rate of 1.7 MW. This equates to a charging range of 264 km, which is referred to as the recharging zone. Concluding, the performance of flight profile B could reduce the turnaround time reduced, because the on-ground charging process is the most time-consuming aspect, as will be elaborated on in Section 4.3.

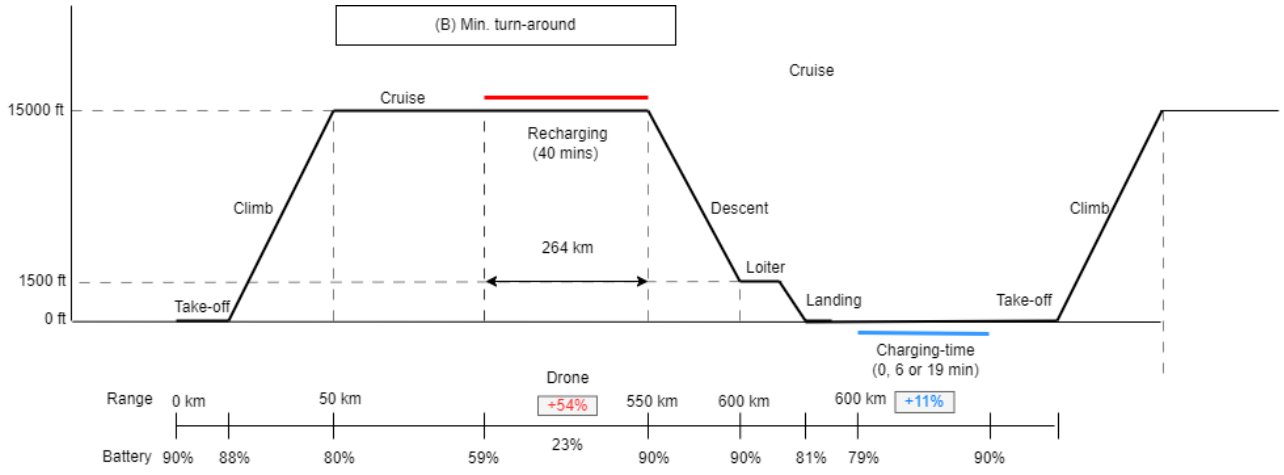

Figure 4.4: *Mission profile optimised for on-ground recharging time*

Flight optimised for range (C)

Finally, diagram C shows flight optimised for range, where perpetual flight can be achieved by recharging n times in the air. For one recharge a total range of 1450 km can be achieved, with an additional 764 km for each consecutive recharge. In this, all of the available energy from the drone is received, which equates to 66% of the total battery capacity, of which 16% is used while flying in the recharging zone. This means that the full charge can be accepted when the battery percentage is 40% or lower. However, 11 minutes of flight time later, at 34% capacity of the battery, the aircraft would face a decision point. At this point, the energy left is equal to the amount of energy required to divert and land. However, this should cause no problems as the drone is required to service the aircraft within 5 minutes upon arrival. Therefore, it is recommended to start the recharging procedure before the aircraft battery reaches 40% capacity. Finally, the ElectriFly will arrive at its destination with the same charge as profile A. To decrease the on-ground recharging time the findings from profile B can be applied to profile C by a second recharge at point A in Figure 4.5.

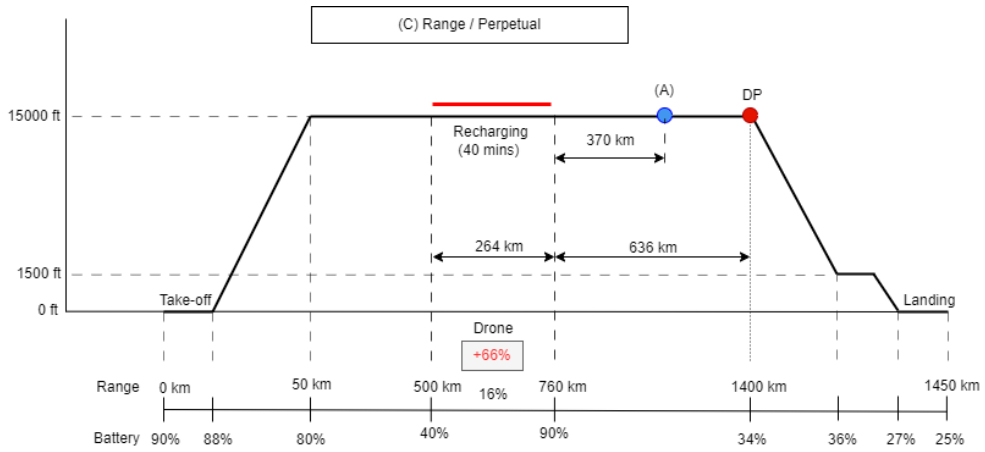

Figure 4.5: *Mission profile optimised for range*

List of assumptions on mission profiles

Table 4.1 shows the assumptions made during the design of the mission profiles. The validity of these assumptions is discussed in Chapter 19.

Table 4.1: *List of assumptions for mission profile calculations*

ID	Assumption
ASM-MISS-01	The aircraft flies in ideal International Standard Atmosphere (ISA) conditions, without weather effects
ASM-MISS-02	The recharging drone mission is not disturbed in terms of time, position and energy.
ASM-MISS-03	The energy required for avionics, take-off, and landing is 2% of the total energy
ASM-MISS-04	FL150 is the optimal cruise altitude
ASM-MISS-05	Regional airports can facilitate a charging rate of 500 kW
ASM-MISS-06	Descent costs no energy
ASM-MISS-07	The descent and climb phase cover 50 km on ground

4.2. Inflight Recharging Operations

Before departure, the flight plan with the desired recharging points will be shared with the recharging system. Then in flight, the drone will meet the aircraft at the desired moment. In this, it is assumed that the drone is flexible in its timing and can account for departure-, headwind- and other delays. To achieve this, the flight plan will be updated in flight to optimise the departure of the drone. The drone will depart from a regional airport located en route. To illustrate the placing of these hubs Figure 4.6 shows the flight path compared to the sphere of influence of the drone. This hub will have a radius of 150 km in which the aircraft can be recharged. In this zone, the aircraft will be recharged for 40 minutes or 264 km at cruise velocity. After recharging the maximum energy provided by the recharging drone equates to 500 km. Taking into account the average wind speed at 15,000 feet (of 18.5 m/s or 36 kts)[2] as a headwind, and a 10-minute delay margin, the maximum distance between the regional airports from which the recharging drone deploys, amounts to 372 km, This means that recharging drones deployed from regional airports within 372 km range of each other can allow the ElectriFly to in-flight recharge.

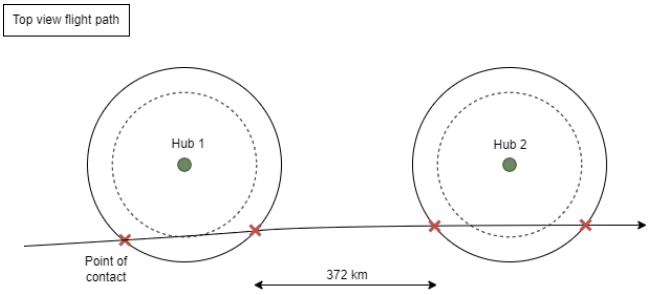

Figure 4.6: *Top view of flight path over the circle of influence of hub*

4.3. Ground Handling

The turn-around time directly affects the efficiency and profitability of the operating airline, as the duration spent on the ground costs money. Turnaround time should therefore be limited in line with requirement OPR-3, to the maximum of 45 minutes. In determining the turn-around time the on-ground recharging time is found with the profiles. These values influence the turnaround time required for the different missions. Additionally, procedures performed

[2]http://large.stanford.edu/courses/2014/ph240/gerrard1/ [Accessed on 20.06.2023]

between docking and undocking have to be assessed.

A top-level overview of all general ground hand-lings on the aircraft is shown in Figure 4.7. Compared to traditional ground handling the difference is recharging instead of refueling. In the diagram, the recharging time on the ground is a variable as it is possible to eliminate the ground charging time altogether with full utilisation of the in-flight recharging system. In the case the on-ground recharging time exceeds 15 minutes it is assumed that the total turnaround time is equal to the on-ground charging time [10].

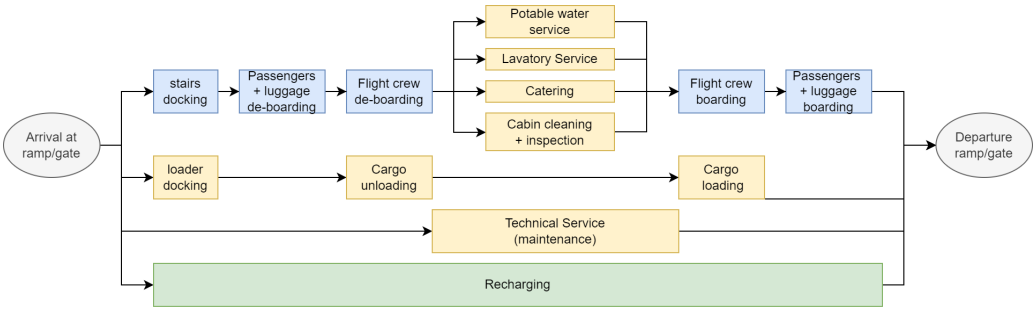

Figure 4.7: *Flow chart of ground handling*

Charging with passengers onboard
Currently, traditional fueled aircraft are only allowed to refuel with passengers onboard in special cases, for specific fuel types and when a fire truck is on standby [3] [1]. For the recharging of propulsion batteries, there are no regulations regarding passengers being onboard yet. However, in electric cars this is possible as there are many systems in place to ensure the safety of passengers while charging. [4]. Therefore, EASA will likely follow in regulation when shown recharging can be performed save, both on the ground and in the air, as will be done in Chapter 7. It is therefore assumed that the aircraft can safely perform on-board and in-flight recharging with passengers on board or (de)boarding, which will be further affirmed with the design of the concerned sub-systems in the following chapters.

Infrastructure requirements
The aircraft demands services and infrastructure from the airports. First of all, standard ground handling equipment used by conventional aircraft needs to be available: examples are passenger stairs and cargo loading trucks. In addition to that, the batteries need to be able to be recharged on the ground. A differentiation could be made between large international airports and smaller regional airports. The former can be anticipated to have special gates with megawatt recharging rate infrastructure, as it is recommended to separate fuelled refuelling and recharging operations for safety reasons. The latter, smaller regional airports can be expected to have a special recharging stand around the airport, as an electrical version of a refuelling truck is not practical. The electrical recharging infrastructure will be less powerful and therefore, flight profile B could allow for limiting the electrical demand in turnaround to these regional airports. [11]

Recharging by cable
For small regional airports, it can be expected that the ground recharging infrastructure will be minimal and slowly developed. For larger airports specialised gates with high-power charging equipment can be expected. A maximal recharge rate of 1400 kW is required from ground facilities when fully recharging in 45 min. In normal operations, this becomes 500 kW for 20 minutes. Compared to present-day electric charging of cars at 250 kW, this would require a system 2 to 6 as fast. This rate has to be facilitated by a cable. This could be done using the recharging interface. However, this would not be beneficial for the standardization of the recharging plugs across airports as a special connection similar to the probe needs to be used. To solve this a connector could be designed to interface standard cables with the recharging interface. In addition to the recharging interface, 2 ports are available which will connect to a standardised plug.

Swapping Modular Batteries
Swapping discharged batteries could increase the window to charge the batteries, spreading the electricity demand on the grid. Additionally, it would reduce the risks of quick and high power charges, and related safety and cycle lifetime issues of the batteries. However, this concept was not used in the final design for the following reasons: Firstly it requires more batteries for the first planes produced. This could turn into a strong point when the life cycles per battery increase, however the batteries are more prone to damage and require specialised equipment. In addition to this, are the storage, and charging of these batteries. Together resulting in more demand placed on regional airports.

[3] https://safetyfirst.airbus.com/safe-aircraft-refuelling/ [Accessed on 20.06.2023]
[4] https://www.tesla.com/ownersmanual/model3/en_jp/GUID-79A49D40-A028-435B-A7F6-8E48846AB9E9.html [Accessed on 20.06.2023]

Additional challenges are: the battery pack sizing will likely not be standardized across the industry, as it is optimised for individual aircraft, and should be designed for easy access for swapping. Lastly, according to regulations, the removal of vital aircraft components like batteries requires inspection [1] [12].

Daily Maintenance

A list of maintenance performed on the aircraft daily is given below [13], of which the first three items are specific for the ElectriFly, followed by some general daily maintenance procedures. Further in-depth maintenance analysis will be covered in the RAMS characteristics in Section 16.4, where a focus will be laid on the unconventional maintenance required for ElectriFly.

- Conditioning of the batteries to the correct operating temperature before discharging, performed by the thermal system described in Section 13.6
- Pre-flight digital inspection of the battery and other systems status.
- Pre-flight visual inspection of the exterior of the aircraft, like propulsion system, (digital twin) sensors and control surfaces.
- Fluids like hydraulics, lubrication and (waste) water require checking and servicing.
- Quick component replacements in the cabin or other aircraft subsystems.
- Routine checks of components or subsystems.
- Record keeping of flights and maintenance, with the use of the digital twin.

4.4. Functional Flows

The functional flow diagram for the aircraft is given in Figure 4.8. This flow describes one mission segment of the aircraft and all the relevant steps. The recharging process on the aircraft, on the ground and in the air are displayed in green, whereas any emergency processes that deviate from the normal operations of the flight are displayed in red. Following the functional flow, the functional breakdown diagram is given in Figure 4.9. This flow breakdown shows all the activities from a subsystem perspective, detailing all the activities required from every subsystem. The recharging system and digital twin subsystem are also detailed in green and yellow respectively.

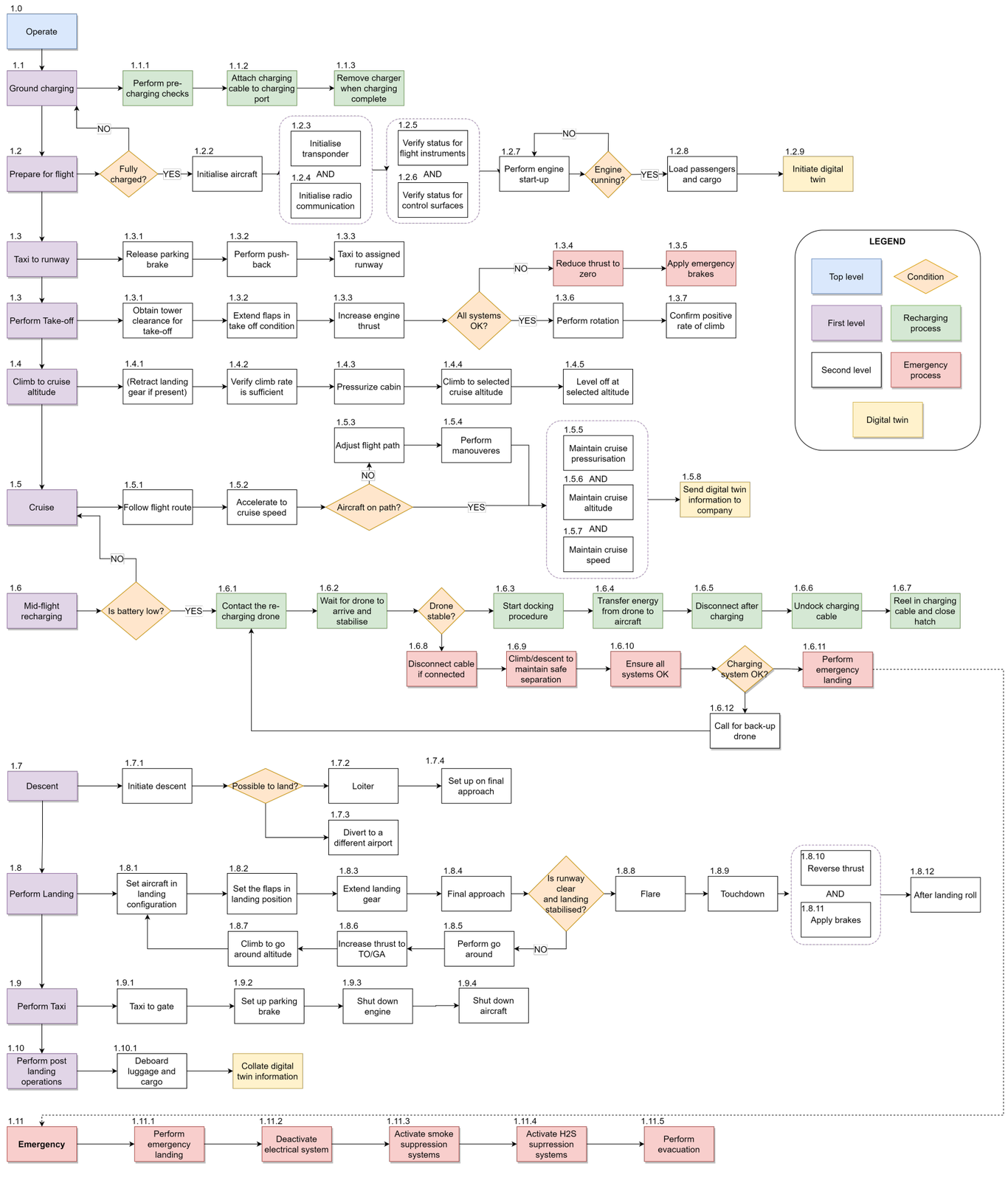

Figure 4.8: *Functional Flow diagram for the Electric General Aviation Aircraft with mid-flight recharging option*

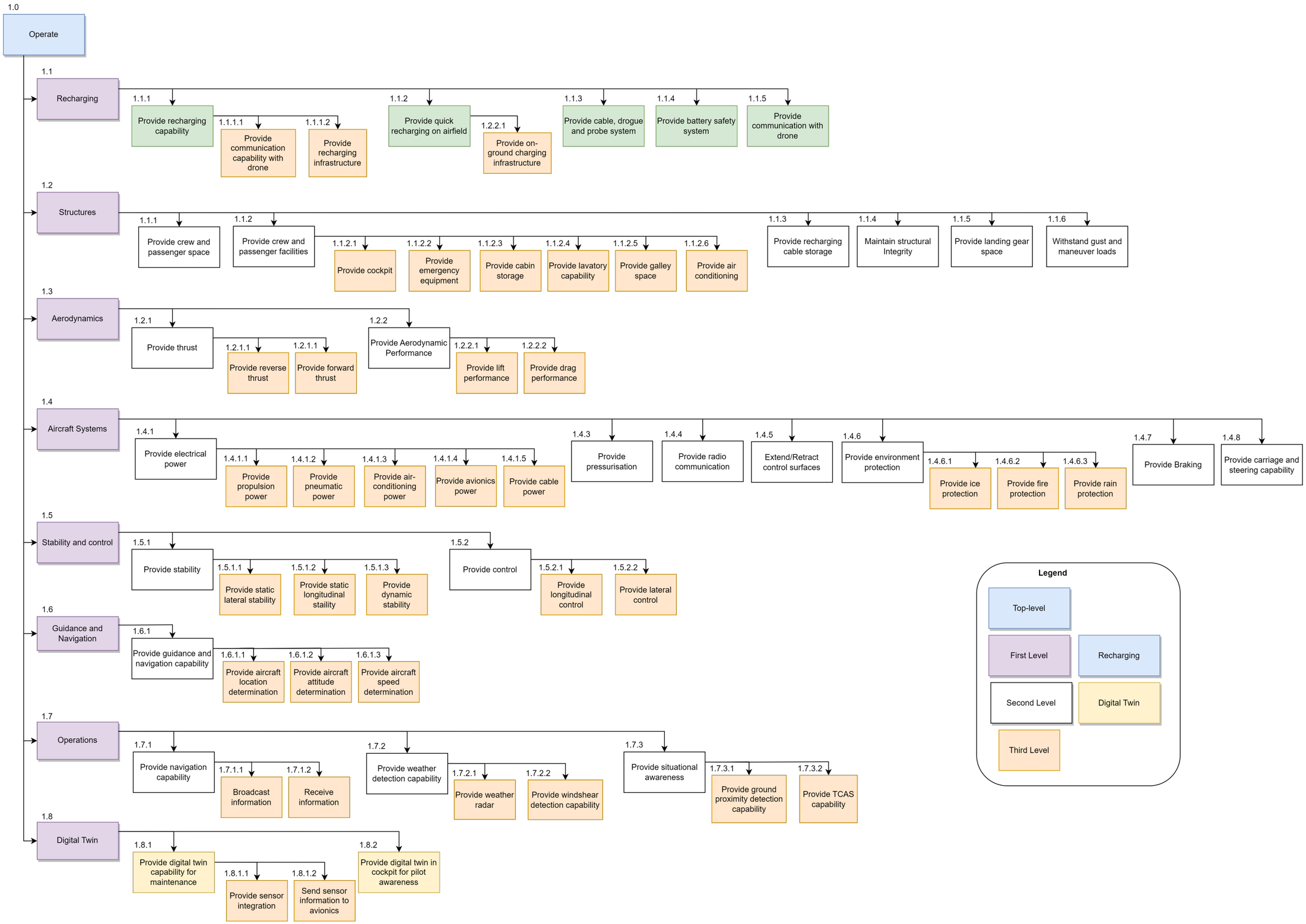

Figure 4.9: *Functional Breakdown diagram for the Electric General Aviation Aircraft with mid-flight recharging option*

5. Resource Allocation

Before the detailed design, it is necessary to assess budgets for critical resources for the given product. The following chapter presents a budget analysis of the mass, cost and electrical energy needed for ElectriFly. The budgets with contingency margins are discussed for mass, cost, and energy in Section 5.1, Section 5.2, and Section 5.3, respectively.

5.1. Mass Budget

Based on the class II weight estimation performed in the midterm report, the design weights for the larger subsystems that fall under the operational empty weight (OEW) of the aircraft were established. At this stage of the design, only preliminary layout calculations were performed, hence the contingency margin was established to be 15% [14] and are presented in Table 5.1. After the iterations of class I and class II weight estimation, the mass budget was also established for the entire aircraft. The battery mass was established from a preliminary analysis only and details on the exact number of batteries are still unknown, especially for the new technology of solid-state batteries, hence the contingency is 20%. The maximum take-off weight (MTOW) is the sum of the components from Table 5.2 and 15% was chosen as it is the maximum contingency that allows the aircraft to be certified under CS23 [15]. The results of the total mass analysis are presented in Table 5.2.

Table 5.1: *The mass budget for subsystems with contingency margins.*

OEW components	Maximum Weight [kg]	Contingency [%]	Design Value [kg]
Wing	495	15	420
Empennage	130	15	110
Gear	389	15	330
Fuselage	1083	15	920
Engine	259	15	220
Systems	659	15	560
Electrical Wiring	200	15	170
Total OEW	3212	15	2730

Table 5.2: *The mass budget for the entire aircraft with contingency margins.*

Mass components	Maximum Value	Contingency [%]	Value [kg]
OEW	3212	15	2730
Battery	4375	20	3500
Payload	1327	5	1260
Total MTOW	8812	15	7490

5.2. Cost Budget

To keep the aircraft competitive in the market, attention has to be paid to the costs. For this purpose, a cost budget is established based on previous preliminary estimations made with the data from the initial conceptual design. This analysis determined the production and development cost based on a method for hybrid-electric aircraft [16]. The outcome of these estimations can be seen in Table 5.3 and Table 5.4 and is depicted by the predicted cost values. A contingency margin of 20% was applied to all costs as they are hard to predict at this design stage. It is expected that after the final design is obtained, the costs for each domain will differ, but the contingency margins should be enough to maintain an acceptable final total cost.

Table 5.3: *Development cost breakdown*

Category	Budget Cost [M$]	Contingency Margin	Design Cost [M$]
Engineering	144.6	20%	120.5
Development Support	23.16	20%	19.3
Flight Test Operations	6.6	20%	5.5
Tooling	48.48	20%	40.4
Total	222.84	20%	185.7

Table 5.4: *Production cost breakdown*

Category		Predicted Cost [M$]	Contingency Margin	Design Cost [M$]
Manufacturing		133.92	20%	111.6
Quality Control		39.36	20%	32.8
Material		79.08	20%	65.9
Avionics		0.096	20%	0.08
Battery & Motor		1.764	20%	1.47
Total	200 units	624.36		520.3
	1 unit	3.1218		2.6015

5.3. Energy Budget

The last part is the electrical energy budget for the primary (propulsion) and secondary systems. The budget is presented in Table 5.5. The energy required for the secondary systems such as avionics, air conditioning and flight control was found in the literature for larger aircraft - Boeing B767 and Airbus A320 [17]. Similar to other budgets, a 20% contingency value was chosen.

Table 5.5: *The energy budget of ElectriFly with contingency*

System	Maximum Energy [kWh]	Contingency margin [%]	Design Energy [kWh]
Propulsion system	1810	20	1448
Other systems	15	20	12
Total	1825	20	1460

6. Battery Analysis

The battery type has a significant influence on how other subsystems develop. This chapter shall examine the expected battery characteristics for ElectriFly in Section 6.1, and the current trends of battery development in Section 6.2. This is followed by the battery selection, where the final battery chemistry is in Section 6.3, and its expected integration with the aircraft is described in Section 6.4.

Due to the iterative nature of aircraft design, it is necessary to define the initial parameters upon which the design will be based on. Battery selection is one of the various parameters that are most limiting in terms of development and is, therefore, the first selection made. The design of other sub-systems directly depends on the battery characteristics chosen. However, the requirements for the batteries cannot be analysed without an initial configuration.

6.1. Battery Requirements

In this study, preliminary calculations revealed battery characteristics that are expected to increase the efficiency of the aircraft in order to compete with the existing performance characteristics. These characteristics can be further defined to quantify the power required for the mission. Therefore at this stage, it is important to set up requirements for the battery performance and quantify desired values for some vital properties. The list below provides an overview of these characteristics and what should be achieved in the battery design.

The values presented in Figure 6.1 and Table 6.1 are derived from a preliminary iteration, consisting of initial calculations for the aerodynamic, structural, propulsive and weight. However, due to the nature of aircraft design, being an iterative cycle, these initial inputs are the most reasonable estimates for the aircraft's characteristics at the given design stage. Over the course of this study, these characteristics shall evolve and these inputs shall be refined, with the battery selection defined in this chapter. Therefore, the final energy and power requirements per phase in Table 6.1 shall differ at the end of this detailed design study but it is expected to follow the same trend as shown in Figure 6.1.

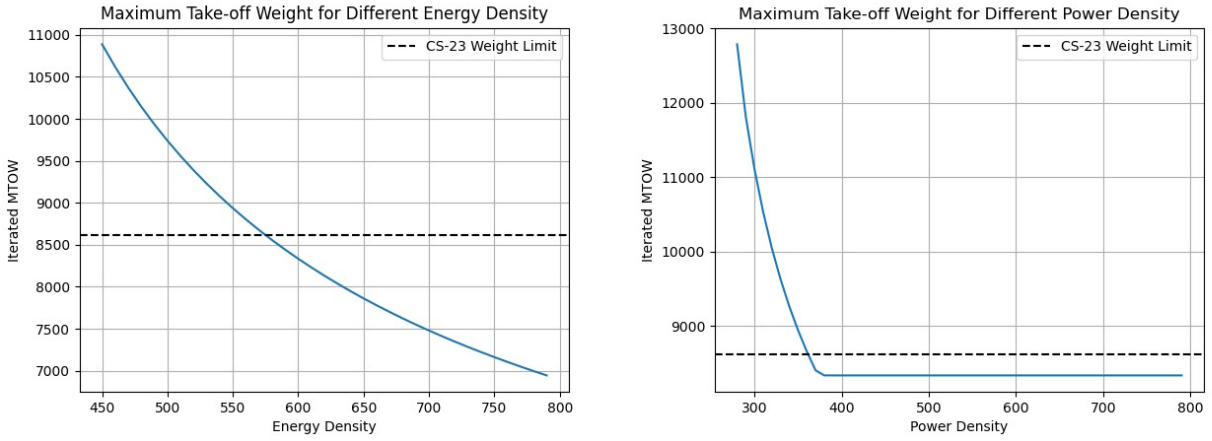

(a) *MTOW vs gravimetric energy density along with the CS-23 limit*

(b) *MTOW vs gravimetric power density along with the CS-23 limit*

Figure 6.1: *Maximum take-off weight (MTOW) vs energy and power density. Figure 6.1a is given for a constant power density of* 500 W/kg, *and Figure 6.1b is given for a constant energy density of* 600 Wh/kg

Table 6.1: *Preliminary estimates of energy and power per phase of Electrifly*

Phase	Energy fractions [kWh]	
Take-off and Climb	164	10.7%
Cruise	816	53.3%
Loiter	167	10.9%
Diversion	310	20.3%
Other [1]	73	4.8%
Complete mission	1530	100%
Battery Capacity	1912	

Phase	Max Power [kW]
Take-off and climb	1165
Cruise	646
Loiter	503
Diversion cruise	819
Diversion climb	**1189**

Energy Density

Energy density is the most important criterion mentioned in the context of electric aircraft, as it directly relates to the aircraft's overall weight. A preliminary iteration is performed for Class I and Class II weight, which considers the conditions for the climb, cruise, loiter and diversion phases, as well as the relationships for different component parts. Figure 6.1a shows the relationship between the maximum take-off weight (MTOW) and the energy density of the battery (Wh/kg). Having performed a preliminary iteration for the maximum take-off weight (MTOW), it was observed that with increasing gravimetric energy density, the MTOW reduces rapidly till a certain point, where the power density of the battery becomes constraining. The iteration between the Class I and Class II weight estimations converges for density higher than the value of 250 Wh/kg. The maximum currently available energy density is provided by Lithium-ion batteries, with a value of 265 Wh/kg. However, this number can result in a very large, heavy and inefficient structure with a very high MTOW, and thus, is not preferred.

According to the CS-23 requirements, the maximum MTOW is set at 8618 kg. As an 8-seater passenger aircraft, this limit is important taking into consideration the cost of certification. Whereas the aircraft could possibly qualify under CS-25, this would significantly increase certification costs and safety complexity [2]. From Figure 6.1a, it can be seen that in order to meet the CS-23 weight limit of 8618 kg, the energy density required is around 570 Wh/kg. Taking into account weight growth during the design process and considering a buffer, a higher energy density of at least 600 Wh/kg needs to be considered.

Power density

The required power that the battery should be able to provide is determined by the most critical phase in the aircraft's mission. As can be seen in Table 6.1, this will be the diversion climb phase which defines a power requirement of 1056 kW. The power density of a specific battery will then determine how many cells of this battery are required to provide this certain power and, therefore, what the battery weight will be. Note that this is only the case if the power requirement is limiting for the battery design. If the energy requirement is the limiting parameter, the battery weight will be determined by the required energy and energy density of the battery. Through further calculations, energy will be the limiting case for the current design and mission profile. Hence, the desired power should be higher than the value at which it actually would become limiting. Figure 6.1b shows that for power densities lower than 400 W/kg, this property becomes constraining and the MTOW rapidly increases. As a result, the battery should have a minimum power density of at least 400 W/kg. The preliminary estimates consider 500 W/kg, and this shall be defined as the power density for a current design stage.

Charging Rate

The charging rate of the battery is also an important constraint as the charging rate determines the endurance of the recharging drone, as explained in Chapter 4. ElectriFly has to be recharged with around 60% of its total energy requirement in 40 minutes by the recharging drone, which gives a required charging rate of approximately 1C, which means the battery can be charged entirely in 1 hour.

Capacity

Battery capacity is an important parameter to determine the depth of discharge for each cycle, which in turn determines the lifetime of the battery. Higher battery capacity (therefore, higher depth of discharge) results in a shorter lifetime but provides higher energy to the aircraft, resulting in weight reductions. This creates a trade-off between the energy capacity that can be provided by the battery vs the lifetime of the battery itself. To preserve battery life, the initial 10% and final 10% of the capacity shall not be used unless in the worst-case scenario where the lifetime of the battery is not a priority (for example, an emergency landing). Therefore, to provide a contingency and extend the lifetime, only 80% of the total battery capacity shall be used. Table 6.1 sums up the energy consumption of the various flight phases and taken with an 80% margin for capacity, the final battery capacity should be 1912 kWh.

Cycle Life

Defining the number of life cycles required for the battery is quite complex as there are multiple factors that have an impact on this. Logically, it is desired that the battery can be used as long as possible without the need for replacement. This is a vital aspect regarding operations, sustainability and minimising costs. On the other hand, this requirement shall not be overestimated as it is uncertain how the development of battery cycle life will evolve in the future. While the depth of discharge has a significant impact, this property also heavily depends on the type of battery chosen and cannot be analysed at this stage. Therefore, a retained and realistic assessment is made, which can potentially change later on. For now, the expectation is that the ElectriFly aircraft will perform 4 flights a day, with 1 recharging cycle in the middle. Assuming 2 recharging cycles for each flight (1 on the ground and 1 in the air), there are 8 recharging

[1] 5% of the energy requirement for the flight phases is considered as the power required for avionics, which includes the environmental control system, pneumatic, and any thermal systems.

[2] https://generalaviationnews.com/2012/09/09/the-cost-of-certification/ [Accessed on 05.06.2023]

cycles in a day. Furthermore, it is assumed that in order to make our mission sustainable, the battery should last for at least 2 years, since the 'heavy' and extensive checks, called C checks, are performed every 18 months to two years, and is a basic benchmark for heavy flight maintenance. Replacing the batteries before this limit shall impose high costs on maintenance as some batteries may be placed under the cabin floor in the fuselage [3]

$$8 \text{ cycles} \cdot 365 \text{ days} \cdot 2 \text{ years} \approx 5840 \text{ cycles} \tag{6.1}$$

From Equation 6.1, this comes down to a desired battery cycle life of approximately 6000 cycles and therefore, this will define the cycle life requirement of the battery.

Identified Requirements

Table 6.2 shows an overview of the technical requirements that were set by the earlier described battery characteristics. These numbers should therefore be taken into account in the battery selection process that will follow in the following section. An important remark that should be made is that there are some more criteria that are relevant regarding battery selection. For example, recycling possibilities and cost are of vital importance, but at this stage difficult to quantify. Therefore these criteria and their impact will be discussed later on for the battery types that comply with the technical requirements that were established.

Table 6.2: *Technical battery requirements*

Parameter	Value	Unit
Energy density	600	[Wh/kg]
Power density	500	[W/kg]
Capacity	1464	[kWh]
Cycle life	6000	[cycles]
Depth of Discharge	80	[%]

6.2. Current Market and Future Trends

With the battery requirements set, the potential candidates can be evaluated. To sketch a picture of the batteries that are currently on the market and evaluate the battery types that are still in development, an analysis is done on the current market and future trends. Research shows that the well-known lithium-ion batteries (LIB) are currently the furthest along in development and have even already been used in aerospace applications [18]. However, even though this battery has gone through quite a bit of evolution, there are some significant limits and restrictions for this type of battery. First of all, there are great concerns regarding the safety of lithium-ion batteries due to their liquid electrolyte. Furthermore, with an achieved energy density of approximately 265Wh/kg, they are not powerful enough to support commuter aircraft in achieving a decent range and performance [18].

Although LIB technology is still improving, recent developments show that there are some alternatives that may be more promising for electric vehicles and the aerospace industry in particular. One of these highly promising alternatives is the solid-state battery. NASA and other research labs and companies are doing research on this specific battery type that uses a solid electrolyte instead of a liquid one. This chemical architecture ensures that the individual cells do not all need their own casing and can therefore be 'packed' much more efficiently whereupon their energy density can increase up to 40% [19]. Furthermore, this solid electrolyte makes the batteries significantly safer than the lithium-ion batteries. However, there still are some challenges regarding the mass production of this battery type as well as achieving a sufficient discharge rate for aerospace applications. According to NASA [19], solid state is state-of-the-art development, but the required technology is not there yet. Chinese battery manufacturer CATL, on the other hand, has actually already launched a 500 Wh/kg semi-solid-state battery that, according to them, will soon be on the market and directly available for the electric aviation industry [20]. Overall, it is noticeable that there are many contradictory pieces of information to be found regarding the current development and applicability of this type of battery.

Two other battery types that are being researched extensively by both scientists and companies lately are the lithium-sulfur (Li-S) and lithium-air (Li-Air) battery [18]. The lithium-air battery has a very high theoretical energy density making it interesting for electric aircraft, however, this battery type would require an air-feed system and pressurization infrastructure of which the technology is still far away [21]. The lithium-sulfur battery also has an excellent energy density, but also this battery type knows some complications regarding its chemical architecture. These include the low conductivity properties of sulfur, parasitic lithium polysulfide intermediate reactions and excessive volumetric expansion during discharge [21]. In conclusion, for both the lithium-air and lithium-sulfur batteries, some significant

[3] https://simpleflying.com/aircraft-maintenance-checks/ [Accessed on 27.06.2023].

research and development steps are required in order to be interesting for the aviation industry.

Solid-state, lithium-air and lithium-sulfur batteries are the correct alternative to consider for the scope of this mission, keeping in mind that the aircraft should be able to operate by 2035 (V. Landgraf[4], R. Darling[5], L. Zivan[6], personal communication). Therefore, it is relevant to perform research on the expected development and performance of these batteries. Figure 6.2 displays the trend of the three earlier discussed battery alternatives with regard to energy density expectation [22]. This graph is important to study as energy density is the most prominent and leading property of the battery and basically forms the key requirement.

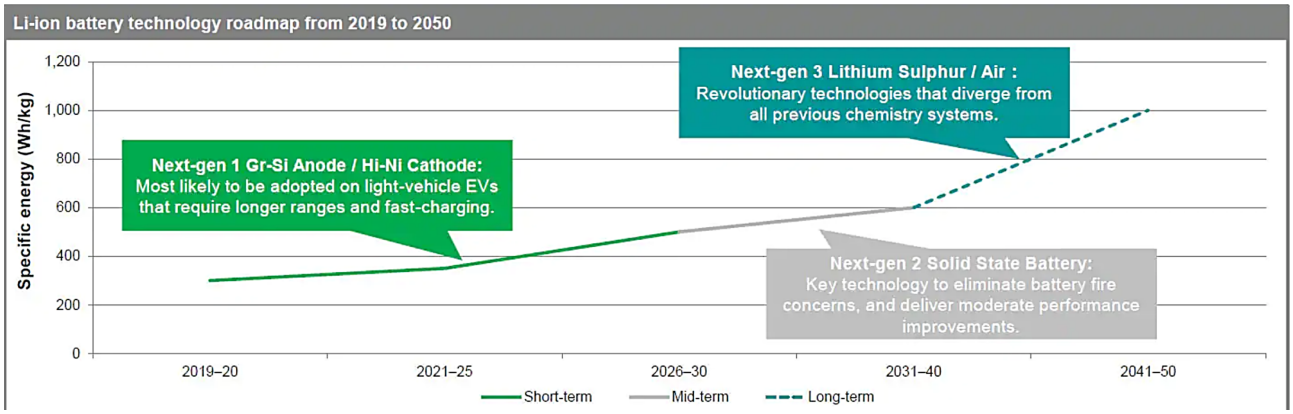

Figure 6.2: *Battery technology roadmap from 2019 to 2050* [7]

Figure 6.2 shows that the conventional lithium-ion battery will not be able to approach a sufficient energy density level before 2035. The solid-state and lithium sulphur/air battery do, in fact, reach the desired value of 600 Wh/kg before that milestone. According to Figure 6.2, the solid-state battery will lead the battery market as a mid-term solution, and the lithium sulphur/air batteries will take over in the long term. However, this shall not occur before 2035 and would also need a highly accelerated rate of development to make it technically and financially viable. Assuming an accelerated rate of development for solid-state batteries, as compared to the rate of development for lithium-ion batteries (between 1980-2020), the solid-state batteries will already be in a high development stage by 2035, and therefore this battery type seems the most logical and perhaps only possible option to choose [22].

6.2.1. Cone of Probability

To get a better picture of the previously outlined expectations and to be confident about the defined assumptions, a probability cone was made. This probability cone is based on the data from Figure 6.2 as well as the personal experience and expectations of the aforementioned experts. The probability cone in Figure 6.3 shows the trend of the three battery types along with their potential energy density range. This range is defined by an optimistic higher-end value and a pessimistic lower-end value. 2035 will be too early to expect lithium-sulfur/air batteries to be applicable in the aviation industry (V. Landgraf, R. Darling, personal communication). Hence, the only option would be to choose the solid-state battery. Figure 6.3 shows that lithium-ion is approaching its theoretical limit. For a solid state, assuming that electrochemical and production issues are not resolved by 2035, the energy density may not be better than 400 Wh/kg (L. Zivan). However, assuming an accelerated rate of development, the best case scenario for solid-state can exceed 600, up to 700 Wh/kg (V. Landgraf).

[4] V. Landgraf, PhD student, Delft University of Technology, working with solid-state battery
[5] R. Darling, Electrochemical researcher at Raytheon Technologies Research Center
[6] L. Zivan, Chief Engineer of Manna Drone Delivery, Former CTO, Eviation

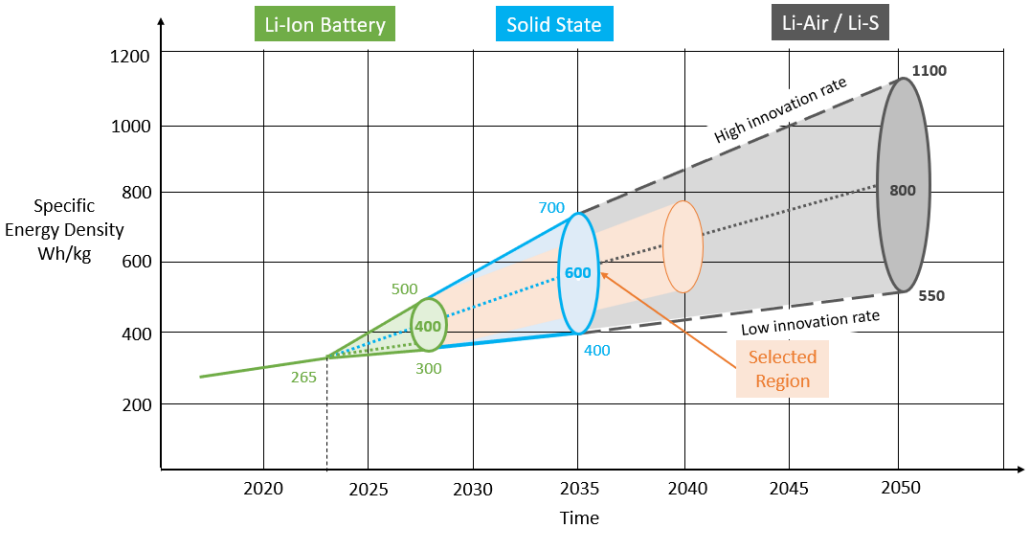

Figure 6.3: *Cone of Probability reflecting the possibilities of energy till 2050. The orange zone represents the most probabilistic scenario.*

6.2.2. Performance of Solid-State on Other Criteria

Although energy density was defined as the key requirement for the battery selection, it is of vital importance to evaluate whether the solid-state battery also meets the other requirements that were set earlier in this chapter.

Power density and Capacity: It is difficult to quantify the exact expectations for 2035, however, due to the bipolar stacking possibility of the solid-state batteries, both the capacity and power density are expected to reach high values [2]. As opposed to cell-by-cell packing in the case of liquid electrolytes, the solid-state batteries can be packed together, reducing weight. Additionally, solid-state batteries will profit from a significantly wider temperature window for the battery cells which is beneficial regarding the cooling requirements of the battery [2].

Cycle Life: Demonstrations have already shown solid-state batteries to achieve 9000-10000 cycles at 1C with a capacity retention of 84.1% [23]. It is expected that this performance will further increase and, more importantly, will also apply to large-scale and high-capacity battery configurations. This latter is especially important regarding ElectriFly's high energy and cycle-demanding mission.

Cost: It is noticeable that at the moment solid-state batteries are still relatively expensive. This is not surprising since this state-of-the-art battery has not been around for long and the production still needs to be developed. However, solid-state technology develops at a significant rate and with a clear market growth [24]. By 2029 the global solid-state market is expected to account for 869.8$ million which is more than four times that of today. Therefore it is fair to assume that by 2035 this battery type will be sufficiently developed to be financially viable [24].

Sustainability: For recycling the battery, there are some challenges due to the new chemical architecture of the battery, however, extensive research has been performed on this matter showing some interesting solutions. These include hydrometallurgy along with direct recycling and regeneration. Both these processes use the benefits of the unique physical characteristics of the solid-state battery in an optimal way [25]. Some further research will have to be done but it is expected that by 2035 the recycling methods will have reached a reasonably high level.

Looking at the overall analysis, it can be concluded that the solid-state battery is well-suited for driving the ElectriFly aircraft and, at the moment, even is the only viable option, keeping in mind the milestone of 2035. It should be mentioned that at a later stage, when lithium-sulfur and lithium-air batteries have made their breakthrough in the aviation industry, they will certainly be considered alternatives. However, this will not be the case during the first life phase of the ElectriFly.

6.3. Battery Components Selection

Various types of solid state batteries exist. This section shall examine the different types of solid-state battery concepts and select an optimum one for ElectriFly. The difference between a lithium-ion battery and a solid-state one solely relies on the electrolyte; in the latter case, this is, as the name says, solid. In this case, there needs to be intimate contact between the electrolyte and the anode material. In contrast to liquid electrolytes, in solid ones, any changes in volume during charging or discharging may affect this contact, which needs to be ensured at all times. In general, the presence of a solid connection between electrodes allows for more flexibility in the choice of the components themselves, which opens a large range of possible combinations, which are shown in Figure 6.4. These components

will be analysed in the following section to choose the best combination.

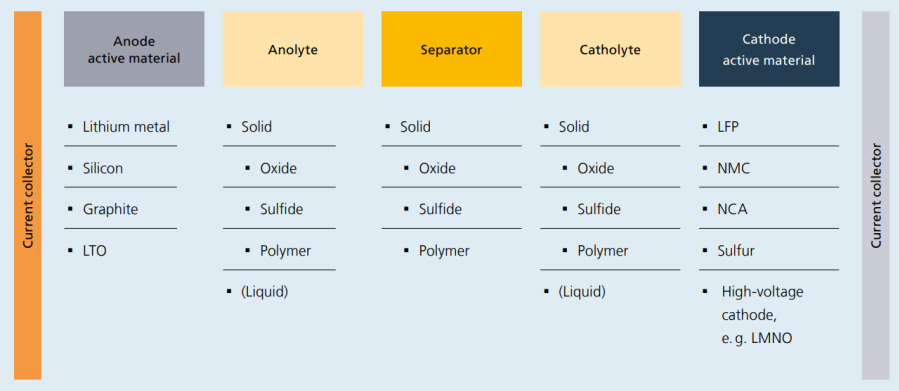

Figure 6.4: *Possible combinations of solid state components [3]*

6.3.1. Anode Selection

With regards to anode materials, there are four main options considered without going too forward into the future. These are graphite, silicon, lithium metal and lithium titanate (LTO). For each of these, some advantages and disadvantages will be reported hereafter.

- **Graphite:** It is the most widely anode material used up until now in lithium-ion batteries but presents limited specific capacity and reactivity with electrolytes. Moreover, it can lead to volume changes of up to 10%, which requires binders to keep the anode connected to the electrolyte.
- **Silicon:** It can work as a stand-alone or as an additive to graphite in the form of silicon oxide or silicon nanoparticles. This is due to it having a very high theoretical capacity, which however comes at the price of a volume change of more than 300%, resulting in a low chemical stability. Investigations are ongoing to try and solve this problem, mainly regarding the use of a matrix structure to embed the particles.
- **Lithium Titanate:** It is the material with the highest chemical stability, leading to a large number of cycles and a fast rate of charge/discharge. However, the price to pay is a low energy density.
- **Lithium metal:** It has the highest theoretical energy density, along with the capacity to enable high voltage and energy cells. However, it is highly reactive and can lead to undesired dendrite growth, which can lead to short-circuiting and thermal runaway.

The main characteristics of the anode materials can be summarised in Table 6.3. In this table, multiple parameters are specified. The specific capacity indicates how much energy the cell can deliver. The potential, compared to the one of lithium, indicates how easy it is for the anode to concede electrons, so the lower, the better. Mechanical stability relates to how much structural complexity needs to be added in order to keep the cell together, related to the change in volume. The chemical stability indicates how easy it is for the components within the cell to interact in an unwanted fashion. Finally, the technological readiness level (TRL) indicates the ease of implementation of the anode material in the battery.

Table 6.3: *Summary of characteristics of possible anode materials*

Material	Specific capacity [mAh/g]	Potential vs Li [V]	Mechanical stability	Chemical Stability	Technological Readiness
Graphite	360	0.1	Low 10%, volume change	Medium, SEI formation	Widely Used
Silicon	3500	0.3	Very Low, High volume change	Low, High loss of Li	Demonstrated as a potential anode in SSB
LTO	175	1.55	High, 1% volume change	High	Demonstrated as a potential anode in SSB
Li-metal	3860	0	High, Negligible volume change	Low Dendrite formation	Challenges of dendrite formation

[7] https://www.spglobal.com/esg/s1/topic/the-future-of-battery-technology.html [Accessed on 05.06.2023]

It can be seen that in terms of delivered energy and mechanical stability, lithium anodes are the most promising, followed by silicon anodes, which have a major disadvantage in mechanical stability and volume change. Therefore, Li-metal and silicon anodes shall be considered. However, before a choice on the best anode can be made, an analysis of the cathode and electrolyte is needed as well to check for the best combination, as the three need to be compatible with one another.

6.3.2. Cathode Selection

Cathode materials can be divided into four main categories. These are NMC/NCA (Nickel Manganese Cobalt Oxides / Nickel Cobalt Aluminium Oxides), Sulfur, LMNO (Lithium Manganese Nickel Oxides) and LFP (Lithium Iron Phosphate Oxides).

- **NMC/NCA**: show the highest performance, further increases in capacity in practical applications require stability improvement. Increasing the energy density will require the substitution of nickel-rich oxides with lithium-rich high-energy NMC.
- **Sulfur**: has a high specific capacity and could be used in combination with lithium metal anode for solid state.
- **LMNO**: have high potential, and are currently used in combination with NMC/NCA offering good stability and reasonably high energy density.
- **LFP**: lowest cost due to low metal and synthesis cost, good safety properties allow direct integration of large volume cells in the battery pack. However, they will likely only be feasible for smaller EVs with limited range and stationary storage applications.

Table 6.4 shows the main characteristics of the cathode materials. Similarly to the anode, high specific capacity and stability are desired. However, when it comes to potential, the cathode benefits from a higher potential as which means it will attract electrons more easily. The technological readiness level (TRL) shows the implementation stage of each material.

Table 6.4: *Summary of characteristics of possible cathode materials [3], [26], [27]*

	Specific capacity [mAh/g]	**Potential (vs Li) [V]**	**Stability**	**TRL**
NMC/NCA	>200	3.8	Needs improvement for capacity increase	Predominant in LIB
Sulfur	93-233	2.15	Low but can be increased	In discussion
LMNO	140	4.6	Good	Used as an additive to NMC/NCA
LFP	160	3.3	Good	In development

It can be seen that NMC presents the highest specific capacity, and is predominantly used in LIBs, followed by LFP, whereas sulphur is not readily being developed and LMNO is used as an addition to existing NMC cathodes. Therefore, NMC and LFP based cathodes shall be considered.

6.3.3. Solid Electrolyte Selection

The electrolyte or the active material largely influences the structure, compatibility and properties of the battery. Its composition can be shown in Figure 6.4. In theory, a solid separator would be enough to impede unwanted reactions between the electrodes. However, the presence of anolytes and catholytes is advantageous for a number of reasons. Indeed, firstly these two components increase the lifetime of the battery. This is because, in this case, the reactions occur within the electrolyte itself rather than at the electrodes, minimising their degradation and thus reducing the maintenance effort and cost while increasing the battery longevity. Moreover, the use of these elements increases the response times, as they have a high ionic conductivity, which decreases recharge times.

There are three main types of solid electrolytes: oxides, sulfides and polymers, each divided into sub-classes based on the chemical composition. For each of these groups, advantages and disadvantages will be presented hereafter, along with a brief discussion of the elements in the sub-classes.

1. Oxides: The main advantage of oxides is their high mechanical stability while at the same time guaranteeing stability toward the lithium metal anode without the need for additional coatings in the case of the Garnet-type. However, this type of electrolyte requires very high sintering temperatures during manufacturing and processing, greatly increasing costs.

- **Advantages:** Oxides have high mechanical stability. They are also chemically stable while presenting a large electro-chemical window, allowing for high-voltage cathodes. Moreover, the overall stability allows for less strict processing environments, as they do not require dry rooms for manufacturing. Finally, they are insensible to temperature changes, being able to work even at high temperatures.
- **Disadvantages:** The main disadvantage of oxides is their brittleness, while at the same time having low ionic conductivity. This entails that the material needs to be kept under high pressure to maintain contact between electrodes and electrolytes. Finally, relatively high sintering temperatures are required to manufacture them, which is highly energy intensive process, and related costs.

Therefore, the low ionic conductivity, contrasted by the large electro-chemical window, makes them ideal as separators but impedes their use as catholyte and/or anolyte.

2. Sulfides: Scientific interest has been growing in this class of electrolytes with the discovery of sulphide-based materials that show ionic conductivity similar to or higher than liquid electrolytes. It is one of the most promising electrolyte concepts for automotive applications.

- **Advantages:** The main advantage is high Li-ion conductivity (higher than oxides). With superior conductivity, Li-ions can exhibit higher mobility. The softness and plasticity of the materials also ease production processes and avoid high-temperature sintering steps. The plasticity also enables better volume change compensation during cycling.
- **Disadvantages:** Sulphides have low electrochemical stability and can react in contact with lithium metal. They are also unstable in air, forming a toxic gas hydrogen sulphide (H_2S) in air. This makes their processing in dry rooms (with an inert atmosphere) necessary in the initial manufacturing steps, and is an important risk.

Therefore, the high ionic conductivity and low volume change make sulphide a promising concept for a solid-state electrode. This is especially advantageous for high charging rates, which is an important design constraint for Electri-Fly to be recharging mid-flight.

3. Polymers: Polymer electrolytes can be seen as an intermediate technology between liquid and solid electrolytes. They are increasingly being explored due to their advantages in cost, flexibility and processing.

- **Advantages:** The main advantages of polymer electrolytes are cost, mechanical stability, and extended calendar life. The processing is well established, making it a cost-effective process for large-scale production.
- **Disadvantages:** Polymer electrolytes have the lowest ionic conductivity, which is insufficient at room temperature. An operating temperature of more than 60deg is required for reasonable ionic conductivity. Compatibility with high-voltage cathodes and dendrite resistance with lithium is also a challenge.

6.3.4. Conclusive Components Selection

To select the optimal cell concept, individual components must also be compared together in terms of compatibility and processability.

1. **Anode:** Lithium metal as an anode provides the highest energy capacity, whereas silicon demonstrates low chemical stability with a volume change of more than 300%. This puts constraints on the casing of this battery, which shall account for such a volume change without affecting the physical properties of the aircraft. Therefore, lithium metal seems like the most promising anode material. With a polymer coating, lithium can be paired with an oxide or sulphide-based electrolyte.
2. **Cathode:** NMC is the most promising cathode material and tends to be used in high-energy applications such as automotive. They can be coated to increase their electrochemical stability.
3. **Electrolyte:** The electrolyte type highly influences the type, processability and characteristics of the battery. Figure 6.5 shows the radar charts for the three different types and their ionic conductivity, long-term operational stability and suitability as a catholyte, While oxide has high Li metal compatibility, only certain types of oxides are compatible with lithium metal. Sulphides show the highest ionic conductivity, and suitability as a catholyte, however, may react with lithium. However, this challenge can be tackled by coating the lithium anode with polymer coating. Moreover, manufacturing poses a less severe challenge than the challenges posed by the high sintering temperature for oxide processing. Therefore, a sulphide-based electrolyte is considered the most optimal solid electrolyte for Electrifly.

   Within sulphide electrolytes, four types of sub-classes exist, that is, LPS, Thio-LISICONs, LGPS, and Argyodites. Argydodites show the highest market potential and show suitability as a catholyte, anolyte and separator.

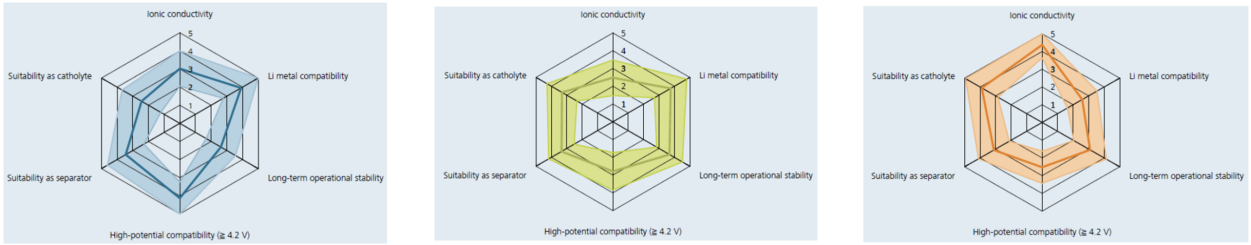

Figure 6.5: *Radar charts of three electrolyte types, with oxide electrolyte in the left, polymer in the middle and sulphide in right [3]*

A lithium-metal (with polymer coating) anode with a sulphide-based electrolyte (Argyodite) and an NMC cathode is considered the most optimal battery configuration for ElectriFly. This is also known as the LiSu concept. By completely omitting a liquid electrolyte, this concept takes advantage of the high ionic conductivity of sulphide electrolytes. A diagrammatic schematic is given in Figure 6.6. Table 6.5 shows the specific performance characteristics of the chosen battery.

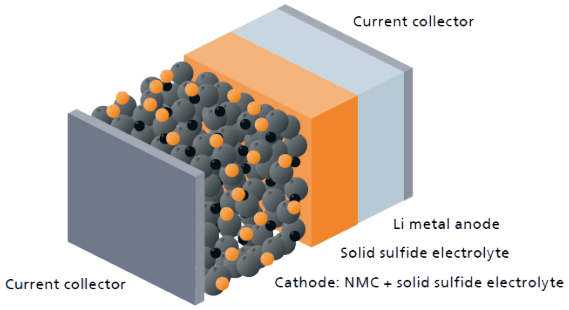

Figure 6.6: *LiSu concept: selected battery for ElectriFly[3]*

Table 6.5: *Battery Overview*

Parameter	Requirement	Battery Property
Energy Density [Wh/kg]	600	600
Power Density [W/kg]	400	500
Cycle life	6000	10000

6.4. Battery Sizing

Now that a battery cell has been designed, the battery system that will power the aircraft can be determined and sized. This section shall discuss the implications of integrating the solid-state battery with the aircraft, and the sizes of the battery modules for the aircraft.

6.4.1. Battery Configuration

The requirements for the number of cells and their configuration come from the total energy needed for the mission, which determines the capacity needed in the battery packs, and the most constraining value for the power required, which determines the voltage and the amperage. The formulas for energy and power are hereafter given in Equation 6.2. In order to reach the required voltage, it is necessary to connect cells in a series configuration, connecting the positive and negative poles of adjacent cells. While doing this, the capacity remains unchanged while the internal resistance adds up. To increase the capacity, it is necessary to connect the positive poles of adjacent cells together in a parallel configuration.

$$E_{tot} = E^* W_{bat} = C_{batt} U_{nom} \tag{6.2}$$

$$P_r = U_{nom} I \tag{6.3}$$

Voltage: Lower Bound

The values for the total energy and constraining power shall be calculated for the final configuration. Starting from the energy, there are two unknowns, namely the voltage and the capacity. One of the two values needs to be set in order

to find the other. The voltage is initially estimated as the batteries need to be at least able to provide enough voltage to power the engines. The motor voltage, as will be explained in Section 9.4, is set to 580 V, which hence gives a lower bound on the voltage needed in the battery pack.

Voltage: Upper Bound

For aircraft, with a high energy requirement, it is preferable to have a step-down voltage from the battery to the motor, as this only entails a rather lightweight DC/DC converter instead of a rather heavy one that needs to upscale the voltage (T. Tomažič [8], personal communication). Moreover, since the power loss in cables is related to the amperage with a quadratic relationship as given in Equation 6.4, to minimise power losses the amperage must be minimised. Notably, this equation is also dependent on the resistance of the battery. In conclusion, the voltage should be as high as possible, and an upper bound for the voltage is needed.

$$P_{loss} = I^2 R \tag{6.4}$$

However, when the voltage increases, more cells are put in parallel, which increases their internal resistance. This also causes loss while at the same time hindering the flow of electrons. Moreover, a higher voltage entails a bulkier and more complex converter. Therefore there must be an upper limit that limits the disadvantages while at the same time maximising the advantages. By looking at current and future electric vehicles, both aerial and terrestrial, it is found that no vehicle is yet able to operate at voltages higher than 800 V[9], both due to battery and to motor limitations. Therefore, it was decided to use this value for the battery pack, which was validated by Robert Darling[10].

Cell Capacity:

Once the value for voltage is set, the needed capacity can be found straightforwardly. This value is calculated as 1860 Ah. On a cell level, the chosen cell, as explained in Section 6.3, has a potential difference of 3.8 V between the electrodes. Regarding the capacity, due to the limited time scope, the chemical composition of the cell components was not examined to translate the specific capacity found in Section 6.3 into the cell capacity. Instead, it was decided to estimate the weight based on the weight estimate of lithium-ion cells and derive the capacity according to the rewritten formula for energy given in Equation 6.4.1. In Equation 6.4.1 C is the battery capacity, E^* is the energy density of the battery, W_{cell} is the weight of the battery cell and U_{cell} is the voltage of the cell.

$$C = E^* W_{cell} / U_{cell}$$

The capacity can then be verified by comparing it to the specific capacity. Indeed, since this is higher than for lithium-ion batteries, it is expected that the cell capacity will also be higher.

Cell Sizing:

The aforementioned battery is a cell concept in development, and has not been developed on a large scale. Therefore, no precendents exist for the expected physical dimensions of the LiSu concept. Moreover, no fixed precedents exist of battery module sizing of electric aircraft, precedents from the battery module structures are derived from commercial electric vehicle models such as Tesla, which uses the lithium ion battery. Several physical parameters can be derived based on the cell type. It is assumed that solid-state battery shall have similar (if not better) properties than LIB.

1. Tesla uses the 18650 cell widely for automotive applications, which is 18.4 mm in diameter and 65 mm in length.

2. A cylindrical cell is considered over a pouch (flat) cell, as it is easier to install due to its negligible thickness due to lower weight and volume. Indeed, for the latter, the decrease in thickness is made up by the increase in the other dimensions, which also increases the weight, which stabilises in a range of 75 g to 225 g. On the other hand, the cylindrical cell averages around 45 g in total weight[11].

3. SSB have a significant advantage over LIB in that due to the absence of liquid electrolyte, every cell does not require a casing. In SSB, a casing around each cell is not needed, as the electrolyte is solid and, therefore, it does not need to be constrained in a certain space as for the case of liquids, and is known as 'Bipolar Stacking' [3]. This difference can be seen in Figure 6.7.

Therefore, on a cell level, the weight for the newer battery type can be up to 30 to 40% lower[12]. To remain on the conservative side, only a weight reduction of 20% is accounted for, with the cell mass being then 36 g. With this weight, the capacity is found to be 5.68 Ah, which is higher than the one commonly found in lithium-ion cells. For instance, the capacity of a Li-ion 18650 cell is about 3.87 Ah.

Module Sizing:

With the cell characteristics defined, the battery pack can now be configured based on the cell voltage and capacity.

[8] Director of Engineering & Programs at Pipistrel

[9] https://insideevs.com/news/580829/ev-industry-shifting-to-800-volt-2025/ [Accessed on 14.06.2023]

[10] Electrochemical researcher at Raytheon Technologies Research Center

[11] https://www.onecharge.biz/lithium-cell-format/ [Accessed on 14.06.2023]

[12] https://www.nasa.gov/aeroresearch/nasa-solid-state-battery-research-exceeds-initial-goals-draws-interest [Accessed on 14.06.2023]

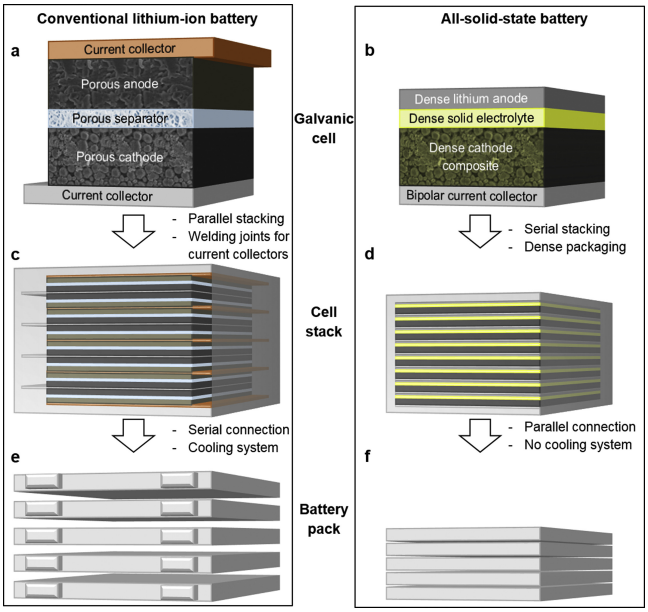

Figure 6.7: *Bipolar Stacking for solid-state battery concepts [28]*

From a manufacturing and maintenance point of view, this would not be beneficial as all of the cells would have to be assembled in bulk and put in the aircraft as a single element. Therefore, the modular approach from Tesla is considered. The car manufacturer splits the batteries into a number of modules, all of the same size, for ease of manufacturing. These modules are an agglomerate of cells in a smaller size to be more manageable, which are then connected to one another to create the battery packs. This helps the production and installation of the vehicle, as well as greatly reducing the maintenance effort. In case a cell failed and modules were not defined, then all of the battery packs would need to be removed at once to replace the single cell. On the other hand, by using modules, these components can be singularly removed[13]. The configuration would then be as shown in Figure 6.8, where it is visualised how the energy increases when more cells are put together into a module, then into a series of modules which make up the battery and finally a number of parallel module/batteries which make the battery pack.

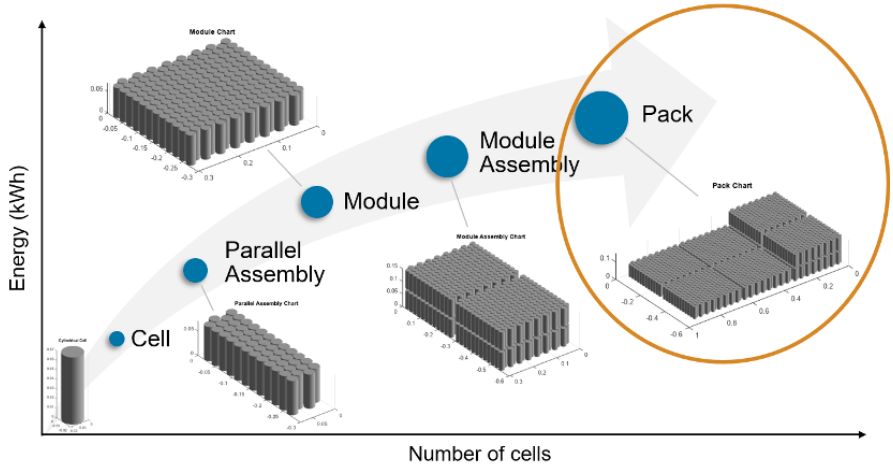

Figure 6.8: *Configuration from cell to battery pack*[14]

Two approaches can be considered to design the cell and module configuration and design. A bottom-up approach, where the configuration of cells within a module can be chosen, or a top-down approach where the number of batteries can be chosen first, which would then derive the cell configuration within a module. The latter approach is chosen as space on an aircraft is limiting, and therefore the volume on a battery pack is more constraining. Three main factors, redundancy, internal resistance and stability, are considered.

1. **Redundancy:** Normally, it would be advantageous to have more than one battery so as to have redundancy to failure. Indeed, the minimum number that is set for the aircraft is 2, as that would guarantee a minimum level

[13] https://resources.altium.com/p/how-tesla-rethought-lithium-ion-cells-through-modular-design-and-vertical-integration [Accessed on 10.06.2023]

of safety. However, this is not enough, as that would entail that if one battery were to fail, then the mission would see its range halved as the capacity becomes half. Therefore, the more batteries, the better from a safety perspective.

2. **Internal Resistance:** However, a disadvantage is present when more batteries are connected in parallel. This is the fact that the internal resistance is inversely proportional to the number of parallel connections. Therefore, the higher the number of connections, the lower the resistance. This is problematic, especially in recharging, as there would not be a high enough resistance to slow it down, and therefore overheating could follow. Since recharging is done per battery and not per module, it would be better to have more parallel connections within a module rather than more modules connected in parallel.

3. **Stability and structures:** In order to take advantage of the high aspect ratio of the aircraft, and reduce span loading, an internal requirement is set in Chapter 12, where it is stated that 50% of the battery pack's weight must reside in the wings, while the remaining 50% has to be in the fuselage. Ideally, 100% of the battery weight would be in the wing, as the distance to the engines would be minimal, and so would the cable loss. However, this is not possible, as the loads on the wing would be too high, and the batteries would go from providing bending relief to causing downward bending. Moreover, by having a lower mass toward the wingtips, the controllability of aircraft improves, as otherwise, it would be difficult to provide roll damping.

Thus, considering all these factors, 4 battery packs are selected: two in the fuselage and one in each wing. The specific location of the battery packs shall be estimated by Chapter 12, as it impacts the centre of gravity location.
Therefore, the module can now be sized. The capacity of a battery is given by Equation 6.5. The cells in a module in parallel can then be given by Equation 6.6.

$$C_{battery} = \frac{\text{Total Capacity}}{4} = 458 \text{ Ah} \tag{6.5}$$

$$C_{parallel} = \frac{458}{5.68} = 80.5 \approx 81 \tag{6.6}$$

It is decided to use the same number that Tesla uses, that is, 6 cells in series. The module voltage is given by Equation 6.7, and the number of modules in a battery pack is given by Equation 6.8.

$$V_{module} = V_{cell} \cdot 6 = 3.8 \cdot 6 = 22.8V \tag{6.7}$$

$$N_{module} = \frac{800V}{22.8V} = 35.08 \approx 36 \tag{6.8}$$

The module weight can be found by simply applying Equation 6.2, which results in a mass of 17.38 kg. This can result in the battery pack weight by multiplying by the number of batteries and the number of modules in series. This results in a value of 2503 kg. This excludes the weight of the casing required to encase the batteries. A visual of the module can be seen in Figure 6.9. Hereafter, in Table 6.6, an overview of the configuration is presented, while in Figure 6.9, a visual can be seen. Concerning dimensions, since a cell has diameter 18.4 mm and length 65 mm, the module will be 0.108 m wide, that is, the side where the 6 cells are connected in series and 1.458 m long, where parallel connections happen. The height will be that of a single cell; thus, the module will be 65 mm high.

Table 6.6: *Battery pack defining parameters*

Parameter	Value	Unit
Cell voltage	3.8	V
Cell capacity	5.68	Ah
Cell diameter	18.4	mm
Cell height	65	mm
Cell weight	36	g
Number of parallel cells in a module	81	-
Number of series cells in a module	6	-
Module voltage	22.8	V
Module capacity	457.59	Ah
Module length	1.458	m
Module width	0.108	m
Module weight	17.39	kg
Number of modules in series within a battery	36	-
Number of batteries in parallel	4	-
Single battery weight	625.99	kg
Battery pack weight	2503.94	kg

[14] https://www.mathworks.com/help/simscape-battery/ug/build-battery-pack-cell-balancing.html [Accessed on 18.06.2023]

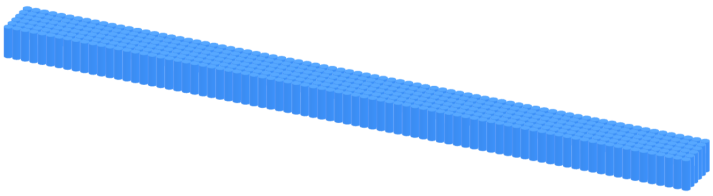

Figure 6.9: *Battery module*

6.4.2. Battery Integration

Now that the battery pack has been sized, it needs to be put into the aircraft. As explained, there will be one battery in each wing, and the remaining two will be placed in the fuselage at positions determined in Chapter 12. The space in the wing and in the fuselage have been determined in Chapter 10 and are shown in Table 10.4 for the fuselage and Figure 10.7a.

Fuselage Positioning:

If one were to put all modules side by side, they would not fit in the fuselage structure as they would be 3.89 m wide. On the other hand, if one were to put them along the length of the fuselage, again, they would be too long. Indeed, the usable fuselage length is only the one of the middle part, shown in Figure 10.3a to have a length of 5.37 m. Therefore, to form the battery, they have to be placed in some other way. By looking at Figure 10.3b, it can be seen that the usable space under the floor can be represented by three boxes, the two lateral of dimensions 0.45x0.20m^2 and the central one of 0.46x0.22m^2. Dividing the full length of 36 modules by the width of one of the boxes, it can be seen that 4 can be fitted side by side, while 3 can be stacked vertically, one on top of another. It must be noted that even though these modules are stacked vertically rather than all in a row, the cable connection remains in a series configuration so as not to decrease the battery voltage. This is not a major challenge, as cabling can be simply moved as long as a positive pole is connected to an adjacent negative one. The same reasoning can be applied to the remaining two boxes so as to fill them entirely with the necessary 36 modules. The length of the battery will be one of a single module, as no module is stacked horizontally along the fuselage. This is decided to leave some space under the fuselage floor for the additional cabling needed for the digital twin, as well as the landing gears. This stacked configuration can be seen in Figure 6.10a. This configuration will be repeated once more to have the two batteries in the fuselage. This will leave a usable fuselage space of 2.45 m. A visual of how the battery packs fit in the fuselage can be seen in Figure 6.10b

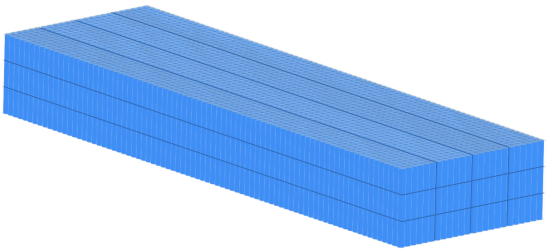

(a) *Fuselage battery pack*

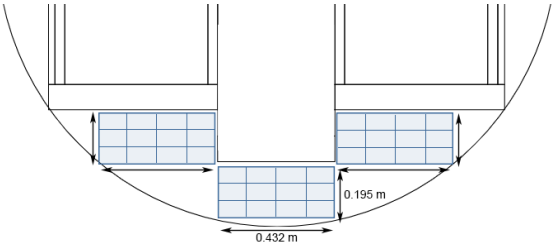

(b) *Fuselage with battery pack installed*

Figure 6.10: *Battery in the fuselage*

Wing positioning:

Regarding the wing, only the wingbox can be considered for storage. This has dimensions as described in Chapter 10. In this case, it is decided to occupy as much space as possible spanwise so as to provide the most bending relief to the wing. Therefore, by dividing the length of the wingbox by the one of a module, it can be shown that 6 of them can be stored horizontally while again keeping the series connection. Taking only the rectangular part of the box so as not to have to be careful when putting modules close to the highly sweep rear part, it can be shown that the maximum number of modules that can be placed along the width is 4. Thus, 8 modules are missing to reach the 36 needed for a battery. It is decided to stack them vertically on top of the first two rows of modules so as not to create a point load somewhere close to the tip but rather close to the root, enhancing lateral stability. This configuration can be seen in Figure 6.11a, along with its positioning in the wing in Figure 6.11b.

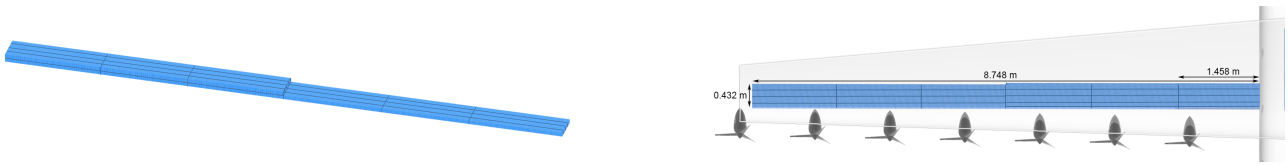

(a) *Wing battery pack*

(b) *Wing with battery pack installed*

Figure 6.11: *Battery in the wing*

Finally, an overview of how the whole battery pack fits into the aircraft can be seen in Figure 6.12.

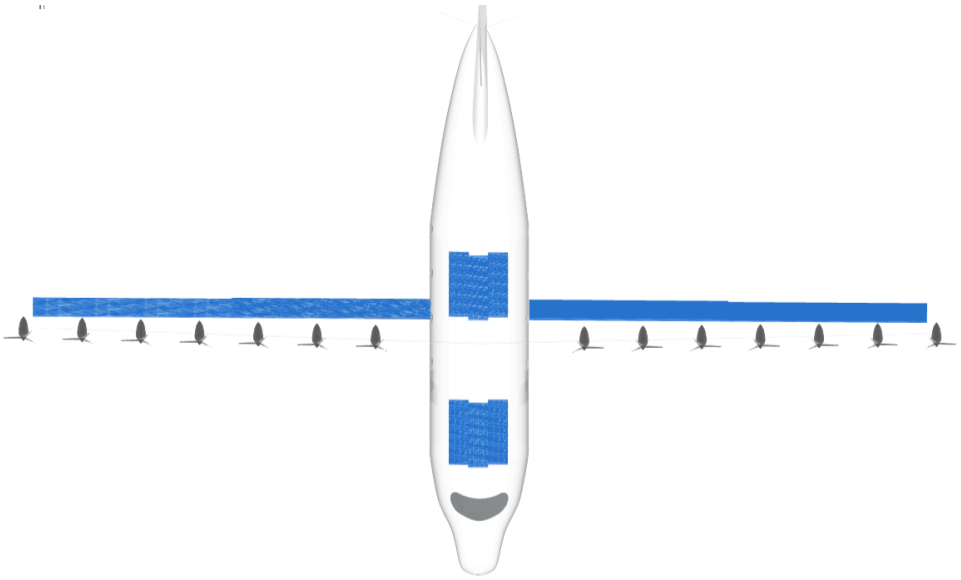

Figure 6.12: *Battery pack in the aircraft*

Operations

For charging the battery mid-flight and maintenance, two aspects are important: the charging rate and the cycle life of the battery.

1. **Charging Rate:** Due to the high ionic conductivity of sulphide electrolytes, the sulphide-SSB can show very fast charging rates. However, with charging rates, the charging rate of LiSu concept today is below 1C. Increasing the charging rate also increases the chances of inhomogeneous lithium deposition, which eases dendrite formation. Controlled heating of the battery can increase the charging rate while ensuring a more uniform distribution. A goal of a 2C charging rate by 2030 is established.

2. **Cycle Life:** Solid-state batteries lose capacity far more slowly than LIB and are therefore predicted to have a higher cycle life than LIB. The lifetime of the battery is highly dependent on several conditions, such as depth of discharge and operating temperature, and is, therefore, complicated to estimate. However, the Coloumbic efficiency of lithium-ion batteries is given as 0.99999 (V. Landgraf, personal communication); this is the loss of capacity per cycle. Therefore, the loss of capacity with every cycle can be calculated over a number of cycles to estimate the battery capacity loss. Therefore, the number of cycles the battery can serve till it reaches 80% capacity (limit defined by IEEE), is given in Figure 6.13 and is 22314 cycles. However, this is the maximum theoretical limit and cannot be achieved realistically.

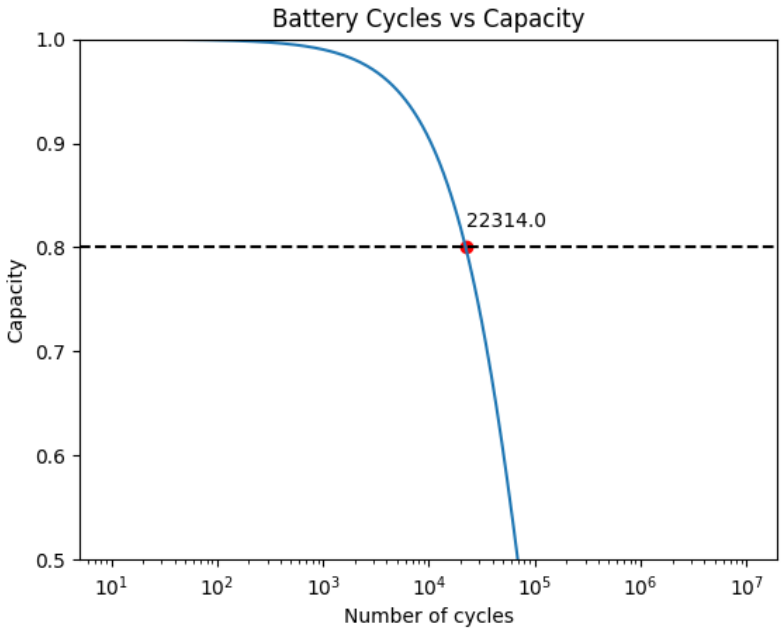

Figure 6.13: *Cycle Life of selected battery*

According to Harvard[15], the cycle life of solid state batteries has already reached 10000 cycles, and it can be expected this can be achieved by 2035[16].

Hazards

The solid-state batteries exhibit higher safety than LIB, due to the absence of an inflammable liquid electrolyte. However, several other hazards still remain: Firstly, The selected battery features a sulphide electrolyte, which is unstable in air and can form poisonous H_2. Secondly, the lithium metal anode can also form dendrites due to lithium deposition on electrodes. This may cause thermal runaway or short-circuiting, which can cause overheating and fire. These risks are investigated further in Chapter 16.

Battery Casing:

To protect the battery from the aforementioned hazards, the battery casing can be designed to take into account all safety aspects. As a minimum, the battery case shall be designed with battery overcurrent protection, battery cooling system, smoke detection system, ventilation system, H_2S absorption system, waterproof and dustproof as defined by IP68 rating and built-in fire suppression system. This battery case shall be integrated with a battery management system (BMS), which shall be connected to the power management and distribution chapters, and further detailed in Chapter 13.

Assumptions: The list of assumptions taken in this chapter are summarised in Table 6.7. The validity of these assumptions is discussed in Chapter 19.

Table 6.7: *Battery analysis assumptions*

ID	Assumption
ASM-BATT-01	The projected energy density of solid-state in 2035 is at least 600 Wh/kg
ASM-BATT-02	The power density of the solid-state battery is at least 500 W/kg
ASM-BATT-03	The cycle life of the battery is 10000 cycles till it reaches 80% capacity
ASM-BATT-04	The cell size is assumed to be similar to a 18650 Li cell
ASM-BATT-05	The weight is 80% of a lithium-ion cell due to the principle of bipolar stacking
ASM-BATT-06	The cost of solid-state battery is 400 $/kg

[15] https://seas.harvard.edu/news/2022/09/fast-charging-over-10000-cycles-future-electric-vehicles-harvard-engineers-solid-state [Accessed on 18.06.2023]

[16] https://www.sciencedaily.com/releases/2021/05/210512115651.html [Accessed on 18.06.2023]

7. Recharging Interface Design

The cable-drogue-probe configuration has been chosen. In this chapter, the conceptual design for the recharge interface is given. In Section 7.1, the application of the recharging interface is explained, after which in Section 7.2 design considerations are made. Thirdly in Section 7.3 the individual components are designed. Finally, an overview of the design is given in Figure 7.3, including the assumptions and validation.

7.1. Operation of the Recharging System

The recharge interface will allow the plane to be recharged during the cruise phase. Therefore, a system similar to a conventional air-to-air refueling system commonly known in military aviation will be designed. The cable, drogue, and probe system were already chosen in the mid-term report. It is vital that the drogue stabilizes the cable and make the connection process as easy as possible for the recharging drone. The drogue will form a semi-rigid connection between the aircraft and the drone, designed to provide safe and reliable energy transfer. A safety system will be integrated that disconnects the drone from the drogue in case of sub-optimal conditions.

The recharging connection process from the point of view of ElectriFly can be described by 10 steps:

Step 1 Drogue is stored in cable unit

Step 2 Drone arrives at trail position as depicted in Figure 7.1

Step 3 Drogue is reeled out

Step 4 Drone has achieved steady, level flight and performs a system check

Step 5 Pilot gives approval, and docking procedure starts

Step 6 Drone arrives at the pre-contact position aided by GPS-positioning and tracks IR-reflectors on the drogue

Step 7 Drone approaches the drogue at the closing rate while correcting its position based on the data from IR-sensors.

Step 8 Probe connects, but the point of connection is still not within the allowed recharging zone

Step 9 The connection point is within the allowed recharging zone as depicted in Figure 7.2, solenoids extend, and energy is transferred

Step 10 Drone leaves charging zone (C) and disconnects

Step 10a Recharging is completed. The drogue is reeled in and the drone returns to trail position, from where it returns to the hub

Step 10b The connection is lost before the required charge is delivered, and the drone returns to step 6

The recharging process for the recharging drone is autonomous. This coordinated flight system is being designed by eCarus and shall see updates in further design. For this, from the moment the pilot has given clearance, the drone has to connect within 5 minutes with a reliability of 99.9%. From the side of the drogue, the connection is aided using thrusters to help steer the drogue toward the probe, and the connection probability is increased by the swivels in the drogue.

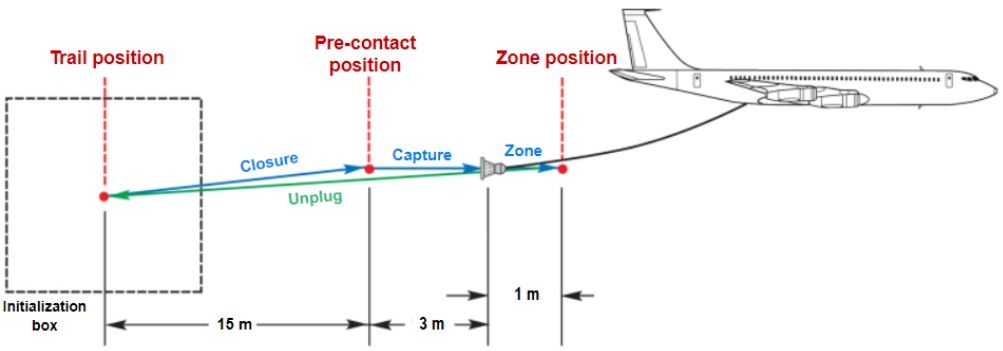

Figure 7.1: *Recharging procedure [29]*

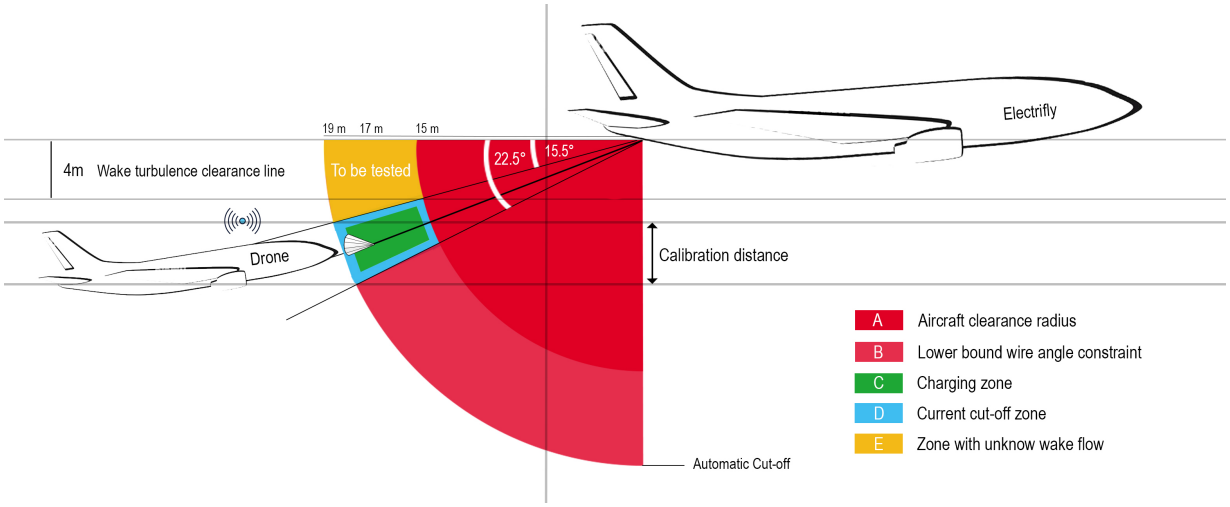

Figure 7.2: *Recharging clearance zones*

As displayed by Figure 7.2, zone C (the charging zone) is the only area where the aircraft can be safely recharged when connected to the drone. The red zones are restricted due to clearance requirements and an angle constraint with respect to the horizon. This latter limit has to be set as the maximum rotation of the drogue with respect to the wire is of 22.5° and therefore, in order to keep the drag net parallel to the free stream, this will also be the maximum angle for the wire. In reality, the cable will have the same angle as the direction of the tension force within the cable. This force at the end of the cable is determined by the weight and drag forces of the drogue. For now, it is assumed they will balance each other out, creating a straight wire.

The blue zone displayed in Figure 7.2 is the area where the drone is still connected to the aircraft, but there is no energy transfer. Here, the current is cut off because the drone is too close to the limits. Indeed, to ensure a safe disconnection, no current will be allowed to flow in the wire. This blue area is hence seen as the safety zone and is recognised by the drone through a continuous signal sent out between the aircraft and the drone.

The lower-bound angle constraint for the wire is set to 15.5°. This angle is derived from a 4-meter turbulence clearance below the aircraft. This provides a 5-degree cone that defines the range of accuracy for the drone to fly in. It is vital to establish this range as the highest accuracy of the autonomous flight system of the drone is required. This is to enhance safety measures by breaking the connection in case the drone fluctuates behind the plane. In addition, by basing the recharging zone on the angle the drogue makes, only two sensors are required to determine the position. One for the angle of the drogue and one for the length of the cable extension.

The total length of the cable is assumed to be 20 meters long. In the military, refuelling pods are used as an optional add-on for certain military planes. The hose in this pod ranges from 15 to 25 meters [1]. Due to the size of ElectriFly, it is assumed that 15 meters is enough distance from the plane. However, at a shallow angle, the 4-meter vertical clearance constrains the use of the cable. Therefore, its total length has to be increased. The 4-meter vertical clearance is partially based on the boom length of the KC-46 tanker plane, which is 8 meters [2]. During the refuelling of another KC-46, the boom obtains a maximum angle with respect to the horizon of 30 degrees. Due to the size of the tanker plane and the use of 4 jet engines [30], it is assumed that this 4-meter clearance is sufficient to avoid the direct wake of the vortexes induced by the ElectriFly aircraft. The vortexes behind Electrifly are expected to be created by wing tips and propeller tips [30]. The real clearance height required can be evaluated more accurately using CFD analysis or by testing the flow in flight which at this point is not possible. Therefore this zone, marked in yellow in Figure 7.2, is for now not included in the potential recharge zone. To create a charging zone large enough to ensure a continuous connection the length required length is assumed to be 19 m. Then finally, to ensure the aircraft will never be pulled back as a result of the backward motion of the drone a total length of 20 m is chosen. This way, there is a 1-meter safety margin to disconnect the drogue in the case of high deceleration.

Similarly, at the point where the wire extension would become less than 15 meters, the drogue is disconnected and the pilot onboard the ElectriFly gets a signal that the drone is advancing onto the plane and the plane needs to accelerate. The pilot will be trained in these evasive maneuvers and military training required for air-to-air refueling.

[1] https://patents.google.com/patent/US6375123B1/en [Accessed on 21.06.2023]
[2] https://www.flightglobal.com/systems-and-interiors/boeing-tankers-refuel-each-other-in-kc-46-milestone-test/127613.article [Accessed on 21.06.2023]

The cable will have to be stored in the plane. However, when the drone moves forward the cable could bend outside of the aircraft which complicates the behavior of the connected system. To prevent this the retraction and extension movement of the wire during recharge is regulated by the velocity of the drone. This could be achieved using springs and dampers in the cable unit. The weight of the cable totals 180 kg and is neglected for now. It is important to keep the stability and controllability of the aircraft in mind for more detailed design. These precautions will significantly reduce the likelihood of collisions and thereby ensure that the energy transfer is as safe as possible.

7.2. Recharging Design Considerations

For the design of the recharging interface, it is important to define what factors should be considered. In this section risks are defined, safety is evaluated and requirements are established.

Safety

Air-to-air refueling in the military is a complex operation with significant consequences in the case something goes wrong. The same will hold when switching to electrical recharging. Although in the recharging operations, safety has been investigated, many risks are undefined. To fill in the gaps, Table 7.1 summarises the most important operational and connection-related risks and their mitigation. Interestingly to note, R-06 refers to the static charge that can build up on a plane. When the two planes come in contact this potential difference can go up to 300 kV [3]. Therefore, the connection should include a point where the static electricity can equalise. Next to this R-02-2 and RSK-PD-05 require the solenoids to become the weak point in the connection. Based on Section 7.2, a compression limit load of 11 kN, a rotation load of 6.6 kN, and a tension limit load of 6.6 kN are assumed.

Table 7.1: *Risk and mitigation for the recharging interface*

	Identifier	Risks	Mitigation
Operational	R-01-1	Drone impacts the aircraft and causes damage	A fixed closing rate will be set to 3 m/s
	R-01-2	The drone fails to comply with the 15 m clearance	Connection breaks, the pilot will be warned and the pilot has been trained in evasive manoeuvres
	R-02-1	The drone failed to manoeuvre the probe in drogue.	The drone will manoeuvre to the standby position and restart the recharging procedure.
	R-07	Drone or plane pulls on cable	Damping in cable unit to mitigate oscillation and weak point in the probe to limit maximum load
Probe-drogue connection	R-05	Short circuit in recharging interface	Both aircraft are equipped with a CPU consisting of a safety switch and fuses in case of a short circuit.
	R-02-2	Failure of locking solenoids makes the probe unable to connect	Use of multiple locking solenoids creating redundancy or diversion
	R-03	Failure of locking solenoids unable to disconnect	The weak point is the solenoid resulting in a maximum load
	R-06	Discharge effect through other parts of the drogue-probe system	CPU will be equipped with discharge wiring to equalise electrical potential over the aircraft and drone
	RSK-PD-05	Failure of rotary swivel	The weak point is the solenoid resulting in a maximum rotational load

To increase the safety of the interface and to aid in connecting the probe with the drogue, the system makes use of multiple sensors. In Figure 7.3, a schematic overview of all sensors is given. The specific sensors are given in Table 7.2. To monitor the health of the batteries and to check for any disruption in the charging, such as short circuits, electrical and thermal sensors are used. This includes the SB and SE type sensors. Sensors that would aid in determining the relative position such as GPS sensors and machine vision (MV) sensors can be used. Here the GPS has an accuracy of up to 0.6 m and could be used up to the pre-contact position [4]. MV can use the IR spectrum to obtain high contrast ratios and accurately determine the relative position of the drogue in the capturing phase. In addition to this, rotation sensors could be used to determine the exact orientation of the drogue and the extension length of the cable. This could be of great help in positioning after the connection is made. Furthermore, force sensors can be used to artificially limit the load in the connection by retracting the solenoids. Finally, there will also be cameras on the back of the plane so the connection procedure can be monitored by the pilots.
The data from the sensors needs to be processed and combined to draw the right conclusions. On the side of the aircraft, this will be done by a control unit and on the side of the drone

[3] https://apps.dtic.mil/sti/pdfs/AD1064517.pdf [Accessed on 21.06.2023]
[4] https://www.gps.gov/systems/gps/performance/accuracy/ [Accessed on 21.06.2023]

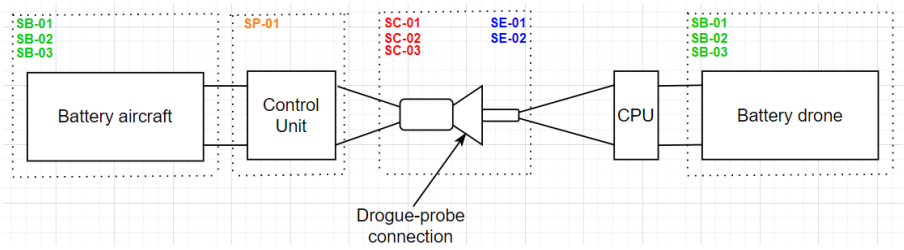

Figure 7.3: *Sensor application in drogue-probe connection*

Table 7.2: *Overview of used sensors for the docking mechanism*

ID	Sensors	Application
SP-01	GPS	Large range navigation of drogue-probe system.
SC-01	MV sensors	close range navigation of drogue-probe system.
SC-02	force sensors	used to measure applied load, can result in separation.
SC- 03	solenoid sensors	sensors used to verify if solenoids are locked to the probe.
SC- 04	rotation sensors	sensors to determine the orientation of the drogue.
SE-01	Charge sensors	sensors measuring volts and current in connection.
SE-02	discharge sensors	sensors measuring the potential discharge in the system.
SB-01	thermal sensor	thermal sensor within the battery.
SB-02	charge sensors	measuring voltage, current, energy capacity of the battery.
SB-03	condition sensors	measuring the battery condition.

Requirements

To finalise, the design considerations, requirements have been set up in Table 7.3. The table includes requirements for the mission, the probe, the cable, and the drogue. Note that not all requirements are used at this stage and serve the purpose of completing the picture.

Table 7.3: *Requirements for the recharging interface*

	Identifier	Requirement
Mission	REQ-PD-MS-01	The drogue-probe system shall have a communication system in terms of system status to both the drone and the aircraft.
	REQ-PD-MS-02	The closing rate of the drone shall be between 2 and 3 m/s.
	REQ-PD-MS-04	The probe/drogue system shall have a vertical clearance of 4 m and a horizontal clearance of 5.7 m.
	REQ-PD-MS-05	The drogue-probe system shall have a system that allows a discharge of 300 kV between the aircraft and the drone.
	REQ-PD-MS-06	The drogue and probe shall be able to determine their relative positions using sensors.
	REQ-PD-MS-07	The drone shall re-dock in case of tension/compression cut-off.
	REQ-PD-MS-08	The drone shall have a maximum of 2 docking procedures.
Probe	REQ-PD-PR-01	The structure of the probe/drogue system shall withstand loads induced during an engagement of 3 m/s.
	REQ-PD-PR-02	In case of extendable probes, it shall be retracted/extended between 5 to 20 seconds.
	REQ-PD-PR-03	The probe's nozzle shall be capable of an off-centre disconnect of 22.5 degrees maximum.
Cable	REQ-PD-CB-01	The drogue-cable shall be inherently stable.
	REQ-PD-CB-02	The drogue coupling shall only rotate due to the drone.
	REQ-PD-CB-03	The coupling swivel ball shall not be mechanically clamped.
	REQ-PD-CB-04	At full extension the vertical and lateral oscillations shall not exceed half the diameter of the drogue canopy. These oscillations shall dampen out to 1/3 of the amplitude after 3 cycles.
	REQ-PD-CB-05	The cable tension/compression shall not exceed 6672 N /11 kN.
	REQ-PD-CB-06	The cable shall be able to carry 1.7 MW.
	REQ-PD-CB-07	The cable shall not exceed the temperature limits of its materials.
Drogue	REQ-PD-DR-01	The drogue shall be aerodynamically stable
	REQ-PD-DR-02	The drogue shall aim towards the probe using thrusters and or swivel connections.
	REQ-PD-DR-03	The probe/drogue system shall not interfere with the air data sensors of the drone.
	REQ-PD-DR-04	The probe shall not fit between the spars of the drogue.
Cable unit	REQ-PD-CU-01	The cable unit shall provide air/liquid to fulfill thrusters.
	REQ-PD-CU-02	The cable unit shall fit inside the aircraft.
	REQ-PD-CU-03	The cable unit shall be able to extend and bring in the cable.
	REQ-PD-CU-04	The cable unit shall include a spring and damper to mitigate oscillations in the distance between the plane and drone.

7.3. Lower-Level Subsystem Design

In this section, the probe-drogue-cable configuration is designed. First, the cable is considered, then the cable unit, continuing to the drogue and finishing with the probe.

Cable

Firstly the cable will be designed. The most important requirement is REQ-PD-CB-06. The cable should support rates up to 1.7 MW. The key constraint afterwards will become REQ-PD-CB-07, as the efficiency of the cable will determine the amount of heat generated. The optimisation of the weight of the cable has to take these requirements into account. To start, the voltage level and the type of electrical current in the wire have to be chosen. The battery of ElectriFly works at 800 volts. For this choice, it will be assumed that the cable losses are smaller than the transformer losses and a specific weight for a step-down transformer of 25 kW/kg will be assumed as discussed with T. Tomažič from Pipistrel. This means 800 volts will be optimal. Then the cable will have to carry a total current of 2125 Amps. Due to the nature of batteries, a direct current is required at the batteries. The total length of the cable should be adequate to allow for safe operation. A clearance of 20 m behind and below the aircraft is chosen as argued before. This length is assumed to be long enough for the drone to avoid the turbulent air created by the motors and wing tips for the design.

The wire materials need to be chosen as well. A commonly used insulator for high-voltage cables (30 kV) is XLPE (cross-linked polyethylene). It has excellent mechanical properties and can withstand temperatures up to 90°C and down to −65°C [31]. Its dielectric is 20 kV/mm, meaning a thickness of 0.04 mm is required. To utilise the mechanical properties of the insulator and ensure the protection of the cable a conservative thickness of 2 mm is chosen. Next to this, a conductor has to be chosen. Commonly used materials are copper, aluminium, and silver. The resistivity[5], density[6] and thermal conductance[7] are tabulated in Table 7.4. To minimise cable losses for the same weight, Equation 7.1 and Equation 7.2 can be used. In those equations, R is the resistance of the cable, ρ_R is resistivity, L is the length of the cable, ρ is the material density, and A is the area of the cable. From this, silver can be eliminated as it is also expensive. Although aluminium has a better combination of resistivity and density it does less well at the dissipation of heat. This makes copper a better choice. Next to this, due to the low resistivity of copper a smaller cross-section is required aiding heat dissipation further. Because of this copper is chosen.

The cross-sectional design of the cable can include many choices. In this cable, compressed air will have to be serviced as well. The compressed air serves as cooling and as a thruster mass. A tube with a diameter of 0.5 cm is assumed to be adequate. The cable will feature a direct current, meaning two sides are required to create a circuit. The main advantage of increasing this amount of multi-core cables (direct current) is that there will be more area for heat dissipation. However, more insulation and space in the cross-section is required, lowering the efficiency or increasing its mass and diameter. Therefore, a two-sided wire with air in the middle is chosen. The cross-section is depicted in Figure 7.4. It is assumed that the cable will behave as if radially symmetric in bending. Concluding the design of the cable, with a weight of 186 kg and an efficiency of 99.86 % which is part of the OEW of ElectriFly.

Table 7.4: *Material properties for conductor material*

Material	Aluminium	Copper	Silver
Resistivity $[\Omega m \cdot 10^{-8}]$	2.58	1.68	1.59
Density $[kg/m^3]$	2600	8960	10500
Thermal conductance $[W/(mK)]$	237	413	403

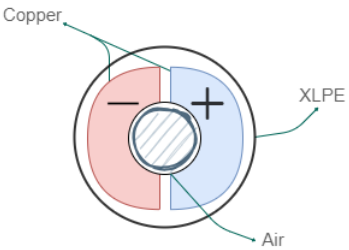

Figure 7.4: *Cross-sectional design cable*

$$R = \frac{\rho_R L}{A} \tag{7.1}$$

$$m = \frac{L^2 \rho_R \rho}{R} \tag{7.2}$$

Cable Unit

The cable and drogue will have to be stored safely inside the aircraft. Figure 7.5 shows an example of such a design. Due to time constraints, a detailed design of the cable unit is postponed and a mass budget of 200 kg is assigned. Interestingly to note, if the copper wire would not consist of individual strands, it would become rigid and therefore hard to roll up. To reduce the force required to bend the cable, the conductor should consist of strands [8]. This also increases the efficiency of the wire according to S. Butterworth (1921), "the sum of the eddy losses in the individual

[5] http://hyperphysics.phy-astr.gsu.edu/hbase/Tables/rstiv.html [Accessed on 21.06.2023]
[6] https://www.engineersedge.com/materials/densities_of_metals_and_elements_table_13976.htm [Accessed on 21.06.2023]
[8] https://blog.keystone-cable.com/a-guide-to-the-different-categories-of-copper-conductors [Accessed on 21.06.2023]

wires shall be less than the eddy loss in the corresponding solid wire" [32]. If the cable can bend with a radius of roughly 0.8 m or smaller, it can fit behind the rear bulkhead. If this is not the case another solution for the cable has to be found. First, this parameter should be taken into account in the conductor material selection. Then other options to the proposed solution in Figure 7.5 should be designed. One option would be to assess the possibility of storing it over the length of the fuselage, another is by using hinges in the cable. For this design, it will be assumed that the cable bends.

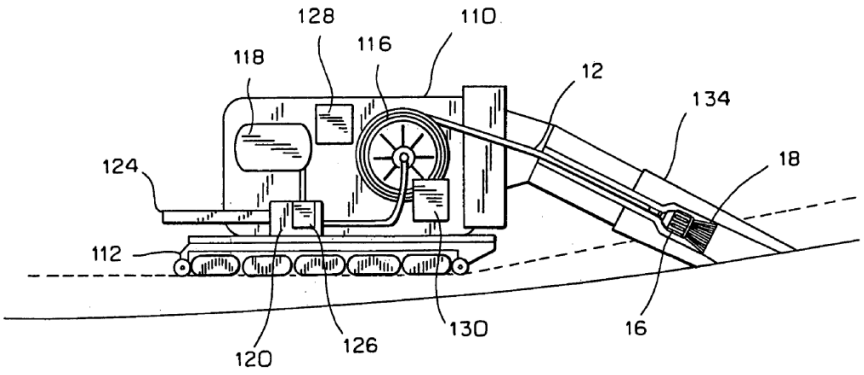

Figure 7.5: *Cable drum unit [33]*

Drogue

The main functions of the drogue will be to stabilise the cable and to aid in making a connection. The unit will look like Figure 7.6. In the figure the parts are listed using numbers. The refuelling hose (12), will be the recharging wire for the application in Electrify. An in-fitting (14) will allow the drogue to rotate around its axis. In addition, there are small holes in the in-fitting (34), these are thrusters working with compressed air. This allows the drogue to make small adjustments and cooperate in connecting. Furthermore, a swivel connected to the housing (16) will allow the drogue to rotate up to 22.5 degrees in all directions. In the housing, some of the sensors can reside. The dragnet (20) features ribs (18) to allow the probe to hit the dragnet and guide it toward the connection. In addition, these ribs provide aerodynamic stability [9]. To stabilise the connection on the aircraft side the dragnet creates tension in the cable. Normally when there is no dragnet the tension in the cable is determined by the weight and drag of the length behind it. This means the end of the cable has little tension and is greatly influenced by aerodynamic instabilities. Next to this the angle of the drogue will be leveled by the dragnet due to symmetry. This is why the dragnet stabilises the cable. To assess REQ-PD-CB-04 analysis with CFD methods or testing is required.

To estimate the drag force on the drogue is assumed to be a cone. The dragnet can feature holes of different sizes, giving different drag coefficients. In [34] experiments on these drag coefficients have been done. A lower drag coefficient is chosen to increase the radius of the drag chute. The wetted area is calculated using Equation 7.3, which is the area of a cone without the bottom. In the calculation a diameter of 35 cm is assumed The drag coefficient chosen is 0.6, this gives a total drag force of 810 N. It should be noted however that the holes in the chute affect the stability of the chute and the CD will have to be chosen carefully to meet REQ-PD-CB-04.

$$A_w = \pi r \sqrt{r^2 + l^2} = 0.29 m^2 \tag{7.3}$$

$$D = C_D \, A_w \, 0.5 \, \rho \, V_\infty^2 = 810 N \tag{7.4}$$

In addition, the drag of the cable can be calculated using Equation 7.5. The formula calculates the drag a cylinder creates perpendicular to its length. Here, the drag coefficient of a cylinder for a $Re = 2.2 \cdot 10^5$ is roughly 1 [35]. To find the velocity perpendicular to its length and to find the drag in the direction of the free stream velocity the same coordinate transformation is required, namely $sin(22.5°)$. This gives a final drag of 183 N. In these calculations, the upstream aerodynamic effects of the body are neglected. Totaling the drag due to the recharging system to 1 kN.

$$D_\perp = C_{D-cyl} L_{cable} D_{cable} \cdot 0.5 \rho V_\perp^2 = 183 N \tag{7.5}$$

[9] https://patentimages.storage.googleapis.com/06/91/47/40dea221758545/US20060065785A1.pdf [Accessed on 21.06.2023]

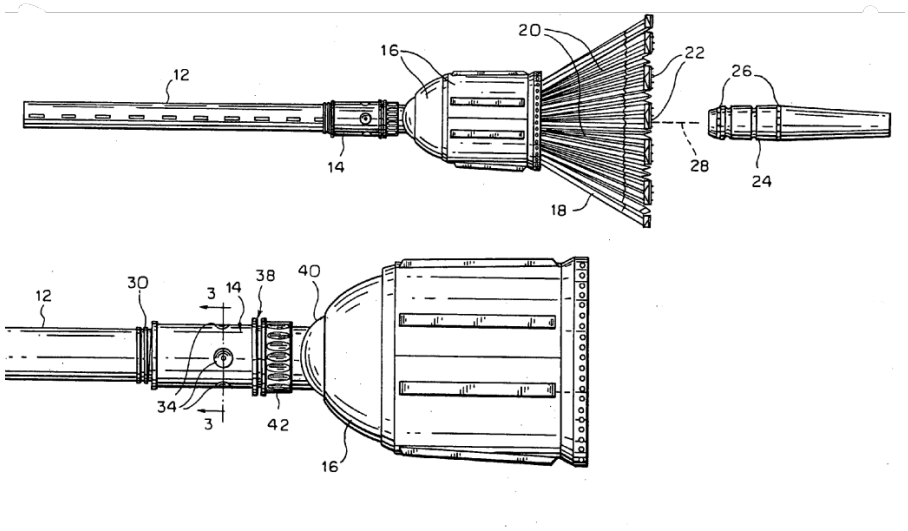

Figure 7.6: *Technical drawing of drogue and probe [33]*

With the weight of the cable, now the angle of the cable can be found using Equation 7.6 and assuming the cable is straight. The found angle with the horizon is significantly higher than the assumed 22.5°. In this calculation, the lift of the cable and the weight is not included. To decrease this angle, either the weight of the cable and drogue should decrease or the drag force of the drogue should increase. Considering the drag of the aircraft in cruise conditions is roughly 5.5 kN this total drag of the recharging system should decrease. However, with the drag of 1 kN the weight of the cable and drogue should decrease to roughly 40 kg. To conclude, for further design it makes the most sense to decrease the drag and weight of the cable and drogue and to increase the mobility of the drogue ball joint.

$$\alpha = tan^{-1}\left(\frac{D_{total}}{W}\right) = 60° \tag{7.6}$$

Probe

The probe connection design has to be well-designed to ensure a high docking success rate while still facilitating the 1.7 MW rate. In normal operation, the drone is required to connect in 99.9% of the cases, the connection has to be easy to disconnect, be safe, and be able to withstand weather conditions. In the cable design, direct current was chosen. Therefore the connection should facilitate the negative as well as the positive wire. To aid the success rate of the connection it is chosen to enforce radial symmetry, omitting the traditional household plug designs. The connection should not stay connected without clamping the connection. So in this, the shape of the connection is the only free variable. A trapezoidal connection is chosen. In this, the core is insulated from the outside. Then the two parts can carry the different poles of the current. On the outside a ridge is present. In this ridge, solenoids could make the connection. A total amount of four solenoids is chosen for redundancy to mitigate the risk of drone connection failure (R-02-2).

In addition, the risk of discharge effects through other system parts (R-06) has to be mitigated. This is achieved using a wire on the outside of the connection on the side of the drogue. The proposed probe connection can be viewed in greater detail in Figure 7.7. Finally, R-01-1 poses an unknown risk. The mitigation presented may give the connection another chance, nonetheless if the same issue occurs again it poses a serious issue as this is a time-sensitive matter. Time could be allocated to allow a second drone to arrive. However, this would mean a window of 30 minutes needs to be created on top of the window present. This equates to 200 km of cruise flight. In theory, you could slow down to the optimal cruise speed to increase endurance and reduce this range in this way, but it would still mean the aircraft would need to do this in normal operations, which is not acceptable. Therefore this issue has to be resolved by testing. The issue can be assumed to resolve on its own for now as the velocity will likely remove all moisture from the probe and moisture present will not include ions meaning it will insulate instead of conduct. It would still prevent a good connection. To prevent corrosion of the copper the connection can be made of silver or be silver plated, as this is a noble metal.

The probe placement is influenced by the aerodynamic effects on the drogue. The probe should be placed anywhere on the front of the drone. It makes sense to place it in the middle of the wingspan to create symmetry. In placing the probe above the nose, the drogue will enter the aerodynamic region of the drone itself or the so-called bow wave.

Therefore, the probe will be placed on the nose of the drone [10].

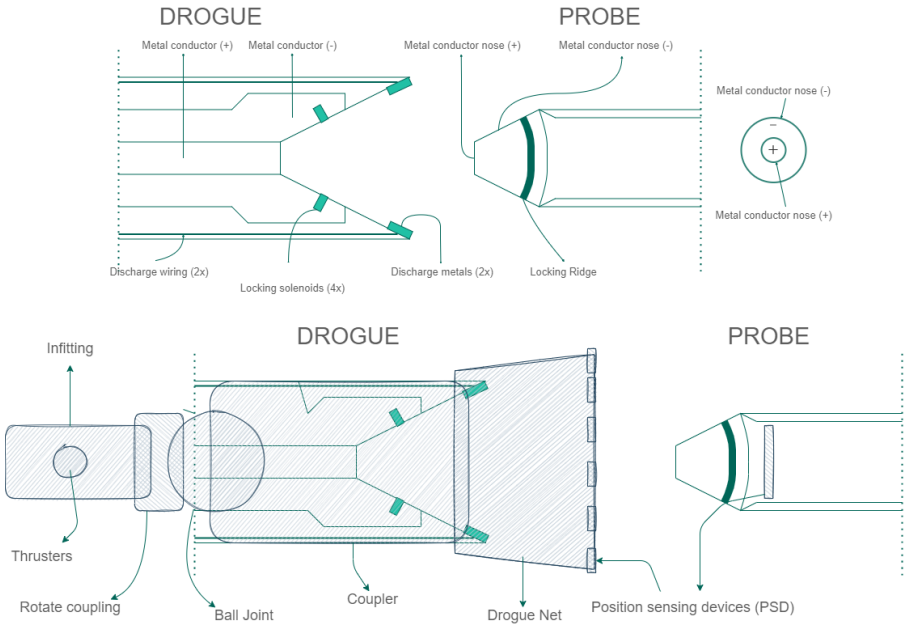

Figure 7.7: *Probe-drogue connection (made in collaboration with Group 10)*

Design Overview

The final design can be seen in Figure 7.8 and 7.9, next to this the parameters of the recharging interface are summarised in Table 7.6. The assumptions used in the design can be found in Table 7.5. The validity of these assumptions is discussed in Chapter 19.

Table 7.5: *List of assumptions for recharging interface*

ID	Assumption
ASM-RECH-01	The extended wire is straight.
ASM-RECH-02	The induced wake is smaller than that of a KC-46 tanker plane.
ASM-RECH-03	The length of the hose in the fuel pod necessary to facilitate Electrifly is able to fit within the fuselage.
ASM-RECH-04	Including a transformer has a lower efficiency than only using a cable.
ASM-RECH-05	A diameter of 0.5 cm for air in the cable is adequate to facilitate the thrusters.
ASM-RECH-06	The cable's bending characteristics are axially symmetrical.
ASM-RECH-07	The cable will bend over a radius of 0.8 m to fit on the fuel pod.
ASM-RECH-08	The cable is able to withstand the heat generated due to power losses.
ASM-RECH-09	There are no upstream effects for the cable a drogue drag calculations.
ASM-RECH-10	Small dislocation of the probe will still result in a successful connection.

Table 7.6: *Design overview parameters*

Parameter	Value
Cable length	20 m
Cable diameter	3.5 cm
Drogue diameter	35 cm
Weight cable	180 kg
Weight cable unit	200 kg
Drag	1000 N
Cable efficiency	99.86%
Recharging rate	1.7 MW

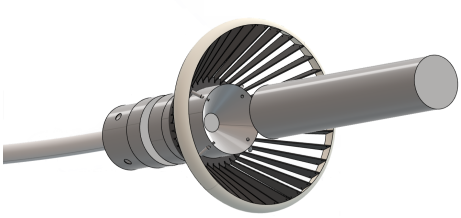

Figure 7.8: *CAD model of the drogue*

Figure 7.9: *CAD model of the connection*

[10] https://link.springer.com/chapter/10.1007/978-981-16-7423-5_80 [Accessed on 21.06.2023]
[10] https://www.engineeringtoolbox.com/thermal-conductivity-metals-d858.*html*[*Accessedon*21.06.2023]

Verification and Validation

To conclude, calculations on the weight, power loss, drag, and cable diameter have been verified by the unit tests in Table 7.7. The unit tests use Excel to recalculate the values. In addition, the design process has been validated by experts. H. Shahzad validated the assumption for the wake of Electrifly based on the KC-46. T. Tomažic validated the assumption for the specific weight of a transformer and its efficiency. The service point from RS Components [11] helped validate the cable design. Finally, the cable drag calculation was validated by A. Viré. In this validation on the drag and stability of the drogue are missing

In the future, four tests or detailed analyses can be considered for the coming stages of the design. Now, little is known about the vertical clearance required between the aircraft and the drone. Firstly, a CFD method should be used, and then the effects of the propellers and the wingtips could be assessed by experiment. Similarly, the aerodynamic characteristics, such as stability, should be assessed for the drogue-cable assembly. Thirdly the bending of the copper cable should be tested. And finally, it is of the essence that the probability of a successful connection is assessed by experimentation. This practical setting will help understand difficulties in connecting and improve the design greatly. This should include the effect of moisture in the air.

Table 7.7: *Recharging subsystem unit tests*

ID	Test	Expected outcome	Actual outcome	Pass/Fail
TEST-RECH-01	W	W = 180 kg	W = 180 kg	Pass
TEST-RECH-02	P_l	P_L = 3793 W	P_L = 3793 W	Pass
TEST-RECH-03	D	D = 1000 N	D = 1000 N	Pass
TEST-RECH-04	D_c	D_c = 3.5 cm	D_c = 3.5 cm	Pass

[11] https://nl.rs-online.com/web/c/power-supplies-transformers/voltage-converters/dc-dc-converters/ [Accessed on 21.06.2023]

8. Aerodynamics Analysis

In this chapter, the wing planform design is presented and the aerodynamic performance of the design is analysed. Section 8.1 revisits the wing design and its initial shape. The lifting capabilities of the designed wing are then estimated in Section 8.2. The high-lift devices and ailerons that contribute to the wing design are discussed in Section 8.3. Following, the aerodynamic drag is estimated in Section 8.4. Lastly, the assumptions and verification of the used models are discussed in Section 8.5.

8.1. Initial Wing Design

The preliminary sizing of the wing is determined with the use of loading diagrams and provides an initial determination of the wing's surface area and aspect ratio. With those preliminary values, a trapezoidal planform area can be described for the wing. For example, the aspect ratio allows for determining the required wing span, as described in Equation 8.1. The planform's sweep also ought to be determined. Since ElectriFly is planned to operate at low subsonic cruising speeds, the sweep's benefits are redundant. Therefore, a straight wing is selected, where the quarter chord sweep is defined as zero: $\Lambda_{0.25c} = 0°$. Lastly, the wing's ideal taper ratio is dependent on the sweep according to Equation 8.2[36]. For straight wings, the ideal taper ratio of 0.45 is selected. With these parameters, the planform area of the wing is designed, for which the dimensions are shown in Table 8.1. The parameters of twist and dihedral are left as zero since the twist is expected to reduce aerodynamic performance[37], while the dihedral can be redefined as necessary for clearance and lateral stability.

$$b_W = \sqrt{S_W A} \tag{8.1}$$

$$\lambda = 0.45 \exp(-0.0375 \Lambda_{0.25c}) \tag{8.2}$$

Table 8.1: *Wing planform parameters*

Parameter	Value
S_W $[m^2]$	35.13
b_W $[m]$	20.53
A [-]	12.00
$\bar{c}$ $[m]$	1.79

An initial airfoil selection is performed for the wing. The wing design lift coefficient is obtained from the cruise condition and includes a 10% contingency margin, as described in Equation 8.3. From this, it is possible to determine the airfoil design lift coefficient by using a sweep correction factor as suggested by Raymer[38], yielding Equation 8.4. Taking these values into account, the NACA 44018 airfoil is selected, of which the parameters are presented in Table 8.2. It should be noted that these values correspond to a Reynolds number of 4.4e6, as estimated in the cruise conditions on the mean geometric chord. For further lift and drag computations, values for each flight condition and for different chord lengths were taken into account.

$$C_{L_{\text{des}}} = 1.1 q \left(\frac{W}{S} \right) \tag{8.3}$$

$$C_{l_{\text{des}}} = \frac{C_L}{\cos(\Lambda_{LE})^2} \tag{8.4}$$

Table 8.2: *NACA 44018 parameters*

Airfoil	NACA 44018
$C_{l_{\max}}$	1.951
C_d at $C_{l_{\text{des}}}$	0.00417
Drag bucket width	1.62
C_m at α_{des}	-0.023

8.2. Lift Polar Estimation

The aircraft's lifting capabilities ought to be assessed, proving compliance with the ElectriFly's mission. In order to obtain an estimation of the lift generation, various estimation methods were performed, mainly concerning DATCOM[39]. A careful distinction should be made between the characteristics of the wing and the entire aircraft, as some estimation methods only concern one or the other. As such, the aerodynamic parameters of the wing will be denoted with the subscript 'w', while those of the aircraft use subscript 'A'. No subscript is used when the parameter is used in a general context.

The aircraft's lifting capabilities are not only covered by its wing and fuselage but also by its empennage. The horizontal tail can contribute either positively or negatively to the overall lift, depending on the required trim condition. As such, a different lift polar exists for different trim conditions, resulting in a convoluted overview. It is therefore decided

to separate the contribution of the tail, which will be discussed in Chapter 12, and to mainly discuss the effect of the rest of the aircraft in this chapter. Respectively, parameters of the horizontal tail contain the subscript 'h', while the complement uses 'A-h' (Aircraft-less-tail).

The slope of the linear regime of the lift curve can be taken as 2π rad^{-1} according to thin-airfoil theory but should be corrected for the 3D wing geometry. The lift slope for the wing is obtained using Equation 8.5[39], correcting with aspect ratio, sweep, airfoil efficiency (η), and the Prandt-Glauert compressibility correction factor, $\beta = \sqrt{1-{M_\infty}^2}$. A value of 95% was initially taken for the airfoil efficiency [40]. The lift slope of the aircraft-less-tail includes the effect of the fuselage's interference with the wing and its own lift contribution. Equation 8.6 provides an estimation of this lift slope, in which S_{exp} is the wing area less the projection of the fuselage onto the wing[41].

$$(C_{L\alpha})_w = \frac{2\pi A}{2+\sqrt{4+\left(\frac{A\beta}{\eta}\right)^2 \cdot \left(1+\frac{tan(\Lambda_{0.5c})^2}{\beta^2}\right)}} \tag{8.5}$$

$$(C_{L\alpha})_{A-h} = (C_{L\alpha})_w \left(1+2.15\frac{b_f}{b}\right)\frac{S_{\text{exp}}}{S} + \frac{\pi}{2}\frac{b_f^2}{S} \tag{8.6}$$

Another aspect of the lift polar to be estimated is the maximum lift coefficient. The wing's maximum lift coefficient can be related to the airfoil's maximum lift coefficient via Equation 8.7. DATCOM suggest a value of 0.9 for the ratio $C_{L_{\text{max}}}/C_{l_{\text{max}}}$ for the current wing design[39]. The correction term $\Delta C_{L_{\text{max}}}$ is only non-zero when accounting for the Mach number at cruise, decreasing $C_{L_{\text{max}}}$ by 0.3[39]. This results in the values as presented in the first row of Table 8.3. It can be seen that the values are lower than the required maximum lift coefficient. However, this requirement is to constrain the aircraft's stall speed, around which the correction for Mach number is irrelevant. One should note that the maximum lift for take-off and landing includes the effect of high-lift devices, of which the design is explained in Section 8.3. Moreover, the contribution of the fuselage is ignored in the $C_{L_{\text{max}}}$ estimation, since the current fuselage shape is assumed to stall before the wing.

$$C_{L_{\text{max}}} = \left(\frac{C_{L_{\text{max}}}}{C_{l_{\text{max}}}}\right) C_{l_{\text{max}}} + \Delta C_{L_{\text{max}}} \tag{8.7}$$

Table 8.3: *$C_{L_{max}}$ for different flight conditions*

Value for	Cruise	Take-off	Landing
$C_{L_{\text{max}}}$	1.46	2.07	2.28
No Mach-effect	1.76	2.07	2.28

Lastly, it is relevant to determine the angle at which the maximum lift coefficient occurs, the stall angle α_s. The stall angle is particularly important for the take-off and landing phases, as the aircraft assumes high angles during these phases. DATCOM preliminary estimates the stall angle as in Equation 8.8, where the correction $\Delta\alpha_{C_{L_{\text{max}}}}$ has a value of 1.7° for the current wing design[39]. The zero-lift angle of attack α_{0L} for the aircraft and the wing is assumed to be the same as for the airfoil. The resultant stall angles are given in Table 8.4. The results again include the effect of the high-lift devices, which are discussed in Section 8.3, and do not include the contribution of the fuselage.

$$\alpha_s = \frac{C_{L_{\text{max}}}}{C_{L\alpha}} + \alpha_{0L} + \Delta\alpha_{C_{L_{\text{max}}}} \tag{8.8}$$

Table 8.4: *Stall angle for different flight conditions*

Value for	Cruise	Take-off	Landing
α_s [°]	15	13	11

A final distinction between the wing and the aircraft can be made by introducing an inclination angle to the wing. The inclination of the wing will shift the aircraft's lift polar, such that an adequate lift coefficient is obtained when the aircraft flies at a zero angle of attack. The optimal inclination corresponding to a designed lift coefficient follows from Equation 8.9. With the current design being susceptible to iterations in weight, size, and mission conditions, the inclination angle is left as variable, but should be explored in further design phases.

$$\alpha_{\text{incl}} = \frac{C_{L_{\text{des}}}}{(C_{L\alpha})_{A-h}} + \alpha_{0L} \tag{8.9}$$

All estimation methods are summarised and displayed in the form of lift polar. The lift polar for the aircraft-less-tail for conditions in cruise, take-off, and landing are displayed in Figure 8.1. The stall regions of the polar are approximated as a parabolic continuation of the linear lift regime and displayed with a dotted curve. The accuracy of this region is lower than the rest of the polar and should be used with considered caution. Moreover, a contribution of the propulsion system to the lift polar exists and will be discussed in Chapter 9. This contribution ought to be included in further design iteration.

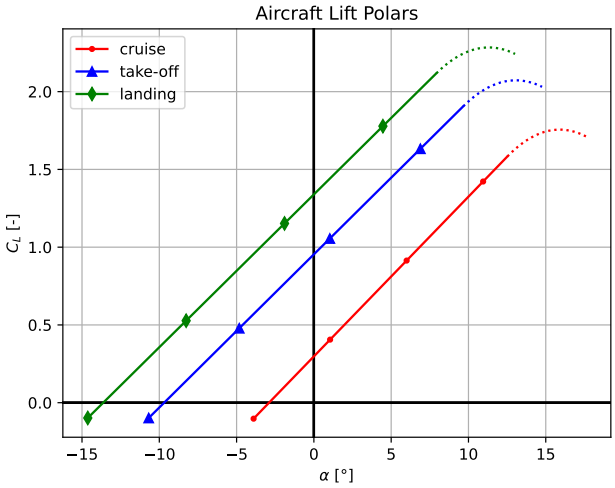

Figure 8.1: *Aircraft (less tail) lift polar*

8.3. Design of High-Lift Devices and Ailerons

The aircraft is required to reach higher maximum lift coefficients for the phases of take-off $C_{L_{max_{TO}}} = 2$, and landing $C_{L_{max_{land}}} = 2.2$, compared to the cruise phase $C_{L_{max_{clean}}} = 1.8$ according to the power loading diagrams analysed at the inital design stage. Therefore, high-lift devices are designed to increase the lift performance for these phases while still optimizing the wing for cruise conditions. Due to the benefits of distributed propulsion in terms of lift generation, while flaps are still needed for redundancy, they do not have to be as effective as if twin-engine propulsion was used. Krueger flaps were chosen for the leading edge as traditional extending slats are not possible due to the use of distributed propulsion. For the trailing edge, single-slotted flaps were chosen to minimise the complexity and the storage space while still providing the required additional lift. A summary of the chosen design characteristics for these flaps can be found in Table 8.5.

Table 8.5: *Characteristics of the flaps*

Placement	**Type**	$\Lambda_{hingeline}$**[deg]**	$\Delta C_{l_{max}}$[-]	$(\Delta\alpha_{0L})_{airfoil}$[deg]	**Beginning position[m]**	**End position[m]**
Leading edge	Krueger	2.045	0.3	-	0.10 b/2	0.95 b/2
Trailing edge	Single Slotted	3.31	1.3	-15 for take-off, -10 for landing	0.10 b/2	0.8 b/2

The performance of these flaps can be analysed using Equation 8.10 for both types of high-lift devices and Equation 8.11 for trailing edge devices as the change in the zero-lift angle of attack is considered negligible for leading edge devices. For take-off, the $\Delta C_{l_{max}}$ of the given flap has to be multiplied by a factor of 0.6 as they are not fully deployed. In addition, the performance of the leading edge flaps and that of the trailing edge flaps needed to be added to obtain the final performance for each condition.

$$\Delta C_{L_{max}} = 0.9\Delta C_{l_{max}} \frac{Swf}{S} cos\Lambda_{hingeline} \quad (8.10) \qquad \Delta\alpha_{0L} = (\Delta\alpha_{0L})_{airfoil} \frac{Swf}{S} cos\Lambda_{hingeline} \quad (8.11)$$

The final performance of the flaps at take-off can then be seen in Table 8.6 and during landing in Table 8.7. This allows the required values for maximum lift coefficient at landing and take-off to be reached and for reasonable stall angles of attack without the contribution of propulsion.

Table 8.6: *Performance of the flaps at take-off*

Parameter	$\Delta_{C_{L_{max\,TO}}}$[-]	$\Delta\alpha_{0LTO}$[deg]	$C_{L_{max\,TO}}$[-]	α_{0LTO}[deg]
Value	0.41	-4.65	2.14	13.9

Table 8.7: *Performance of the flaps during landing*

Parameter	$\Delta C_{L_{max\,land}}$[-]	$\Delta\alpha_{0Lland}$[deg]	$C_{L_{max}land}$[-]	α_{0Lland}[deg]
Value	0.69	-6.98	2.40	11.3

According to CS23, the aircraft is required to be able to perform a 60-degree roll in less than 9.7 seconds in take-off and less than 6.8 seconds in approach conditions. To meet these requirements, the ailerons were designed according to the parameters presented in Table 8.8.

Table 8.8: *Aileron design parameters*

Parameter	δa_{max} [deg]	**Beginning position[m]**	**End position[m]**	c_a/c[-]	τ [-]
Value	13.1	0.8 b/2	0.95 b/2	0.25	0.45

To know how the rolling moment changes with the deflection, the aileron control derivative can be calculated using Equation 8.12. In addition, information on how the rolling moment changes with the roll rate is needed and is given by the roll damping coefficient which is given by Equation 8.13.

$$C_{l_{\delta a}} = \frac{2c_{l\alpha}\tau}{S_{ref}b}\int_{b_1}^{b_2} c(y)ydy \tag{8.12}$$

$$C_{l_p} = -\frac{4(c_{l\alpha}+c_{d_0})}{S_{ref}b^2}\int_0^{b/2} y^2 c(y)dy \tag{8.13}$$

The time to roll can then be calculated using Equation 8.14 which uses the roll rate given by Equation 8.15 as an input. Differential ailerons are used to minimise the adverse yaw, with each aileron deflecting a maximum of 15 degrees, resulting in a δa_{max} with a value of 13.125 degrees.

$$\Delta t = \frac{\Delta\Phi}{P} \tag{8.14}$$

$$P = -\frac{C_{l_{\delta a}}}{C_{l_p}}\delta a_{max}\left(\frac{2V}{b}\right) \tag{8.15}$$

The obtained roll performance can be seen in Table 8.9. As the value for the time to roll for both conditions is lower than the required, the CS23 roll requirements are met. The final wing planform with the addition of high-lift devices and ailerons can then be seen in Figure 8.2

Table 8.9: *Roll performance*

Parameter	P_{TO} [deg/s]	Δt_{TO} [s]	$P_{approach}$ [deg/s]	$\Delta t_{approach}$ [s]
Value	8.7	6.9	9.4	6.4

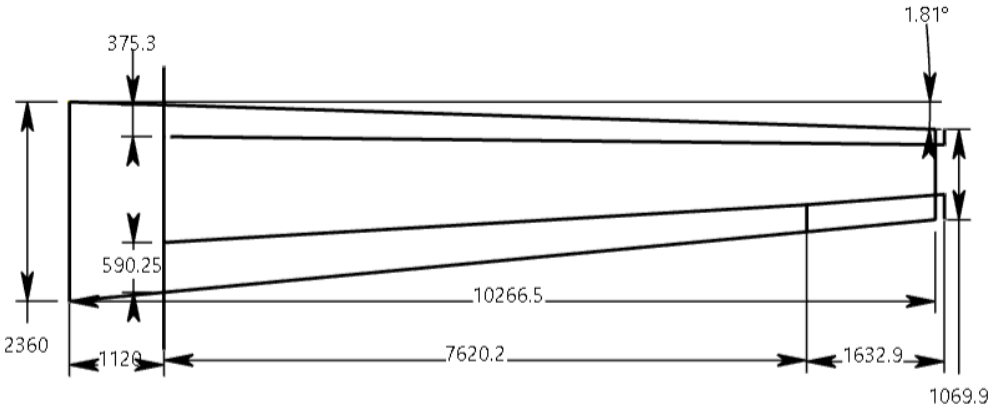

Figure 8.2: *Wing planform with high-lift devices and ailerons*

8.4. Drag Polar Estimation

The calculation of the ElectriFly's drag is essential for the design of the propulsive system that counteracts the drag. The drag is estimated using the drag build-up method as in Equation 8.16. Different parameters for each aircraft component are obtained using the process established for this method and are given in Table 8.10 for cruise conditions[40]. Besides the drag of each component, other contributions to the drag may be present. These consist of drag added by the flaps, the recharging cable, wave drag, and other miscellaneous contributions, such as fuselage upsweep and base drag, landing gear drag, trim drag, excrescence, and twist effect. The latter miscellaneous drag is left to be estimated but is now taken as a 20% contingency. The drag of the flaps and wave drag is estimated for each flight condition[40], while cable drag is discussed in Chapter 7.

$$C_{D_0} = \frac{1}{S_{ref}}\sum C_{f_c}\cdot FF_c\cdot IF_c\cdot S_{wet_c} + \sum C_{D_{misc}} \tag{8.16}$$

Table 8.10: *Drag build-up parameters per component for cruise condition*

Component	C_{f_c} [$\cdot 10^{-4}$]	FF_c [-]	IF_c [-]	$S_{wet_c}[m^2]$	$(C_{D_0})_c$ [$\cdot 10^{-4}$]
Wing	18	1.54	1.20	64.9	61
Horizontal tail	20	1.34	1.04	11.1	9
Vertical tail	15	1.34	1.04	11.1	7
Fuselage	18	1.36	1.20	63.5	52

Besides the zero-lift drag, ElectriFly will also experience drag induced by the lift it generates. The total drag coefficient account for both contributions as described in Equation 8.17, using the lift coefficient for the respective condition. The Oswald efficiency of the aircraft is estimated as given by Kroo[36]. Furthermore, the induced drag can be reduced by 34% when the effect of wing tips is included, which will be further discussed in Chapter 9. With the inclusion of all the contributions to drag, the estimation can be made for all flight phases. For reference, the estimated drag contributions are given for take-off conditions[1] in Table 8.11 and their distribution is displayed in Figure 8.3.

$$C_D = C_{D_0} + k_2 C_L^2 \quad \text{with} \quad k_2 = \frac{1}{\pi A e} \tag{8.17}$$

Table 8.11: *All estimated drag contributions during take-off*

Contribution	C_D [$\cdot 10^{-4}$]
Wing friction	56
Horizontal tail friction	8
Vertical tail friction	6
Fuselage friction	56
Flaps ($\delta_f = 20$)	79
Cable (not extended)	0
Wave drag	0
Other	51
Total zero-lift drag	256
Induced drag for $C_L = 1.09$	258

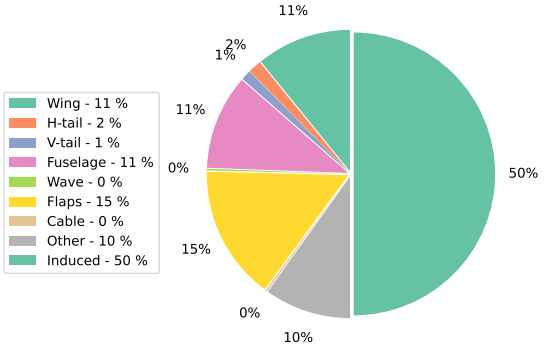

Figure 8.3: *Composition of drag for take-off conditions*

Finally, the drag can be plotted for a variety of lift coefficients and flight conditions, yielding the drag polar. The drag polar for cruise, take-off, and landing are to be seen in Figure 8.4 with C_L ranging from -0.5 to $C_{L_{max}}$ as found in Section 8.2. Within the drag polar an optimum is defined, where the lift-to-drag ratio is maximum. This optimum is given in Table 8.12

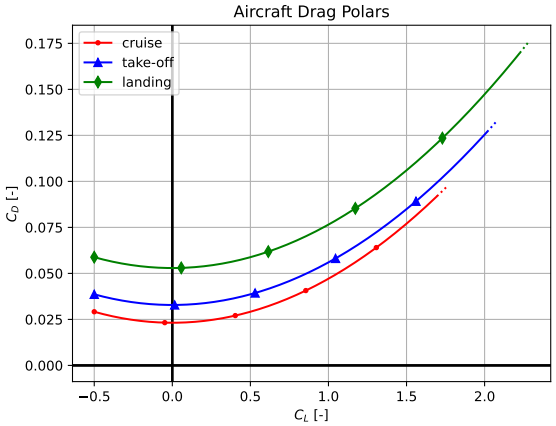

Figure 8.4: *Aircraft drag polars*

Table 8.12: *Summary of optimal lift-to-drag ratio for different flight conditions*

Condition	$C_{L_{opt}}$	$C_D(C_{L_{opt}})$	$(L/D)_{max}$ [-]
Cruise	0.85	0.032	26.6
Take-off	1.09	0.051	21.1
Landing	1.42	0.092	15.6

[1] The optimal value for the lift coefficient from Table 8.12 is chosen to display induced drag

8.5. Aerodynamic Design Assumptions and Verification

Within the aerodynamic analysis, various assumptions were included in the estimation procedures. Besides the assumptions inherent to the estimation procedures and used equations, a set of specific assumptions were made to reduce the complexity of the calculation. The latter is labelled and described in Table 8.13. The validity of the mentioned assumptions will be discussed in Chapter 19.

Table 8.13: *List of assumptions for the aerodynamic analysis*

ID	Assumption
ASM-AERO-01	Wing planform shape is purely trapezoidal
ASM-AERO-02	Fuselage lift is negligible within the stall region of the wing
ASM-AERO-03	Zero-lift angle of attack is the same for airfoil as for wing and aircraft
ASM-AERO-04	The effect of wing inclination on the drag polar is negligible
ASM-AERO-05	Minimum aircraft drag is found at zero lift coefficient

The methods of designing the aerodynamic aspects of the aircraft ought to be verified. A variety of tests are performed on the calculations used for various shapes of wings. A selection of the initial unit test is shown in Table 8.14, in which the test input, expected output, and actual output are described. TEST-AERO-01 till -03 intend to show that insensible inputs yield errors in the calculation. However, TEST-AERO-02 and -03 show that calculation is performed even with insensible surface area and sweep, meaning these parameters should be manually constrained. Moreover, TEST-AERO-06 shows that the calculation could also produce insensible outputs. This corresponds to the estimation methods being only applicable for a specific design space, which in turn should constrain the allowed inputs.

Table 8.14: *Aerodynamics Unit Test*

Test	Input	Expected	Actual	Result
TEST-AERO-01	$A = 0$	Error	Error	Pass
TEST-AERO-02	$S = 0$	Error	No Error	Fail
TEST-AERO-03	$\Lambda_{0.25c} = \pi/2$	Error	No Error	Fail
TEST-AERO-04	$\lambda = 0$	$c_t = 0$	$c_t = 0$	Pass
TEST-AERO-05	$\lambda = 1$	$c_t = c_r$	$c_t = c_r$	Pass
TEST-AERO-06	$0 < e < 1$	True	False	Fail
TEST-AERO-07	$C_{D_0} > 0$	True	True	Pass
TEST-AERO-08	$\lim_{A\to\infty} C_{L_\alpha} = 2\pi$	True	True	Pass

To elaborate on a specific unit test, the calculation of the linear lift curve slope, C_{L_α}, will be discussed. The estimation method for C_{L_α} is as in Equation 8.5 and is a correction on thin airfoil theory. It is therefore expected that the theorised lift slope of 2π rad$^-1$ is given when an infinite straight wing is estimated, for which no correction is needed. The infinite wing is approached when the aspect ratio approaches infinity, thus $C_{L_\alpha} \approx 2\pi$ for large inputs of aspect ratio, as is proven by TEST-AERO-08.

9. Electric Propulsion Unit Design

This chapter will examine the electric propulsion unit (EPU), that is, everything that connects the battery to the propeller, for the ElectriFly mission. Firstly, the requirements governing the EPU design shall be specified in Section 9.1, and then the EPU configuration shall be elaborated upon in Section 9.2. Once the configuration has been chosen, the motor will be decided on in Section 9.4. Following, the concept of regenerative braking shall be analysed in Section 9.5, where a propeller that can work in both propulsive and regenerative phases is also sized. Then the auxiliary systems needed for the functioning of the propellers are given in Section 9.6. Finally, an overview of the final EPU, a list of assumptions, along with the V&V will be given in Section 9.7.

Due to the ambiguity surrounding the term 'engine' in the context of an electric aircraft, the term electric propulsion unit, or EPU, shall be used as the all-encompassing term for the entire propulsion sub-system. The EPU shall be used to refer to the entire sub-system comprising the battery, electric motor, gearbox, propeller, controller, and any other relevant components. An overall schematic is presented in Figure 9.1.

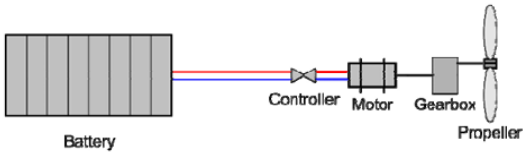

Figure 9.1: *Overview of components in an EPU [42]*

Figure 9.2: *Requirements from design[38, 42]*

Parameter	Value
Maximum Power (kW)	1189
Controller Efficiency	0.98
Motor Efficiency	0.95
Gearbox Efficiency	0.98
Propeller Efficiency	0.80
Total System Efficiency	0.73

9.1. EPU Requirements

The requirements that govern the design of the propulsion system of an electric aircraft can be divided into the requirements resulting from design as well as the requirements issued from regulations.

Design requirements

The propulsion subsystem will be designed around the battery configuration of Chapter 6 and the power requirements from Chapter 8. Typically, the efficiency chain from the battery to the motor shaft can be described as the product of the efficiencies of each component, listed in Figure 9.2 [38, 42]. However, based on the method from Riboldi C.E.D. and the expert opinion from Dr.ir. Reynard de Vries[1], efficiencies up to 0.86 are achievable, and hence a maximum system efficiency is also established at this value. In Figure 9.3, it can be seen that battery-powered propulsion has significant advantages over conventional turboprop or turbofan engines in terms of overall efficiencies due to the absence of fuel-to-mechanical power conversion.

Requirements Dictated from Regulations

While regulations around electric aircraft have not been fully developed, special conditions from EASA[44] have been released recently for the certification of EPUs. SC-E-19 is a special condition by EASA for the certification of electric or hybrid propulsion systems. These regulations intend to ensure the safe operation of the engine and have a similar structure to CS-E[2]: the regulations for fuel-powered engines. In general, the EPU require a specific maximum take-off power and maximum continuous power rating and should account for fire protection. It should also be resistant to vibrations, rain, birds/foreign matter and ice. Additionally, the EPU should be equipped with a cooling, control and lubrication system.

9.2. EPU Configurations

To select the most efficient EPU configuration, the number of engines is an important factor. Here, the concepts of single, twin and distributed propulsion systems are discussed.

[1] Researcher at Delft University of Technology and author of the used reference
[2] https://www.easa.europa.eu/en/document-library/easy-access-rules/easy-access-rules-engines-cs-e [Accessed on 19.06.2023]

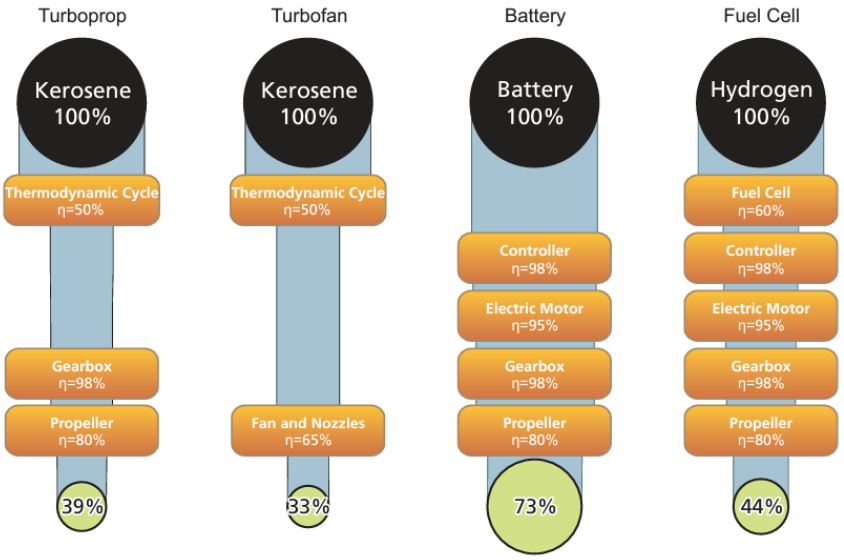

Figure 9.3: *Efficiency of conventional vs electric aircraft [42]*

Single Engine

The well-known single-engine configuration is especially advantageous for smaller 1 to 2-passengers aircraft requiring a limited amount of power. Despite ensuring easy maintenance, it has several disadvantages:

1. **Power:** The amount of power that can be provided by a single engine is limited, and therefore the speed that can be achieved by the aircraft would be limited as well.
2. **Safety:** One engine is detrimental to the safety of the pilot and passengers on board in case of a long-haul (multiple-charges) flight. In case of an engine failure, the aircraft would become a glider that only has one attempt at an emergency landing if any airport is within feasible distance at all. Having multiple engines simply provides redundancy that enables the pilot to safely divert to an airport nearby and perform an emergency landing.
3. **Noise:** This configuration produces more noise than configurations that distribute the power over multiple engines. This is a significant downside for both the passengers on board as well as people on the ground.
4. **Differential Thrust:** Lastly, the principle of differential thrust is not possible with the single-engine configuration as this requires a minimum of two engines. Differential thrust minimises the control surfaces required and therefore reduces the overall weight of the aircraft. This is very advantageous as, due to the heavy battery, overall weight reduction is a vital focus within the design.

In conclusion, the disadvantages of the single-engine configuration outweigh the few advantages, making it unsuitable, and this configuration will thus be discarded.

Twin-Engine Configuration

A twin-propeller is a popular configuration that allows for a fine balance between safety/maintenance and power supplied. Furthermore, as opposed to single-engine, the concept of differential thrust can be applied as well. As opposed to distributed propulsion, this configuration offers some advantages:

1. **Safety:** Contrary to a single engine, it provides more redundancy in case of OEI conditions. Moreover, due to more clearance around each engine, in case of blade failure or similar failures, high energy debris shall not affect other engines as in the case of distributed propulsion.
2. **Maintenance:** It is a popular configuration and has simple cabling and integration structures compared to distributed propulsion.

In conclusion, a twin-propeller configuration can be considered for this design and will be analysed against distributed propulsion.

Distributed Electric Propulsion (DEP)

Distributed propulsion is considered as multiple (more than 2) electrically-powered propellers placed on the wing in order to improve airflow characteristics and therefore lift generation. Electric motors offer a lot of variability in terms of placement and size, as they are generally smaller and lighter. Distributed propulsion was considered based on the literature study, as it offers beneficial safety, structural and aerodynamic features [45]:

1. **Lift:** As ElectriFly is operating at a relatively low speed as defined in Chapter 8, the leading-edge propellers can offer enhanced lift generation by increasing dynamic pressure. However, the effect of distributed propulsion on aerodynamic properties needs to be quantified to establish the most beneficial configuration.
2. **Weight:** Smaller, light propulsion units placed close to the wing can result in the decrease of weight and drag of large pylons and nacelles, as well as using lighter motors.
3. **Noise:** Considering several smaller engines, less noise can be generated by the overall system and further away from the fuselage.
4. **Cable loss:** By having multiple engines, the power requirement per motor is reduced, and thus the amperage that needs to flow through the cable connecting each of these to the batteries is lowered, hence lowering the power loss.
5. **Optimisation:** A configuration with multiple propellers can be optimised for specific flight phases and power settings required in different phases of the aircraft.

Based on the many advantages, it is decided to analyse in detail the concept of distributed propulsion to analytically check whether it is beneficial for the design of Electrifly. These results will then be compared with a twin-propeller configuration to decide which one will be implemented in the design.

9.3. Analysis of Distributed Electric Propulsion

In order to quantify the aerodynamic benefits of DEP, the change in ΔC_L and ΔC_D must be examined. The method for quantifying is modified from the method developed by de Vries et al.. The results are dependent on the number of engines put on the wing (N_{en}) and the span fraction occupied by the distributed-propulsion system (ΔY), used as variable inputs. Further, the clearance distance between the tip of two adjacent propellers as a fraction of propeller diameter (Δy) is assumed to be half of the diameter (D_P). This is because, as discussed with Dr.ir. Tomas Sinnige[3], when the distance is of at least one radius, the interaction between propeller tips can almost be discarded. This interaction will, however, be further analysed in Subsection 9.3.1. The geometry parameters are visualized in Figure 9.4.

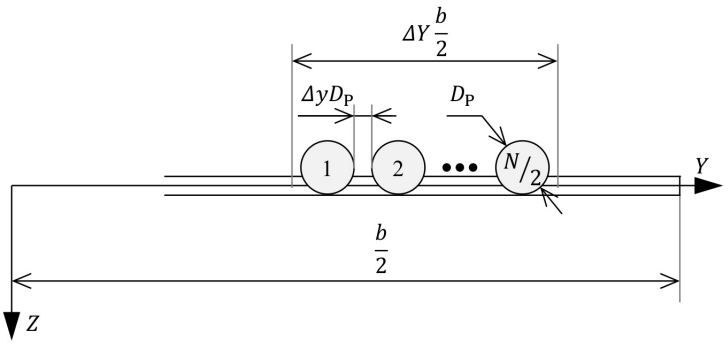

Figure 9.4: *Main geometric parameters of distributed propulsion system [46]*

As per this figure, the propeller diameter can be found as given in Equation 9.1.

$$D_p = \frac{\Delta Y}{N_{en}(1+\Delta y}b \tag{9.1}$$

Naturally, this is dependent on the above-specified parameters and should decrease with an increasing number of engines. The diameter can also be expressed in terms of the MTOW, by expressing it as a function of the wing loading, that is, as expressed in Equation 9.2.

$$\frac{D_\mathrm{p}^2}{W} = \frac{\Delta Y^2}{N_{en}^2(1+\Delta y)^2}\frac{A}{(W/S)} \tag{9.2}$$

This can be interpreted as how much propeller area is needed per weight to propel the aircraft. It can be thought of as the inverse function of the disk-loading. When determining the geometrical parameters of the DEP system, it is important to verify that the thrust coefficient (T_c), while needing to be enough to propel the aircraft forward at all times, should not exceed the maximum theoretical propulsive efficiency ($T_{c,max}$). This is because if a large number of propellers is chosen and the thrust-to-weight ratio is high, there might not be a possibility to produce thrust efficiently with the given disk area. Actuator disk theory defines $T_{c,max}$ for a specific propulsive efficiency (η_{dep}) in Equation 9.3. A safety factor of 85% will be applied to prevent efficiency overestimation. Furthermore, using Equation 9.4 thrust coefficient can be found for each configuration considered. The thrust ratio of the DEP system (χ), that is, the ratio

[3]Assistant professor at the Department of Flight Performance and Propulsion at Delft University of Technology

between the thrust provided by the distributed system and the one provided by the primary propulsion system, equals 1, as the whole thrust is produced by the DEP system. The minimum propulsive efficiency limit for thrust coefficient was chosen as 0.73, as described in Figure 9.2. All designs which violate the minimum or maximum limit are not included.

$$T_{c,\max} = \frac{\pi}{8}\left[\left(\frac{2}{\eta_{\text{dp, isolated}}} - 1\right)^2 - 1\right] \tag{9.3}$$

$$T_c = \frac{1}{N_{en}} \frac{\chi\ (T/W)}{\rho V^2 \left(D_P^2/W\right)} \tag{9.4}$$

To translate the power loading found in Chapter 8 into the thrust loading shown in Equation 9.4, it is enough to factor in the velocity as shown in Equation 9.5.

$$\frac{T}{W} = \frac{1}{V(W/P)} \tag{9.5}$$

The thrust coefficient can be used to determine the axial induction factor of the propeller disk with Equation 9.6. This factor describes a fraction of velocity increase in the propeller. The contraction causes the slipstream velocity on the wing to be higher than at the propeller disk. Equation 9.7 was used to obtain the contraction ratio of the slipstream (R_W/R_P), where the position of the propeller with respect to the leading edge (x_P/R_P) is chosen to be 20%.

$$a_P = \frac{V_P - V}{V} = \frac{1}{2}\left(\sqrt{1 + \frac{8}{\pi}T_c} - 1\right) \tag{9.6}$$

$$\frac{R_W}{R_P} = \sqrt{\frac{1 + a_P}{1 + a_P\left(1 + \frac{x_P/R_P}{\sqrt{(x_P/R_P)^2 + 1}}\right)}} \tag{9.7}$$

Conservation of mass for incompressible flow can be used to arrive at Equation 9.8, with which the increase in velocity that arrives at the wing leading edge due to propeller-generated thrust was obtained.

$$a_w = \frac{a_P + 1}{(R_W/R_P)^2} - 1 \tag{9.8}$$

Then, once all these parameters are known, the increase in the sectional lift coefficient can be found as per Equation 9.9, where the angle of attack and the sweep of the wing have been found in Chapter 8.

$$\Delta c_l = 2\pi\left[\left(\sin\alpha_w - a_w\beta\sin(\alpha_P - \alpha_w)\right)\sqrt{\left(a_w\beta\right)^2 + 2a_w\beta\cos\alpha_P + 1} - \sin\alpha_w\right] \tag{9.9}$$

In this equation, β is a slipstream correction factor to correct for the change in the flow in the propeller slipstream. Ignoring this factor can lead to a significant overestimation of the increased lift coefficient, especially for higher numbers of engines considered [46]. Patterson's approach was used to estimate this effect [47].

$$\begin{aligned}
K_0 &= \begin{bmatrix} 0.378269 & 0.748135 & -0.179986 & -0.056464 & -0.146746 & -0.015255 \end{bmatrix} \\
K_1 &= \begin{bmatrix} 3.071020 & -1.769885 & 0.436595 & 0.148643 & -0.989332 & 0.197940 \end{bmatrix} \\
K_2 &= \begin{bmatrix} -2.827730 & 2.054064 & -0.467410 & -0.277325 & 0.698981 & -0.008226 \end{bmatrix} \\
K_3 &= \begin{bmatrix} 0.997936 & -0.916118 & 0.199829 & 0.157810 & -0.143368 & -0.057385 \end{bmatrix} \\
K_4 &= \begin{bmatrix} -0.127645 & 0.135543 & -0.028919 & -0.026546 & 0.010470 & 0.012221 \end{bmatrix}
\end{aligned} \tag{9.10}$$

With this, the wing lift coefficient increase is given by Equation 9.11.

$$\Delta C_L = \Delta C_l \Delta Y \tag{9.11}$$

Now that the increase in lift coefficient is found, it is clear that an increase in drag will follow, especially concerning the lift-induced part. Indeed, the increase in drag is given by Equation 9.14.

$$\Delta C_{D_0} = \Delta Y a_w^2 c_f \tag{9.12}$$

$$\Delta C_{D_i} = \frac{\Delta C_L^2 + 2C_{L,airframe}\Delta C_L}{\pi A_w e} \tag{9.13}$$

$$\Delta C_D = \Delta C_{D_0} + \Delta C_{D_i} \tag{9.14}$$

This method was applied step by step, and some values were obtained for the increase in lift. The shape of the graphs seemed to be sensible, as there should be a levelling-off in the ΔC_L curve as, at some point, adding more engines will not increase the lift anymore as each will be very small. On the other hand, the efficiency should decrease as it is inversely proportional to the number of engines. However, it seemed like these were far too low, in the order of 0.030, as shown in Figure 9.5a. Indeed, these results were low compared to the ones shown in the source itself, which attained increases in the lift coefficient in the order of 1.0-1.5, which, however, seems too high for cruise flight. Therefore, three experts were contacted to validate the method, namely Reynard de Vries, Robert Nederlof[4] and Brandon Litherland[5]. All of three experts confirmed that the implementation was correct and that some higher values should have been achieved. Again, all 3 came to the same conclusion, that is, that the method must be flawed in some way. Two bug

[4] PhD Candidate at Delft University of Technology

[5] AST, Aerospace Vehicle Design & Mission Analysis at NASA Langley Research Center

fixes were proposed by the group and deemed possible by the experts. These concern the fact that the lift described in the paper might not be the full increase in lift over the wing, but rather either the one of a single engine or the one of a portion of the span. If the correction of multiplying the increase obtained by the span were to be applied, the results would, of course, be higher, but then the dimensional analysis would not be sensible anymore, as the lift would be defined in m. Therefore, it is more sensible to apply the correction for the number of engines, that is, multiplying the value of ΔC_L, shown in Figure 9.5a per engine configuration, by the number of motors engines chosen. This number will be based on the maximum increase in lift coefficient and minimum loss in efficiency. These two factors, along with the most beneficial motor parameters, will be accounted for in Section 9.4.

Naturally, when increasing the lift coefficient, the drag will also increase. This can be accounted for by the fact that the wing now needs to produce less lift, as some of it is produced by the engines, and therefore can fly at a lower angle of attack or be more efficiently designed. This decreases some of the drag. Moreover, it was decided that this method would be improved by placing wingtip-mounted propellers. This was not a random choice but was based on research from Robert Nederlof which experimentally proved that, when the rotation of the propeller is in the correct direction and it is mounted on the wingtip, this is able to reduce the induced drag greatly [48]. Indeed, the propeller has an upsweep side on which the blade goes up and a down sweep side in which it goes down. Thus, this creates firstly an upwash and then a downwash. As the rotor moves more and more towards the tip and rotates clockwise on the right wing, only the upwash will come into play as the downwash falls outside of the wing surface region. This upwash, caused by the clockwise rotation, contrasts the vortices that are created on the tip; that is when the higher-pressure region under the wing manages to reach the upper side, creating a rotatory movement around the tip. This has a counterclockwise direction, looking at the right wing, and is therefore contrasted by the wingtip-mounted propeller. The decrease in induced drag can be up to 34%. Naturally, the same process occurs on the left wing, although in the opposite direction. Thus, the propellers on the opposite wings will have to be counter-rotating to make use of this advantage. While the one produced by turbulence and not considered in this analysis will be treated in Subsection 9.3.1. Finally, in Figure 9.6, the graphs for the aerodynamic performance of the DEP can be seen for the climb conditions. Considering that the values are now to be thought of as per engine, the graphs still make sense, as there should be a ceiling, after which the increase in lift provided by the single propeller cannot increase anymore as the interaction between many small ones becomes too high.

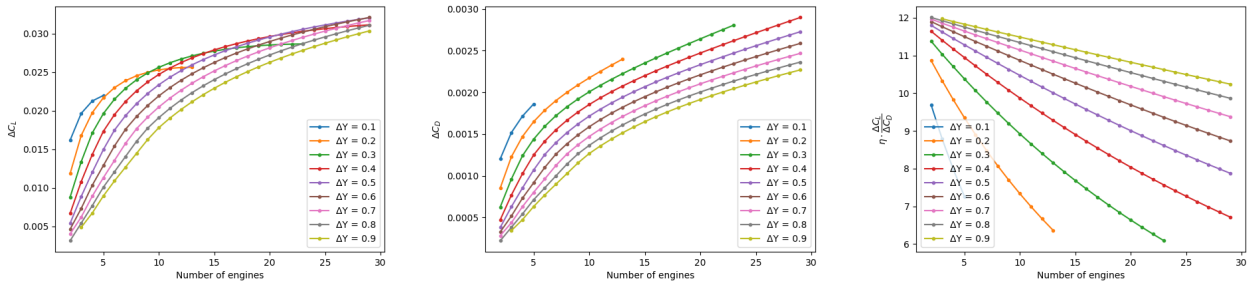

(a) *Increase in lift coefficient per engine* **(b)** *Increase in drag coefficient per engine* **(c)** *Efficiency times increase in lift/drag ratio per engine*

Figure 9.5: *Aerodynamic performance of distributed propulsion in cruise*

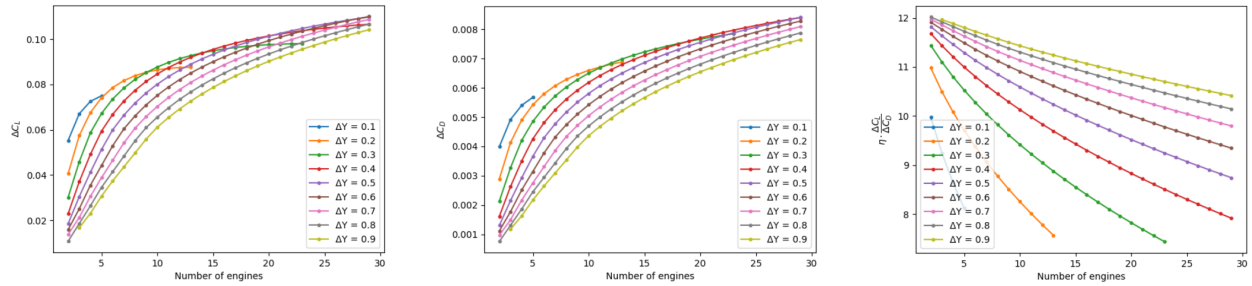

(a) *Increase in lift coefficient per engine* **(b)** *Increase in drag coefficient per engine* **(c)** *Efficiency times increase in lift/drag per engine*

Figure 9.6: *Aerodynamic performance of distributed propulsion in climb*

Power Constraint Diagram

To examine the effect of the increase in lift and drag, as compared to a conventional twin-propeller configuration, a power-loading diagram can be used to depict the effect of constraints. Six constraints were used: stall, take-off, landing, cruise, climb rate, and climb gradient. The constraint diagram is given in Figure 9.7, based on the constraints given in Table 9.1. The aerodynamic parameters that are considered for each phase are given in Table 9.2. The increase in lift coefficient, ΔC_l, and the induced drag components ΔC_{di} is given for each phase in Table 9.2. Increase in the zero-lift drag and ΔC_{d0} is negligible therefore not included in the table. Since the lift and drag coefficients were only obtained for the cruise and climb conditions, the coefficients are assumed to be constant for the other flight conditions of take-off, stall and landing. The zero-lift drag was found to be negligible; hence the induced drag is the main drag component. From the graph, it can be seen that due to the increase in the lift coefficient, the wing loading increases by around 250 kN/m^2, while there is no considerable change in the power loading.

Table 9.1: *Flight conditions*

Parameter	Value
Stall Speed [m/s]	40
Take off distance [m]	1000
Landing distance [m]	1000
Cruise altitude [m]	4572
Cruise speed [m/s]	110
Climb rate [m/s]	9
Climb gradient [%]	10

Table 9.2: *Aerodynamic parameters*

Parameter	Configuration	ΔC_L	$\Delta_{C_{D_i}}$
Stall	Clean	0.294	0.0224
Take-off	Flaps - Takeoff	0.294	0.0224
Cruise	Clean	0.294	0.0224
Landing	Flaps - Landing	0.294	0.0224
Climb	Clean	1.05	0.07

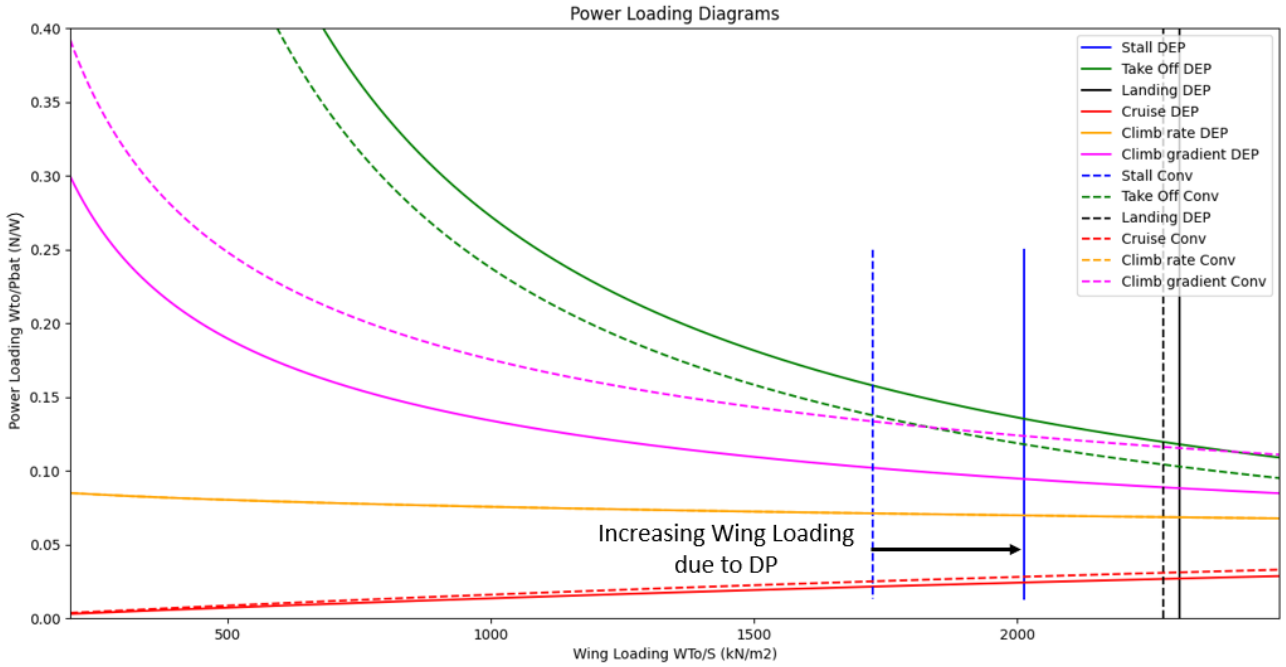

Figure 9.7: *Power loading diagram. The full lines indicate the constraints for the DEP configuration, and the dashed lines indicate the constraints for the conventional configuration.*

9.3.1. The effect of turbulence

An important factor that was not considered in this study is the interaction between propellers. Indeed, when only one propeller is installed on a wing, it can be considered isolated, and its interaction with the wing and the fuselage are not constraining. On the other hand, by placing many on the same surface, it is evident that an aerodynamic interaction will have to be accounted for. This, naturally, depends on the spacing between engines as, when this increases, the propeller can be considered more and more as an isolated one. This was already touched upon when implementing the method, as it was decided not to follow the indication in the paper of spacing the propeller by a low percentage of the diameter. Instead, it was decided to choose a constant distance of a radius between each engine so as almost to discard any interaction, an assumption that was validated by Dr. Ir. Thomas Sinnige[6]. However, the

[6]Expert on Propeller and Propeller Aerodynamics at Delft University of Technology

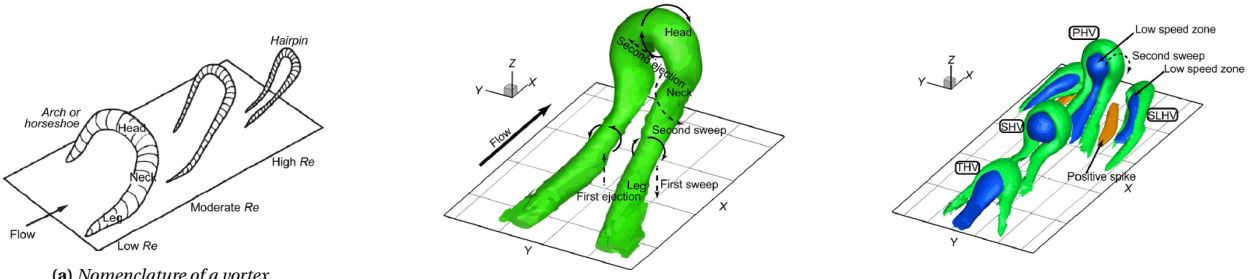

(a) *Nomenclature of a vortex*

(b) *3D sketch on a hairpin vortex*

(c) *Schematic of a vortex packet [50]*

Figure 9.11: *Vortex visuals [50]*

aerodynamic interaction cannot be fully discarded. Indeed, Koutsoukos, among others, proved that the aerodynamic performance of multi-rotor systems degrades due to the rotor-rotor interaction as a function of distance. Normally, all single propellers produce a wake, that is, a series of trailing-edge vortices that propagate from the blades, which normally contract as they move downstream. However, in the case of multiple propellers, specifically two adjacent ones, it is demonstrated that contraction occurs more slowly, as these vortices are "dragged" by the adjacent ones. This result can be visualised in Figure 9.8.

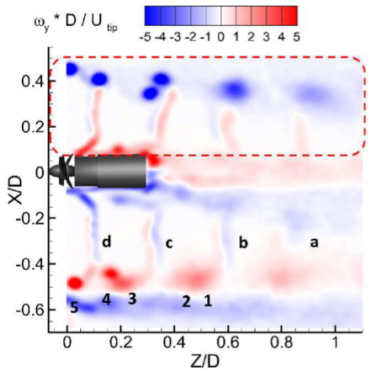

Figure 9.8: *Vorticity evolution of twin propeller [49]*

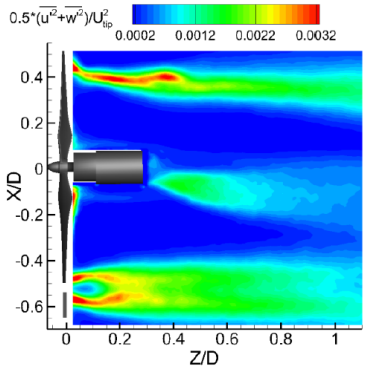

Figure 9.9: *Normalized turbulent kinetic energy contours for twin propeller [49]*

The interaction between vortices is particularly significant at small distances, as the wake flows lose their structure and merge into each other. However, even at larger distances, as the vortices move downstream, they coalesce and then split into multiple smaller vortices that create turbulence and, therefore, additional drag. Indeed shedding vorticity, that is, the oscillatory motion of vortices, is related to the turbulence produced by the blade, which therefore results in an increase of turbulent kinetic energy. In Figure 9.9, it can be seen how the increase in kinetic energy is related to the interaction between tip vortices between two blades, happening at -0.5 X/D.

Thus, the flow behind a propeller must be different in the cases of isolated and multiple. In particular, it can be seen how the fully symmetrical velocity contour of the single propeller becomes asymmetric, with a region of separated flow identifiable in Figure 9.10. This region, coming from the upwash of the blade and the radial flow, entails an increase in turbulent energy, as it would happen for flow separation over a wing [49]. To understand how to reduce the turbulence phenomenon associated with the tip interaction, it is first necessary to understand what the vortices look like. This can be seen in Figure 9.11.

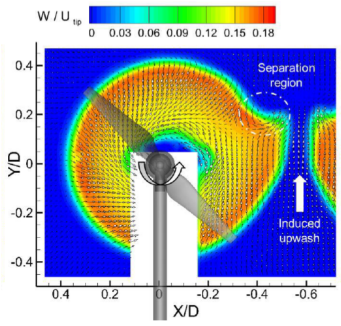

Figure 9.10: *Velocity contours for twin propeller [49]*

The difference between a horseshoe vortex and a hairpin one solely relies on the dimensions, as the former is almost as wide as tall, while the latter is narrower. As seen in Figure 9.11b, the vortex is made up of three main parts, that is, two counter-rotating quasi-streamwise vortices close to the wall surface, known as legs. The counter-rotating vortices assume different names based on their rotation direction. Indeed, if they tend to push the vortex away from the body, they are referred to as ejections, while in the opposite case, as sweeps. The legs work as an engine to generate low-speed zones by rotation and create shear layers with surrounding high-speed neighbouring fluids. Then, the Ω-shaped ring head, which moves the vortex forward, is connected to them via the necks. One thing to note is that vortices are not singular events but rather appear in packets, as shown in

Figure 9.11c [50].

9.3.2. Plasma Actuators

The boundary layer formed over a wing can be thought of as an assembly of hair-pin vortices distributed quasi-periodically in time and space. As explained, the sweep events are found on the downwash side of the legs and bring the high-speed flow, while the injection events are found on the upwash side. Logically, due to their velocity, it is the sweep events that are responsible for the turbulent skin-friction drag, when the fluid falls onto the wall surface. Thus, to reduce the turbulence, it is necessary to reduce the sweep event close to the wall surface. Many methods have been attempted to solve this problem, such as the creation of weak streamwise vortices or the presence of an active Gaussian bump, but all the methods have been found to have too little effect. A method that has been under development recently and could have a larger effect is the use of plasma actuators. These are relatively simple devices, as they do not entail any moving parts or ducting but are purely electric and only include a few small components. Their applicability to this specific design purpose still needs to be thoroughly investigated, especially with respect to high flight speeds. However, turbulence is a phenomenon difficult to reduce and this concept provides an elegant possible solution. These actuators are able to create a body force close to the wall and can be manufactured as lightweight, thin sheets that can easily adhere to the wing surface. Indeed, they are normally composed of two electrodes, separated by a thin solid dielectric layer, about 1 mm thick. A visual representation can be seen in Figure 9.12.

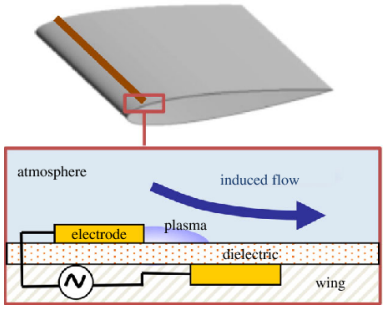

Figure 9.12: *Plasma actuator [51]*

One of the two electrodes is placed on the external side and thus exposed to the incoming airflow, while the other is constrained between the dielectric and the wing skin. When a high-voltage DC or AC signal, in the order of a few kilovolts, is applied, plasma appears on the wing [52]. This voltage can be easily scaled up from the battery voltage with the alternators present in between the batteries and motors and then wired to the electrodes. Naturally, plasma does not appear out of thin air, but it is the result of the interaction between particles. Indeed, a potential difference is created between the two electrodes, which creates a flow of electrons. These move towards the negative electrode, while the other one pulls the nucleus of the dielectric. This component has a limit, which is stressed above its limit when the voltage is increased and turned the material from an insulator to a conductor by ionizing it. This follows the Townsend avalanche, that is, a process where the collision between electrons and neutral atoms separates the charges of the latter into ions and more electrons. This creates a snowball effect that exponentially increases the number of charged particles, turning the dielectric into a highly-conductive material, the plasma [53].

Once this is created, the electrically charged particles are propelled through the air by the electric field, generating a small jet of fast air moving parallel to the wing surface. When not in use, however, it does not affect the airflow, as it only entails one small strip of electrode[7]. When activated, the induced flow creates clockwise rotating vortices, which "drag" the propeller-induced vortex into the wall and dissipate it. This can be seen in Figure 9.13, where plasma is applied in cases (ii) and (iv) [53]. In the case of (ii), the plasma is applied at the second row of black electrodes when the turbulence arrives from upstream. Then, this newly created vortex will expand as it moves, so another vortex will have to be created in case (iv), where the plasma is activated upstream from the turbulence.

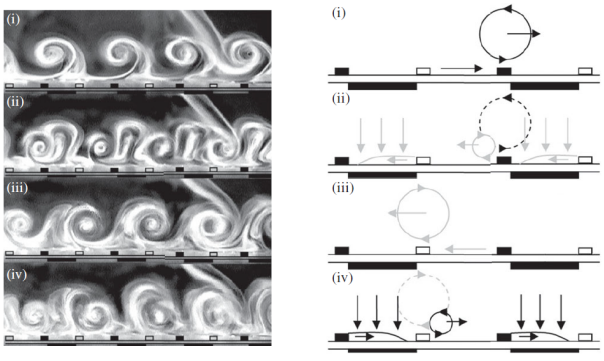

(a) *Flow visualisation* **(b)** *Schematic of flow*

Figure 9.13: *Flow interaction with plasma [53]*

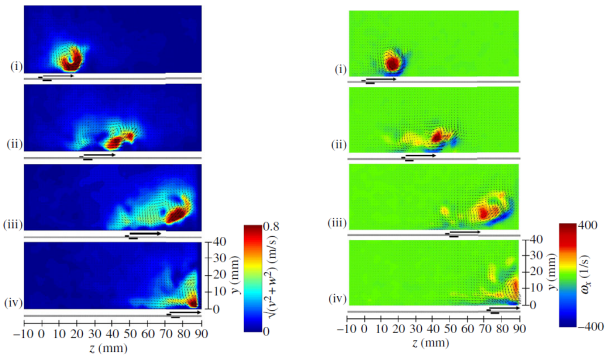

(a) *Velocity magnitude* **(b)** *Streamwise vorticity*

Figure 9.14: *Effect of spanwise travelling vortices [53]*

In Figure 9.14, it is actually possible to see how the plasma-actuated vortices help to slow down the flow and reduce

[7] https://www.scientia.global/wp-content/uploads/Huu_Duc_Vo_Njuki_Mureithi/Huu_Duc_Vo_Njuki_Mureithi.pdf [Accessed on 17.06.2023]

its vorticity while at the same time keeping it attached to the wall. Indeed, it might happen that by slowing down the flow too much, this undergoes separation, which is even more deleterious than turbulence. Therefore, it can be seen that when vortices are close to the wall surfaces, plasma actuators are able to contrast their effects to an acceptable extent. Moreover, the additional flow created by these devices can also serve as over-the-wing cooling to decrease the boundary layer temperature and, additionally, to a certain extent, one of the battery packs stored in the wing [54]. Since this is a new technology, there are many unknowns to its functioning, especially in non-ideal conditions. Especially it appears that, at the moment, plasma actuators are sensible to temperature changes along the flight [55] and to different climate conditions. For the second case, a new study has shown that for rain conditions, the actuator is able to quickly recover its performance even when wet [56], but further investigation is needed. A comprehensive study on plasma actuators is left for the iterative phase, but it is already clear how this technology can be of great help.

9.4. Motor Choice

Table 9.3 displays all potential motor types that would be applicable to ElectriFly. Most of these motor types are already on the market. However, models currently in development and available within the next few years, are also listed. These are included in the trade-off as the number of existing electric motors is limited and ElectriFly is designed to enter service in 2035. Therefore it is imperative to use the latest technologies and include the promising lightweight designs that will enter the market in the close future. To determine the total amount of motors required for a specific motor type, two vital performances need to be evaluated. These are the maximum achievable peak power during the constraining phase and the continuous power requirement during the cruise phase. As specified in Section 6.1 the peak power requirement is set by the diversion climb, which demands 1189 kW, and the cruise phase sets a continuous power requirement of 646kW. This means that depending on the specific motor characteristics, either the maximum power or continuous power will be limiting and therefore define the number of motors required for that specific type. For each motor type, this required number along with the corresponding total mass is displayed in Table 9.3.

In Section 9.3, it was examined what the increase in lift corresponding to the varying potential number of engines in the distributed propulsion configuration is. This analysis shows that the more engines the aircraft has, the more ΔC_L will be created by the DEP principle. This ΔC_L can therefore be estimated for all the motors as the required number of motors is known. It is vital to note that each potential motor type results in a different total motor mass. This mass is seen as weight, which requires additional lift. By specifying this required extra lift, $\Delta C_{L_{motor}}$, for the mass of the motors, it can be concluded what the net ΔC_L is for each motor type. This net ΔC_L is thus computed by subtracting the $\Delta C_{L_{motor}}$ required for the motor weight from the $\Delta C_{L_{DEP}}$ induced by the distributed propulsion configuration. By analysing this number, it becomes clear which motor types and their corresponding configuration perform best. The extra lift required due to the motor weight is calculated accordingly:

$$\Delta C_L = \frac{2 \cdot W_{motor}}{\rho \cdot V_{cruise}^2 \cdot S} \tag{9.15}$$

Hence, the Equation 9.16 is used in order to find the net change in lift.

$$\Delta C_{L_{net}} = \Delta C_{L_{DEP}} - \frac{2 \cdot m_{motor} \cdot g}{\rho \cdot V_{cruise}^2 \cdot S} \tag{9.16}$$

In which $\Delta C_{L_{DEP}}$ is determined by the number of motors required for a specific type and the ΔC_L found in Section 9.3.

Table 9.3 displays the net ΔC_L analysis for all motor types. Before comparing these values and making a trade-off, it is relevant to first discard the configurations that are not viable. Therefore, some motor types were discarded based on two criteria: total motor mass and the total amount of motors required. Earlier in the design stage, the total motor mass was estimated to be around 300 kg. There is room for some potential increase in mass, however, in order not to affect the MTOW too much, it was decided to allow this increase up to a maximum of 50%. Therefore all the motor configurations that have a mass higher than 450 kg are not optional. Additionally, it was chosen to eliminate all types which require a number of 16 motors or more in order to meet the power requirement. This is done because of multiple reasons. Firstly, it is not efficient to put a significant number of engines on a relatively small wingspan. Assessed by ElectriFly's wing geometry, it was concluded that implementing 16 motors or more would cause problems in terms of both spacing and interference of the airflow, resulting in a reduction of the achievable thrust. Furthermore, it is a great deal of effort to maintain such a high number of engines which, looking at operational costs, will be unattractive to airlines.

Table 9.3: *Comparison of potential motors with corresponding properties. Selected one marked in blue and discarded ones marked red.* [8] [9] [10] [11] [12] [13] [14] [15]

Motor	Company	P_{peak} [kW]	P_{contin} [kw]	N	Mass motors [kg]	$\Delta C_{L_{weight}}$	$\Delta C_{L_{DEP}}$	$\Delta C_{L_{net}}$
HPDM-250	H3X	250	200	6	96	0.005754611	0.06	0.054245389
HPDM-30	H3X	41	33	30	123	0.007373096	0.9	0.892626904
Magni350EPU	MagniX	350	280	4	542	0.032489576	0.026	-0.006489576
Magni650EPU	MagniX	640	560	2	496	0.029732158	0.004	-0.025732158
KM-120	KiteMagnetics	120	120	10	230	0.013787089	0.18	0.166212911
SP260D	Siemens	261	261	6	300	0.01798316	0.06	0.04201684
SP90G	Siemens	65	65	20	260	0.015585405	0.5	0.484414595
Emrax188	Emrax	60	37	20	158	0.009471131	0.5	0.490528869
Emrax208	Emrax	86	56	14	144.2	0.008643906	0.294	0.285356094
Emrax228	Emrax	124	75	10	135	0.008092422	0.18	0.171907578
Emrax268	Emrax	210	117	6	133.8	0.008020489	0.06	0.051979511
Emrax348	Emrax	400	210	4	175.6	0.010526143	0.26	0.249473857
REB50	MGM	50	40	24	288	0.017263834	0.648	0.630736166
REB60	MGM	60	45	20	306	0.018342823	0.5	0.481657177
REX90	MGM	70	50	18	311.4	0.01866652	0.45	0.43133348
REB90	MGM	80	70	16	380.8	0.022826625	0.368	0.345173375
YASA-P400	YASA	160	100	8	192	0.011509223	0.12	0.108490777
YASA-750R	YASA	200	70	10	370	0.022179231	0.18	0.157820769
E811	Pipistrel	57.6	49.2	22	499.4	0.029935967	0.572	0.542064033

Evaluating the remaining options, it is apparent that the winner is the Emrax208 with a net ΔC_L of 0.2854 (marked in blue in Table 9.3). It can thus be established that the Emrax 208 is the best option and will therefore be chosen to propel the ElectriFly. The specific characteristics of this motor are given in Table 9.4. Lastly, it is important to note that after the iteration of ElectriFly's preliminary design, the chosen configuration still meets the requirements set by the new power and energy demand. Furthermore, the Emrax 208 still came out as the best choice regarding net ΔC_L and therefore, no design changes are required regarding the motor choice. Setting the number of engines at 14, the propeller design entails a diameter of 0.88 m and propulsive efficiency of 0.80.

Table 9.4: *Emrax 208 motor specifications*

Mechanical		**Electrical**	
Type	Axial flux motor / generator	**Max voltage**	580 V
Casing diameter	208 mm	**Peak power**	86 kW
Axial length	85 mm	**Continuous power**	56 kW
Dry mass	10.3 kg	**Peak torque**	150 Nm
Stator cooling	Air / Liquid / Combined	**Continuous torque**	90 Nm
Mounting	Front: 6x M8 threaded holes Back: 16x M8 threaded holes	**Efficiency**	92 - 98 %

9.5. Energy-harvesting Mode and Propeller Design

Considering the high energy and power requirements of electric aviation, methods of reducing this energy consumption must be explored. In particular, one of the most interesting methods that are currently being investigated is the harvesting of the kinetic energy contained in the flow. This can only happen in the descent phase, with the propeller in windmilling mode, as in this configuration, it creates negative thrust, that is, drag, that is undesired in any other flight phase. Although the amount of energy that can be actually harvested from a propeller is relatively low, it can still be useful to relieve the stress put on the recharging drone by lowering its energy requirement. However, this must not

[8] https://www.h3x.tech/hpdm-3000 [Accessed on 10.06.2023]
[9] https://magnix.aero/services [Accessed on 10.06.2023]
[10] https://kitemagnetics.com/home-page-electric-motors/products [Accessed on 10.06.2023]
[11] https://press.siemens.com/global/en/feature/electric-flight [Accessed on 10.06.2023]
[12] https://emrax.com/ [Accessed on 10.06.2023]
[13] https://www.mgm-compro.com/electric-motor/80-kw-electric-motor/ [Accessed on 10.06.2023]
[14] https://yasa.com/technology/ [Accessed on 10.06.2023]
[15] https://transportup.com/headlines-breaking-news/vehicles-manufactures/pipistrel-certifies-its-e-811-engine-available-to-other-oems/ [Accessed on 10.06.2023]

come at the price of a decrease in the performance of the aircraft in design, as that would be more damaging than not utilising this concept entirely.

To give a general overview of the phases of performance of a propeller, Figure 9.15 can be used. Here, the performance of a propeller is shown in terms of efficiency, propulsive and regenerative, and the thrust and power coefficients. These are presented as a function of the advance ratio J, that is, the ratio between the axial and rotational velocity of the propeller. Therefore, it can be seen that, in order to switch from the propulsive to the regenerative regime, it is necessary to increase the rotational velocity of the propeller so that negative angles of attack are created and the thrust and power output are both negative. The negative power, or torque, will therefore be used to power the motor-generator, already chosen in Section 9.4, which in turn will translate the rotational energy into electrical. Therefore, logically, the design of the propeller greatly affects its ability to regenerate energy. Indeed, it is impossible to optimise the design for both the propulsive and regenerative phases, as these are opposite, and the propeller cannot generate both maximum positive and maximum negative thrust. A good compromise would be to use a symmetric airfoil along the full blade profile, as this type can create positive and negative thrust equally. However, while presenting good performances in energy-harvesting conditions, the one in propulsive mode is highly limited. In fact, the main characteristics for an airfoil to be able to perform well in both phases are:

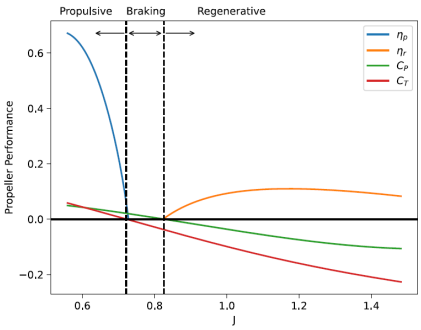

Figure 9.15: *Performance of a propeller[57]*

- High positive L/D ratio over a wide range of angles of attack in propulsive mode
- Low negative L/D ratio over a wide range of angle of attack in regenerative mode
- Thickness-to-chord ratio between 10% and 20%
- Good low and high-speed performance
- Benign stall characteristics

While the reasoning behind most of these characteristics is straightforward, the choice of thickness is due to the mission profile of ElectriFly, in particular, to the modest velocities that it needs to attain. Therefore, an analysis performed by van Neerven shows that the best airfoil for the desired performance is the NACA 4415. This is because its performance is considerably superior to other airfoils, especially for higher angles of attack, which are expected on the majority of the blade and for the regenerative regime. By using a symmetric airfoil, a 2% decrease in efficiency would be expected, while by choosing a low-cambered airfoil, such as the NACA 4415, instead of a highly-cambered one, the loss in efficiency can be considered negligible.

Once the airfoil has been chosen, the propeller type needs to be chosen. For this, three possibilities are present based on the blade pitch angle and rotational speed. Indeed, these are the constant pitch, variable RPM (CPVR), the variable pitch, constant RPM (VPCR) and the variable pitch, variable RPM one (VPVR). In general, the idea behind using variable parameters is due to the change in airspeed during the various flight phases. Indeed, when airspeed increases, the angle of attack decreases, increasing the RPM, and therefore the blade pitch angle needs to increase to maintain the desired rotational speed value. As explained by van Neerven, the use of a variable pitch, variable RPM blade (VPVR) is especially preferable in case the principle of energy-harvesting is to be utilised. Indeed, in general, the rotational velocity must be changed dynamically along the different flight phases, and in particular, the coupling between this and the blade pitch angle is important for the regenerative regime as it can guarantee the highest intake of energy.

Moreover, aircraft design generally considers between 2-8 propellers. As each blade generates thrust, increasing the number of blades generally increases the overall thrust of the propeller while at the same time decreasing the overall efficiency of the propeller. To balance these two components, van Neerven performs an analysis on each of these three configurations for only 2 and 3-bladed propellers. In addition to this, it can be noted that in order to achieve the required thrust requirement without excessively increasing the solidity of the propeller, 3-blade propellers are typically used for aircraft of similar speed [59], and thus are chosen in the current design.

Moreover, when compared to the other two types, VPVR presents lower total energy values for the climb, cruise and descent phases, and especially in the latter, it is able to regenerate up to 2.5 kWh more. Then, it can also be noted that for the case of the VPVR, the optimal solidity for the descent phase can be decreased as there are more possible combinations to meet the thrust requirement in both climb and cruise due to RPMs and pitch being both variables. In general, the maximum RPM can also be increased over the limit of 2250 rev/min presented by the VPCR, contributing more to the increase in section angles of attack and, as a result, similar angles of attack can be attained at lower blade angles in the VPVR case. However, a gearbox is still needed as the maximum suggested RPM for most propellers is of

2700 rev/min. Naturally, the propeller could spin faster, and could even reach the 6000 rev/min of the motor, but the problem would be the tip velocity and the structural loads on the propeller hub. Indeed, tip velocity can be found as follows [60]:

$$V_r = RPM \cdot \pi D_p \tag{9.17}$$

$$V_{rel} = \sqrt{V_r^2 + V_{TAS}^2} \tag{9.18}$$

$$M_t = V_{rel} / a \tag{9.19}$$

Thus, the tip Mach number for the case where the propeller spins at 6000 rev/min is 0.92, which is almost sonic, while in the case where the propeller spins at about 2700 rev/min is of 0.51. Obviously, the propeller should not spin at sonic speeds or close to them, as that would entail high noise and high structural loads on the blade and on the hub. Therefore, although the gearbox adds weight to the engine structure, it is considered to be more beneficial than having the propeller spin at almost sonic speeds. Following these considerations, in this report, only the 3-bladed VRPR propeller is considered.

Hereafter, the optimal blade pitch angle distributions for the three main phases are presented in Figure 9.16. These are different based on which way the propeller is optimised, but in the case of the current design, the cruise phase is the most time expensive and, thus, the defining phase for the design of the blades. The blade pitch angles can be superimposed to the ones at zero angle of attack presented in Figure 9.17 to present the total twist distribution of the propeller in the various phases of flight.

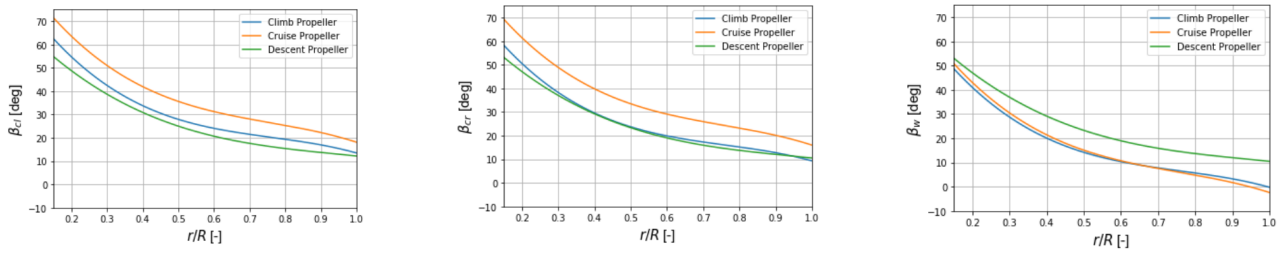

(a) *Climb blade angles* **(b)** *Cruise blade angles* **(c)** *Descent blade angle*

Figure 9.16: *Blade angles for VPCR, B = 3 [58]*

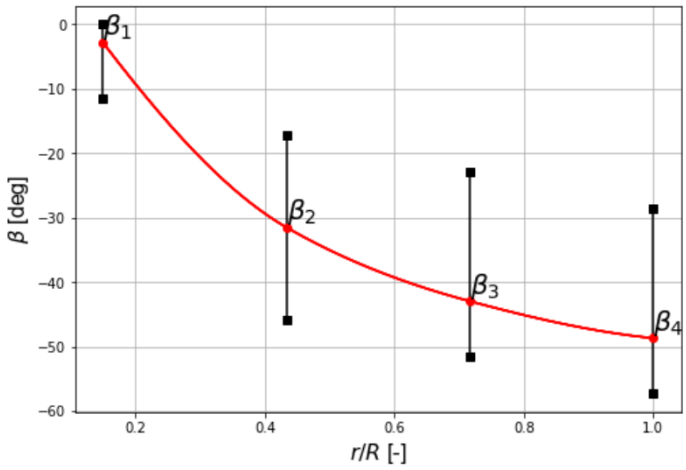

Figure 9.17: *Twist distribution at zero angle of attack [58]*

Moreover, with the propeller diameter found in item 9.2, it is also possible to find the chord distribution along the blade, with the help of Figure 9.18. These distributions tend to change for short cruise distances, but level off for longer ones, so they can be considered constant in this design.

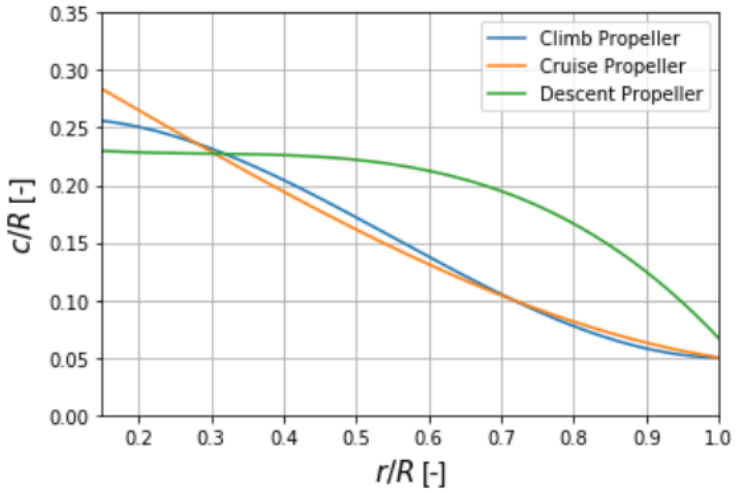

Figure 9.18: *Chord distribution for VPCR, B = 3 [58]*

Finally, now that the propeller is fully designed, the graph for the regenerating efficiency, along with the cruise and climb ones, can be seen in Figure 9.19, where once more it is possible to see that the 3-bladed configuration behaves better also in descent.

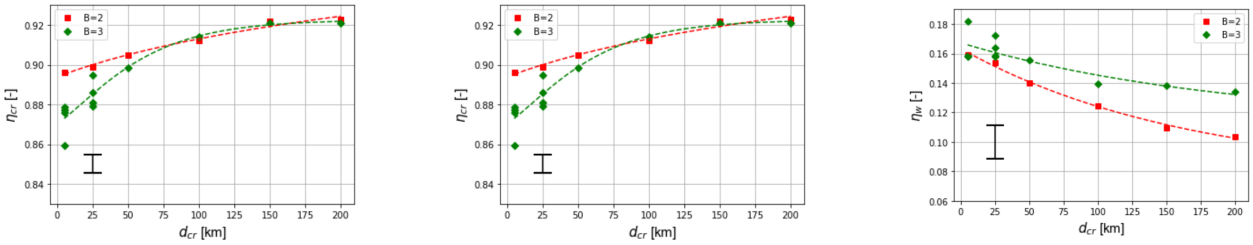

(a) *Climb efficiency*

(b) *Cruise efficiency*

(c) *Descent efficiency*

Figure 9.19: *Efficiencies for VPVR, B = 3*

Therefore, for increasing range, the efficiency seems to flatten out at a value of around 13%. With this value and the formula for energy-harvesting efficiency shown in Equation 9.20, it is possible to compute the regenerated power.

$$\eta_r = \frac{|P|}{\frac{\pi}{8}\rho_\infty V_\infty^3 D^2 N_{en}} \tag{9.20}$$

Here, ρ_∞ and V_∞ are the values for the descent, where the descent velocity is given as 60.55 m/s in Chapter 11. The regenerated power is hence:

$$P = 13\% \cdot \frac{\pi}{8} \cdot 0.77 \cdot 60.55^3 \cdot 0.88^2 \cdot 14 = 94608W$$

To get to the maximum energy that can be recuperated during descent, it is enough to multiply the regenerated power just found with the maximum descent time. This time follows from the current mission profile and the optimum descent slope, as discussed in Chapter 11. This maximum descent time is found to be 1718 s. It must be noted that this is not the optimal descent time, as the aircraft would be flying very close to its stall speed and would considerably reduce its range. However, this value gives an upper estimate of the possible benefits of the energy-harvesting phase.

$$E = P_{reg} \cdot t_{descent} = 94608 \cdot 1718 = 162537264J = 45.15kWh$$

A problem that might arise from the use of propellers in regenerative mode during descent is the fact that, by decelerating the flow, control surfaces and HLDs might not function properly. This would be catastrophic, as the aircraft might not be controllable in descent anymore. A solution for this has already been used for other purposes in Subsection 9.3.2, where plasma actuators were introduced. These devices can be useful in this case as well. Indeed, they can also function to control the aircraft[16] and to force the newly-produced flow to go over the control surfaces, helping their functioning again [61]. Considering the low percentage of energy that can actually be harvested from the flow, swirl recovery devices could also be considered in future iterations.

[16] https://www.scientia.global/wp-content/uploads/Huu_Duc_Vo_Njuki_Mureithi/Huu_Duc_Vo_Njuki_Mureithi.pdf [Accessed on 17.06.2023]

9.6. Auxiliary Propulsion Subsystems

Although the motor and propeller are the most prominent components of the propulsion system, there are some other subsystems required to properly transfer the electrical energy from the battery into the desired mechanical energy. These sub-components are listed below:

- **Converter:** The converter converts the current from the battery to the right form and voltage required for the motor. As the EMRAX208 is a brushless DC motor and the battery generates direct current, a DC/DC converter is needed to provide the required voltage to the motor. Each motor has a separate converter in order to optimise the overall efficiency.
- **Driver:** The driver is used to switching the DC currents to the motor windings and thereby produce magnetic fields. Additionally, it adapts the amplitude and phase of the DC current pulses to control the power, speed and torque of the motor. It is vital that each motor has its own driver so that the principle of differential thrust can be accurately applied and each propeller can perform at a very specific thrust level.
- **Gearbox:** The gearbox is directly connected to the output of the driver and allows the propulsion system to run in multiple gears, enabling the required conditions defined by the driver. In the case of Electrifly, only a 2:1 gearbox is needed as that is the ratio of maximum rotational velocities of motors and propeller.
- **Cooling system:** The cooling system that is equipped with the propulsion system is used for cooling the motor, driver, gearbox and converter. As the total power of the aircraft is divided over 14 engines in total, the heat augmentation of the engine components will be within a reasonable limit, and therefore, the weight of the liquid cooling system will be acceptable as well. A more in-depth analysis of the thermal system will be presented in Section 13.6.
- **Fairing:** The Fairing is important as it protects all the engine components from external threats and provides the structural connection to the wing.

The weight of these components must be accounted for in the total engine weight determination. As it is very difficult to accurately approximate the weight of these individual components, these parts together are seen as a group of which weight is determined based on literature. For this, it is relevant to look at similar electric aircraft with the same size and mission profile. As the electric aviation market is still in the absolute early stages of its development, there is currently only 1 aircraft that has the same order of magnitude as the ElectriFly and can therefore be analysed. This is the 9-passenger aircraft by Alice Eviation [17]. As the engines of conventional non-electric aircraft differ significantly and are in no way comparable to electric propulsion systems, there is no point in performing a fractional weight analysis on them. Therefore, the weight fractions of Alice Eviation were examined and showed that the motor contributes to approximately 67.5 % of the total engine weight. This means that the other 32.5 % is distributed over the propeller, converter, driver, gearbox, cooling system and fairing of the engine[18]. Therefore this is also assumed for the Electrifly, yielding a total engine weight of 15.26 kg per engine resulting in 213.63 kg for the total propulsion system.

9.7. Propulsion Design Overview, Assumptions and Verification and Validation

The analysis of the propulsion system yielded values for various parameters. These values are summarised and provided in Table 9.5.

Table 9.5: *Overview of engine characteristics*

Parameter	Value	Unit
Number of engines	14	-
Spanwise portion occupied by engines	0.9	-
Total weight of engines	144.2	kg
Propeller Diameter	0.88	m
Propeller clearance	0.44	m
Propulsive Efficiency	0.80	-
Propeller RPM max	2700	rev/min
Number of blades per propeller	3	-
Thrust per propeller	985	N

Hereafter, in Table 9.6, a list of all assumptions used for the design of the propulsion system. The validity of these assumptions is discussed in Chapter 19.

[17] https://www.eviation.com/ [Accessed on 21.06.2023]

Table 9.6: *List of assumptions for the propulsion system design*

ID	Assumption
ASM-PROP-01	The total system efficiency is 0.73
ASM-PROP-02	The distributed propulsion method works for large Δy as well and not only for small ones
ASM-PROP-03	The distributed propulsion method can fit wingtip mounted propellers by changing the wing span
ASM-PROP-04	The aerodynamic effect of wingtip mounted propellers can be superimposed on the design
ASM-PROP-05	The effect of turbulence can be reduced with the use of plasma actuators
ASM-PROP-06	Propulsive efficiency, throttle setting and power ratios stay constant with each flight phase
ASM-PROP-07	The assessed flow is incompressible

To check whether the results of the model make sense from a physical point of view, the functions can be unit tested to see the outcome of changing some inputs or whether their returns comply with the expected ones. For the propulsion system, some of these unit tests are presented in Table 9.7. Naturally, all of the code was verified, and these are only examples representative of some parts of the code.

Table 9.7: *Propulsion subsystem unit tests*

ID	Test	Expected outcome	Actual outcome	Pass/Fail
TEST-PROP-01	$\lim_{N_{en}\to\inf} D_p$	$D_p = 0$	$D_p = 0$	Pass
TEST-PROP-02	$\lim_{\eta\to 0} T_c$	$T_c = \inf$	$T_c = \inf$	Pass
TEST-PROP-03	$V_p > \mathrm{V}$	True	True	Pass
TEST-PROP-04	$\Delta C_L > \Delta C_l$	True	True	Pass
TEST-PROP-05	$a_p < 1$	True	True	Pass

Out of these, TEST-PROP-01 is picked as an example to show the method. This test verifies Equation 9.1 for extreme values. Indeed, as shown in the formula, when the number of engines increases, the diameter should decrease, as to fit more propellers, these have to be smaller. The code implementation of this formula shows that this behaviour is respected; that is, when N_{en} becomes larger, then the diameter gets closer and closer to 0.

The results initially obtained from the model seem to entail that the gain in the lift was almost negligible. Therefore, expert validation was requested and performed by Reynard de Vries, Robert Nederlof, and Brandon Litherland. According to them, the gain in the lift should be in the order of one order of magnitude higher than the one initially found. Once a suggested fix was applied, the found values resemble the hypothesized one. Therefore, these can be considered validated.

10. Structural Subsystem Design

In this chapter, the structural aspects of the design are discussed. After defining the reference frames, the flight envelope is developed in Section 10.2. The material choice for the fuselage and wingbox elements is then made in Section 10.3. Next, in Section 10.4 the interior and exterior of the fuselage design are summarized. The initial design is followed by the analysis of internal loads and stresses in the fuselage. Section 10.5 covers the design of the load-carrying structure of the wing. Finally, after providing the final weight distribution, the assumptions and V&V procedure for the relevant models are discussed in Section 10.7.

10.1. Reference Frames

The reference frame used is a right-handed, body-fixed coordinate system. For the fuselage analysis, the fuselage reference frame is used, where the origin is placed at the middle nose of the aircraft as seen in orange in Figure 10.1. The positive X_f-axis is directed from nose to tail, the Y_f-axis points positive outwards along the right wing. The positive Z_f-axis points vertically up. The wing analysis is done with respect to the wing reference frame (subscript 'w'), which has the same orientation as the fuselage reference frame, but has a different origin, as seen in blue in Figure 10.1. The origin of the wing reference system is in the middle of the fuselage at the root chord. The coordinate system is presented in Figure 10.1, and is constant throughout this chapter.

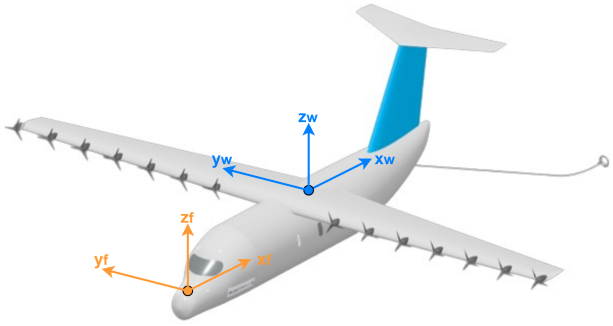

Figure 10.1: *The reference frames used for structural analysis*

10.2. Flight Envelope (V-n Load Diagram)

The flight envelope is a diagram used to find the ultimate load factor n to which the aircraft will be subjected. It is a combination of both the manoeuvring envelope and the gust envelope. The ultimate load factor was further used to calculate the maximum internal forces and loads in the fuselage and wing [1]. The procedure is further described in Section 10.4. The flight envelope is constructed for the three major phases of flight: take-off, cruise and landing. The parameters used for each of the loading cases are shown in Table 10.1, and their plots are shown in Figure 10.2.

Table 10.1: *The loading cases for which flight envelopes were developed*

Phase	Speed [m/s]	Weight [kg]	Altitude[ft]	Air Density [kg/m3]	Clmax	n positive [-]	n negative [-]	n ult [-]
Take off	49	7960	0 (Sea lvl)	1.225	1.8	3.63	-1.63	5.45
Cruise	110	7960	15000	0.7708	1.6	2.88	-1.18	4.45
Landing	60	7960	0 (Sea lvl)	1.225	1.8	3.63	-1.63	5.45

[1] Expert consultation on 07.06 with Dr.Ir. Calvin Rans (Delft University of Technology)

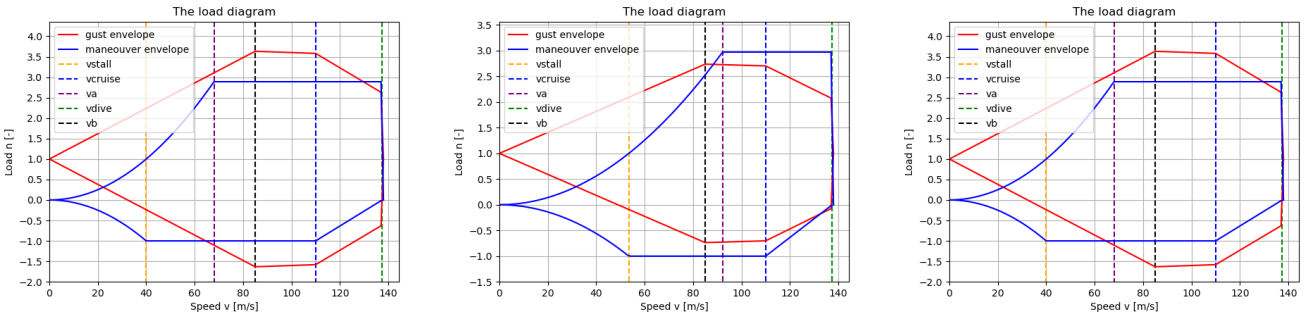

(a) *The flight envelope for take-off*

(b) *The flight envelope for cruise*

(c) *The flight envelope for landing*

Figure 10.2: *The manoeuvre and gust envelopes for the 3 flight conditions.*

The most limiting load cases were found in take-off and landing with a maximum load factor of 3.63 and a maximum negative load factor of -1.63. The ultimate load factor is then acquired by multiplying the largest load factor in magnitude by a safety factor of 1.5, yielding $n_{ult} = 5.25$.

The manoeuvre envelope limits were found using statistical equations depending on the maximum take-off weight (MTOW) - Equation 10.1 and Equation 10.2. The parabolic connection between these two lines is dependent on lift characteristics and determined using Equation 10.3. [62].

$$n_{max} = 1 + \frac{24000}{21000 + MTOW} \quad (10.1) \qquad n_{min} = -0.4 * n_{max} \quad (10.2) \qquad n = \frac{qC_{L_{max}}}{(W/S)} \quad (10.3)$$

For the gust envelope the change in load due to gust at 3 different speeds - cruise, dive and the speed for which the maximum lift and angle of attack occur v_B [62], must be found using Equation 10.5 [62]. The load change is then added to or subtracted from 1 to find the load at the different speed conditions as shown in Equation 10.4 [62].

$$n = 1 + \Delta n \quad (10.4) \qquad \Delta n = \frac{\rho v C_{L_\alpha} u}{2(W/S)} \quad (10.5)$$

In Equation 10.5 u represents the speed of wind gusts. It is found by applying the factor K (see: Equation 10.7) to standard gust velocities $\hat{u}$ as shown in Equation 10.6 [62]. The μ parameter value is defined as Equation 10.8 [62].

$$u = K\hat{u} \quad (10.6) \qquad K = \frac{0.88\mu}{5.3 + \mu} \quad (10.7) \qquad \mu = \frac{2(W/S)}{\rho g \bar{c} C_{L_\alpha}} \quad (10.8)$$

10.3. Material Analysis

After the analysis of the structures and the stresses, the material choice could be made to optimize the designed structures for the given material properties.

Wingbox Material Choice Method

Material choice and the geometry of the stringers and skin are interrelated, and they are both variables affecting the weight of the part. This is a chicken and egg problem, among many other aspects of aircraft design. To solve this, a material can be selected first for an appropriate objective function. Materials are chosen based on the main purpose the part serves in the system.

For the wingbox, a simple single-celled tapered rectangular box is considered. The main internal parts considered at this stage are the stringers and the skin panels (consisting of the top panel, bottom panel and front spar, rear spar). For the skin panels, their objective function is minimizing weight and they should be designed for shear yield, i.e. maximizing shear yield stress [63]. Equation 10.9 shows the relationship between the cross-sectional skin panel area and the mass density of the material. The A_{skin} relates to the maximum shear flow in the cross-section, and since the shape of the skin is thin-walled, the relation of the geometry to the shear yield τ_{yielf} of the material is complicated to derive, however, a material index can still be derived. Since A_{skin} is inversely proportional to the τ_{yield}, when minimizing the mass of the skin Equation 10.9, the material index to be maximized is Equation 10.10 [64].

$$m_{skin} = \int_0^{\frac{B_w}{2}} A_{skin}(y)\, dy \cdot \rho_{skin} \quad (10.9) \qquad Min(m_{skin}) -> M_{skin} = Max(\frac{\tau_{yield}}{\rho_{skin}}) \quad (10.10)$$

Similarly, the stringers can be designed with the same objective function of minimizing mass, however, their purpose should be for the highest tensile yield, i.e. maximizing tensile yield stress [63]. The mass of the stringers can be estimated with Equation 10.11. Deriving the material index again shows to maximize the material index ratio as seen in Equation 10.12 [64].

$$m_{stringers} = \frac{6 \cdot M_{max} \cdot z_{max} \cdot B_w}{2 \cdot h^2} \cdot \frac{\rho_{stringers}}{\sigma_{yield}} \quad (10.11) \qquad Min(m_{stringers}) -> M = Max(\frac{\sigma_{yield}}{\rho_{stringers}}) \quad (10.12)$$

Fuselage Material Choice Method

The fuselage structure has been simplified to having stringers and a circular skin panel along the cylinder. Similar to the wingbox material choice methods in Section 10.5, the material indices to maximize the two parts of the fuselage can be derived. Similar to the wingbox skin panels, it is assumed that the fuselage skin panels primarily carry the shear stresses and thus shall be designed for maximizing shear yield stress. Additionally, the stringers of the fuselage are assumed to primarily carry the normal stresses and thus shall be designed for maximizing normal yield stress. The objective function of minimizing mass remains the same, and thus the material index to maximize for the fuselage skin panels is shown in Equation 10.10, whereas for the fuselage stringers are shown in Equation 10.12.

Material Comparison and Selection

Traditional metals like aluminium alloys are included in the considered materials, as these are well-tested in aerospace applications and are of aerospace grade. The most used aerospace-grade aluminium alloys are aluminium zinc (ALU7075) and aluminium copper (ALU2024). Recycled aluminium was investigated, but turned out to be too degraded in quality for aerospace grade [2]. Exemplary materials representing other aerospace-grade alloys such as titanium and magnesium were also compared in the analysis.

Composites have a high stiffness-to-weight ratio, and are flexible in design, by allowing for the optimisation of properties for different mixes and orientations of fibres and matrices. However, their sustainability and recyclability is not feasible for all available composites. Notably, there are companies such as Lineat that have created a process called "Aligned Formable Fibre Technology" that recycles carbon fibre into uni-directional tapes[3]. Initially, natural fibre composites, such as hemp and flax, were considered for sustainability production reasons. However, the natural material properties were insufficient aerospace-grade for this design. So more demanding fibres like carbon and glass are considered, which have challenges in the coming years in terms of standardizing their recycling. The matrix filler found to possess the best combination of material properties is 'Polypropylene'[65]. Additionally, since this material is thermoplastic, it can easily be recycled by heating and reshaping.

The materials considered for the structural components of the wingbox and the fuselage are shown in Table 10.2 with their most important properties. The data was found in literature or, for composites some of the properties were calculated using the rule of mixtures [66].

Table 10.2: *Considered materials and their properties*

Material	E [Gpa]	σ_{yield} [Mpa]	τ_{yield} [Mpa]	ρ [$g/cm\hat{}3$]	σ_{yield}/ρ	τ_{yield}/ρ
ALU2024 [4]	73	324	283	2.78	116.5	101.8
ALU7075 [5]	72	503	331	2.81	179	117.7
Std_CFRP/Epoxy (60% fibers) [6]	135	110	90	1.6	68.75	56.25
CFRP:T700/PP (60% fibre) [7] [8]	140	262	83.5	1.450	181	57.6
CFRP:T700/PEEK (60% fiber) [9] [10]	140	3450	109	1.6	2158	68
CFRP:T700/EPOXY (60% fiber) [11] [12]	151	2700	136	1.6	1690	84
BeAl-363 [13]	202	213.7	247.5	2.16	98.93	114.6
AlB4C06 [67]	90	148.2	141	2.688	55.13	52.5
Titanium Grade 5 [14]	114	880	550	4.43	199	124
Magnesium Alloys [15]	45.2	164	145	1.81	90	80

[2] https://www.aerospacemetals.com/ [Accessed on 13.06.2023]
[3] https://lineat.co.uk/ [Accessed on 13.06.2023]
[4] https://asm.matweb.com/search/SpecificMaterial.asp?bassnum=ma2024t4 [Accessed on 13.06.2023]
[5] https://asm.matweb.com/search/SpecificMaterial.asp?bassnum=ma7075t6 [Accessed on 13.06.2023]
[6] http://www.performance-composites.com/carbonfibre/mechanicalproperties_2.asp [Accessed on 13.06.2023]
[7] https://www.toraycma.com/wp-content/uploads/T700S-Technical-Data-Sheet-1.pdf [Accessed on 13.06.2023]
[8] https://www.matweb.com/search/DataSheet.aspx?MatGUID=08fb0f47ef7e454fbf7092517b2264b2&ckck=1 [Accessed on 13.06.2023]
[9] https://www.toraycma.com/wp-content/uploads/T700S-Technical-Data-Sheet-1.pdf [Accessed on 13.06.2023]
[10] https://www.matweb.com/search/datasheet_print.aspx?matguid=2164cacabcde4391a596640d553b2ebe [Accessed on 13.06.2023]
[11] https://www.toraycma.com/wp-content/uploads/T700S-Technical-Data-Sheet-1.pdf [Accessed on 13.06.2023]
[12] https://www.matweb.com/search/datasheet_print.aspx?matguid=956da5edc80f4c62a72c15ca2b923494 [Accessed on 13.06.2023]
[13] https://www.matweb.com/search/datasheet.aspx?matguid=846c277e1e584def9de088172cb0e4c3&ckck=1 [Accessed on 13.06.2023]
[14] https://asm.matweb.com/search/SpecificMaterial.asp?bassnum=mtp641 [Accessed on 20.06.2023]
[15] https://www.matweb.com/search/datasheet_print.aspx?matguid=4e6a4852b14c4b12998acf2f8316c07c [Accessed on 20.06.2023]

As seen for the skin panels of the wingbox and fuselage, the maximum ratio of $\frac{\tau_{yield}}{\rho}$ is achieved by the titanium (124), followed by ALU7075 (118). Titanium is an extremely expensive material that is difficult to process and recycle [63]. Aluminum offers the possibility of recycling with a downgrade to less critical uses, hence it can be sustainable. The difference in the performance of those materials is not significant in shear, so it was decided that the aluminum alloy should be chosen for the skin. The highest performance in terms of tensile yield-to-density ratio was found for Carbon Fiber T700 combined with PEEK resin. PEEK as thermoplastic is easier to recycle than thermosets such as epoxy, hence its sustainability was judged as acceptable. Novel methods of recycling carbon fiber are also presented in the Sustainability chapter. The percentages of weights of both the aluminum alloy and composite materials are given in Table 10.5. The highest modulus of elasticity is presented by a beryllium-aluminum metal matrix composite. Working with beryllium, however, is extremely difficult as this metal in its clean form is toxic [67]. Thus, it will be avoided and for good stiffness properties, composites shall be used.

Fuselage & Wingbox Geometry Selection

Using the materials chosen in the previous subsection, the maximum allowed normal stresses and shear stresses can be defined using a safety factor of 1.5 in Equation 10.14 and Equation 10.13, respectively. Additionally, a third of the normal yield stress for the composite should be taken, since it is a theoretical value. Therefore, the resultant maximum allowed stresses in both the fuselage and wingbox are $\sigma_{allowed} = 766MPa$ and $\tau_{allowed} = 220MPa$. For simplicity, only stringers and skin are considered. The ribs and frames are not designed at this iteration stage. In a more detailed analysis, details of the relevant failure modes should be accounted for and other parts such as ribs could be designed.

$$\tau_{allowed} = \frac{\tau_{yield}}{1.5} \tag{10.13}$$

$$\sigma_{allowed} = \frac{\sigma_{yield}}{3 \cdot 1.5} \tag{10.14}$$

10.4. Fuselage Design

The first large structural component that was designed is the fuselage. The section starts with a brief summary of the previous design process resulting in the internal and external layout design as well as the dimensions of the fuselage. Then, the fuselage loading and structural idealisation are discussed, the internal loading is found and the axial and shear stress in the whole structure is assessed.

Fuselage Preliminary Sizing

The first step in the fuselage design is the interior layout, to ensure that it can fit the required passengers, cargo and systems. The cross-section of the fuselage is determined to be circular, as it is the optimal shape for pressurization and offers sufficient space for the payload. The inner diameter is determined by the width and number of seats abreast, and the width of both the aisle and floor, for which standard business class dimensions are chosen [68]. The dimensions of the fuselage interior can be found in Table 10.4, and the cross-section in Figure 10.3.

The next step was arranging the interior amenities (cockpit, luggage hold, passenger seat rows, lavatory, tail space) within the fuselage. A total of 8 passengers are fit within the fuselage, with two seats abreast this yields a total of 4 rows. Based on these, the length of the fuselage could be assessed using statistical relationships for commuter aircraft [68]. The top view and internal layout are shown in Figure 10.3a. The view does not include batteries that are stored under the floor of the fuselage. The exact lengths of the fuselage parts are shown in Table 10.3.

Table 10.3: *Fuselage top view parameters*

Parameters	Amount	Unit
Nose length/diameter	1.2	[-]
Nose length	2.69	m
Tailcone length/diameter	2	[-]
Tailcone length	4.48	m
Cockpit length	2.5	m
Fuselage length/diameter	5.6	[-]
Fuselage length	12.54	m
Pressure diffrential	18.62	kPa

Table 10.4: *Fuselage cross-section parameters*

Parameters	Value	Unit
Seat width	56	cm
Armrest width	3.8	cm
Aisle width	0.46	m
Aisle height	1.8	m
Clearance	2.5	cm
Cabin width	1.778	m
Floor height	0.1	m
Wall thickness	0.04	m
Inner diameter	2.2	m
Outer diameter	2.24	m

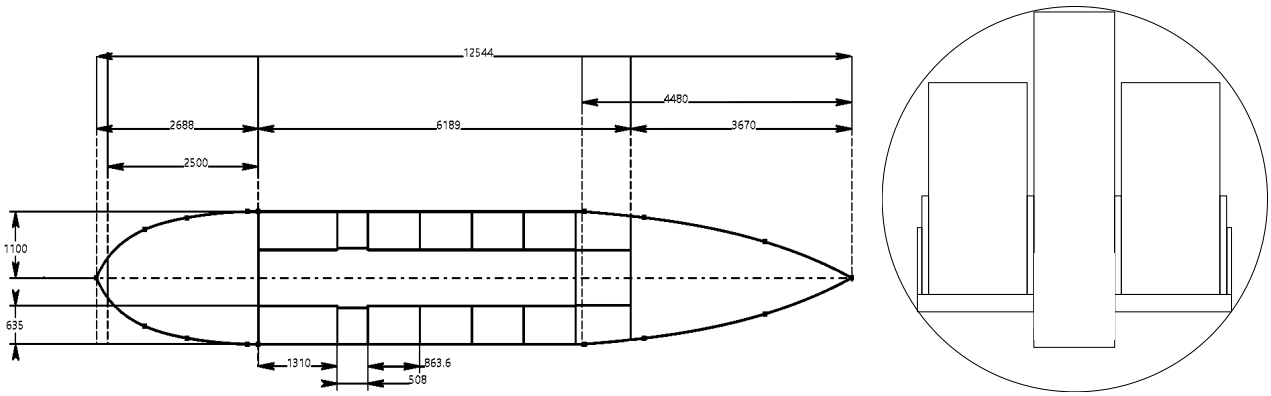

(a) *The top view of the fuselage*

(b) *The cross-section of the fuselage*

Figure 10.3: *The fuselage design for ElectriFly*

Fuselage Model

The coordinate system used for the analysis of the loading into the fuselage, is the same as the coordinate system throughout the report, as shown in Figure 10.1. All forces, moments and their resulting stresses acting on the fuselage structure, were assessed separately and superimposed.

For the structural analysis, several assumptions were made. It was assumed that the fuselage can be treated as a cylindrical, thin-walled beam with a ring cross-section. Additionally, it was assumed that thrust and drag contributions are negligible [69]. Similarly, the contribution of the average force due to tension in the recharging cable was assumed negligible as safety mechanisms will be used to ensure the connection stops when a high force is exerted on the cable. Due to the limited duration and scope of the project, only forces in the z-x plane were considered - torsion and forces on the vertical stabilizer were not assessed specifically, however, they were accounted for by taking an appropriate safety factor.

The moment of inertia is required in these structural calculations and defines the resistance to loading as a function of area and distance to the neutral axis. In order to simplify the calculation of the moment of inertia of the fuselage cross-section, the concept of structural idealisation is applied. As shown in Figure 10.4a, the area of both the stringers and outer skin is concentrated in the booms. The most prominent bending will occur around the y-axis, for which the moment of inertia was found using Equation 10.15 [70][69]. The floor structure will carry loads and strengthen the fuselage, which is simulated by including its area in the booms closest to its attachment. The total moment of inertia around the Y-axis is then found using Equation 10.15.

$$I_{yy} = \sum_{n=1}^{N_b} \left[t_{sk} l_{sk} z_{sk}^2 + t_{fl} w_{fl} z_{fl}^2 + \frac{E_{str}}{E_{sk}} A_{str} z_{str}^2 \right] \tag{10.15}$$

Internal Loads

The first loading contribution is the stress caused by a pressure difference ΔP between the atmosphere at cruise (15000 ft), and the internal pressure set to 8000 ft for comfort. Consisting of both a hoop stress, i.e. around the circumference, and the longitudinal stress, can be calculated using Equation 10.16 and Equation 10.17, respectively [71].

$$\sigma_{hoop_{circ}} = \frac{\Delta P \cdot r}{t} \tag{10.16}$$

$$\sigma_{hoop_{long}} = \frac{\Delta P \cdot r}{2t} \tag{10.17}$$

To find the loading in the fuselage, a side view was used with a free-body diagram of a similar fuselage found in literature [69]. The model is shown in Figure 10.4b. Here, weights of the payload and internal systems like passenger, cargo and furniture are modelled as distributed forces, ranging from q_1 to q_6. The first and longest load - $q1$ contains the weight of the fuselage itself, the floor, the air conditioning system, the furnishing, the interior electrical system, the hydraulics and the avionics. $q2$ and $q3$ include everything that is stored in respectively the front and rear cargo bay - in ElectriFly it is only batteries. $q4$ contains support structures for the wing. $q5$ consists of the tail support structure weight and the recharging system weight. $q6$ is the space in front of the front bulkhead and due to the small space available in ElectriFly, it is assumed to be empty. Additionally, the loads induced by the two spars of the wing (front F_{fs}, rear F_{rs}), the weight (W_{tail}) and lift (L_H) of the empennage, the weight of the pressure bulkheads (W_{rbh} and W_{fbh}), and the weight of the landing gear(main: W_{mlg}, nose: W_{nlg}) are modelled as point forces F.

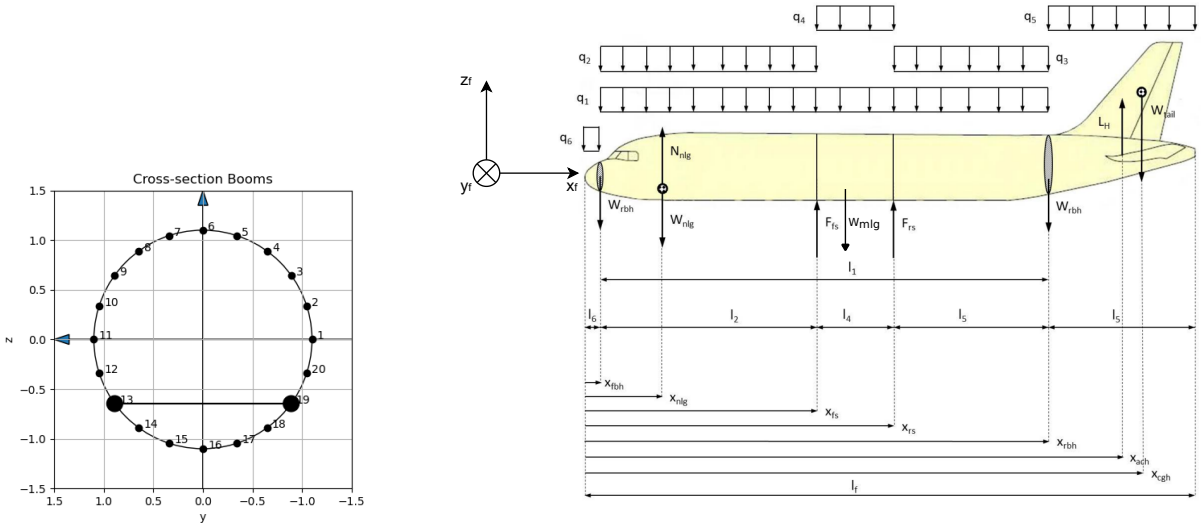

(a) *Cross-section idealisation* **(b)** *Side view [69]*

Figure 10.4: *Fuselage free body diagrams*

The distribution of the forces along the fuselage was used to calculate the internal normal forces, shear forces and bending moment. Equation 10.18, Equation 10.19 and Equation 10.20 were used to calculate these internal loads respectively [72]. To obtain a conservative estimate of the worst-case scenario, the internal loads were then multiplied by the ultimate load factor found from manoeuvre envelopes [16]. The maximum value of each of the forces was found for each point on the span of the wing. The plots of the maximum force value are shown in Figure 10.5.

$$N(x) = \int_0^x -q_x dx + \sum_{i=0}^{n} -F_{x_i} \quad (10.18) \qquad V_z(x) = \int_0^x -q_z dx + \sum_{i=0}^{n} -F_{z_i} \quad (10.19)$$

$$M(x) = \int_0^x V_z dx + \sum_{i=0}^{n} -M_{0_i} \quad (10.20)$$

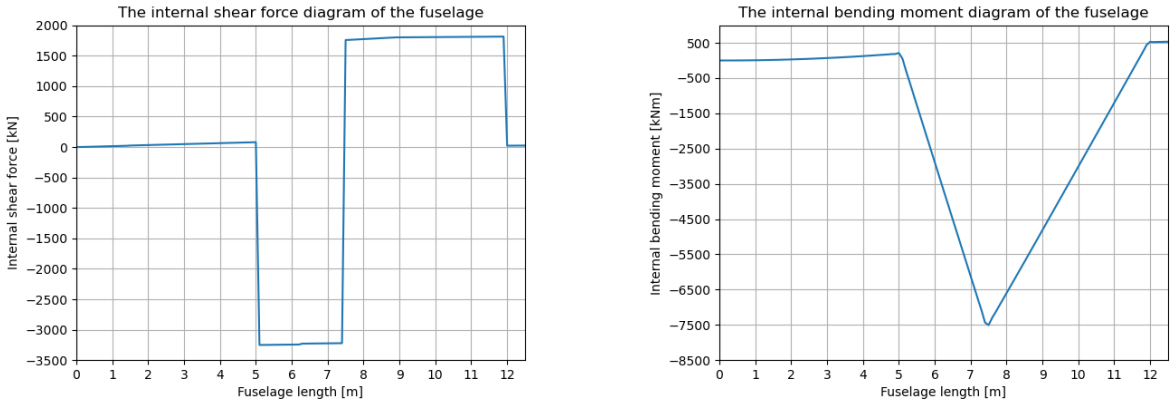

(a) *The internal shear force* **(b)** *The internal bending moment*

Figure 10.5: *The internal forces along the fuselage*

From both figures, it becomes clear that the largest load on the fuselage occurs near the wing mounts and at the tail. The biggest influence on the shape of the graphs has the lift force from both the tail and the wing that must be compensated. Therefore, the structure around the wing should be reinforced to withstand the loads carried by that part.

Internal Stresses and Geometry Selection

From the internal force values, the axial and shear stresses due to those loads were calculated for each point of the fuselage. Finally, the total stresses were found as a sum of the hoop stress, stress due to bending and stress due to internal shear force in the correct directions [72]. Equation 10.21 and Equation 10.22 were used for this calculation.

$$\sigma_{axial} = \frac{N_x}{A} + \frac{M_y \cdot z}{I_{yy}} + \sigma_{hoop_{long}} \quad (10.21) \qquad \tau = \frac{V_z \cdot Q}{I_{yy} \cdot t} + \frac{T \cdot r}{J} + \sigma_{hoop_{circ}} \quad (10.22)$$

[16] Expert consultation on 07.06 with Dr.Ir. Calvin Rans

By optimisation and enforcing the maximum stress limits as indicated in Section 10.3, the final fuselage design parameters were found. The cross-section of the fuselage as shown in Figure 10.4a displays the optimal design. It has constant thickness walls of $t_{fuselage} = 1\,\text{mm}$, and 20 stringers with an area of 300mm^2 evenly spaced around the circumference. The shape of the stringer was not analysed and may be further detailed in the next design stage. The properties of the materials were taken from the Table 10.2. Additionally, the Young's modulus for aluminium was found in the literature to be $E_{AL7075} = 72\,\text{GPa}$ [17] and the modulus for the CFRP/PEEK composite was calculated using the rule of mixtures to be $E_{CFRP/PEEK} = 140\,\text{GPa}$ in the fibre direction [66].

For the optimal configuration, the maximum normal stress was found to be: $\sigma_{x_{tension}} = 585\,\text{MPa}$ in tension and $\sigma_{x_{compression}} = 566\,\text{MPa}$ and the maximum shear stress was $\tau = 150\,\text{MPa}$. All the values fit within the limit boundaries set by Section 10.3. The distribution of the stresses in the fuselage model is shown in Figure 10.6b and Figure 10.6a. Since the in-flight condition is shown, the fuselage is bent by the lift forces concave up so that it is compressed at the top and in tension at the bottom. For on-ground conditions, the situation is reversed. The stress concentrations occur in the short region where the wings are attached. It suggests that an additional detailed design of this part must include significant strengthening, while the other parts may be designed with a lower thickness or fewer stiffeners to optimise their weight. The changes in the sign of the shear stress indicate the changes in direction which would imply that significant twists are present near the wing region. This should be further analysed in the next design step.

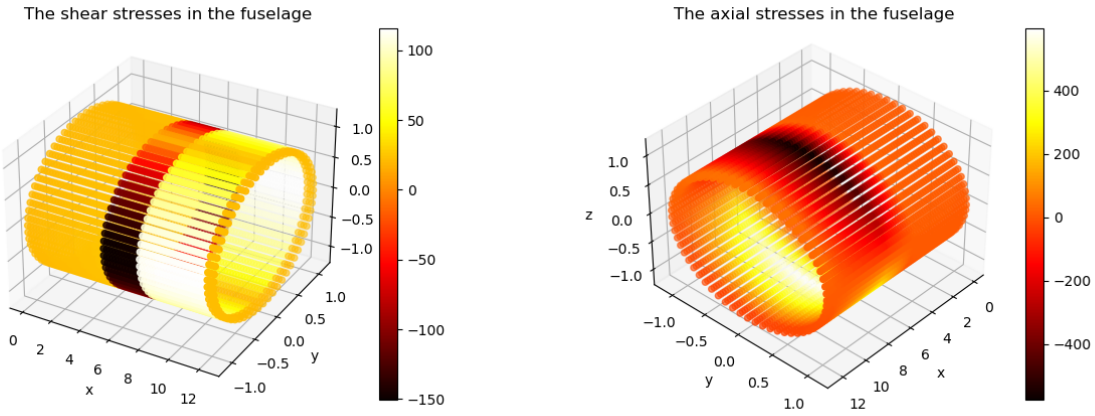

(a) *Shear stresses in the fuselage in MPa*

(b) *Normal Stresses in the fuselage in MPa*

Figure 10.6: *3D view of fuselage stresses*

10.5. Wingbox Analysis

The first step of the wingbox analysis is creating a free-body diagram of the wingbox that shows all the external and reaction loads considered. As the wing is much stiffer in the x-axis direction and the loads in the x-y plane are much smaller than the loads due to lift and weight, only forces in the y-z wing reference frame were considered, meaning thrust and drag loads will be neglected. Additionally, only the shear stress due to internal shear force V_z and normal stress due to internal bending moment M_x will be considered to ease the complexity. The torsion influence will be neglected as its influence is smaller than the aforementioned loads[18]. As one of these different assumptions, fuselage and wingbox structural analyses are not linked directly and require further engineering.

The wingbox is modelled with Figure 10.7a and Figure 10.7b, for which the coordinate system is the same as the one presented in Figure 10.1. The external loads that will be considered are the lift distribution on the wing, generated with XFLR simulation, uniform wing weight distribution, and point weight forces due to the main landing gear and the engines.

[17] https://asm.matweb.com/search/SpecificMaterial.asp?bassnum=ma7075t6 [Accessed on 20.06.2023]
[18] Expert consultation on 07.06 with Dr.Ir. Calvin Rans (Delft University of Technology)

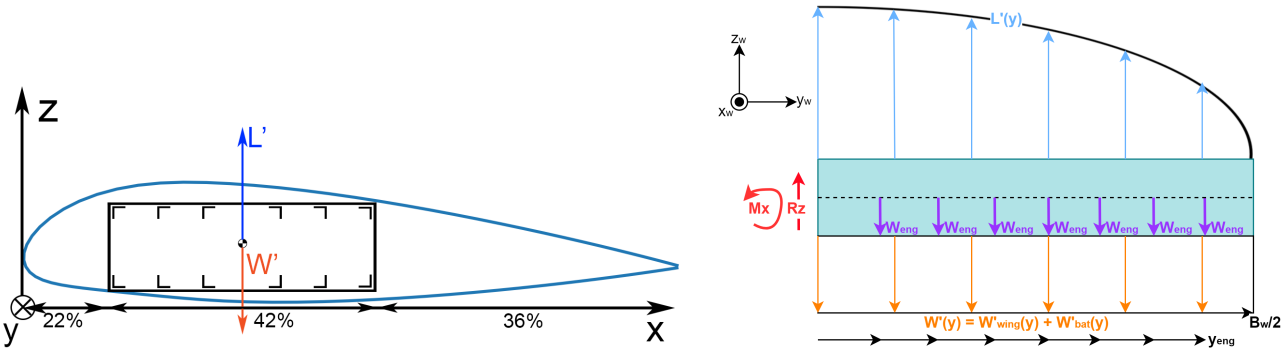

(a) *Cross-section x-z reference frame*

(b) *Spanwise y-z reference frame*

Figure 10.7: *Free body diagrams of the wingbox*

Reaction Loads

As shown in Figure 10.7b, the vertical reaction force is defined as R_z positive upwards, and the reaction moment as M_x counter-clockwise positive. These were calculated using the vertical equilibrium equation in Equation 10.23 and the moment equilibrium equation of Equation 10.24, respectively. The resulting reaction force and moment yield $R_z = N$ and $M_x = N \cdot m$, which corresponds to a reaction force acting in the negative z-direction, and the reaction moment acting counter-clockwise positive.

$$\Sigma F_z : \int_0^{\frac{B_w}{2}} L'_w(y)\,dy - \int_0^{\frac{B_w}{2}} W'_w(y)\,dy - W_{MLG} - n_{eng} \cdot W_{eng} + R_z = 0 \tag{10.23}$$

$$\Sigma M_x : \int_0^{\frac{B_w}{2}} L'_w(y)\,dy \cdot \bar{x_L} - \int_0^{\frac{B_w}{2}} W'_w(y)\,dy \cdot \bar{x}_W - W_{MLG} \cdot l_{MLG} - \Sigma(W_{eng} \cdot l_i) + M_x = 0 \tag{10.24}$$

Internal Loads

Similarly to the fuselage design, the internal loads: normal and shear force and the bending moment in the wingbox were calculated. Based on the FBD, the forces were again calculated with Equation 10.20, Equation 10.19 and Equation 10.18. The forces were also multiplied with the ultimate load factor of $n_{ult} = 5.25$ found in Section 10.2, to account for the worst-case condition in a similar way as in the fuselage design. The plots of the internal forces value along the span of the wing are presented in Figure 10.8.

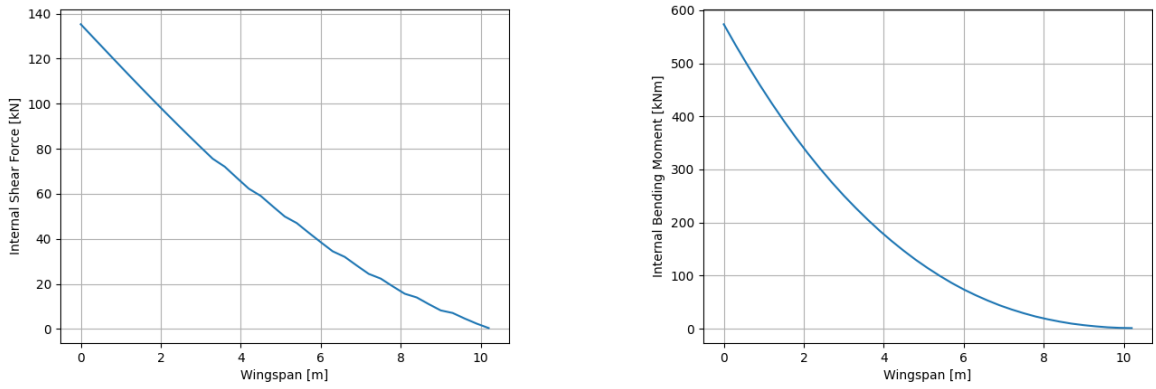

(a) *The internal shear force in wingbox*

(b) *The internal bending moment in wingbox*

Figure 10.8: *The internal forces in the wingbox along the span.*

Internal Stresses and Geometry Selection

As in the fuselage analysis, the internal axial and shear stresses were found for the wingbox. To obtain the normal stress, Equation 10.25 was used, and to calculate shear Equation 10.26 was simplified and evaluated [70]. For the normal stress, its maximum was considered in each cross-section, meaning Equation 10.25 was maximised. It is important to note, that the normal force component N_y is zero, and thus only normal bending stress contributes.

$$\sigma_y = \frac{N_y}{A_{wingbox}} + \frac{M_x \cdot z}{I_{xx}} \tag{10.25}$$

$$\tau_z = \frac{q_s}{t} = \frac{(\frac{-V_z}{I_{xx}} \int_0^s tz\,ds + q_{s0})}{t} \tag{10.26}$$

Calculating shear stresses requires ample derivation. It is most critical to determine the location and value of the maximum shear stress that occurs in the wingbox cross-section since this constrains the area. An equation can be derived to calculate the maximum shear stress for each cross-section along the span. Since the internal shear force decreases along the wingspan as seen in Figure 10.8a, it is expected that the same occurs with the maximum shear stress. Due to the geometry of the wingbox cross-section as seen in Figure 10.7a, the maximum shear stress will occur at the neutral axis, which is in the middle of the front and rear spars [70]. The closed section can be cut at the point where the internal shear force is applied, as shown in Figure 10.9. After which the shear flow can be determined at the middle of the spars, which is the maximum shear flow used to calculate the maximum shear stress Equation 10.27. It is important to note, that the shear forces and shear stresses displayed in graphs are considered positive in the downward direction, and negative in the z_w direction.

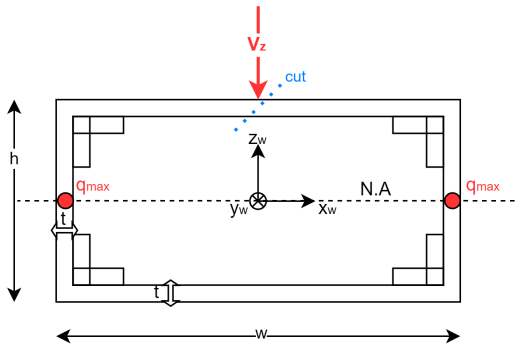

Figure 10.9: *Location of the maximum shear flow in wingbox cross-section*

$$q_{max} = \frac{V_z \cdot t \cdot h^2}{8 \cdot I_{xx}} + \frac{V_z \cdot t \cdot h \cdot w}{4 \cdot I_{xx}} \tag{10.27}$$

The stress is highly dependent on the cross-sectional geometry as well as the material properties chosen for the skin and stringers. Since the material choice was done in Section 10.3, only the geometry has to be optimized for the stresses to remain below the allowable stresses. The graph of the maximum normal bending stress and shear stress along the span of the wing is shown in Figure 10.10. From the graph it was found that the total maximum tensile stress in the wingbox is $\sigma_{tensile_{max}} = 726\,\text{MPa}$, the maximum compression stress is: $\sigma_{comp_{max}} = -726\,\text{MPa}$ and the maximum shear stress occurring is $\tau_{max} = 108\,\text{MPa}$. Observations can be made in the graphs, for example, the small kinds in the shear stress graph along the wingspan Figure 10.10a represent the effect of the weight of the engines. Since the shear force is taken positively downwards, these weights contribute positively to this graph. For the axial stress Figure 10.10b, simply a smooth parabolic decaying line can be seen, without any kinks due to the way it is being calculated. It is most important to note for a sanity check, that both stresses, just like the loads, go to zero at the tip of the wing.

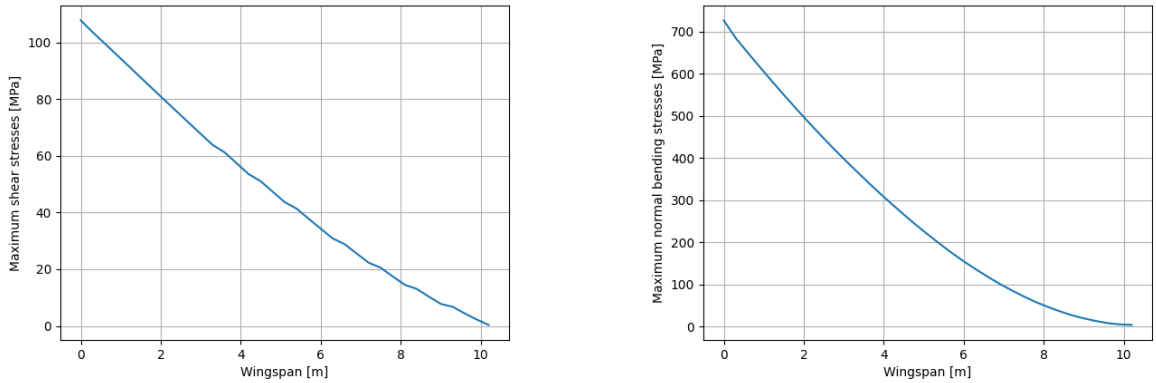

(a) *The maximum shear stress τ_z*

(b) *The maximum axial stress σ_y*

Figure 10.10: *The maximum stresses in each cross-section of the wingbox along the span.*

The cross-section of the wingbox as shown in Figure 10.7a, has been optimised for thickness and amount of stringers using the defined allowed stresses, and the calculated internal stresses, as found in the previous subsections. As a

result, the wingbox has a constant wall thickness of $t_{wingbox-skin}$ = 0.6 mm, and 10 stringers of the cross-sectional area of 300 mm^2, all evenly spaced on the top and bottom skin panels as seen in Figure 10.7a.

10.6. Final Material Weights

The final material weight percentages within the fuselage and wingbox are shown in Table 10.5, with only the stringers and skin components considered. As seen, the PEEK material stringers make up the majority of the weight in the wingbox. Whereas for the fuselage it is the skin made of aluminum that constitutes slightly over 50% of the total mass. The best strategy for total mass reduction could in that case be the reduction of the fuselage thickness and compensating it with additional stiffeners.

Table 10.5: *Material weight percentages*

Material	Fuselage	Wingbox	Total
ALU7075	51%	42%	49%
PEEK	49%	58%	51%

10.7. Structures Model Assumptions and V&V

During the modelling of the structural system, various assumptions were used. A set of specific assumptions were made to reduce the complexity of the calculation. These assumptions are labelled and described in Table 10.6. The validity of the mentioned assumptions will be discussed in Chapter 19.

Table 10.6: *List of assumptions for the structural analysis*

ID	Assumption
ASM-STRC-01	Skin primarily carries all the shear stress
ASM-STRC-02	Stringers primarily carry all the normal stress
ASM-STRC-03	The fuselage can be idealised in booms, which have no skin thickness
ASM-STRC-04	The battery weight is distributed uniformly in the wing, just like the wing weight
ASM-STRC-05	The fuselage is a thin-walled structure
ASM-STRC-06	The fuselage has a cylindrical shape
ASM-STRC-07	The thrust and drag loads are negligible for the internal loads
ASM-STRC-08	Skin and stringers are the only two components in the fuselage and wing

For the verification of the structures subsystem model, examples of 5 unit tests are shown that were performed. Similar to these, the verification and validation of the entire model was done with several other unit tests, during the buildup of the code.

Table 10.7: *Structures subsystem unit tests*

ID	Test	Expected outcome	Actual outcome	Pass/Fail
TEST-STRU-01	V_{tip}	$V_{tip} = 0$	$V_{tip} \approx 0$	Pass
TEST-STRU-02	M_{tip}	$M_{tip} = 0$	$M_{fuselage-tip} \neq 0$	Fail
TEST-STRU-03	$lim_{t=0}(\tau)$	$lim_{t=0}(\tau) = 0$	$lim_{t=0}(\tau) = 0$	Pass
TEST-STRU-04	$M > V$	True	True	Pass
TEST-STRU-05	Wing deflection < 10m	True	True	Pass

As seen in Table 10.7, the first two tests check whether the internal shear force and bending moment at the tips of the wing and fuselage go to 0, which to ensure equilibrium must be true. Both of these hold for the wingbox, however for the end of the fuselage, the internal bending moment does not go to 0 whereas the internal shear force does. This is unexpected since the bending moment is the integral of the shear force, therefore the behaviour should carry through. Therefore, it is assumed that it is an error in the integration function, and the bending moment should step down to 0 at the end. However, due to the graphs not showing this, this is the only failure, but it should be noted that it is a minor error. The rest of the unit tests are sanity checks, concerning physics and methodology.

As for the validation of the model, certain structural analysis experts such as Dr. Calvin Rans were contacted for the methodology of the fuselage and wingbox design. He approved the procedure and guided the team to make several simplifications to yield the results presented in this report. Additionally, the material choice was another significant factor in structural analysis, and for this, an expert in composite materials Dr. Bariș Çağlar was contacted, who validated the material indices approach to select materials. He also suggested using aerospace grade T700/PEEK material, which has extremely good material properties, as found in the selection process.

11. Flight Performance Analysis

In this chapter, the flight performance of the ElectriFly mission will be assessed. In the assessment, the feasibility of the mission profile will be discussed with respect to the aerodynamic and propulsive characteristics of the aircraft, which are discussed in Chapter 8 and Chapter 9 respectively. The flight performance will concern the aircraft's available and required power with the use of the performance diagrams in Section 11.1. The performance diagrams will provide a theoretical flight ceiling, which is discussed in Section 11.2. Finally, the aircraft's range is analysed with respect to its mission in Section 11.3.

11.1. Performance Diagrams

The performance diagrams aim to display the aircraft's required and available flight power during a certain steady flight condition. The power required for flight is to overcome the drag, which follows from the aircraft's aerodynamics, discussed in Chapter 8. The drag's dependence on airspeed differs between the lift-induced drag and zero-lift drag, as per Equation 11.1. Figure 11.1 shows the behaviour drag, but it should be noted that only the regime above the stall speed is applicable, as steady flight cannot be achieved in stall.

$$D = D_0 + D_i \begin{cases} D_0 = C_{D_0} \cdot \frac{1}{2}\rho V^2 S \\ D_i = \frac{C_L^2}{\pi Ae} \cdot \frac{1}{2}\rho V^2 S = \frac{W^2}{\frac{1}{2}\rho V^2 S \pi Ae} \end{cases} \tag{11.1}$$

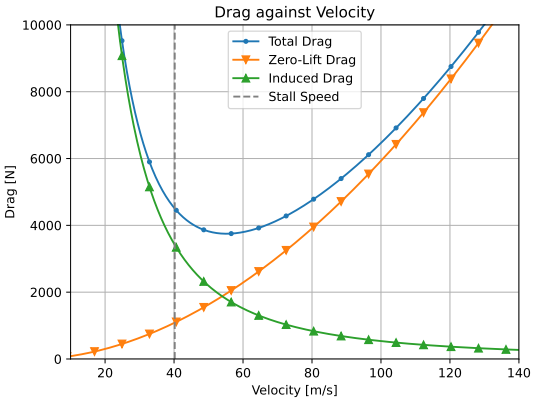

Figure 11.1: *Aircraft drag as a function of velocity for steady flight at sea-level*

The required flight power is defined by the aircraft's drag and airspeed, while the available power is determined by the propulsion system and will show little dependency on airspeed. The required and available power can be plotted against airspeed but varies with altitude. Due to the reduction of density for higher altitudes, the speed has to scale as per Equation 11.2 to attain the same lift coefficient, while the drag remained the same for the respective speed. The provided power will decrease with lower densities, but the exact dependence is determined by the physics of the propulsion. The dependence can preliminarily be taken as in Equation 11.3. Available power is taken as 990 kW at cruise altitude with regard to the results of Chapter 9. In combination with the aircraft's drag, this allows for the generation of performance diagrams. Figure 11.2 shows the diagram for sea level and cruise altitude.

$$V_2 = \sqrt{\frac{\rho_1}{\rho_2}} V_1 \tag{11.2}$$

$$P_{a_2} = \left(\frac{\rho_2}{\rho_1}\right)^1 P_{a_1} \tag{11.3}$$

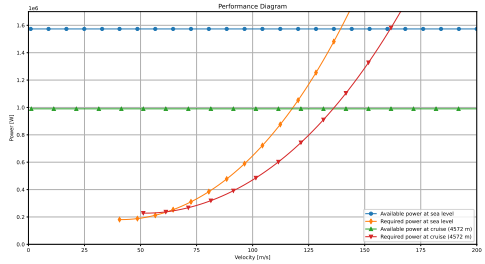

Figure 11.2: *Peformance diagram at sea level and cruise*

11.2. Theoretical Flight Ceiling and Optimal Conditions

An aircraft is only capable of steady flight within theoretical limits. For one, it is required to have more available power than the required power. This introduces a power limit for both a lower and higher speed at which the available and required power are equal. Another limit is formed by the stall speed, usually occurring before the lower power limit until higher altitudes are considered. These limits form the theoretical flight ceiling. The ceiling for the ElectriFly aircraft is presented in Figure 11.3.

Within the flight regime below the ceiling, optimal flight conditions exist. One could possibly optimize for range or for endurance, requiring minimum drag or required performance respectively. The former requires optimization of the

lift-to-drag ratio, while the latter needs optimal lift-to-drag over airspeed. The corresponding optimal lift coefficients are as described in Equation 11.4 and Equation 11.5 respectively. These lift coefficients correspond to an optimum airspeed for each altitude and are depicted within our flight regime as in Figure 11.4. These optimal flight conditions for range and endurance do not only account for a steady cruise but also for steady climb and descent. As such, the optimum range condition also yields the smallest descent angle, while the optimum endurance yields the longest descent time and the highest rate of climb.

$$(D)_{\min} \longrightarrow \left(\frac{C_L}{C_D}\right)_{\max} \longrightarrow C_{L_{opt}} = \sqrt{C_{D_0}\pi Ae} \tag{11.4}$$

$$(P_R)_{\min} \longrightarrow \left(\frac{C_L^{3/2}}{C_D}\right)_{\max} \longrightarrow C_{L_{opt}} = \sqrt{3C_{D_0}\pi Ae} \tag{11.5}$$

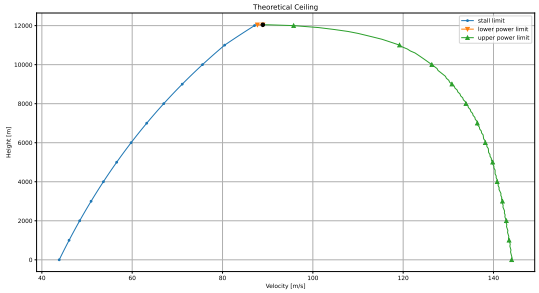

Figure 11.3: *Theoretical flight ceiling imposed by the stall and power limits*

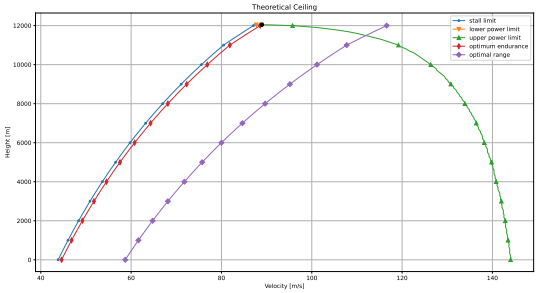

Figure 11.4: *Optimal airspeed and altitude regarding range and endurance*

Discussion on Performance Optimization

During the climb phase, it is beneficial to reach the cruise altitude as fast as possible. The path of optimal endurance (and of the highest rate of climb) as shown in Figure 11.4 should be followed for this purpose. However, it should be noted that this optimum airspeed is significantly close to the stall speed, making the operation unsafe. It is therefore recommended for the current design to climb at speeds higher than the optimum, though consequently lowering the rate of climb. The optimum climb speed could still be designed to be obtained, by either lowering the stall speed or increasing the optimum speed, both of which regard the aerodynamic aspect of the design.

Even though the flight could be optimized for range or endurance, the feasibility of the optimal conditions should always be checked against the mission of the flight. To be competitive in the market, higher airspeed is preferred. To adhere to the optimum range path as in Figure 11.4, higher airspeed is more optimal at higher altitudes. On the contrary, high speed and altitude put more constraints on other aspects of the design and the mission. It is therefore important that iteration is performed between the mission, design, and optimal conditions during detailed design phases.

11.3. Range Analysis

The range that ElectriFly is able to reach covers one of the top requirements and should therefore be assessed in more detail. The equation developed by Hepperle [59] is used to estimate the range of an electric aircraft. The final calculation yields Equation 11.6, relating range to the battery's specific energy (E^*), efficiency, and mass. Moreover, the range relates to the aircraft weight and the lift-to-drag ratio, validating that Equation 11.4 corresponds to the optimal range. This calculation verifies the compliance with the top-level requirement of reaching 500 km.

$$R = \frac{3.6E^* \cdot \eta_{\text{tot}}}{g}\left(\frac{C_L}{C_D}\right)\left(\frac{m_{\text{batt}}}{m}\right) \tag{11.6}$$

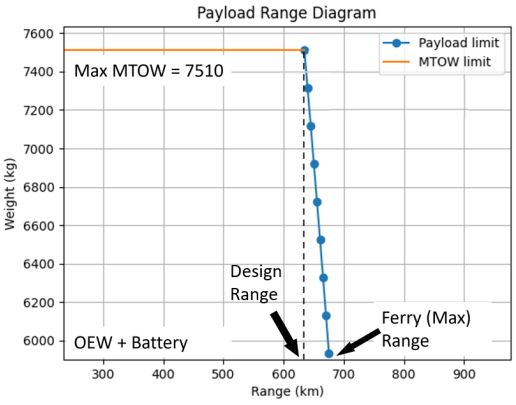

Figure 11.5: *Payload range diagram*

A more detailed analysis of the range of ElectriFly is performed, focusing on the transported payload weight. A payload range diagram is displayed in Figure 11.5 to show the relationship between the payload mass and range. The maximum number of 8 passengers is limited by MTOW, while the maximum range that can be achieved (the ferry range) concerns the weight with no passengers. The calculated range accounts for the distance traversed and power consumed in all flight phases, but still considers a 20% energy contingency in the battery.

11.4. Performance Assessment Assumptions and Verification

During the assessment of the performance, various assumptions were used. A set of specific assumptions were made to reduce the complexity of the calculation. These assumptions are labelled and described in Table 11.1. Besides these assumptions, all assumptions made in Chapter 8 during the estimation of the drag coefficient are also applied. The validity of the mentioned assumptions will be discussed in Chapter 19.

Table 11.1: *List of assumptions for the performance assessment*

ID	Assumption
ASM-PERF-01	The variation of drag coefficient with Reynolds number is negligible
ASM-PERF-02	The variation of drag coefficient with Mach number is negligible
ASM-PERF-03	The available power is invariant with airspeed
ASM-PERF-04	The available power provided by the propeller is directly proportional to air density

The methods of assessing ElectriFly's flight performance ought to be verified. A variety of tests are performed on the calculations used for various shapes of wings. A selection of the initial unit test is shown in Table 11.2, in which the test input, expected output, and actual output are described. Each of the mentioned tests intends to show whether the model gives a physically sensible result. TEST-PERF-05 is not passed, implying that higher excess powers are found in the vicinity of the presumed velocity with maximum excess power $V_{P_{\max}}$. Further investigation showed that the error likely originates from the calculation on a discrete data-set, rather than a continuous set. Although the effects on the outputs that follow after the calculation appear to be minimal, this anomaly ought to be resolved before further design iterations.

Table 11.2: *Performance Unit Test*

Test	Input	Expected	Actual	Result
TEST-PERF-01	$V_s(h_1) > V_s(h_2)$ for $h_1 > h_2$	True	True	Pass
TEST-PERF-02	$D_i(V_1) < D_i(V_1)$ for $V_1 > V_2$	True	True	Pass
TEST-PERF-03	$D_0(V_1) > D_0(V_1)$ for $V_1 > V_2$	True	True	Pass
TEST-PERF-04	$D > 0$	True	True	Pass
TEST-PERF-05	$P_{\text{excess}}(V_{P_{\max}}) < P_{\text{excess}}(V_1)$ for $V_1 \neq V_{P_{\max}}$	True	False	Fail

12. Stability Analysis

In this chapter, the tail configuration and sizing will be described in Section 12.1. Next, in Section 12.2 the longitudinal and lateral stability will be assessed respectively, followed by Section 12.3 covering the loading diagram and scissor plot. The ground stability and gear will then be designed in Section 12.4. Finally, the relevant assumptions and the V&V procedure are discussed in Section 12.5.

12.1. Tail Configuration & Sizing

In the trade-off phase of the design, several tail configurations were considered. These are listed in Table 12.1, with their respective positive and negative aspects. The final configuration was chosen to be a T-tail, with the horizontal stabilizer mounted on top of the vertical stabilizer. This allows for less wing downwash and propeller wake effects. Additionally, the end-plate effect will decrease induced drag, where the horizontal tail acts as a winglet for the vertical tail tip vortex. However, some downsides are the need for a heavier internal structure due to the bending of the horizontal stabilizer with respect to the vertical stabilizer. Also, a phenomenon called deep-stall should be taken into account when pitching [73]

Table 12.1: *Tail configurations trade-off [73]*

	Pro's	Con's
Conventional tail	+ Simple design + Well researched + Structurally efficient	- Downwash - Propeller wake
Cruciform	+ Less downwash + Less propeller wake	- Difficult design (due placement trade-off) -Heavier due bending
T-tail	+ No wing downwash, so reduced tail size + No propeller wake so fewer vibrations/fatigue + Well researched + End-plate effect	- Heavier structure due bending (Hs onto Vs) - Deep stall possible (Hs in wing wake at high pitch angles)
V-tail	+ Reduce size + Lighter structure + Minimal reduction in drag	- Complex coupled control system, - Less long./direct. stability, - Susceptible to dutch roll, - Adverse roll yaw coupling
H-tail **(double tail/triple)**	+ No fuselage/prop wake + End-plate effect, + Saves size of vertical stabiliser + Better lateral control	- Tedious design, - Heavier due support of Vs

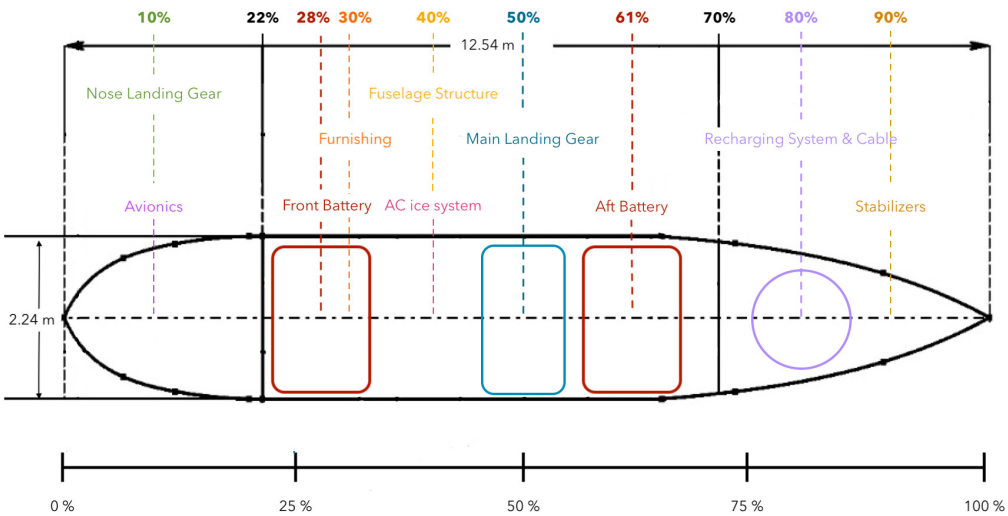

Figure 12.1: *Location of the aircraft sub-components as a percentage of the fuselage length*

To start the sizing of the horizontal and vertical stabilisers the location of the centre of gravity of the aircraft (X_{cg}) was found. This can be done by splitting the aircraft into a wing, fuselage and battery group. The longitudinal position of the centre of gravity c.g. operative empty weight can be calculated using Equation 12.1. Half of the battery weight was included in the wing group, while the other 50% was placed on the floor of the cabin, contributing to the fuselage group. Furthermore, the centre of gravity of the wing group X_{cg_W} is at 40% of the mean aerodynamic chord (MAC) [74].

$$X_{cg_{OEW}} = \sum \frac{W_W X_{cg_W} + W_F X_{cg_F}}{W_W + W_F} \tag{12.1}$$

Afterwards, the initial positioning of the wing with respect to the fuselage was determined using Equation 12.2[74]. Where X_{lemac} is the distance from the nose datum to the leading edge of the mean aerodynamic chord (MAC). The mass ratio (M_F/M_W) considered was found using W_F and W_W and equals 0.93.

$$X_{\text{lemac}} = X_{cg_F} + \bar{c}\left[\left(\frac{x}{\bar{c}}\right)_{cg_W}\frac{M_W}{M_F} - \left(\frac{x}{\bar{c}}\right)_{cg_{\text{OEW}}}\left(1+\frac{M_W}{M_F}\right)\right] \tag{12.2}$$

The horizontal and vertical tail volume coefficients and other geometrical parameters were determined using statistical data from books of Roskam [37], Torenbeek [76] and Obert [77] and later on optimized for the design. The values have been documented in Table 12.2a and used in Equation 12.3 and Equation 12.4 to determine the horizontal and vertical tail surface area respectively. The vertical tail volume used in the design is reduced by 20% from the vertical tail volume found in historical data, as the distributed propulsion system allows for vectored thrust, beneficial for lateral stability and control [78]. Which in turn, could reduce the planform size of the vertical stabilizer. The final tail design parameters were documented in Table 12.2b.

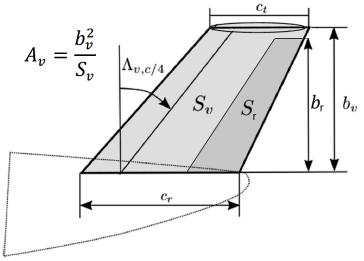

Figure 12.2: *Vertical tail dimensions [75]*

$$S_h = \frac{S\ \bar{c}\ \bar{V}_h}{(X_h - X_{cg_{aft}})} \tag{12.3}$$

$$S_v = \frac{S_W\ b_W\ \bar{V}_v}{(X_v - X_{cg_{aft}})} \tag{12.4}$$

Table 12.2: *Stabilizers Sizing*

(a) *Parameters used for stabilizer sizing [76] [37] [77]*

Parameter	Symbol	Value	Unit
Vertical Sweep	Λ_v	30	deg
Vertical Taper ratio	λ_v	0.55	-
Vertical Aspect Ratio	A_v	1.5	-
Vertical Tail volume	$\bar{V}_v$	0.04	-
Horizontal Sweep	Λ_h	13	deg
Horizontal Taper ratio	λ_h	0.46	-
Horizontal Aspect Ratio	A_h	4.5	-
Horizontal Tail volume	$\bar{V}_h$	0.53	-

(b) *Geometry parameters obtained*

Parameter	Value	Unit
S_v	5.30	m^2
b_v	2.82	m
$C_{v_{tip}}$	1.33	m
$C_{v_{root}}$	2.43	m
S_h	5.27	m^2
b_h	4.87	m
$C_{h_{root}}$	1.48	m
$C_{h_{tip}}$	0.69	m

The rudder is the control surface of the vertical stabilizer and is used for lateral yaw control. Its sizing is shown in Figure 12.2 and is based on statistical data. The rudder chord c_{rud} is 30% of the vertical tailplane chord, and covers nearly the full height. The rudder deflection δ_r is limited to 30° [79].

12.2. Longitudinal & Lateral Stability

For both horizontal and vertical stabilizers the NACA0012 airfoil was selected from reference aircraft. It has a thickness over chord ratio $t/c = 12\%$, and its symmetrical features are favourable as the stabilizers are expected to produce lift in both directions, depending on the situation [73].

Static longitudinal stability can be assessed using the coefficient C_{m_α}, which should be negative in sign. It is of importance for the following reason. Initial steady flight in equilibrium has moments around the c.g. equalling zero ($C_m = 0$). An external (wind) disturbance can cause the angle of attack α to increase, which should result in a negative moment (pitch nose down) in order to counteract the increased angle of attack and stabilize the aircraft back to equilibrium. So for static longitudinal stability, the condition yields C_{m_α}, which can be calculated with Equation 12.5 [80].

$$C_{m_\alpha} = C_{N_\alpha}\left(\frac{X_{cg} - X_w}{\bar{c}}\right) - C_{N_{h_\alpha}}\left(1 - \frac{d\epsilon}{d\alpha}\right)\left(\frac{V_h}{V}\right)^2\frac{S_h l_h}{S\bar{c}} \tag{12.5}$$

Here, C_{N_α} and $C_{N_{h_\alpha}}$ respectively represent the slope of the lift curve of the wing and horizontal stabilizer, under the assumption that $L \approx W$. The slope of the wing lift curve was calculated using XFLR in Chapter 8, and the slope of the horizontal stabilizer lift curve was calculated using Equation 12.6[81]. The speed ratio $\frac{V_h}{V}$ can be assumed to equal 1 for T-tail aircraft.[81] However, the down-wash coefficient cannot be said to equal zero due to the high wing configuration and was calculated in Section 12.3. The tail volume coefficient $\bar{V}_h = \frac{S_h l_h}{S\bar{c}}$ uses the dimensions established in Section 12.1, and the rest of the wing dimensions were established in Chapter 8. The resulting value of $C_{m_\alpha} = -3.25$ indicates static longitudinal stability.

$$C_{L\alpha_h} = \frac{2\pi A_h}{2 + \sqrt{4 + \left(\frac{A_h \beta}{\eta}\right)^2 \left(1 + \frac{\tan^2(\Lambda_{h_{c/2}})}{\beta^2}\right)}} \tag{12.6}$$

The lateral stability of the aircraft follows from the vertical stabilizer, as sized in Section 12.1. The major requirements yield static longitudinal stability in case of sideslip airflow β (weathervane stability), and lateral control in case of engine inoperative. Stability derivatives in terms of side slip, roll rate and yaw rate are to be determined during wind-tunnel testing of the design, thus will not be covered in this report.

One engine inoperative (OEI) implies a required zero side-slip angle for this condition. For twin propulsion, due to asymmetric thrust, it would highly depend on ailerons and rudder impact. The design uses distributed propulsion system and the motor driver is able to adjust the individual speed of the remaining propellers. This condition was not analyzed in a typical manner, as assumed to be inherently stable.

A Dorsal fin was added to the vertical stabilizer, in order to increase its lateral stability. Additionally, it will delay the onset of stall and rudder lock for high angles of sideslip β [82].

12.3. Loading Diagram & Scissor Plot

In order to analyse the range of the centre of gravity, the loading diagram of Figure 12.3 was constructed. In order to calculate the c.g., a similar methodology was used as described by Equation 12.1. For this analysis, the battery weight was not included in the $X_{cg_{\text{OEW}}}$ calculation, in order to show the significant contribution the battery placement has on the shifting of the c.g. Therefore, its placement and the effect thereof were analysed using the loading diagram. The weights and longitudinal placement of cargo, passengers and their luggage were determined in Chapter 10. The effect of their loading on the c.g. shift is also shown, where a distinction was made for loading passengers front row first or last row first. Finally, using this diagram the most forward and aftward position of the centre of gravity due to different loading cases can be visualised, $X_{cg_{\text{forward}}}$ and $X_{cg_{\text{aft}}}$ respectively. A safety factor of 2% MAC was added[81].

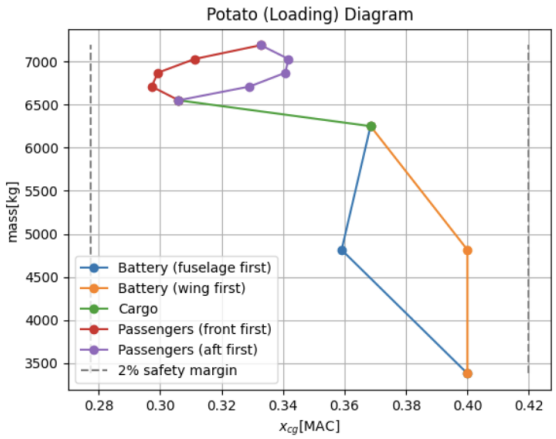

Figure 12.3: *Potato (loading) diagram*

The scissor plot is a diagram tool that can be used to assess the stability and controllability of the aircraft. This is plotted with respect to $X_{c.g.}$[%MAC] on the horizontal axis and $\frac{S_h}{S}$ on the vertical axis. These are respectively: the centre of gravity in the percentage of the mean aerodynamic chord, and the ratio of horizontal stabilizer area over-wing area. The final diagram is shown in Figure 12.4.

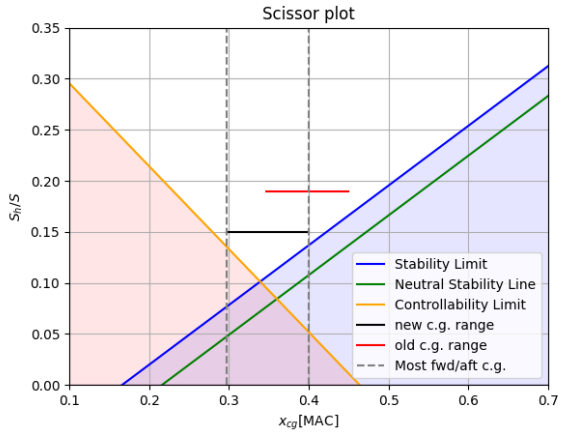

Figure 12.4: *Scissor plot*

Equation 12.7 shows the stability limit line, which is derived from the three-point FBD [80] and neutral point equation [81]. It is assessed for cruise condition and is dependent on the following: The ratio of lift curve slope $C_{L_{\alpha_{A-h}}}$ and $C_{L_{\alpha_h}}$ of the wing and horizontal stabilizer respectively, which have been calculated in Section 12.2. The calculation of the down-wash gradient $\frac{d\epsilon}{d\alpha}$ was done using the methodology in [83], and the aerodynamic centre $\bar{x}_{ac}$ was determined using a method in [81]. The tail length l_h is the distance between the aerodynamic centres of the wing and horizontal stabilizer, $\bar{c}$ is the main aerodynamic chord and the speed ratio $\frac{V_h}{V} = 1$ for T-tail aircraft. Lastly, SM

represents a safety margin of 5% MAC [81].

Equation 12.8 shows the control limit line, which is derived from the three-point FBD [80] and moment coefficient equation [84]. It is assessed for landing conditions, as this phase is the most constraining for aircraft control due to slow speeds. In addition to the parameters discussed for the stability limit, the control limit also depends on the following. First of all, the maximum lift coefficient $C_{L_{A-h}}$ with full flaps deployed. Secondly, the lift coefficient of the horizontal stabilizer $C_{L_h} = -0.8$, for horizontal stabilizers with adjustable incidence angle i_h [84]. Lastly, the moment around the aerodynamic centre $C_{m_{ac}}$ was determined using Xfoil.

By plotting both the control and stability limit lines, the combination of $\frac{S_h}{S}$ and X_{cg} should be positioned between both limits. The initial and new c.g. range position is shown, on which an optimising iteration was performed: By shifting the longitudinal location of the wing aftward w.r.t. the fuselage (X_{lemac}), the centre of gravity range will be shifted forwards w.r.t. the mean aerodynamic chord. This allows for optimising the placement of the c.g. range in the graph both vertically and between the white line space of the two limits. By doing so, the ratio of horizontal stabilizer area over-wing area could be minimised to $\frac{S_h}{S} = 0.15$. Based on this, the horizontal stabilizer was resized to a surface area of $S_h = 5.27 m^2$, and its final value was updated in Table 12.2b.

$$\text{Stability limit} \quad \frac{S_h}{S} = \frac{1}{\frac{C_{L\alpha_h}}{C_{L\alpha_{A-h}}}\left(1-\frac{d\varepsilon}{d\alpha}\right)\frac{l_h}{\bar{c}}\left(\frac{V_h}{V}\right)^2}\cdot\bar{x}_{cg} - \frac{\bar{x}_{ac} - SM}{\frac{C_{L\alpha_h}}{C_{L\alpha_{A-h}}}\left(1-\frac{d\varepsilon}{d\alpha}\right)\frac{l_h}{\bar{c}}\left(\frac{V_h}{V}\right)^2} \tag{12.7}$$

$$\text{Control limit} \quad \frac{S_h}{S} = \frac{1}{\frac{C_{L_h}}{C_{L_{A-h}}}\frac{l_h}{\bar{c}}\left(\frac{V_h}{V}\right)^2}\cdot\bar{x}_{cg} + \frac{\frac{C_{m_{ac}}}{C_{L_{A-h}}} - \bar{x}_{ac}}{\frac{C_{L_h}}{C_{L_{A-h}}}\frac{l_h}{\bar{c}}\left(\frac{V_h}{V}\right)^2} \tag{12.8}$$

12.4. Ground Stability & Gear Placement

The stability on the ground is dependent on the longitudinal and lateral placement of the gear with respect to the longitudinal and vertical position of the centre of gravity. First of all, the loading and placement of both the nose gear and main landing gear were determined using the following requirement: The nose wheel loading should be between 8-15% of the MTOW, in order to allow for efficient steering and braking. The tip-back angle $\theta > 15°$ in order to prevent tail strikes, and has been used in the sizing of the tail cone.

The longitudinal placement of the main gear is dependent on the position of the most afterwards centre of gravity $X_{cg_{aft}}$, and the vertical position of the centre of gravity z_{cg}. This is shown in Figure 12.5. The vertical c.g. position was established as follows: the half/half ratio of batteries in the high wing and batteries in the bottom of the fuselage will result in an approximate vertical c.g. position halfway positioned in the fuselage diameter. By adding the ground clearance height set at $z_c lr = 0.75m$, z_{cg} was found to be positioned at 1.758 m. Using a safety angle of $\beta = 15°$, the longitudinal position of the main landing gear was designed to yield: $X_{MLG} = 6.326$ m.

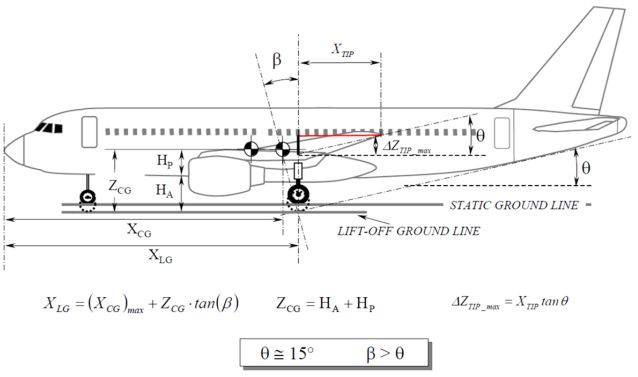

Figure 12.5: *Longitudinal gear positioning [79]*

The lateral placement of the main gear (y_{MLG}) was determined using Figure 12.6. This takes into account the sideways tip-over constraints of the aircraft, using the height of the centre of gravity and the gear track width. For save ground operations, the angle $\Psi < 55°$, resulting in a track width $y_{MLG} = 1.4m$ [79].

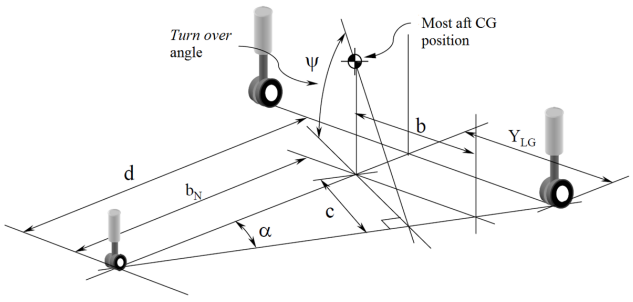

Figure 12.6: *Lateral gear positioning [79]*

The load classification number LCN was determined to be 10, for aircraft that land on paved runways in poor condition. This corresponds to a maximum allowed tire pressure of 50-70 psi or 3.5-5 kg/cm^2 [38]. A tire database of Michelin [85] was used for determining a feasible tire configuration, as this is a French/European manufacturer. Specific wheel parameters found are listed in Table 12.3.

Table 12.3: *Tire sizing parameters [85]*

	No. struts	No. Wheels per strut	Type	Diameter [m]	Width [m]	Inflation $[kg/cm^2]$	Loading [kg]	Placement w.r.t. nose [m]
Main Gear	2	2	Michelin Bias type III 8.5 - 10	0.65	0.221	3.86	2000	6.39
Nose Gear	1	1	Michelin Bias type III 6.0 - 6	0.445	0.16	3.86	1065	1.15

The nose and main landing gear will be mounted from the fuselage, because of the high wing configuration and the lack of engine nacelles under the wing. Both will also be retracted into the fuselage in order to remove their drag effects during flight, as is shown in Figure 12.7. The space required for the retraction mechanisms should be accounted for. However, the mechanisms' specifics are out of this design's scope. Because of the limited size under the fuselage floor, an extra nacelle for the gearbox was designed around the retracted main landing gear.

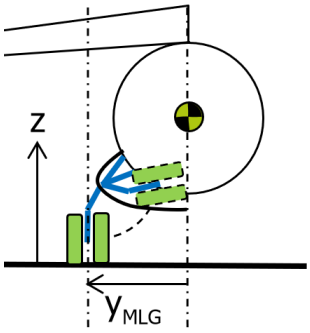

Figure 12.7: *Main gear retraction system [74]*

12.5. Stability Model Assumptions and V&V

In the assessment and design of both the stability of the aircraft and its gear, several assumptions have been made. These have been listed in Table 12.4. The validity of the relevant assumptions is discussed in Chapter 19.

Table 12.4: *Assumptions made in stability/gear*

ID	Assumption
ASM-STAB-01	Lift L is approximately equal to weight W
ASM-STAB-02	The c.g. of the wing X_{cg_w} is at 40% of the MAC
ASM-STAB-03	The c.g. of multiple fuselage components are as described with respect to the length of fuselage l_f
ASM-STAB-04	The c.g. of the OEW, $X_{cg_{OEW}}$, can initially be taken 40% of the MAC
ASM-STAB-05	Vertical tail volume is 20% smaller than the statistical value
ASM-STAB-06	Three point FBD used for equations of controllability and stability lines
ASM-STAB-07	Horizontal tail has adjustable incidence angle i_h
ASM-STAB-08	The airspeed over the horizontal tail is almost equal to the free stream airspeed

The assessment and design of both the stability of the aircraft and its gear were coded using Python in an iterative and modular way. Unit testing was performed on this code, to check whether the final results make sense from a physical point of view. For example, check whether the results comply with the hypothetically expected values. Additionally, the coding can be checked on sensitivity: assess the change in output for a varying input. Lastly, the extreme value tests will show what happens if inputs go to either 0 or infinity. For the stability assessment, some of these unit tests are presented in Table 12.5. It should be noted that all of the code was of course verified, however, this table only shows some representative examples for clarity reasons.

Table 12.5: *Stability unit tests*

ID	Test	Expected outcome	Actual outcome	Pass/Fail
TEST-STAB-01	$\lim_{W_W \to \inf} X_{cg_{OEW}}$	X_{cg_W}	$X_{cg_{OEW}} = X_{cg_W}$	Pass
TEST-STAB-02	$\lim_{M_W/M_F \to 0} X_{lemac}$	$X_{cg_F} - X_{cg_{OEW}}$	$X_{lemac} = X_{cg_F} - X_{cg_{OEW}}$	Pass
TEST-STAB-03	$\bar{X}_{np} > \bar{X}_{cg}$	True	True	Pass
TEST-STAB-04	$\sum_i W_i$	$MTOW$	$MTOW$	Pass
TEST-STAB-05	$C_{m_\alpha} < 0$	True	True	Pass

The results of the stability assessment and gear sizing have been validated as follows. The methodology used was presented in bachelor courses. complimented by expert validation by the DSE teaching assistant. Additionally, results were compared to reference aircraft mentioned in Chapter 3, and compared to aircraft on which the initial sizing was based. -

Figure 12.8: *Rendered model with gear and fairing*

13. Aircraft Systems

This chapter will elaborate on the various aircraft systems of the ElectriFly. Firstly, an overview of the three main aircraft systems: electrical, hydraulic and thermal is presented in Section 13.1. This is followed by the hardware, electrical, software and data diagrams, explaining the flow of information for hardware and internal avionics and the electrical architecture of the aircraft, presented in Section 13.2, Section 13.3, Section 13.4 and Section 13.5.

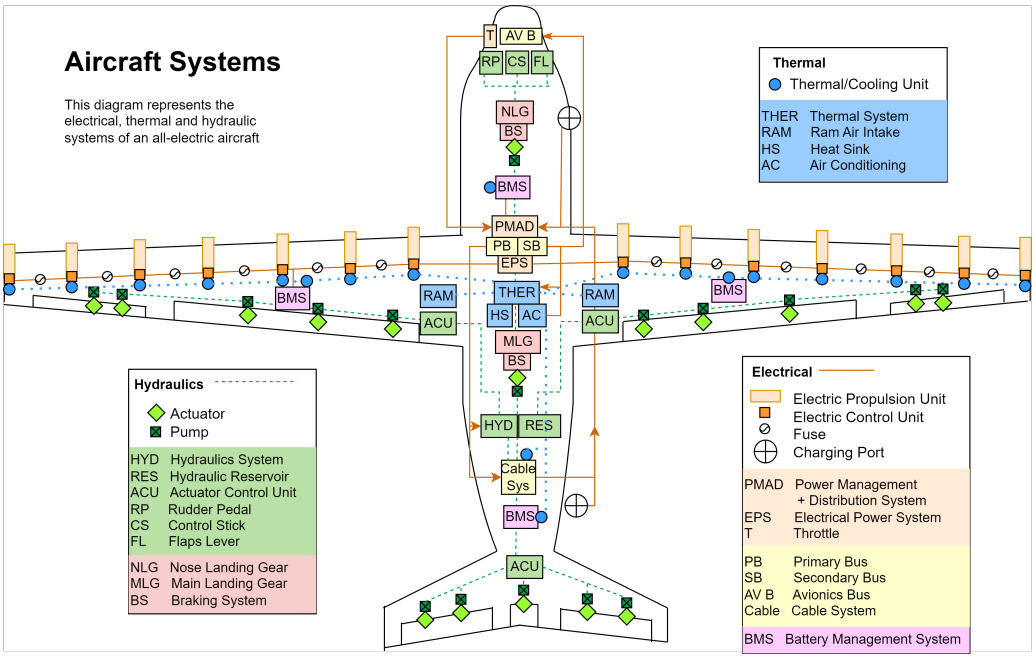

Figure 13.1: *Overview of Aircraft Systems*

13.1. Overview of Aircraft Systems

In contrast with a conventional fuel-powered aircraft, an all-electric aircraft does not need a fuel system. The three main systems become the electric, thermal and hydraulic systems. How these systems provide propulsion, and the control surface actuation, is presented in Figure 13.1.

1. **Electrical System:** The electrical system originates from the throttle. The throttle settings are sent to the power management and distribution system (PMAD), which is connected via the electric propulsion system (EPS) to the 14 distributed propellers. Each propeller also has a corresponding engine control unit (ECU) that coordinates the transfer of energy when the propellers are in regenerative mode. Each motor features a fuse to account for overcurrent safety. The primary bus (PB) and the secondary bus (SB) also send power to other subsystems of the aircraft, such as the environmental control system (ECS). The ECS includes the pneumatic system, the cable deployment system, air-conditioning, and the avionics bay. The PMAD also distributes power to the hydraulic system computer, to power the servo-actuators. Finally, the battery is monitored by a battery management system (BMS), also connected to the PMAD.

2. **Hydraulic System:** The hydraulic system inputs originate from the flight deck in the cockpit: from the rudder pedals (RP), flap levers (FL) and control stick (CS). These inputs go through the hydraulic system and the hydraulic reservoir to the corresponding control surfaces: ailerons, flaps, rudder, elevators and trim tabs. Each control surface has a corresponding actuator control unit (ACU), and 2 or more actuator pumps to account for redundancy in case of actuator failure. The hydraulics are also connected to the braking systems of each landing gear (nose and main).

3. **Thermal System:** The thermal system is responsible for the cooling of the battery systems and motors by providing a heat sink, as well as circulating cabin air in tandem with the air-conditioning system of the environmental control system. The ram air intake (RAM) provides an air intake for cooling which is utilised by the cooling units (placed next to each motor and battery). The heat losses from the motors, battery and air-conditioning system are dissipated to the heat sink.

13.2. Hardware System

The hardware diagram in Figure 13.2 depicts the relationship between the aircraft's electrical, thermal, and hydraulic components. Power management and distribution (PMAD) is at the heart of this, supplying power to all components of the aircraft via two separate buses, the primary bus and the secondary bus.

1. **The primary bus** supplies power to the electrical power system, which sends power to the engine control unit (ECU), which provides thrust to the electric motor, which drives the propeller. When the propeller is in regenerative mode, it applies power to the motor, which now serves as a generator, and charges the battery maintained by the battery management system. The primary bus also supplies power to the cable deployment mechanism, through which the battery can be recharged.

2. **The secondary bus** provides power to various other systems, such as the thermal system, the environmental control system (ECS), the hydraulic system, as well as other cabin loads and sensors. As stated in Section 13.1, the thermal system is in charge of cooling the aircraft, the battery, and the propulsion system. This is done in tandem with the environmental control system, which manages the air conditioning system. The hydraulic system also draws power from the secondary bus to activate the electro-mechanical servos. The secondary bus additionally provides power for the cabin loads, the digital twin sensors and the avionics bay. This electricity is also supplied to the avionics system, which allows the pilot to manage the hydraulic and propulsion systems via the throttle, control stick, rudder pedals, and flap levers.

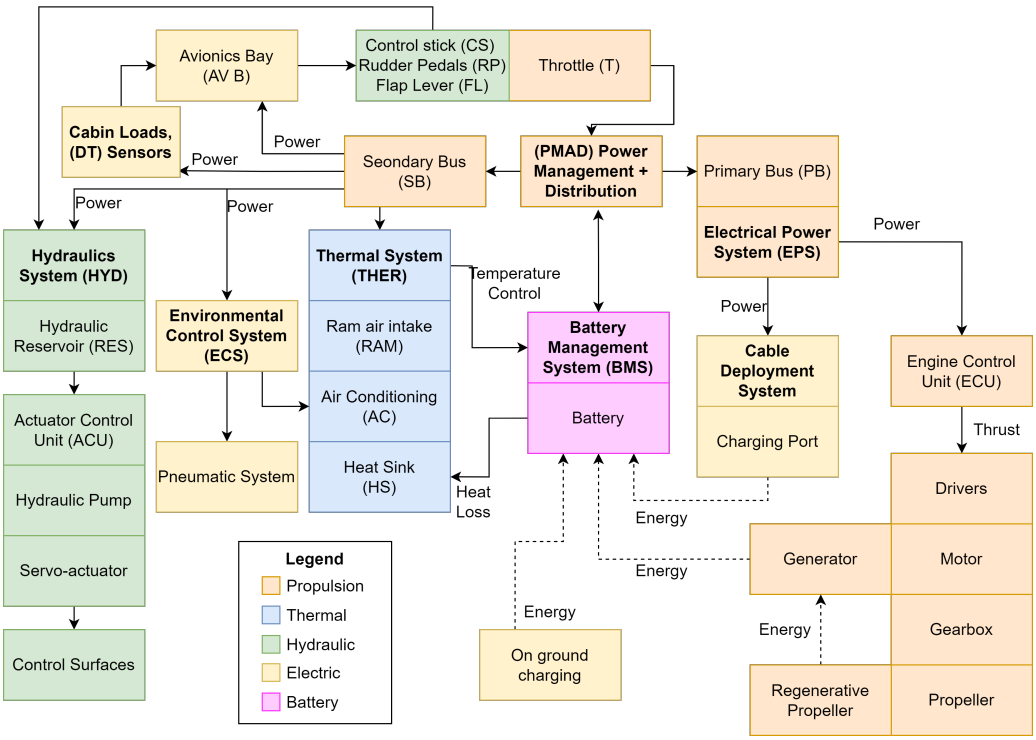

Figure 13.2: *Hardware Block Diagram*

13.3. Electrical System

The electrical block diagram displayed by Figure 13.3 provides a blueprint of the relations between the electrical systems on board the ElectriFly. It is noticeable that the power management system (PMS) forms the core of the electrical system and plays a vital role in regulating power. It does this via the primary and secondary bus, whereas the battery management system is directly connected to the PMAD. The primary bus directs power to the engines and the cable deployment system, while the secondary bus directs the received power to other subsystems such as the avionics bay, ECS, ice protection, hydraulics, sensors and cabin loads.

Here, the propulsion system, and the battery management system (pink) are further detailed. The battery charging system can receive power from three different sources. These include an on-ground recharging system, the recharging drone and generative power from the propulsion system. The BMS incorporates battery overcurrent protection systems, battery cooling systems, and isolation switches to isolate malfunctioning battery modules.
Note: As opposed to a normal fuel-powered aircraft, an APU is not needed on an all-electric aircraft, while on the ground. This is because the turbofan/turboprop is

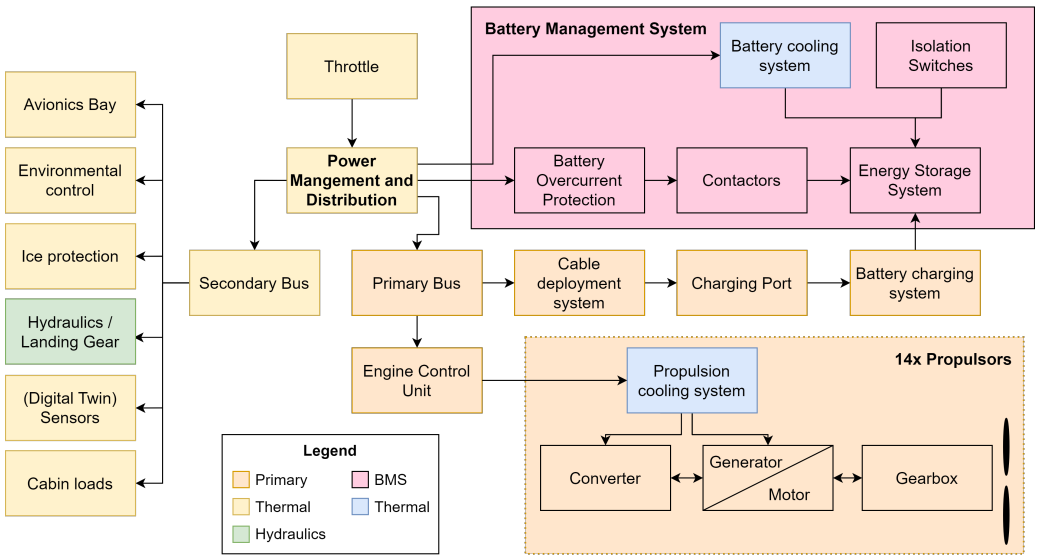

Figure 13.3: *Electrical Block Diagram*

13.4. Software and Avionics Systems

The aircraft shall feature a fly-by-wire cockpit, equipped with an automatic flight guidance system capable of providing autopilot functionality. The software block diagram in Figure 13.4 differs from the hardware block diagram in that it depicts the interaction between the various components of the aircraft as well as the software flow between them to demonstrate how the aircraft may be operated. The software block diagram is divided into three sections: on the left are the inputs that can be given by the pilot in the flight deck and the sensors; on the middle are the computers and processing units; and on the right are the outputs of the commands given, which can be in the form of a display to the pilot, or actuation of the control surfaces, and power supply to the engines.

1. First, the pilot provides inputs via the flight deck's interface, to send information to the flight management system (FMS), including the flight plan, and then, depending on whether the autopilot is turned on or off, the FMS collaborates with the flight guidance system (FGS) to enable the autopilot and auto-throttle. Both the FMS and FGS send inputs to the flight control system (FCS), which controls the actuation of the control surfaces.

2. The primary flight control computer and the secondary flight control computer comprise the flight control system. The primary flight control computer is in responsible for controlling the main control surfaces, such as the elevator, rudder, and trim tabs, which allow the pilot to control the aircraft and make turns and manoeuvres. The secondary flight control computer commands the flaps during the landing and takeoff phases.

3. The flight deck, along with the antennas also provide information to the navigation system, which can constantly track the aircraft's position, heading, and speed.

4. The surveillance system is in responsible for ensuring safe clearance of the aircraft from the ground and other aircraft, and for ElectriFly ensures sufficient clearance from the recharging drone. It is also equipped with a weather radar in the radome of the aircraft to detect bad weather, such as thunderstorms, heavy rain and wind shear.

5. The communication system is in charge of communicating with ATC via the Automatic Dependent Surveillance–Broadcast ADS-S, and the Controller–pilot data link communications (CPDLC).

6. The flight management system collaborates with the power management and distribution system, which controls the throttle through the ECU and distributes power through the secondary bus to the ECS, landing gear, ice protection systems, and cable deployment systems.

7. The sensors block is divided into digital twin sensors and antennas that are generally utilised for routine aircraft operations. The digital sensors send data to the digital twin computer, which directs relevant information for the pilot to the FMS. It also acts as a data collector for the digital twin information, which can be downloaded by the airline at the end of each flight.

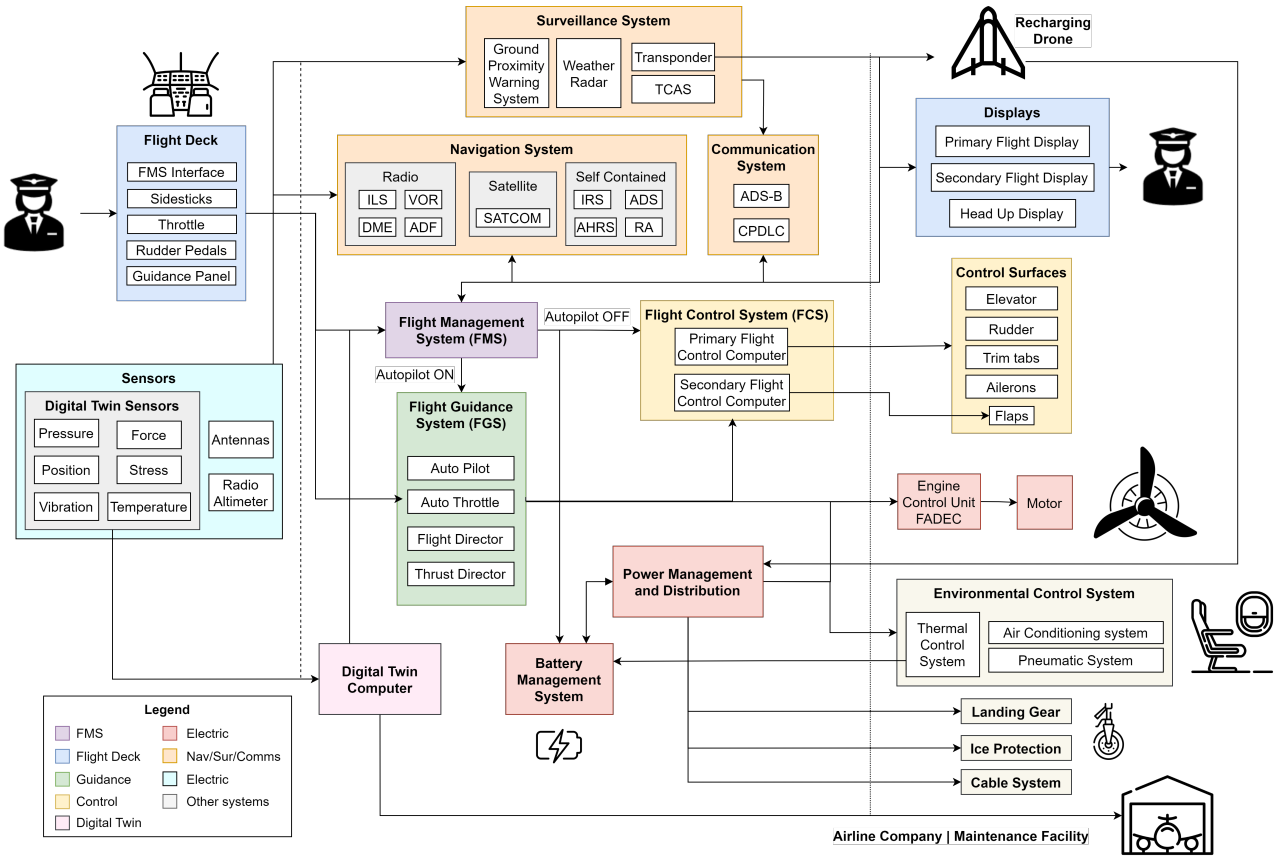

Figure 13.4: *Software block diagram*

13.5. Data Flows

While ElectriFly must perform the standard communications as a commercial aircraft, in addition, it has to communicate with the recharging system as well. The data handling block diagram, shown in Figure 13.5, shows the input and output flows of data from Electrify. There are three types of communications:

1. **Air-to-Space:** Electrifly communicates with satellites constellations like other conventional aircraft via satellite communication (SATCOM) module to obtain its GPS position.

2. **Air-to-Air:** ElectriFly shall use the existing traffic avoidance collision systems, or TCAS, to maintain a safe vertical and horizontal clearance from other flying aircraft. Additionally, it shall also feature an internal collision avoidance system (CAS) to maintain a clear separation from the recharging drone. It also communicates the relative position, relative speed and docking status for the recharging cable to the drone and the pilots.

3. **Air-to-ground:** Electrify additionally communicates with the ground ATC or control area centres and regularly broadcasts its position, heading, speed, and call sign. It shall also be able to communicate with instrument landing systems (ILS), and the aforementioned ADS-B and CPDLC links. Electrify also communicates with the airline operations control centre, and additionally transmits sensor data to the air operations control centre. The air operations control centre then directs this data to the maintenance hubs for the creation of a digital twin. Maintenance can then communicate an action plan in case of any emergency, to Electrify. For for the recharging system, Electrify must notify the recharging hub at least 20 minutes before it requires recharging. The recharging hub shall then deploy the drone, and the communicate with its drone the speed, position, heading, and recharging status throughout the recharging process.

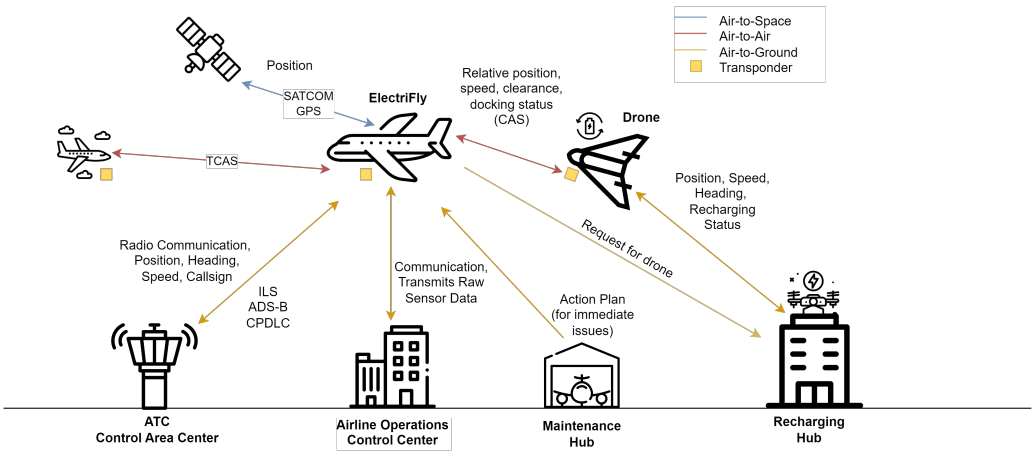

Figure 13.5: *Data handling block diagram*

13.6. Thermal Management

In-flight energy will be drawn from the battery. Due to the internal resistance, the battery will heat up. Batteries have limited operational temperature ranges therefore, cooling will be required. In this section, this thermal control will be sized based on the battery; in addition, the transformer and motor heat flow will be included.

Heat Generated

During the operation of the aircraft, energy is dissipated due to the Joule effect. The heat generated by each component needs to be analysed in order to assess which kind of cooling system is required. The main components that generate heat affecting the battery are the battery itself, the motor and the transformer. The energy dissipated in the battery is directly related to its internal resistance. There are complex methods that can be used to estimate the heat generated by a battery but here it is approximated to an equivalent circuit, with the heat due to chemical losses being neglected. As explained in Chapter 6, the batteries are made up of cells combined into modules. To calculate the internal resistance of the battery, the internal resistance of each module has to first be calculated. In a module, there are 81 parallel branches of 6 cells in series. Based on the internal resistance of each cell, the internal resistance of the module can be calculated using Equation 13.1. With the module resistance known, the total internal resistance of the battery can be obtained using the same procedure as shown in Equation 13.2. The resistance of a single cell is 0.05 Ω.

$$R_{module} = \frac{\text{Nr cells in series} \cdot R_{cell}}{\text{Nr cells in parallel}} = 0.0037\Omega \qquad (13.1)$$

$$R_{battery} = \frac{\text{Nr modules in series} \cdot R_{module}}{\text{Nr modules in parallel}} = 0.033\Omega \qquad (13.2)$$

Using the internal resistance, the heat generated can be determined using Equation 13.3. The current flowing into the battery can be obtained by considering the power required for the flight phase.

$$\dot{Q} = P_{dissipated} = RI^2 \qquad (13.3)$$

$$P_{required} = UI \qquad (13.4)$$

Furthermore, the heat generated by the transformer and the motor can be determined by calculating the amount of power dissipated from their efficiency and useful power provided as shown in Equation 13.5.

$$\dot{Q} = P_{dissipated} = (1 - \eta_{component}) \cdot P_{useful} \qquad (13.5)$$

The dissipated power corresponds to the rate of heat flowing out of the component. This heat needs to be dissipated with the help of a cooling system if it causes an increase in temperature above the operational range. For the motors, an efficiency of 0.95 is assumed. For the transformer, an efficiency of 0.98 is assumed based on conversations with Dr.ir. P. Bauer and Dr. T. Tomažic.

Temperature Profile

The heat generated determined in the previous section causes a change in the temperature of the battery, ΔT. This change in temperature can be calculated by first converting the heat flow rate into heat using Equation 13.6 and then writing it as a function of the time interval, Δt, as in Equation 13.7. This equation is used to plot how the temperature in the battery increases during flight and the resulting graph can be seen in Figure 13.6.

$$Q = \frac{\dot{Q}}{\Delta t} \qquad (13.6)$$

$$Q = mc\Delta T \rightarrow \Delta T = \frac{\dot{Q}}{mc}\Delta t \qquad (13.7)$$

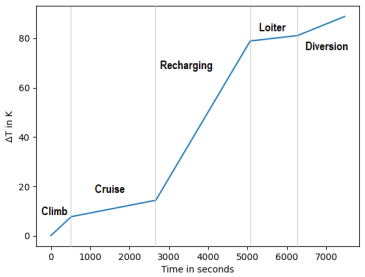

Figure 13.6: *Temperature over the different phases*

Where m is the total mass of the batteries, totalling 2940 kg. And c the specific heat capacity of the battery. The specific heat capacity of the battery should be equal to the mass-weighted average of the heat capacity of the different battery components. The specific heat capacity of Lithium is $3490 J/(kgK)$, and the specific heat capacity of NMC is $1040 J/(kgK)$[1]. The heat capacity of the electrolyte has not been tested often. However, as the mass fractions per material are not known, a conservative estimation is made by using the value of NMC.

As the change in temperature depends on the time interval and the power used, the change for each phase of flight needs to be computed. The change in temperature of the battery throughout a flight of roughly two hours including a recharging phase can be seen in Figure 13.6. As can be seen from the graph, the recharging phase causes the most and the fastest change in temperature. Therefore, special attention has to be given to this phase during the sizing of the thermal system. With the losses of the motors and transformers, a maximum heat flow rate of 114 kW is found. An overview of the heat flow rate for the different flight phases can be found in Table 13.1.

Current solid-state batteries operate at relatively high temperatures, between 50 to 80°C [3]. These operating temperatures are expected to reduce with further developments but as it is not known yet by how much, it is important to ensure that ElectriFly's batteries can be at this operational temperature. To ensure that they are above the minimum temperature, the use of a heating system to have the battery reach a temperature of 50°C before the beginning of the flight should be considered. It should be investigated if the energy dissipated during on-ground recharging can be used for this purpose. During the flight, the operation of the battery will heat itself up due to its internal resistance, causing the maximum temperature to be exceeded. The recharging phase is of special concern due to the high rate and amount of temperature change. Furthermore, as the batteries operate at a high temperature in comparison to the optimal temperature in the rest of the aircraft, proper insulation needs to be applied and possibly cooling for the outer region so that the heat does not propagate throughout the aircraft.

Sizing

For the heat generated to be removed, a liquid cooling system is used. Water was chosen as the liquid due to its high specific heat and ease of handling. Two heat exchangers shall be placed. One will take in RAM air and cool down the water, and the other will transfer the heat from the batteries to the water. A simple diagram can be seen in Figure 13.7. As the particularities of the thermal management system are outside the scope of the project, the focus will be on the heat exchange between the battery and the water only. Further analysis will need to be done for the RAM air heat exchanger.

For a first, preliminary estimation, it is assumed that the temperature of the water before crossing the battery will be 10°C, and that it will increase to 50°C after leaving the battery. The water will then have to have a certain mass flow rate to be able to remove all the heat from the battery. The specific heat capacity of water is 4186 J/(kgK). The values obtained can be found in Table 13.1. This value can be calculated for each flight phase using Equation 13.8. A pump is included in the system to regulate the flow.

$$\dot{m} = \frac{\dot{Q}}{c_{water} \Delta T} \tag{13.8}$$

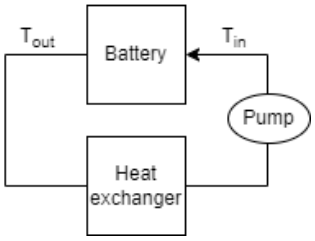

Figure 13.7: *Thermal system diagram*

Table 13.1: *Heat generated and water mass flow required at each flight phase*

Heat Generated [kW]		Mass Flow [kg/s]	
$\dot{Q}_{take-off}$	87.4	$\dot{m}_{take-off}$	0.52
$\dot{Q}_{climb}$	112.1	$\dot{m}_{climb}$	0.67
$\dot{Q}_{cruise}$	39.8	$\dot{m}_{cruise}$	0.24
$\dot{Q}_{recharging}$	114.1	$\dot{m}_{recharging}$	0.68
$\dot{Q}_{loiter}$	28.8	$\dot{m}_{loiter}$	0.17
$\dot{Q}_{diversion}$	63.6	$\dot{m}_{diversion}$	0.38

[1] https://www.batterydesign.net/specific-heat-capacity-of-lithium-ion-cells/#: :text=Lithium%20Nickel%20Manganese%20Cobalt%20(NMC)%20%3D%201040%20J%2Fkgv [Accessed on 26.06.2023]

14. Final Design

With the subsystem design complete, the final design for ElectriFly is obtained. All relevant parameters are shown in Section 14.1. Due to the vastness of the design space, there exist possibilities for optimisation for the technical design by increasing the accuracy and fine-tuning several parameters. Some strategies are examined in Section 14.2,

14.1. Aircraft Design Parameters

The complete aircraft design is presented, for geometry, performance, structures, aerodynamics, and battery. Geometrical parameters of ElectriFly are given in Table 14.1. The performance parameters are given in Table 14.2. The weights of the components comprising the OEW are given in Table 14.3a, and the MTOW components in Table 14.3b. The structural parameters are given in Table 14.3c.

Table 14.1: *Overview of all geometrical parameters of ElectriFly*

Wing		Fuselage		Tail		Propeller	
S_W	35.13 m^2	Nose length	2.69 m	S_v	5.3 m^2	Blades/prop	3
b_W	20.53 m	Tailcone length	4.48 m	b_v	2.82 m	Propellers	14
A	12 -	Cockpit length	2.5 m	Λ_v	30 deg	Clearance	0.44 m
$\bar{c}$	1.79 m	Fuselage length	12.54 m	S_h	5.27 m^2	Diameter	0.88 m
λ_W	0.45 -	Outer diameter	2.24 m	b_h	4.87 m		
$\Lambda_{0.25c}$	0 deg			Λ_h	13 deg		
Airfoil	NACA 44018			Airfoil	NACA0012		

Recharging		HLD & Control Surfaces		Landing Gear		Motor	
Cable length	20 m	LE flaps span	85%	y_{mlg}	1.4m	Casing diameter	208 mm
Cable diameter	3.5 cm	TE flaps span	70%	l_{mlg}	6.39m	Axial Length	85 mm
Drogue diameter	35 cm	Ailerons span	15%	l_{ng}	1.15m		

Table 14.2: *Performance parameters*

Parameter	Value	Notes
Minimum drag	3750 N	at cruise altitude
Minimum required power	228 kW	at cruise altitude
Available power	990 kW	at cruise altitude
Maximum speed		at specific altitude
Theoretical ceiling	12000 m	
Max range	640 km	at MTOW

Table 14.3: *Breakdown of Aircraft Parameters*

(a) *OEW Breakdown*

Component	Weight
Wing	737.28
Empennage	165.31
Fuselage	945.58
Landing gear	335.43
Engines	419.19
Electronics	452.73
Flight controls	202.43
Recharging	300
Digital twin	50
OEW [kg]	3607.74

(b) *OEW Breakdown*

Part	Weight
OEW	3607.74
Battery	2904.37
Payload	1260
MTOW	7772.1

(c) *Relevant Structural Parameters*

Parameter	Material	Wing	Fuselage
Number of stringers	T700/PEEK	10	20
Stringer cross-section area [mm^2]		300	300
Skin thickness [mm]	ALU7075	0.6	1

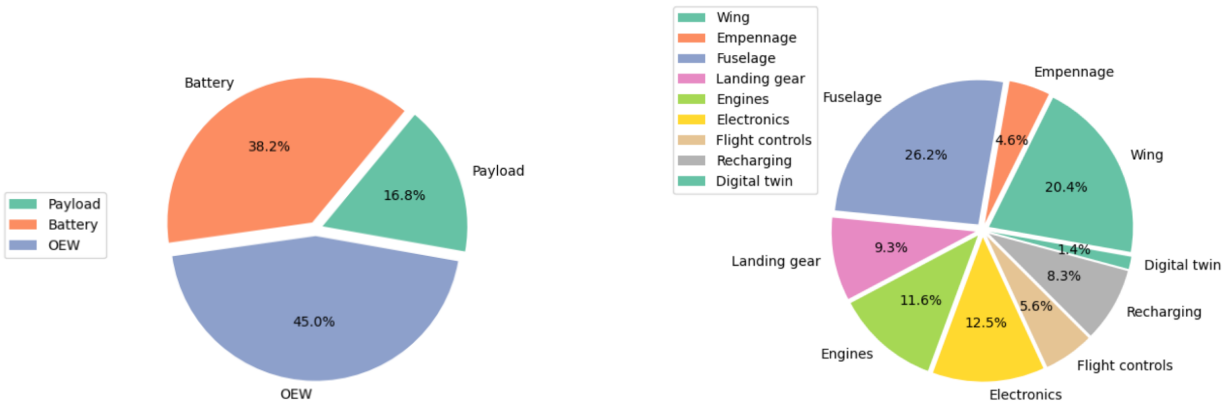

(a) *MTOW percentage breakdown*

(b) *OEW percentage breakdown*

Figure 14.1: *MTOW and OEW breakdowns*

Aerodynamics, Battery, Propulsion: The relevant aerodynamics, battery and propulsion characteristics are given in Table 14.4a, Table 14.4b, Table 14.4c.

(a) *Aerodynamics parameters*

Parameters	Values
$C_{L_{cruise}}$ [-]	0.85
$C_{D_{cruise}}$ [-]	0.032
$(L/D)_{max}$ [-]	26.6
$C_{L_{max\,cruise}}$ [-]	1.76
$C_{L_{max\,TO}}$ [-]	2.07
$C_{L_{max\,land}}$ [-]	2.28

(b) *Relevant battery parameters*

Parameter	Cell	Module
Voltage [V]	3.8	22.8
Capacity [Ah]	5.68	457.59
Length [m]	0.0184	1.458
Width [m]	0.0184	0.108
Height [m]	0.065	0.065
Weight [kg]	0.036	17.39

(c) *Relevant propulsion parameters*

Propeller		Motor	
Individual thrust	985.23 N	Max RPM	6000 rev/min
Max RPM	2700 rev/min	Peak power	86 kW
		Continuous power	56 kW
		Voltage	580 V
		Efficiency	92-98%
		Continuous torque	90 Nm

14.2. Optimisation Possibilities

The design process involved the consideration of numerous parameters for the design of each subsystem and technical aspect. However, due to the vastness of the design space, fine-tuning each parameter and updating the design of other subsystems, as a result, was not feasible within the time scope of this project. Therefore, the final design is an efficient overview but gives rise to several optimisation possibilities, which are left as suggestions for the subsequent design phases.

1. A more in-depth analysis of distribution propulsion and the interaction between propellers can be performed.
2. The wing can be resized based on the new gains in aerodynamic performance provided by the distributed propulsion and the plasma actuators. This is because, as of now, the lift distribution is more than needed and thus, high-lift devices would not even be necessary. The wing could be optimised, hence reducing the weight.
3. The fuselage diameter could be decreased by placing all batteries in the wing, as even after optimisation, there will be enough space. This allows for a decrease in the drag produced by the fuselage and, thus, the aircraft's weight.
4. The need for a tail could be re-analysed. Indeed, one of the advantages of distributed propulsion is the possibility of using vectorial and distributed thrust to control the aircraft. Thus, an analysis could evaluate the need for a tail, which could greatly decrease the weight of the aircraft.
5. More detailed analysis of structural failure modes to determine additional parts in the structure such as ribs, longerons, curved skin and so on. This can be combined with additional analysis of failure modes such as vibrations and buckling.

The first three of these techniques show that an improvement on any of the shown parameters will lead to a reverse snowball effect that might greatly improve the weight, and therefore the efficiency of the aircraft.

Payload Range for Other Energy Densities

The energy density of the battery has a significant impact on the design of the aircraft, and therefore the payload and range of the aircraft that it can carry. To compare how energy density affects the range of the aircraft, Figure 14.2 shows the payload range diagram iterated for the energy density of 400 and 500 Wh/kg. ElectriFly is represented by the dark blue lines. From the graph, it can be seen that with lower energy density, the range reduces, the MTOW increases, and the aircraft can no longer qualify under the CS-23 weight limit.

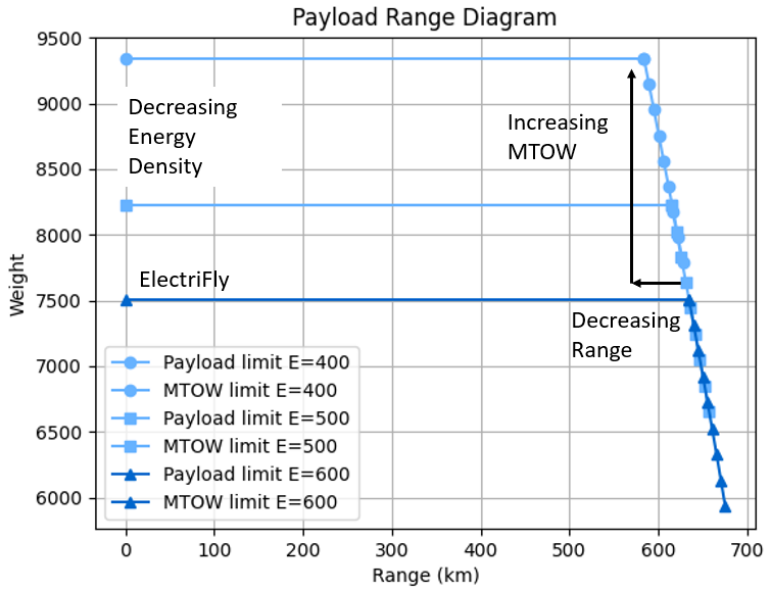

Figure 14.2: *Payload Range for other energy densities. 'E' stands for energy densities. The dark blue represents ElectriFly's mission.*

Three view

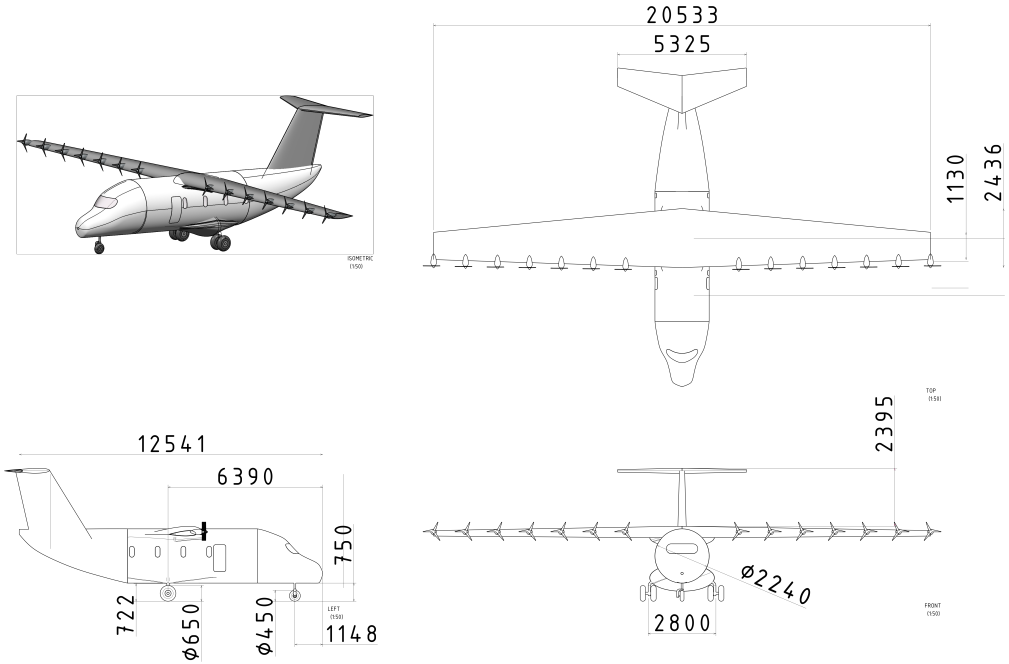

Figure 14.3: *Three-view of the ElectriFly*

15. ElectriFly Digitalization and Manufacturing

Currently, modern techniques such as data-driven design, AI, digital twins and advanced manufacturing processes are being introduced to the aerospace industry in order to find more sustainable and economically viable solutions for aviation [86]. The following chapter shall describe how those novel techniques can be used during the life cycle of ElectriFly. This will be done in an order that follows a so-called Digital Thread. First, the concept of the Digital Thread will be described. Then, the analysis will start with material acquisition and move to the manufacturing of parts and assemblies, in Section 15.1. After the production phase, the concept, functions and applications of a digital twin are examined in the context of aircraft operations in Section 15.2.

Digital Thread

The digital thread is a name for the set of data that contains information about the product and all its parts from the beginning of the product life until the end-of-life [86]. Collecting, storing and processing the digital thread allows companies to predict the product's functionality, possible issues, life duration, maintenance needs, and most likely failure modes as well as to perform many other in-depth predictions and analyses related to the product [87]. It forms an example of a data-driven approach to engineering products that can result in decreased cost and waste of both time and materials during the entire lifecycle of the product, hence, as the technology matures, it can revolutionize the aerospace industry [86].

In the case of ElectriFly, the digital thread will be mostly focused on the operations of the aircraft and the digital copy of the systems - the digital twin. However, it must also be ensured that the manufacturer chosen for ElectriFly also uses the appropriate product lifecycle management strategy that also supports it. An external cloud database will be needed for storing the entire thread through the life of the aircraft. Appropriate data mapping techniques must be used to facilitate the analysis of the database. Additionally, an analytic interface, likely AI-based, must be built and trained to be able to provide real-life data insights and predictions for the future. The model can be trained on the data available in the cloud and incorporated into in-flight computers for instance to analyse the data in real time. The data from the main database must be easy to share with external companies - for instance in case the maintenance is outsourced. A special analytics department may be formed that makes sure that the data from the digital thread and twin are correctly utilised.

The data regarding ElectriFLy should not stop at the product itself and extend to the organisational level. It should be clear what personnel worked with or is responsible for a particular part of the product so that the human impact can also be monitored and accounted for in the overall analysis of the health of the aircraft. Additionally, this can contribute to work cell optimisation which reduces the cost and time of assembly and part manufacturing [88]. It can be stored in a separate digital thread, however, the analysis of the two threads should be done together.

Data for Material Acquisition

The digital thread should start as soon as possible - even with the raw materials. Data on the acquisition such as company, time, geographical locations, or chemical composition may be gathered and used to effectively source the best quality materials already at the start [1]. At the very beginning of the process, also data about the pre-fabricates such as aluminium alloy sheets or carbon fibres can be provided by the different suppliers so that samples most satisfying for the customer can be chosen. In addition, transportation and delivery data can also be gathered so that the organisation can choose the most efficient cooperation strategy with suppliers [2]. This data should further be shared with manufacturing companies that can use it for their analysis of the previous life of the materials they use for the benefit of rapid and efficient design cycle [86].

15.1. Manufacturing Overview and Production Plan

This section describes the current state of manufacturing of aviation structural components. Then, the manufacturing techniques specific to ElectriFly are presented and evaluated. Afterwards, sensor integration for digital thread at manufacturing and their benefits are briefly discussed. Finally, an overview of possibilities for battery manufacturing is given.

[1] https://braincube.com/resource/understand-value-of-digital-thread-manufacturing/ [Accessed on 15.06.2023]
[2] https://specright.com/media/how-a-digital-thread-can-revolutionize-your-supply-chain [Accessed on 15.06.2023]

Manufacturing and Production Plan of Structural Components

The traditional structural components of aircraft such as fuselage, wing, and empennage are typically made of aluminium, magnesium, and titanium alloys or high, aerospace-grade composites [89]. The latter usually consists of continuous carbon fibres combined with thermoset resins such as epoxy or phenolic resins [90]. Alternative fibres such as kevlar, nylon, aramid or glass fibres can also find their application in various avionic structures [90]. Since the materials used are common for most aircraft, certain traditional manufacturing techniques are used for metals and composites to produce aircraft parts and assemble them [91]. Those techniques vary per part type and specific material, however, in this report, the main focus is given to aluminium alloys and polymer resin composites as those are the materials used for the biggest and most crucial structural components in ElectriFly.

Aluminum alloys: They can be used in many parts of the aircraft and depending on its application different prefabricate and manufacturing techniques must be used. Aluminium alloys used for skin are prepared as metal sheets. Then the curvature can be achieved by bending, stretch forming or for parts requiring smaller radii, deep drawing and rubber forming [91]. Stringers can also be made from aluminium sheets using rubber forming or deep drawing. Other options are also available such as extrusion which involves pushing liquid metal through an opening and allows for more complex stringer cross-sections [91]. Flat aluminium parts with cutouts such as wing ribs can be made using machining techniques [91]. In ElectriFly the skin of the fuselage and wingbox is supposed to be made of AL7075. For that, the traditional techniques of manufacturing can be used which means that most likely bending or stretch forming will have to be used to create a skin with big radii of curvature.

Composites: They are another prevalent material in aerospace applications due to their great mechanical properties and low weight. For structural applications mostly synthetic fibres combined with thermoset resins are used and it is reflected in the manufacturing options [89]. Composite parts manufacturing starts with lay-up. The fibres have to be laid into layers in the mould with an appropriate shape. It can be done manually or sometimes fully automatically. The former requires more time and high labour costs while the latter is done with expensive equipment [91]. Then the resin is introduced to the mould using processes like resin transfer moulding or vacuum infusion using pressure difference [91]. Sometimes compression moulding or drape forming must be used to achieve the desired final shape [92]. Finally, the setup has to be cured in an autoclave at elevated temperatures until the thermoset bonding is finished [91]. Both stringers, skin parts and other components can be manufactured in this way [92]. An alternative option is also possible for stringers or frames - pultrusion which is a process similar to extrusion except for the material is pulled rather than pushed. It can be more cost-effective, highly automated and continuous, hence it decreases the overall time needed and cost and can be favoured over other processes for stringers if possible [92].

Materials for ElectriFly Production

In Chapter 10, the biggest components - the fuselage and wingbox were discussed and material selection for them was performed based on mechanical properties. The aluminium alloy AL7075 is currently commonly used in the industry and traditional manufacturing techniques can be used to process it [89], as mentioned previously. The current composites, however, are often not efficiently recycled and they are not a sustainable solution. Therefore, more environmentally friendly alternatives were researched and a novel combination of high-performance carbon fibre and PEEK resin was chosen [93].

The composite material chosen for ElectriFly is different from the composites traditionally used in aerospace. The main difference is that the matrix used is a thermoplastic and not a thermoset polymer. Thermoplastics display different properties - instead of being cured and solidifying at elevated temperatures, they must be (re)melted in high temperatures (over 343 °C for PEEK [3]), shaped into the desired form and cooled down to solidify [91]. The temperatures used for melting thermoplastics are also, on average, higher than those of curing thermosets. What follows is that the typical process of infusion and autoclaving cannot be used for this composite and other methods must be found. The fibre infusion would have to take place in a very hot chamber which poses a large manufacturing difficulty.

Novel procedures are developed to produce high-performance continuous fibre thermoplastic resin composites [94] [95] [96]. Usually, this type of material requires pre-impregnation of the fibres with the resin to create prepreg [97] [94]. Several procedures can be used to make it, an overview of which is presented below:

1. **Hot melt impregnation:** a process where a fibre spool is unwound and pulled through a hot resin pool, then wound around a drum and cooled [98].
2. **Solution impregnation:** a process that requires dissolving the thermoplastic in a solvent, then impregnating the fibres and chemically or thermally removing the solvent [98].

[3] https://www.xometry.com/resources/materials/polyether-ether-ketone/ [Accessed on 19.06.2023]

3. **Dry powder impregnation:** a process in which thermoset in powder is introduced between the fibres and it is heated to sinter into the fibres.

4. **Film stacking:** the fibre sheets are stacked with polymer sheets and consolidated under pressure [98]

5. **Fibre Co-mingling:** Fibres of the thermoplastic and reinforcements are mixed to form continuous filament yarns [98].

So far PEEK was successfully combined with carbon fibre utilizing quasi-solution impregnation with aqueous solutions [99] and melt impregnation process [4] and those processes can be used for the initial production of the prepreg. It is recommended, however, that the other possibilities for mass production of the prepreg could be investigated regarding their cost, efficiency, and sustainability.

The next production step is the prepreg lay-up on a protective film placed in the part mould [97] [91]. Traditionally, for many parts, it was done manually which resulted in a long time and high cost of part production [91]. For ElectriFly production the highest possible automation level should be used to facilitate the process. For large parts such as the fuselage, Automated Tape Layering (ATL) can be used. It is a well-established automated composite manufacturing technique that involves a machine laying wide unidirectional tapes of the prepreg onto the part mould [100]. Despite the high cost, this process offers advantages over manual lay-up such as higher speed, more control, fewer errors, and a reduction in material waste [100]. For smaller parts and parts not suitable for ATL (due to, for instance, high contour) Automatic Fibre Placement (AFP) can be used. In this process, several parallel prepreg tows or slit tapes are simultaneously laid by a computer-controlled fibre placement delivery head following mandrel contours [100]. Additional features are offered by AFP modules - cutting, clamping or restarting during operation is possible which lowers the tolerances, offers more control and enables incorporating cutouts and openings into the process [100]. Other processes such as Tailored Fiber Placement or Fiber Patch Performing are also being developed, but they do not seem promising for the aerospace industry yet.

There are multiple methods which are currently used for trajectory optimisation of fibre placement. Usually, the principal stress method, load path method and genetic algorithms are used [100]. Those methods focus on laying the fibres in the directions where the most loads are carried. Those directions are determined from analytical methods like Finite Element Analysis in an iterative process [100]. In the future, further algorithmic improvements could be possible with the use of machine learning or AI algorithms that could predict stress patterns based on previous experiences, simulations, and possibly real-life data from digital twins stored in the digital thread.

The last step of the process requires consolidation of the resin and fibres to achieve the final product. After lay-up, the shape can be subjected to drape forming in a mould, then, put into a vacuum bag and heated up, possibly in an autoclave to melt the thermoplastic and consolidate the product [92]. Alternatively, if the AFP process is chosen, the delivery head can be equipped with a heater that can heat the prepreg during layering which causes immediate consolidation and bonding [100]. For ElectriFly, the latter would most likely be preferable, due to the overall less number of tools which decreases the cost, as well as more flexibility in composite and form choice.

For certain parts with continuous cross-sections, it is also possible to make use of pultrusion. The prepreg fibres are then pulled through a heating die with a certain cross-section and consolidation and shaping take place at the same time there [101]. This process is simpler and less expensive than the ones described above, but the main limitation is the geometric shape that can be created. Also, an expensive mould is required and the mould can be only used for one specific part [5]. If only the stringers of ElectriFly would be composite and if the stringers would have a constant cross-sectional shape, as it is now at the stage of preliminary design, highly automated pultrusion may be used to produce those. The overview of all the processes for thermosets is given in Figure 15.1.

[4] https://www.youtube.com/watch?v=umi6Q-bNN8E [Accessed on 15.06.2023]
[5] https://www.unicomposite.com/advantages-and-disadvantages-of-frp-pultrusion-process/ [Accessed on 15.06.2023]

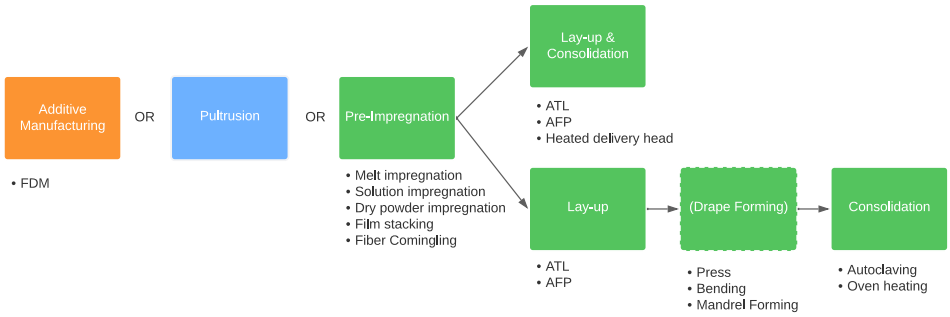

Figure 15.1: *An overview of processing thermoplastic-based composites. Both existing and future methods are included.*

Additive Manufacturing

Another recently emerging possibility for thermoplastic resin composites is additive manufacturing (AM). The main advantage of AM methods is the ability to produce very complex geometries at a reasonable speed and without material waste as well as relatively low costs [102]. However, as those methods result in poor interlayer bonding of the printed composite, the final parts offer significantly lower mechanical and thermal properties which makes it impossible to use them for high-performance structural applications [102]. Thus, it is not possible yet to use AM methods for ElectriFly structures production. Nevertheless, as research is being conducted on the possibility of improving the AM products by infrared pre-heating or special laser preheat of fused deposition modelling (FDM) nozzles [102], additive manufacturing may become the future of manufacturing of thermoplastic-based composite both with continuous and shorter fibres. This process is also added to the overview in Figure 15.1.

Assembly Process

Once the metal and composite parts are manufactured, assembling procedures are needed to combine them into sub-assemblies, assemblies and finally the aircraft itself. In ElectriFly, 2 different material types are used - metal and composite which creates an additional challenge for assembling the parts that have to be taken into consideration in assembly method choice. Numerous commercial methods are used in the aviation industry such as - riveting, bolting, adhesive joining and welding [91].

1. **Bolting and Riveting:** Both bolting and riveting are traditionally used in fuselages and wingboxes and they can also be applied to ElectriFly. Those methods are cheap, relatively fast and allow for easy disassembly of the fasteners [91], thus they can be successfully used for ElectriFly. As the different materials vary in properties, fracture or yield occurs at different conditions for composites and metals, yet, the failure of one of them results in the failure of the entire fastener [91]. Additional attention must be given to stress analysis around the fasteners and special techniques like pre-loading can be applied to relieve the stresses [91].

2. **Adhesive Bonding:** Adhesive bonding is also possible, but the adhesives are often not recyclable, making product disassembly at the end of life more difficult or impossible and they often require time or special conditions to cure which creates additional waste in the manufacturing process [91]. For those reasons, adhesive bonding of ElecriFly components shall be avoided at all costs.

3. **Welding:** Welding of composites is traditionally not possible as thermoset matrices are used in them and the thermoset compounds decompose in high temperatures [6]. Not all metals are weldable, but some aerospace aluminium alloys can be combined using this procedure [91]. In the case of dissimilar materials, welding is also sometimes possible but may turn out to be difficult, complicated, costly, or even disadvantageous and must be done by specialised, expert welding facilities [7]. Thus, any potential welding of thermoplastic parts could only be conducted between the parts made of the same composite. An interesting possibility is offered by ultrasonic welding thermoplastic composites. As thermoplastics can be remelted to stick together, this technique is explored for composite-only aerospace structures [103]. It would be recommended to conduct a further, deepened analysis to decide whether it is indeed beneficial to use separate materials for fuselage and wingbox stringers and skin or maybe welding of thermoplastic gives enough weight advantage and the lack of weakening fasteners to compensate for worse material properties. Both riveting, bolting and welding can in principle be done by an automated robotic arm which would be preferable for better time and cost performance.

AI and Data-Driven Manufacturing

The digital thread that was started with gathering data about the materials used for production can be continued in manufacturing. During every process sensors can be used to gather data about every specific part produced in the

[6] https://www.compositesworld.com/articles/welding-thermoplastic-composites [Accessed on 20.06.2023]
[7] https://www.titanovalaser.com/blog/an-introduction-to-laser-welding-for-dissimilar-metals/ [Accessed on 15.06.2023]

factory. The data can be later analysed and checked for possible process anomalies if the part turns out to underperform. Additionally, given enough data, AI models can be trained that are able to detect anomalies in an ongoing process, based on real-time data [86]. In that case action can be taken either automatically by appropriate algorithms or by machine operators to either adjust the process or even stop it completely. What is more, damages and defects can be predicted and observed in parts based on process data analysis, hence better quality control can be assured [104]. This data can be later used in combination with sensors from the digital twin to achieve a more in-depth understanding of the entire aircraft health [86].

A general overview of potential sensors that should be included in the manufacturing process of ElectriFly and the data they capture can be given at the preliminary stage. Since skin processing involves processes based on material deformations followed by heat treatment, mainly stresses, stress cycles, and strain data from different places on the sheet should be gathered. Additionally, sensors for metal crack detection (for instance microwave [105]) could be added to monitor the quality of the part. The composite parts processing consists of several stages and each stage can offer its own unique data. In the hot melt impregnation, the temperature in the various parts of the system is important for proper impregnation [106] [94]. Additionally, flow sensors and pressure sensors in the system can detect the health of the overall procedure [106] [94]. Finally, the force on the fibres could be measured, as often high forces can occur that damage the fibres [106] [94]. In the aqueous suspension solution method, the cooling temperature and time cycle, and the exact molecular composition of the solution are important factors that can be measured to fully understand the process [107]. Moreover, post-consolidation analysis should be conducted to make sure that there is no solvent (water) remaining at the end of the process [107]. During the lay-up, the speed, material flow through the delivery head and the temperature of the material can be measured, especially if the consolidation process is combined with the lay-up. What is more, one of the most time-consuming tasks after automated lay-up is done is a necessary manual inspection of the parts. Thermal cameras may be used in the process to monitor it and machine vision defect detection can be successfully applied to speed up the process [108]. If the consolidation is conducted separately to lay-up, the temperature in the oven (or autoclave) should be measured at various places of the part - with thermal cameras for instance to ensure no hot spots are created in the cooling process. In case pultrusion is chosen for stringers, the temperature of the process and the pulling force could be measured together with strains in the part [101]. Finally, in the assembly process, crack sensors such as PZT together with stress and strain sensors could be used to identify potential defects in riveting and bolting [109]. In welding, the temperature of the process, speed, current, voltage and weld groove can be measured to find any possible anomalies [110].

The data-driven in manufacturing does not have to be limited to specific parts only. Data can also be gathered on the entire line of assembly for instance to identify bottlenecks and improve the organisation's work. Easy access to people responsible for specific parts can make it easier to brainstorm solutions in case of part failure [86]. ElectriFly can in the future make augmented data flow and gathering one of the manufacturer's company selection criteria.

In addition to data-driven manufacturing, artificial intelligence (AI) and machine learning algorithms should be used to support modern manufacturing processes. AI can be used for manufacturing process monitoring for instabilities and further decision-making based on real-time data processing which decreases the overall reaction time needed in case of anomaly detection [86]. Examples from composite manufacturing are, for instance, finding lay-up defects [104] or optimizing fibre placement strategies [111]. The AI models can also predict the mechanical properties of parts as manufactured and not as designed which gives more insight into further part functioning [112]. To be able to achieve that, the system containing models must be able to simultaneously read multiple inputs and feed them to a pre-trained AI model. Then, predictions must be made on the outcome of the process and recommended courses of action should be presented by the model [86].

Another way in which artificial intelligence can contribute to manufacturing is by optimising the existing processes [113]. It can contribute to an improved production line by applying machine learning to optimise the overall logistics, inventory levels and workflow architecture of the various production phases. This can also ensure a significant reduction in costs and increase the overall efficiency of the production process [114].

Thermoplastics in Contemporary Aircraft

The use of thermoplastic polymer resins in high-performance applications is not widespread yet. However, pilot programs are currently being conducted such as STUNNING where the entire fuselage is built from thermoplastic and synthetic fibre prepreg using automated lay-up and composite welding [92]. Even though no large structural parts are yet made of reinforced PEEK, several smaller components made of this material are already present in aircraft [8]. With the need for more sustainable composite solutions and increasing interest in high-performing thermoplastic composites, it may be expected that the use of new materials such as carbon fibre-reinforced PEEK will become prevalent

[8] https://www.ptonline.com/articles/victrexs-40-carbon-fiber-reinforced-peek-results-in-a-40-savings-in-both-weight-and-production-costs-over-the-incumbent-aluminum-part [Accessed on 15.06.2023]

also in the aviation industry by 2035.

Battery Manufacturing

Battery manufacturing is typically not done by aircraft manufacturers and instead, batteries are bought as an off-the-shelf product. Since the battery is a crucial part of ElectriFly, the company has to be aware of the current state of the art of manufacturing of those and potential issues, costs and environmental problems related to that. Therefore, a brief overview of production methods for the solid-state battery used in ElectriFly is presented in the report.

Currently, there are no mass-scale industrial methods for this new battery type [115]. Some variations of possible processes are discussed based on the current lithium-ion battery manufacturing and focusing on the main differences between those [3]. Generally, the production process consists of cathode, anode and solid-state electrolyte (SSE) production, battery assembly and packaging.

Battery cathodes can be produced by either wet methods or dry processing. The former involves creating a slurry solution of a solvent, binder and cathode active material [3]. For the solid-state batteries, SSE also has to be added to the slurry which greatly limits the possibilities of choice of the solvent and binder due to the high reactivity of sulfides used for ElectriFly [3]. Typically a non-polar organic solvent must be used for this SSE type. The slurry is then cast on a collector and the solvent is evaporated. As the solvents are often expensive and harmful to the environment, they also have to be carefully collected after separation and reused [3]. After cathode densification, it is subjected to calendering which smoothens and compresses the material by passing a continuous sheet through heated rolls. The dry methods are based on the extrusion of a mixture of the cathode active material, solid electrolyte and conductive agent followed by calendering [3]. It is not yet clear how to combine the solid electrolytes into the mixture and, hence, the more mature wet method should most likely be used in the near future for ElectriFly battery mass production.

As the battery anode, ElectriFly uses lithium metal for which the exact manufacturing processes have not yet been developed despite intense ongoing research. The most mature process at the current stage of development is the dry extrusion of thin lithium foils followed by calendering and lamination [3]. The foils can be laminated on both a collector and the solid electrolyte itself. Since the process uses lithium metal it must be conducted in a dry, inert atmosphere to avoid potential reactions with nitrogen, oxygen and other air components [3]. Another possibility is melt processing in which lithium is liquefied and deposited onto a non-porous collector or electrolyte or, alternatively, infiltrated into a porous electrolyte or anode [3]. Similarly to extrusion - special conditions such as an inert atmosphere must be used due to the presence of highly reactive liquid lithium. The main advantage of this process over extrusion is the significantly lower thickness of the foils that can be achieved [3]. The maturity of melt processing is low, but by 2035 it may offer a promising manufacturing technology for ElectriFly batteries. Another promising process with low maturity is in-situ plating in which the lithium ions from the cathode are plated onto the anode current collector [3]. It has an advantage over the two former processes as no special conditions need to be applied - the lithium metal is not handled in its pure form. If this process is further research for large batteries it may also offer a possibility for ElectriFly manufacturing in the future.

The last part of the battery that has to be manufactured is the solid electrolyte. ElectriFly is going to use sulfur-based SSE. For this type of electrolyte wet production methods must be used. In this process, a slurry is created from organic solvents, binders and the electrolyte substance [3]. The solution can be integrated into the cell by applying it directly on the cathode or making it separate and stacking it with the electrodes afterwards. Then, the solvent must be evaporated and after that compaction with pressure or temperature must be done. Other techniques are used for other SSE types - powder-based processing for ceramic electrolytes and solvent-free methods such as extrusion for polymers are being developed [3].

After all battery components are manufactured, the cell has to be assembled. First, the elementary stacks are cut into pieces and restacked into cell stacks. Then, the cell stack is pressed together and heated creating the cell [3]. The last step consists of welding the current collectors to the contact tabs and packing the cells into cell housing.

15.2. Digital Twin

Digital twins have become a trending topic of discussion inside the aerospace industry. It has several use cases, however the focus of this digital twin will be on making the maintenance process leaner by reducing the time to correct action. The immersive digital twin whose set up will be discussed here, will be on its use during the operational life of ElectriFly. Not only will the digital twin be used for predictive maintenance, but also to isolate large fleet based issues and to give the pilots further insight into the aircraft. First, its functional requirements shall be set up, after which appropriate sensor and ground integration can be set up.

15.2.1. Functions of the digital twin

For the scope of this project, it is useful to discuss what purpose the immersive digital twin shall serve in the operational life of the aircraft. Therefore, below is the list of these functions that shall be integrated into the aircraft:

- FUNC-DT-01: The digital twin shall assess the overall health of the aircraft at any given time.
- FUNC-DT-02: The digital twin shall detect any issues, assess their severity, detect the cause and give a plan of action to resolve them.
- FUNC-DT-03: The digital twin shall predict the occurrence of any potential issues through analysis of the probability of occurrence.
- FUNC-DT-04: The digital twin shall give a plan of action for preventative maintenance.
- FUNC-DT-05: The digital twin shall calculate the expected lifespan of the aircraft, given its history and planned maintenance.
- FUNC-DT-06: The digital twin shall use sensors to capture data and send analysed data feeds to the maintenance hub, to minimise downtime.

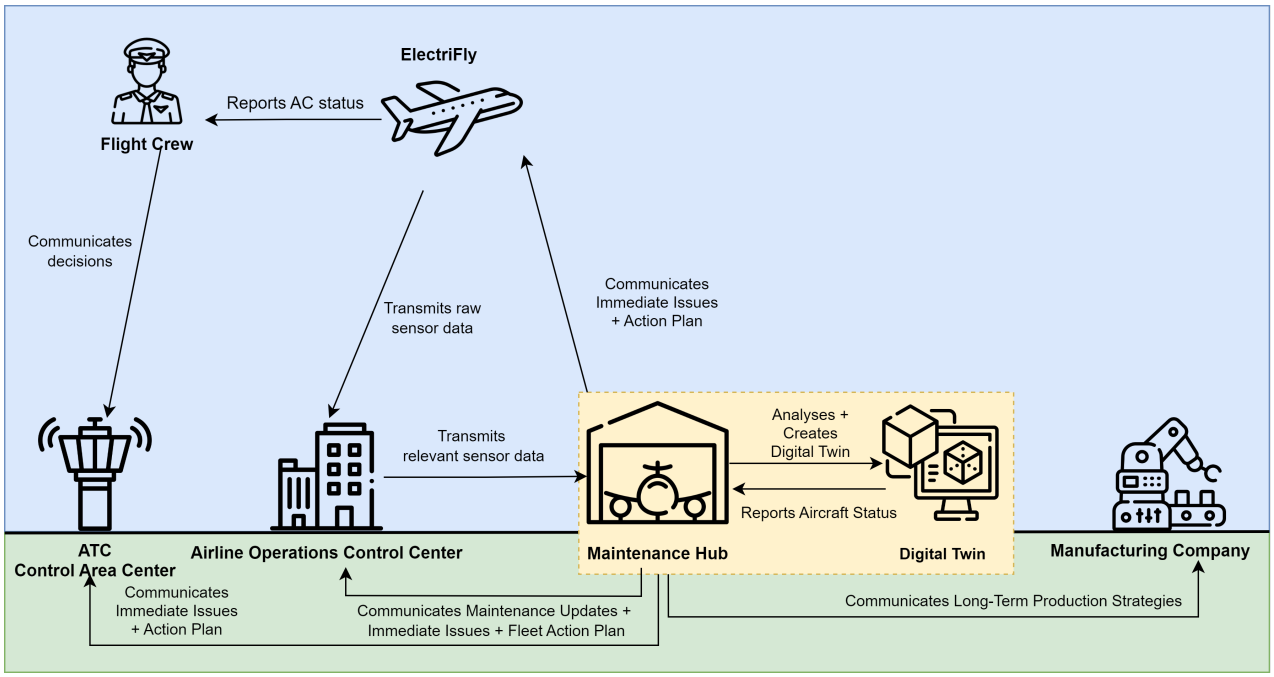

Figure 15.2: *Aircraft Digital Twin*

The health of the aircraft can be defined by assessing the structural health and integrity of the aircraft components [86]. Any issues occurring on the aircraft can be detected live through the use of sensors. These sensors should detect several indicators such as stresses, strains, motion sensors such as rotations per minute, etc... These sensors can then relay data to the onboard aircraft computer that analyzes if it is powerful enough, or send the data directly to the airline company as shown in Figure 15.2. This airline company can choose which data they want to make accessible to the maintenance hub, and then send this raw data to them instantly. The measured indicators shall help the maintenance hub in performing analysis to estimate the structural health of the components, detect the severity of issues, and calculate the probability of failure occurrence as well as the expected lifespan of the aircraft. This analysis, in the form of graphs, pie charts, as well as values can be used to create the digital twin. AI can be used to conduct this analysis in real-time, as well as to come up with an action plan to resolve any issues. This is the primary purpose of the digital twin since it can create these action plans, which can be sent to the airline company and ATC towers. These ATC towers can then send these action plans to the aircraft itself, in case of immediate action. This describes the set-up of the digital twin generally, however, a more detailed analysis of the set-up shall be made to implement it in practice.

15.2.2. Integration of the digital twin system

To satisfy the 6 functions of the digital twin, the crucial components of the digital twin are the sensors that measure data in real-time. It is important to first understand the types of sensors that exist on the aircraft, without the concept of digital twin. On general aviation aircraft, the common types of sensors are pressure sensors, force sensors, position sensors, temperature sensors and vibration sensors. Some of which, can be seen in Figure 15.3 that displays it for business jet aircraft. Even though ElectriFly is a propeller aircraft, most of these jet aircraft sensors are relevant. The

[9] https://www.ameteksfms.com/markets/business-regional-jets [Accessed on 16.06.2023]

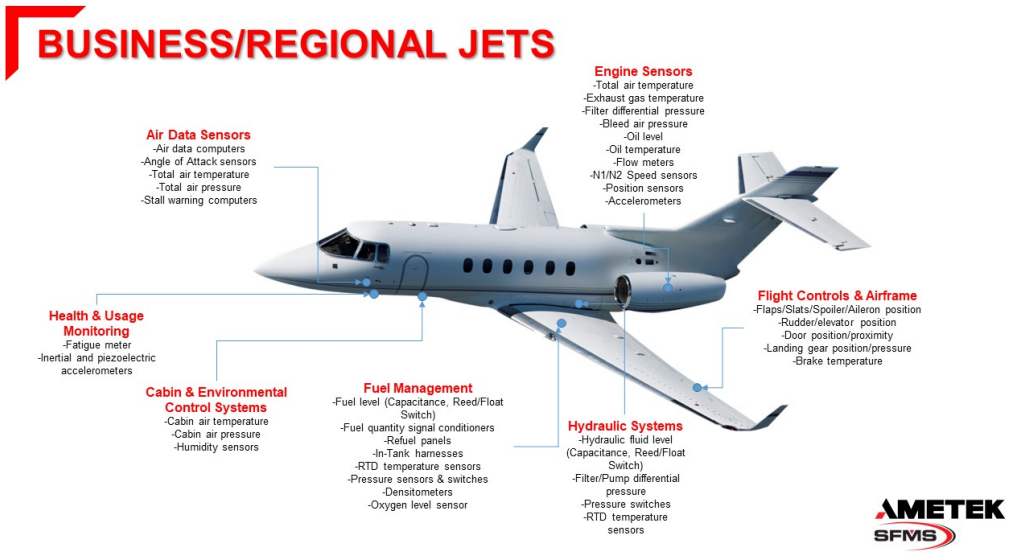

Figure 15.3: *Distribution of sensors on a general business jet aircraft* [9]

followings are the main functions of these sensors and the places they will be useful in:

1. Pressure sensors: These are used to measure pressure in hydraulic systems, this can be useful in determining if a hydraulic component failed [116]. They are also used to measure cabin air pressure if it is pressurised (applicable to ElectriFly), which is important for the safety of passengers in case of leaks. ElectriFly will require around 50 of these pressure sensors, that do the same functions as they would for a normal aircraft without a digital twin.

2. Force sensors: These are primarily used in finding the force and torque in flight controls, actuation and braking systems [116]. This is useful in detecting the responsiveness of the controls concerning pilot inputs. Around 30 of these sensors should suffice.

3. Position sensors: These are linear position sensors that detect the motion of movable parts such as the landing gears [116]. They provide this feedback to the pilot who judges whether the part has deployed correctly. Around 20 position sensors shall suffice for the aforementioned functions.

4. Temperature sensors: These measure the temperatures of the free-stream air, internal cabin, and braking system and shall be used to measure it for the battery, which is quite relevant for ElectriFly [116]. The battery temperature needs to be regulated continuously throughout the flight, otherwise, the battery will overheat and not provide the energy required. Therefore these battery temperature sensors are essential for ElectriFly. For fuel-based aircraft, they are also used to measure the temperatures in the engine due to combustion, however, that is not relevant for an all-electric, emission-free aircraft. Since in Chapter 6 it was decided to have 4 batteries, each with 36 modules, it would be important to regulate and monitor the temperature of each of these modules. Due to this, the battery system needs 144 thermal sensors. Additionally, the rest of the aircraft needs about 16 additional thermal sensors, for cabin and engine temperature. The AS-TE temperature sensor can be chosen, with each sensor on average weighing 46g, the weight due to thermal sensors is just under 7.5kg [10].

5. Vibration sensors: These act like accelerometers which measure the vibrations and flutter of aircraft surfaces such as the horizontal tail [117]. This information is typically used by the flutter dampers that try to minimize this vibration frequency, to prevent resonance which is a severe risk. Around 10 of these sensors shall suffice, since these vibrations only need to be detected for the wing and tail control surfaces.

In addition to these commonly used sensors for aircraft, some additional sensor types are of interest for the digital twin interface. These are stress sensors or strain gauges, that can be used to measure the shear and normal stresses. This will directly be able to calculate the structural health and integrity of the main external components under stress.

6. Optical fibre strain sensors: These measure the strain on the part of the aircraft where they are placed. This is the most important type of sensor for the implementation of the digital twin. Traditionally, strain gauges were used, which are singular sensors to be placed on the surface of aircraft. There exist biaxial strain gauges that calculate the strains

[10] https://www.fluidcomponents.com/aerospace/aerospace-products/temperature-sensors/as-te-temperature-sensor [Accessed on 16.06.2023]

in two perpendicular directions, which is useful in determining the stresses in 2 directions [11]. However, this is the old method that requires a lot of individual parts, meaning added complexity and weight. Instead, in the current state-of-art, optical fibre wired strain sensors can be used [118]. These give measurements at thousands of points, giving more accurate strain data for the entire structure. It is essentially a wire, that can be placed outside or inside the surface of aircraft, that detects changes in light transmission when the attached object experiences a load [12]. These optical fibre strain sensors measure strain in a single direction, however, the wire can be looped smartly to measure data in two directions in the plane. Additionally, there has been development in optical fibre sensors that can measure strain in their transverse direction as well. As a result, these will completely outmatch the traditional strain gauges [119]. Therefore, upon time of implementation, this newer technology can also be used to attain its benefits.

A small calculation of the set-up can still be made if the fibre wires are placed as seen in Figure 15.5. A more zoomed-in image can be seen in Figure 15.4 which shows the way the rings will be created on the leading edge of the wing, taken from an unpublished TU Delft paper from 2nd-year aerospace project [120]. If the optical fibre strain sensor SMW-01 is considered, it has a density of 1.65 g/m [13]. For the fuselage, if a spacing of 2.5m is kept along the length, 5 rings can be made, giving an estimated fibre wire length of 50m. With a similar method and determining arbitrary spacing, since the spacing is inversely proportionate to the accuracy of data, the wing needs a conservative fibre wire length of 120m with ring spacing of 1m (20 rings) and taking the perimeter of the airfoil at root chord (5m taken from 3D model Chapter 14) assumed to be a constant for all 20 rings. Lastly for the empennage, with a ring spacing of 1m, it requires 5 rings for the horizontal tail and 3 for the vertical tail. While using a ring perimeter of 3.3 m and 5.5 m for horizontal vertical tail respectively, it gives an empennage fibre wire length of 41 m. With this information, and the mass density found before, the estimated total weight of the optical fibre strain sensors is 0.35 kg. In comparison, if traditional strain gauges will be used, they will weigh around 8kg, which is 23 times more heavy [121].

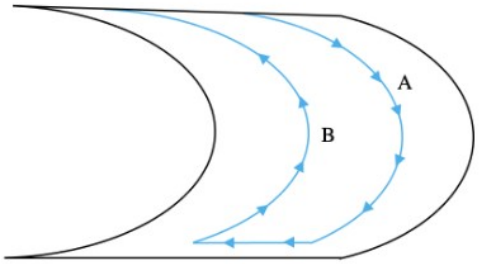

Figure 15.4: *Sensors on the leading edge of a wing [120]*

7. Damage detection sensors: This is another sensor type useful in structural health monitoring, namely the Embedded PZT sensors. These sensors use lamb waves, which is a non-destructive test, to detect damages and cracks on a structure [122]. Their primary use is in composite structures, which is useful since a significant portion of our aircraft is composite. However, due to their versatility, it is assumed that they can also be used to detect cracks on aluminium surfaces. Since these are individual components, unlike the optical fibre strain sensor, they should be placed where essential. Therefore, to minimize complexity and weight, it has been decided to place these sensors on structurally significant items (SSI), which are components whose structural failure could affect the structural integrity required for the safety of the aircraft and its passengers [123]. Most importantly, these sensors can be placed in the propeller hub of each of the 14 engines, on the 14 motors connected to these engines, as well as on all the control surfaces and their hinges since they can have micro-cracks and go through fatigue failure. Due to this, an estimated 60 of these embedded PZT sensors shall be placed on the aircraft as seen in Figure 15.5.

15.2.3. Digital Twin Analysis

The digital twin that will be created by the maintenance hub shall give enough insight to perform all the functional requirements listed above. A method to meet each of the 6 functions can be briefly discussed in this part.

Structural health: The digital twin can estimate the overall structural health of the aircraft, by using the data acquired from the optical fibre strain sensors. This strain data can be distinguished in two directions, after which the normal and shear stresses can be calculated. If these stresses are close to the stresses required for any of the failure modes such as buckling, yielding, cracking and so on, then this can be raised as an issue. However since stresses don't tell the full story, micro-cracks can be detected, at least for the safety-critical components, with the help of the embedded PZT sensors. Detection of crack-propagation of a safety critical part on the aircraft in real-time is extremely useful to perform an emergency landing, and replacing this part before it has a chance to cause a potentially risky scenario.

Detect issues: The digital twin can certainly use its surface sensors to detect any structural issues. In addition, it can also detect thermal issues of the battery with temperature sensors, as well as the common issues of aircraft with the help of the commonly used aircraft sensors as described before. With these sensors, it can also detect the cause, and then artificial intelligence can be fed training data and used to construct an action plan to resolve issues.

[11] http://www.instrumentationtoday.com/strain-gauge/2011/08/ [Accessed on 16.06.2023]
[12] https://tacunasystems.com/knowledge-base/how-does-an-optical-strain-gauge-work/ [Accessed on 18.06.2023]
[13] https://fbgs.com/components/strain-sensor-smw-01/ [Accessed on 18.06.2023]

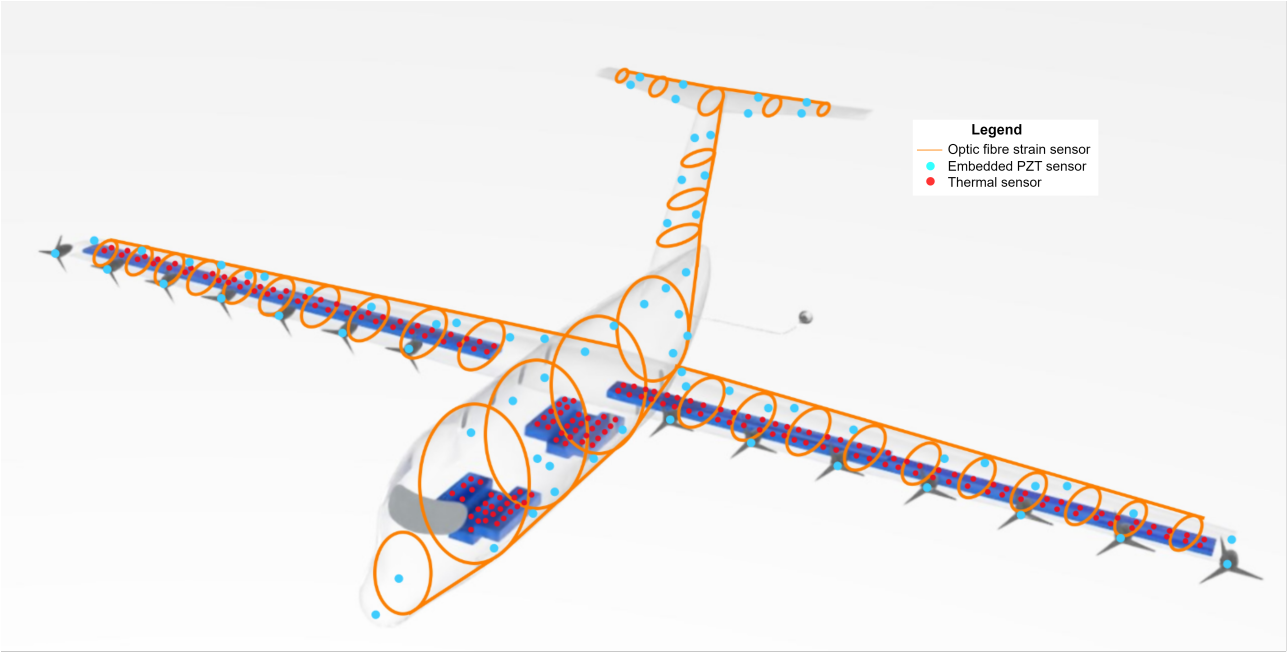

Figure 15.5: *To show sensors on the aircraft*

Occurrence of potential issues: This is where the digital twin can use the digital thread database to predict trends and patterns that can lead to a hazard. Using time-based trends, the digital twin can calculate the probability of occurrence as a function of time. This way, it can predict which issues can occur and when.

Preventative maintenance: Related to estimating the occurrence of potential issues, if the digital twin knows when which issues can occur, using artificial intelligence and training data, it can once again give an action plan to prevent this from happening. This preventative maintenance plan can be then communicated to the airline company, manufacturer, and directly to the flight crew in case immediate action is required.

Expected lifespan: Whilst the digital twin assesses the structural health of the aircraft after every flight, this percentage shall deteriorate as the number of cycles increases. If a structural health percentage is set, below which the aircraft should no longer be operated, then using trends of deterioration and maintenance, the lifespan can be calculated.

Data extraction: The digital twin has a large number of sensors from which it gathers a large amount of raw data. Apart from the digital twin-specific sensors as seen in Figure 15.5, several other types of data recorded by the traditional aircraft sensors are used in the digital twin. This other data entails information such as weather in flights, distance flown and flight paths. Out of this raw data, the digital twin needs to wisely select data that is the most critical and useful, perform analysis with this data, and store the high-level results in the database that's used to build up the model. Notably, the sensors onboard will collect raw data and send it to the flight management system computer, which will transmit this unrefined raw data to the ground as shown in Figure 15.2. In case any of the sensors fail, this can be easily detected if a specific sensor is giving drastically different information relative to nearby sensors, as well as if a specific sensor is giving no information. This can be detected by the maintenance hub, and a stock of sensors can be kept at airports where these can be replaced straight after detection.

15.2.4. Digital Twin Applications

Now that the set-up of the digital twin system has been analysed and discussed, it is useful to mention the primary use cases. Firstly, As discussed before, predictive maintenance is one of the main functions of the digital twin and is therefore its primary application. It is found that oftentimes, the number of times maintenance is done and the types of maintenance performed are excessive. This is mainly due to the lack of knowledge the maintenance hub has about what the root of the issue actually is. Digital twin's predictive maintenance aims to fill this knowledge gap by making the maintenance process leaner, which maximizes operation time and minimizes downtime. To elaborate, a specific example scenario can be described in detail. Let's say a group of battery cells in a module start to overheat, as detected by the thermal sensors. If the module starts to overheat and exceed the operational temperature range, then the capacity of the battery decreases, decreasing the energy stored in the battery. Due to all 36 modules in a battery connected in series, this single module overheating can cause all 36 modules to overheat, and decrease the capacity and energy of the entire battery. This could become a catastrophic failure since it decreases the range of the aircraft, as

a quarter of the energy could be lost. This can be prevented with the use of thermal control that uses thermal sensors to monitor each module's temperature and use the water coolant to decrease the temperature of this specific module. The edge devices on board can conduct this process, and solve this issue on board the aircraft. However, when the aircraft lands, the maintenance hub can investigate with the help of the digital twin, which modules in the battery overheated, and more specifically, which area of cells overheated. Instead of replacing a whole battery, the root module can be found with the help of the thermal sensors that detect an initial spike in the region, and this module can then be replaced. This not only saves cost but also saves time in trying to test which module started the issue. In turn, this minimizes downtime, and the airline can use the aircraft for a larger operational life.

Secondly, the digital twin has the capability to isolate the problem for certain aircraft by using the digital thread database, instead of grounding the entire fleet which would excessively increase the downtime. This is similar to the previous point, in terms of making the maintenance process leaner. Lastly, a new emergent application of the digital twin can be to give the pilots further insight into the aircraft and its issues, in case of emergencies or critical scenarios. This would require the flight crew to receive digital twin data from the maintenance hub directly, helping them to identify any structural failures and conduct a safer landing. These are two additional use cases which show the added value of the digital twin and can be elaborated on in a further detailed analysis.

16. Risk Management

In the systems engineering universe, risk can cause potential problems related to technical performance, cost and schedule. These risks should be accounted for in order to ensure successful project completion. Firstly, a risk management program plan is set up in Section 16.1. Then, the technical risks are identified and mitigated in Section 16.2. Then, the reliability, availability, maintenance and safety (RAMS) are examined in Section 16.4.

16.1. Risk Management

This section will address technical risk management with respect to the design, production and operation of the aircraft in general. Firstly, all risks that could potentially harm the project/system risks are identified. These identified risks are then qualitatively assessed on their probability and consequence metrics, as stated in Figure 17.1. Next, an analysis by means of a risk map is performed to identify all unacceptable risks. Lastly, these unacceptable risks are mitigated by reducing the probability and/or consequence. Other operational risks, like passenger/pilot causes, are not incorporated here, as it is the responsibility of the (airline) operator to assess these risks.

Figure 16.1: *Qualitative metrics for risk assessment*

Probability metrics		**Consequence metrics**	
Very low	PR < 1%	Catastrophic	Project failure Large underperformance
Low	1% <= PR < 30%	Critical	Questionable project success Medium underperformance
Moderate	30% <= PR < 50%	Considerable	Noticeable impact on project success Small underperformance
High	50% <= PR < 70%	Marginal	Degradation of sub-projects Slight underperformance
Very high	PR >= 70%	Negligible	Inconvenience Minor performance impact

16.2. Technical Risk Identification & Assessment

Through a technical SWOT analysis for an electric aircraft, an evaluation of the system flowchart and an evaluation of all subsystems, all areas of possible risks were identified. All technical risks and their assessment are summed up in Table 16.1. It states their identifier, description and impact, complemented by their probability and consequence assessment. The risk identifiers are coloured according to their probability and impact as in the risk map, which will be described in Subsection 16.2.2.

Table 16.1: *Risk table*

Risks	Description	Probability	Impact	Consequence
		Recharging		
R-01	**Drone impact damage**	**Low**	**During the charging process, the drone and plane collide**	**Catastrophic**
R-02	**Drone operational malfunction , (fail to connect or solenoids fail to lock)**	**Low**	**Aircraft does not attain recharging, damages other parts**	**Considerable**
R-03	**Drone operational malfunction, (fail to disconnect or solenoids fail to unlock)**	**Low**	**Loss of control, can cause stability issues for drone or aircraft higher risk of collision, part separation**	**Critical**
R-04	**Drone logistics malfunction (drone is too late, or communication with the drone is interfered)**	**Moderate**	**Aircraft does not attain all recharging**	**Considerable**
R-05	**Drone charging system malfuncion (overcharging, slow charging, short circuit)**	**Low**	**Both aircraft and drone battery system get damaged, cable catches fire**	**Critical**
R-06	**Discharge effect through drogue shute system**	**Moderate**	**All electric systems damaged by electric loads**	**Considerable**
R-07	**Tension/Compression forces exceeded**	**Moderate**	**External forces on the aircraft affect stability**	**Considerable**
		Structures		
S-01	Loads on critical components turn out higher than designed for	Very low	Yielding/failureof components/structures	Critical
S-02	Mechanical failure of materials due yielding or breaking	Very low	Failure of components/structures	Critical
S-03	**Fatigue in material/structure**	**Low**	**Cracks in material/structures lower its properties, causing possible faillures**	**Critical**
S-04	Material/structures heating due batteries	Very low	Lowering in properties, possible failure	Critical
S-05	Fuselage is perfurated by an object	Very low	Loss of pressurisation	Critical
S-06	Failure/deformation of structure causing battery damage	Very low	Battery damage, fire, loss of power supply	Critical
S-07	Bonding between different material types fails	Very low	Failure of components/structures	Critical

		Propulsion		
P-01	Propulsion System catches fire, (due cooling system fail)	Very low	The engine must be turned off and the aircraft loses power	Critical
P-02	Blade failure	Very low	Propeller blade deforms or breaks off, possible perforation of fuselage	Critical
P-03	**Single engine failure, (due to its subsystems failing)**	**Low**	**Loss of thrust from engine, lateral stability problems**	**Marginal**
P-04	**Multiple engine failure**	**Very low**	**Loss of thrust on one engine side, lateral stability problems**	**Considerable**
P-05	Engine operating inefficient, (due subsystem failure, like failure or lubrication)	Moderate	Leakage of oil in engine system, possible inefficiency/failure of engine	Marginal
P-06	Propulsion entangling the flow over control surfaces	Low	Unexpected interaction of propeller wake to control surfaces	Marginal
		Battery		
B-01	**Charging malfunction or unavailable**	**Moderate**	**Batteries not fully charged, possible flight diversion**	**Marginal**
B-02	**Operational temperature exceeded (due cooling system failure)**	**Low**	**Overheating, fire, no energy provided**	**Critical**
B-03	**Batteries do not deliver expected power**	**Moderate**	**Not enough thrust is provided, possible flight diversion**	**Marginal**
B-04	**Overcharging**	**Low**	**Damage and overheating, loss of battery performance**	**Critical**
B-05	**Short-circuit/thermal runaway, due dendrite formation of the solid lithium**	**Low**	**Direct current path occurs that ensures rapid discharge, possibly explosion**	**Critical**
B-06	**Chemical contraction/expansion causing cracks**	**Low**		**Critical**
B-07	**Toxic gas release H2S**	**Low**	**Sulfide in contact with water releases toxic gas**	**Critical**
		Design		
D-01	Incorrect assumptions made	Moderate	Incorrect assumptions require re-design	Considerable
D-02	Infeasible design	Low	Design turns out infeasible for requirements/mission	Considerable
D-03	Certifications/regulations change	Low	Design does not comply with new regulations for electric a/c	Considerable
D-04	Wrong estimations in conceptual design	Low	Wrong estimations in aerodynamics, performance, structural, stability, sustainability etc...	Considerable
D-05	Verification & Validation insufficient	Low	Delay in production	Considerable
		Avionics		
I-01	Communication system failure	Low	Critical information from ATC is not received	Marginal
I-02	Navigation system failure	Very low	Aircraft is unable te determine its position	Marginal
I-03	Cockpit display failure	Very low	The pilot is unable to receive vital flight data	Marginal
I-04	Software/coding Bugs	Moderate	The Software doesn't work as it is supposed to	Marginal
I-05	Radar System Failure	Very low	The Aircraft can colide with external obstacles	Marginal
I-06	Instrumentation errors	Low	The Aircraft gives incorrect readings for important parameters	Considerable
		Control		
C-01	Control surface stuck at certain deflection angle	Very low	Aircraft has to rely on other control surfaces for maneuvres	Critical
C-02	Control surface detaches from aircraft structure	Very low	Aircraft has to rely on other control surfaces for maneuvres, control surface may harm the environment	Catastrophical
C-03	Control surface reacts unexpectedly to inputs (too sensitive, too spongy, too heavy)	Moderate	Aircraft becomes harder to operate and may violate certification criteria	Marginal
C-04	HLDs do not extend when required	Very Low	Extensive downward acceleration causes potentialy dangerous landing	Considerable
C-05	Eigenmotion damping mechanisms perform worse than anticipated	Moderate	Higher g-forces may occur during flight	Marginal
C-06	Payload shift causing control issue's	Low	Payload shifting can cause changes in center of gravity, affecting the control & stability of the aircraft	Considerable
C-07	Landing gear flat tire or not deploying	Low		Considerable
C-08	Brake failure	Low	High reverse thrust required, landing distance increased, possible runway excursion	Marginal
		Aerodynamics		
A-01	Stall occurs at Lower AoA than expected	Very low	Pilot recovers	Considerable
A-02	Aerodynamic moment is higher than expected	Very low	Extra counteraction required during flight	Marginal
A-03	Aircraft is unexpectedly unstable at certain trim condition	Moderate	Aircraft becomes increasingly harder to operate at certain trim condition	Marginal
A-04	Drag is higher than anticipated	Low	Fuel performance will be decreased	Considerable
		External		
E-01	Bad weather conditions (icing, winds, visiblit)	Moderate	Disturbed or postponed flight, turbulence that may shift battery	Marginal
E-02	Bird strike	Low	Damage to aircraft surface	Marginal
E-03	Lightning Strike	Low	Damage to aircraft electrical components and surface	Considerable
E-04	Mid air collision	Very low	Severe damage or total destruction	Catastrophic

16.2.1. Technical Risk Analysis

The magnitude of a risk is defined as the product of its probability and consequence. This can be analysed by means of a risk map/matrix as shown in Figure 16.2, where the horizontal and vertical axis correspond to consequence and probability respectively. This allows for classifying risks on a map from negligible in the lower left corner, to unacceptable risks in the upper right corner. The legend also indicates what colours correspond to what degree of risk magnitude.

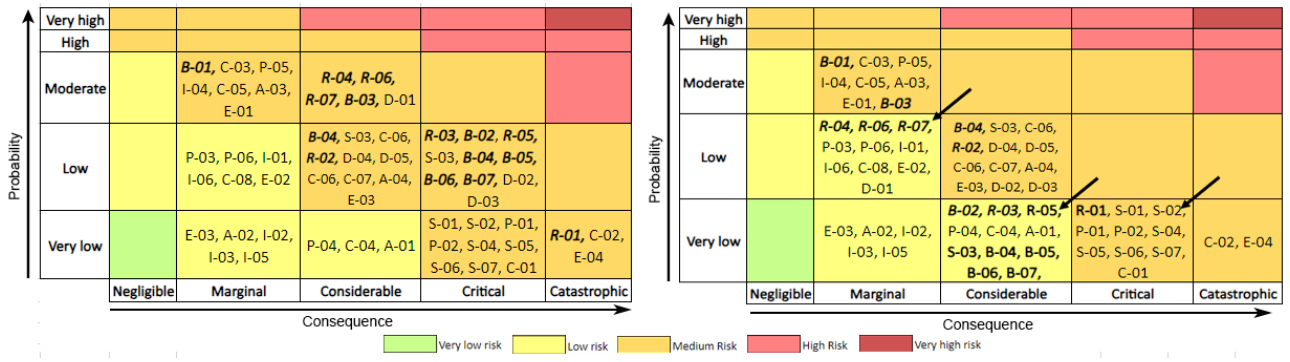

Figure 16.2: *Risk map before and after mitigations*

16.2.2. Technical Risk Mitigation

All unacceptable risks identified by the risk maps are listed below. Some mitigation strategies include removing, reducing, accepting and transferring. However, in reality, risk mitigation is a combination of all strategies [79]. When a risk would still cause a problematic event despite effective mitigation strategies, a contingency management plan should be constructed to handle the impacted circumstances.

- **R-01: Drone impact.**
  A collision is a catastrophic event with moderate risk. It can be mitigated in the following ways: careful approach procedures and a limited closing rate of $3 m/s$. If the recharging drone comes in too close vicinity of the ElectriFly, a warning will be given in the cockpit and the recharging is (temporarily) aborted. The vicinity is measured by a GPS coordinated flight system and the elongation/shortening of the cable. Further elaboration is described in Chapter 7.
  Contingency plan: In case an impact between the ElectriFly and the recharging drone still occurs, damage should be assessed via the digital twin sensors. This will assess whether the aircraft is still safe to continue the flight and/or try another recharging procedure. Afterwards, a thorough investigation and possible extra pilot training are required.
- **R-05: Drone charging system malfunction**
  Such as overcharging or short circuits. The short circuit between two flying bodies is critical for both flying bodies. This can be prevented by designing an integrated BMS (battery management system) which can detect and prevent any surcharge, and trigger disconnect in case it detects any malfunction in the electrical system of either aircraft so that the risk is not transferred from the faulty body to the other body.
  Contingency Plan: In case of this, the charging should be immediately disconnected, and an emergency landing should be performed in order to assess the damage by both the aircraft and the drone.
- **R-06: Discharge effect**
  Due to the difference in potential between the drone and the aircraft, a discharge can occur when contacting via the drogue-probe system. To prevent the discharge from damaging the aircraft's electronic components, the CPU will be equipped with discharge wiring, see Chapter 7.
  Contingency: In case a discharge still occurs, damaged electrical components should be checked and backup systems activated.
- **R-07: Tension/compression force exceeded.**
  The movement of the drone and aircraft with respect to each other can cause tension or compression forces through the cable, affecting stability. This is mitigated by a damping system and a release mechanism of the solenoid locking system, which will break the connection at a specific force. Additionally, the probe of the recharging drone has the break/weak point of the complete system, as described in Chapter 7. **Contingency plan:** Emergency decouple.
- **R-4: Operational malfuction**
  Operational malfunction of the recharging drone consists of any problems with the recharging drone logistics, such as the recharging drone arriving too late, the communication system failing or the drone failing to connect. Consequently, Electrifly does not attain the required recharging energy for the mission. This is mitigated by extensive pre-flight planning of the route and recharging point. Live updates on flight schedules and progress, like delays and current position, will optimise the deployment of the recharging drones.
  Contingency Plan: In case of a failing recharging operation, the flight will have to be diverted.
- **B-02: Operational Temp**
  The operational temperature of the solid-state batteries should stay within a range of 0 - 27 $°C$. Especially during fast charging in flight or on the ground, heat build-up can be a problem. This can be mitigated by a water-cooling system as described in Section 13.6. Additionally, the digital twin, as described in Chapter 15, contains sensors to measure battery temperature. This allows the battery management system (BMS) to intervene by increasing cooling to lower the temperature to acceptable levels.
  Contingency plan: In case a battery pack overheats despite mitigation strategies, it will be shut off entirely by the BMS and assessed on damage by the digital twin sensors. In case this cannot be shut off, the casing is designed in a way that the damage will be limited to one battery only and will not affect the remaining ones. Flight operations continue with 3 out of the 4 battery packs remaining, only decreasing the capacity, with the possibility for diversion.
- **B-04: Overcharging**
  Exceeding the maximum charge percentage of 90% could harm the batteries. This will be mitigated as follows. Sensors as part of the digital twin that are incorporated in the battery and charging system can detect potential overcharging. Consequently, the battery management system (BMS) as described in Chapter 6 can intervene and stop the charging.
  Contingency plan: In case the BMS is not able to stop the charge flow, the pilot can manually disconnect the recharging cable. Damage will be assessed via digital twin sensors that can re-calculate the new expected battery life.

- **B-05:Short-circuit or thermal runaway due dendrite formation**.
  Solid-state batteries are typically safer than other battery types; however, they could still suffer from thermal runaway (e.g. short circuit). This occurs due to the formation of dendrites on the solid lithium anode. ([3]. This probability will be mitigated by the producer of the batteries by coating the anode with a polymer coating. Additionally, the design of the battery casing, as described in Subsection 6.4.2, will help protect the battery cells. Additionally, the battery management system (BMS) controls and monitors the battery's performance. It could detect and prevent short-circuit dangers by disconnecting specific battery cells and will add to the digital twin as described in Section 15.2.
  Contingency plan: In case a battery short circuit occurs, only one of the four battery packs will be affected. The remaining battery packs could still be used for the most important electronic systems and short periods of flight propulsion needed for diversion.
- **B-06: Chemical contraction/expansion**
  Due to the chemical process during the recharging and discharging of the batteries, the volume increases and decreases respectively[3]. However, this expansion is negligible, especially after mitigation: the battery casing as designed in Subsection 6.4.2 will prevent any expansion or contraction. Additionally, the battery management system, combined with the digital twin sensors, will detect excessive expansion and intervene.
  Contingency: In case excessive expansion/contraction cannot be avoided, the cell will likely crack. The casing is designed in a way that no toxic gas will leave the pack.
- **B-07: Toxic gas release**
  The solid-state batteries contain the chemical Sulfur (S); when this enters in contact with water it will release very toxic sulfuric acid (H_2S) [3]. This can be prevented by the battery management system in combination with the battery casing, which allows for air ventilation. The digital twin system will incorporate h2s detection sensors.
  Contingency plan: If the toxic gas H_2S is still released, an absorption system designed according to [124], which is installed in the cabin can be activated [124]. Additionally, the standard required overhead installed oxygen masks [1], can be modified to allow for H_2S protection. Or, all passenger seats can be equipped with industry-standard portable oxygen tanks acting as gas masks, as used by pilots in the present day.
- **S-03: Fatigue causing failure of the structure.**
  This phenomenon can occur everywhere in the entire aircraft structure and therefore it is of vital importance to minimise this as much as possible. The digital twin concept described in Section 15.2 can aid in the on-time detection of internal fatigue, reducing the probability of failure due to fatigue load and thereby preventing the critical impact.
  Contingency plan: If a structure does fail due to fatigue load, it must be figured out what factor caused the structure to fail, by use of the digital thread.
- **D-01: Design assumptions**
  Assumptions made during all design phases should be carefully considered. If they turn out invalid for specific cases, design estimations and calculations might become invalid. To mitigate this, every chapter in this conceptual design reports all assumptions made in a clear table.

16.3. Cost & Schedule Risk Management

Cost and schedule risks are those related to the financial resources available, and related to the design phase and delivery time. Both are listed in Table 16.2. These risks are then organised in a risk map, both before and after mitigations in Figure 16.3. The various mitigation strategies, applied to reduce the probability of occurrence and magnitude of the consequence of cost and schedule risks, are also listed below.

Table 16.2: *Risk table cost & schedule*

ID	Description	Probability	Impact	Consequence
		Costs		
CST-01	Increased costs due: inflation, forex, energy price, unforeseen, Material price, infrastructure price, 3rd party systems, labour, government	Moderate	Reduction of effective budget in general, Reduction of sales profit	Considerable
CST-02	Design changes impacting cost	Low	With progressing project phase, design changes will cost increasingly more	Marginal
CST-03	Cost estimation inaccuracy	Moderate	Unacceptable inaccuracy in cost estimation will require new estimation and budget allocation	Considerable
CST-04	Rebuilding due faillures in testing	Low	Unforeseen extra matrial and building costs are induced	Marginal
		Schedule		
SCH-01	Certification faillure or delays	Moderate	Delays in aircraft delivery, impacting schedule, possible design changes require	Critical
SCH-02	Supply chain delays: material/subsystem scarcity, transportation delays	Moderate	Delays in production, impacting schedule, possible new supplier or material required	Considerable
SCH-03	Production delays	Low	Delay in aircraft delivery	Considerable
SCH-04	Additional testing required	Low	Delay in readiness to fly	Considerable
SCH-05	Manufacturing flaws	Moderate	Improper use of machinery can require re-production of parts/structures, impacting schedule and cost	Considerable

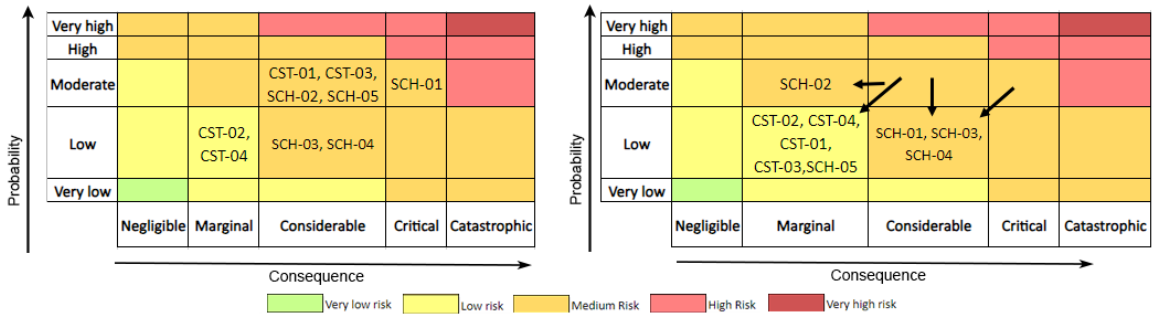

Figure 16.3: *Risk map cost & schedule*

- **CST-1 Cost increase due to forex, inflation, materials and production, etc.**
  Working in foreign markets comes with the risk of exchange fluctuations, causing the sales profit and effective budget to possibly be reduced. A way to mitigate the impact of this risk is to distribute the risk, cost and reduction in profit amongst the different parties and investors. The price of raw materials required for production can increase due market fluctuations. If the economic resources are spread between different entities it is easier to compensate for increases in cost as the impact is divided among them. Therefore sharing the economic load by means of investors and partners can reduce the impact. It is not possible to predict all scenarios therefore during a project's lifetime, there are circumstances that result in unforeseen costs. These costs are those that were not accounted for in the budget. In order to reduce the probability of this risk, a set budget for unforeseen costs should be established. This is a form of accepting the risk. In this way, there is money reserved for unexpected circumstances taken into account by the overall budget. However, this implies that there are fewer economic resources for the other domains.
- **CST-3 Cost estimation inaccuracies**
  Cost estimation is required to know the magnitude of the needed resources. If this is not performed correctly, there will be issues with budget allocation. It will be needed to reallocate the budget and perform a new estimation. In addition, it can result in a problematic scenario where the budget reallocation will result in major design compromises which is undesirable. This risk has to be reduced. For this purpose, it is important to use margins in cost estimation to reduce its probability of occurrence. In addition, the cost estimation should be extensively verified independently in the early stages of the project and consistently monitored so that any reallocation can be made early and therefore its impact mitigated.
- **SCH-01 Certification failure and delays**
  Aircraft certification is a lengthy process. If any of the requirements based on regulations are not met, this will result in certification failure. Modifications will then be needed to correct the problems seen in certification. This will delay the delivery of the aircraft to the market. The probability of this risk can be reduced by ensuring that the certification regulations are an integral part of the design, that is, that every member is consulting the regulations when making decisions and is aware of the different requirements. In addition, there should be an internal member responsible for making sure that the aircraft is meeting the certification requirements throughout the design and performing a preliminary check before the certification assessment of external entities. With the implementation of these measures, the impact of the risk is also reduced as corrections shall be then related to minor components which can be modified in a short time frame.
- **SCH-02 Supply chain delays: material scarcity**

When there are delays in the supply chain, the materials required for production will not arrive on time. This causes the production to be delayed or the need to find a new supplier depending on the magnitude of the delay. For mitigation purposes, the production schedule should account for possible delays in the supply chain and possible alternate suppliers should be defined beforehand. This reduces the probability of the risk. In addition, the supplier should be chosen carefully and their ability to meet the delivery times in the past should be inquired.
Some structures have to be supplied by external manufacturers. These will integrate the production at specific stages. If they do not arrive on time, the production will be delayed. This delay will affect the schedule as the different production tasks will have to be pushed forward. To reduce the probability of this risk, scheduling margins need to be applied. These margins will reduce the delay of consequent activities as there is an extra interval of time accounted for delays. In addition, it is important to work with high-performance companies that have a high reputation in terms of punctuality.

- **SCH-03 Production delays**
  Delays in production can occur and can increase the delivery time of the aircraft. To prevent them, it is important that the production schedule takes into account possible delays by applying margins. This reduces the probability of the risk. Moreover, it is important to have a highly qualified workforce with strict planning policies.
- **SCH-05 Manufacturing flaws**
  Manufacturing is a critical process. Mistakes in manufacturing will result in underperformance. Therefore, parts are checked for imperfections before and after delivery. If these have not been correctly produced due to improper use of machinery or faulty machinery, they have to be re-produced which will delay their availability and in consequence, the progress of other production activities. It is important to reduce the probability of occurrence by only working with certified manufacturers so that it is known that they have the appropriate training and facilities. Moreover, the impact is reduced by including a margin for the re-production of parts in the schedule.

A general contingency plan can be developed for all cost risks. The budget could be increased either by attracting more investments, creating partnerships with other companies or governmental agencies, or as last option loans. Secondly, the budget resources should be redivided if any of the cost risks causes problematic effects, as it would affect the total and all other cost budgets. In case scheduling risks cannot be avoided, the delivery time will have to be postponed. To protect the project from the consequences this brings such as fines and prosecutions, clauses related to delays caused by the scheduling risks need to be included in the contracts with the customers.

16.4. RAMS Characteristics

The reliability, availability, maintainability and safety (RAMS) characteristics describe ElectriFly's operational performance. These parameters are interrelated but will be separately discussed in the following subsections, where a focus is laid on the most unconventional aspects of the ElectriFly.

Reliability

A proper definition of reliability would be the probability that the system will function as anticipated without failure for a given duration and environment. Its most important parameter is the failure rate (λ), which relates to reliability (R) via $R(t) = e^{-\lambda t}$. The failure rate of a system experiences changes throughout the system's lifetime. Typically, the failure rate follows a 'bathtub curve', as displayed in Figure 16.4. During most of the operational lifetime, the failure rate assumes a constant nominal value, determined by the risk present in this stage. The failure rate is higher in the phases both before and after the useful-life phase, because of production process risks and degradation respectively. Failure rates can be minimized with adequate design methods before production starts. Such methods entail risk management, resource management, and verification and validation.

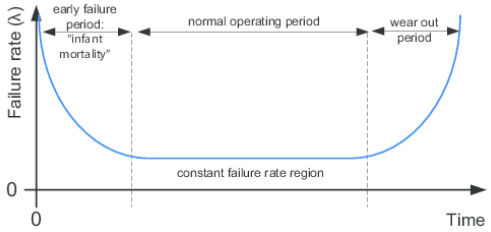

Figure 16.4: *Typical failure rate over lifetime curve [125]*

Distributed propulsion system

The distributed propulsion system consists of 14 motors. In the case one of the individual motors is inoperative, the effect on the ElectriFly's performance and safety is negligible. The aircraft will still be laterally stable and controllable, and even its performance in range and speed will be relatively unaffected. In fact, the minimum number of engines required to still perform the same cruise conditions is 9. The reliability of the individual EMRAX 208 motors can be assessed using their documentation [126]. Stating that it can withstand high powers and torques, and due to the use of high-quality materials and magnets, it is corrosion-resistant and mechanically strong. However, no actual failure rate is provided. In general, for electric motors up to 1000 V, the failure rate $\lambda = 0.0824$, which results in an operative

lifetime of up to 20 years [1].

Recharging
The reliability of the docking procedure is designed to be as high as possible. Using tests the reliability of the design will be pushed to its limits. In this sensors will also be used to ensure the safety of the procedure together with redundancy. This is required especially for external factors like wind, weather and icing.
Batteries
As described in Subsection 6.4.1, the battery packs are designed in a total of 4 packs. In case one of the packs would fail, the capacity and consequently the range would only decrease by a factor of 1/4th. The overall reliability of the complete battery system is thus increased by redundancy, operated by the battery management system (BMS). The reliability of the individual batteries is dependent on conditions. For example, they are less reliable in charging, as dendrites could form. However, this is prevented by special coating. By containing the batteries in low temperatures and restraining usage to low discharge rates, the lifetime can be maximised. The battery casing as designed in Subsection 6.4.1 will also help with increasing the reliability.

The reliability of the battery can be assessed by assuming the failure rate of a single solid-state cell to be equal to that of a single lithium-ion cell, which is 1 in a million [2]. Additionally, the failure rates of other battery system components such as $5.29E(-6)$ for the battery management system (BMS), $1.62E(-7)$ for power electronics and $1.01E(-06)$ for sensors [127]. Out of these 4 components, the BMS is the most failure sensitive, and due to this, the 99% reliability is met when a value of 1500 operational hours is taken as seen in Table 16.3. With 4 flights a day, each operating the battery for 3 hours, it means that the battery system needs to be checked every 130 days. It is to be noted, that primarily the BMS needs to be maintained and possibly replaced every 130 days, but the actual batteries don't need to be, since individually their reliability is >99%. This means that the top-level requirement SAF-01 is met.

Table 16.3: *Reliability of battery system for 1550 operational hours*

Battery components	Reliability [%]
Solid state battery (4x)	> 99.99
Battery management system	99.18
Power electronics	99.97
Signal detection sensors	99.84
Total battery system	99.00

Digital twin
The digital twin concept is implemented into the aircraft using a large set of sensors, as was shown in Figure 15.3. All sensors are built redundant, such that if one sensor fails to give information, it is automatically recognised and can be replaced. So in a sense, the digital twin can provide predictive maintenance on itself. Alternatively, if one sensor provides false data, it can be compared to a similar redundant sensor. The long optic fibre strain sensors reduce weight, complexity and therefore failure rates. The reliability of individual sensors is hard to estimate and can be assessed in the detailed design phase.

Conventional subsystems
The reliability of conventional aircraft subsystems like avionics, landing gear and structures, can be assessed by looking at the reference aircraft presented in Chapter 3.

Availability

The availability is a measure of to what extent the ElectriFly is available to perform its mission during a certain time interval. There are several reasons why the ElectriFly may be temporarily out of service. For example, due to expected matters such as maintenance, or due to unexpected cases such as weather conditions, defects, safety regulations or short-notice logistic conflicts. Availability is highly dependent on the other factors within the RAMS principle. A product that is reliable, safe and not requiring maintenance, is more likely to be operationally available.

During the day-to-day operation of the aircraft, turnaround time is a measure of availability. The ground time required between two consecutive flights and its process is described in Chapter 4. The specific flight profile C described in Chapter 4 will optimise for minimal turnaround time. It minimises the biggest demand on ground time: recharging the batteries, which is done by the use of mid-flight recharging. This way, the availability of the ElectriFly can be improved.

A different perspective on availability is that of materials and machinery during the production phase of the aircraft. The same principles apply here. The availability of these resources is essential for the smooth running of the production process. If a certain crucial material is not available, the entire production process comes to a standstill. This is

[1] https://theramreview.com/regarding-your-electric-motors-general-reliability/ [Accessed on 14.06.2023]
[2] https://batteryuniversity.com/article/bu-304a-safety-concerns-with-li-ion [Accessed on 14.06.2023]

costly and therefore undesirable. So also at this level, evaluating availability is crucial.

Maintainability

Maintainability concerns a system's ability to be easily and timely maintained. At this stage of the design process of the electric aircraft, maintainability will be preliminarily assessed, with a scope on the whole life cycle. There are strict regulations for existing aircraft in terms of maintenance, documented in the CS-23 [1] certification specifications for commuter-sized aircraft. For all parts in the aircraft system that require (regular) maintenance or inspection, proper serviceability and accessibility should be designed. As described in Section 15.2, the routinely scheduled maintenance can be limited by the use of predictive maintenance of the digital twin concept. Maintainability challenges concern the batteries, recharging ports and electric engines new to aviation, which are still in development and will require regular inspection and maintenance. However, the benefits are that electric engines have less movement and heat build-up of their parts. Additionally, due to the distributed propulsion's added complexity, there are more engine parts to maintain, but this is again made easier with the help of the digital twin.

Present-day, maintenance is periodically planned in advance, with different levels of maintenance dependent on the flight hours or the number of cycles of an aircraft. Table 16.4 shows conventional maintenance checks used by airline operators, which according to inspection programs regulated by airworthiness authorities like EASA [1]. This can be considered as the minimum of checks an operator has to perform, and intermediate required maintenance on certain parts is inevitable. The digital twin concept ties into this by its predictive maintenance aspects as described in Chapter 15. The timeline of maintenance can be optimised. Additionally, industry-wide implementation of the digital twin concept will result in new regulations regarding its predictive maintenance. This will eventually increase reliability, maintainability and safety.
As mentioned before, the batteries require an inspection every 1500 flight hours. Replacement of the batteries at the end of life required further engineering effort. The battery packs in the fuselage section are accessible, however, the batteries incorporated in the wing are a bigger challenge to replace.

Table 16.4: *Maintenance checks [13]*

Type	Limit	Required Time	Maintenance activities
Preflight	Every flight	5 minutes	Quick visual inspection
A check	200-300 cycles 400-600 hours	50-80 man hours Typically 6-8h night shift	Inspection of flight controls, avionics, gear, fluids
Battery Inspection	1500 hours	10-20 man hours	Inspection of batteries
B check	Every 6-8 months	150-200 man hours Typically 1-3 days	Thorough inspection of flight controls, avionics, gear and fluids
C check	Every 20-24 months	6,000 man hours Typically 1-2 weeks	All of B-check + inspection of structural and electrical systems
D check	Every 6-10 years	50,000 man hours Typically 2-3 months	Inspection and overhaul of all aircraft parts

Safety

Safety is the protection of the system and passengers when faced with dangerous situations. Multiple aircraft functions are safety-critical, that is, they need to be fail-safe for the integrity to be preserved. In case they fail, the aircraft, its passengers and its crew will be in danger. The safety-critical functions per field are listed in the functional flow diagram shown in Figure 4.8. The biggest safety risks of the ElectriFly have been listed and mitigated in Section 16.1.

17. Sustainability

This chapter presents the sustainability analysis for the design of ElectriFly. First, the carbon emissions are examined in Section 17.1. Then the sustainability of the aircraft structure and the battery is elaborated on in Section 17.2 and Section 17.3. Finally, a noise analysis is presented in Section 17.4.

17.1. Carbon Emission Analysis

Since the main focus of the ElectriFly is to offer sustainable air travel, it is of utmost importance to check whether this goal is actually achieved. One of the top-level requirements that were set concerning sustainability states that ElectriFly's emissions shall be fewer than 50% compared to conventional non-electric aircraft [REQ-SUS-03]. In order to check whether this requirement, is met, an analysis is performed comparing the ElectriFly with a conventional turboprop aircraft that would perform the same mission. It should be noted that emissions can be evaluated on various levels. In this analysis, the carbon footprint of both aircraft is evaluated as CO2 is currently the most threatening pollutant regarding global warming and climate change [128]. In order to perform this analysis, some assumptions were made. These assumptions are listed in Table 17.1.

Table 17.1: *Sustainability Assumptions*

Identifier	Assumption
ASM-SUS-01	The ElectriFly has a lifetime of 25 years
ASM-SUS-02	The ElectriFly performs 4 flights each day
ASM-SUS-03	During each flight, the aircraft is recharged once
ASM-SUS-04	The characteristics and flight mission of the ElectriFly and turboprop aircraft are equal
ASM-SUS-05	ElectriFly flies on renewable energy
ASM-SUS-05	The solid-state battery will have a cycle life of 10 000 cycles
ASM-SUS-06	Carbon footprint of production and transportation is included for both kerosine and renewable energy

Table 17.2 gives an overview of the parameters that were taken into account in the carbon footprint calculation of both the ElectriFLy and the compared turboprop aircraft. Both calculations are based on the total energy requirement during the life span of the aircraft. Knowing that 1863 kWh is required for a single (recharged) flight, this can be translated into a total energy requirement of 67999500 kWh, assuming that the aircraft performs 4 flights each day in a time span of 25 years. Based on the efficiencies of the combustion engine and the electric propulsion system, the total required energy is determined for both aircraft. These values are subsequently used to determine the carbon footprint for the different energy resources. For the turboprop aircraft, it stops here in terms of direct CO2 emission. For the ElectriFly, also the batteries have to be taken into account as the production process of the used solid-state batteries is energy consuming and furthermore, the batteries have to be replaced multiple times during the life span of the ElectriFly. As emissions resulting from the production of other subsystems are considered equal, they are not considered in this analysis. The recyclability of these components and the materials used will be discussed later in this chapter. Looking at the results displayed by Table 17.2, it is noticeable that the CO2 emission of the Electrifly compared to a similar turboprop combustion aircraft is nearly 3.5 times lower and therefore, in terms of carbon footprint, requirement [REQ-SUS-03] is more than satisfied. It should be noted that as of this moment, the development of the solid-state battery is still at an early stage and it will be likely that the mass production techniques of the battery will improve significantly and therefore the required energy will decrease as well [1]. This means that the performed analysis is quite conservative and might provide even more beneficial results in the future.

[1] https://www.nasa.gov/aeroresearch/nasa-solid-state-battery-research-exceeds-initial-goals-draws-interest/ [Accessed on 15.06.2023]

Table 17.2: *Carbon emission comparison of a conventional turboprop aircraft and the ElectriFly on the same mission*

Turboprop Aircraft		**ElectriFly**	
Efficiency combustion engine	0.39 [2]	Efficiency electric engine	0.73 [3]
Kersosine energy required during lifetime [kWh]	174357692.3	Electric energy required during lifetime [kWh]	93150000
Energy density kerosine [kWh/kg]	12[4]	CO2 emissions [kg] per kWh renewable energy	0.05 [5]
Required kerosine weight [kg]	14529807.69	**CO2 emmision due to electric energy [kg]**	**4657500**
CO2 emission [kg] per kg kerosine	3.66 [6]	CO2 emission of battery production [kg/kWh]	1045 [7]
Total CO2 emission [kg]	**53179096.15**	Energy capacity of the solid-state bettery [kWh]	1464.3
		CO2 emmision due to battery production	**1530193.5**
		Cycle life solid-state battery	10 000
		Cycles used per flight	2
		Estimated amount of flights during ElectriFly's lifetime	36500
		Estimated amount of cycles during ElectriFly's lifetime	73000
		Required battery replacements	7
		CO2 emission due to all batteries used in total lifetime	**10711355**
		Total CO2 emission [kg]	**15368855**

17.2. Sustainability of Aircraft Structures and Materials

One of the top-level requirements for ElectriFly regarded the reusability of its structures. REQ-SUS-1 stated that the structural components must be at least 80% reusable. To achieve that different parts and their materials are analysed in this chapter. First, an overview of aircraft recyclability is provided. Then, the largest structures - the wing and the fuselage are analysed together with their materials - AL7075 and 60% carbon fibre peek matrix composite. Finally, other structures that constitute the OEW are briefly analysed to confirm that 80% of the mass of the aircraft (excluding the batteries) can be recycled.

Recycled Materials in Part Manufacturing

The sustainability measure for aircraft parts can be started already at the manufacturing stage. Using recycled materials instead of new ones can lead to significant savings of energy and equivalent CO_2 generated. A summary of the exact amounts for the most popular types of aerospace materials can be found in Table 17.3 and Table 17.4 below. It can be seen that the benefits are especially visible for aluminium and composite materials as those require the most energy and contribute the most greenhouse gases.

Table 17.3: *Energy consumption [129]*

Energy Consumption in Production [MJ/kg]	Aluminium	Other metal	Composites	Rubber
New materials	47	16.9	234 (CFRTS)	80
Recycled materials	2.4	10.6	33 (CFRTS)	14
Energy saved	44.6	6.3	231	66

Table 17.4: *CO_2 Generation [129]*

CO2 generated [kg CO2 / kg material]	Aluminium	Other Metal	Composites	Rubber
New Materials	3.83	1.25	12	3.4
Recycled Materials	0.29	0.44	2	2.4
CO2 Saved	3.54	0.81	10	1

ElectriFly primarily uses composites and metals - aluminum alloys, which offer an opportunity for decreasing emissions in production by using the highest possible fraction of recycled materials. However, as the materials undergo recycling their microstructure often changes which leads to a decrease in the mechanical properties of metal alloys

[2] https://elib.dlr.de/78726/1/MP-AVT-209-09.pdf [Accessed on 15.06.2023]
[3] https://elib.dlr.de/78726/1/MP-AVT-209-09.pdf [Accessed on 15.06.2023]
[4] https://medium.com/@celions/decarbonizing-aviation-energy-density-deadacf72b34 [Accessed on 15.06.2023]
[5] https://www.wri.org/insights/setting-record-straight-about-renewable-energy [Accessed on 15.06.2023]
[6] https://www.offsetguide.org/understanding-carbon-offsets/air-travel-climate/climate-impacts-from-aviation/co2-emissions/ [Accessed on 15.06.2023]
[7] https://www.sciencedirect.com/science/article/pii/S0306261916301982##b0070 [Accessed on 15.06.2023]

and polymers [130] [66]. Thus, it is not possible to build critical structural components of an aircraft entirely from recycled materials and new materials must have been chosen for ElectriFly. It is possible, however, to choose recycled plastics, metals and composites for less critical applications - for instance, the interior of the passenger cabin. Aircraft seats are typically made of aluminium, carbon fibre and plastic for withstanding the dynamic loads during flight, as well as faux leather for passenger comfort [8]. It is recommended that ElectriFly seats use recycled aluminium and plastic, coming from another disassembled plane, if possible.

Aircraft Disposal Overview

According to the Airbus Forecast, by 2032, 10334 aircraft will be retired[9]. The dismantling and disassembly of an aircraft is a difficult problem that is currently being investigated by aerospace companies and university researchers. At the end of life, the aircraft disposal process can be divided into three steps [131]:

1. Decommissioning: Cleaning, removal of fluids, safety procedures
2. Disassembly: Equipment and part removal
3. Dismantling: Final draining of systems, hazardous materials, and dismantling

At the end of this process, aircraft parts are divided into two categories. One of them is still in good shape and can be further used in another aircraft [131] or in other upcycling applications such as interior design [10]. The rest of the parts have to be separated into individual materials that can be later reused or recycled. A brief overview of the material flow at the end of aircraft life is shown in Figure 17.1.

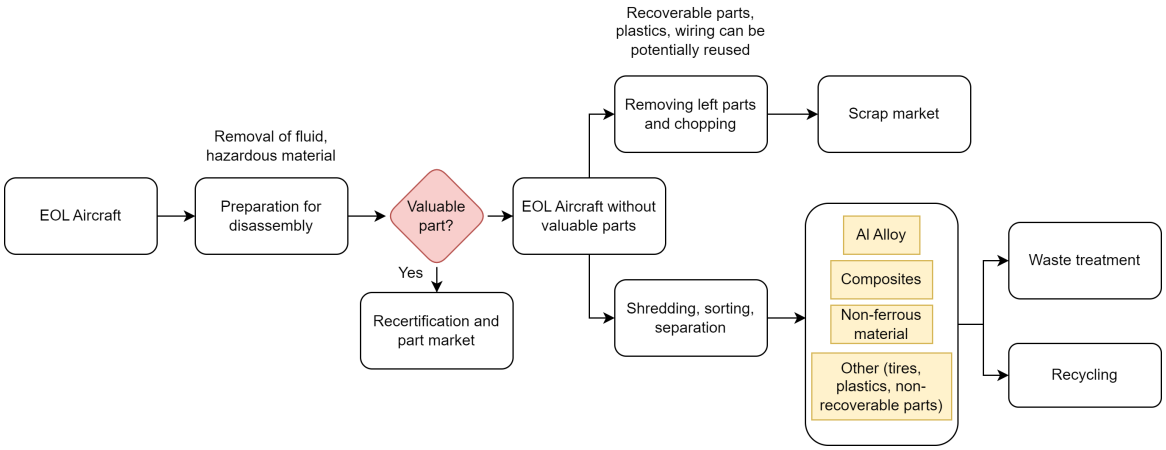

Figure 17.1: *Material Flow Analysis [132]*

Material Recyclability Overview

To minimise the necessity of disposal and waste, the recyclability of different material types has to be investigated. The main building blocks of aircraft - aluminium alloys, composites, non-ferrous metals, and other materials will be shortly presented below.

1. **Aluminium:** Most aircraft aluminum alloys belong to high Cu (2xxx Series) and high Zn (7xxx Series) alloys with small additions of other minor elements to increase fracture toughness [133]. Should those alloys be sorted and recycled appropriately, they can be further used for non-critical aircraft components that carry low and medium loads and do not critically depend on fracture toughness [134].

2. **Composite:** The three main EOL solutions for composites are landfill, incineration, and recycling. The former two are getting increasingly restricted due to the high negative impact on the ecosystem. At the same time, the increasing use of CFRP- and glass-fiber-based composites in aerospace, wind energy and automotive industries facilitates the development of novel recycling technologies [135]. The possibility of recycling composites largely depends on the resin types. Thermoplastic composites can be recycled relatively easily - by remelting them at high temperatures [66]. Thermosets, however, decompose at high temperatures and are very hard to recover [66]. Three main methods of thermoset exist:

   (a) Mechanical: This consists of mechanical shredding processes to reduce waste into recyclates. Mechanical recycling for carbon fibres yields the least tensile strength fibres but is more environmentally promising as it involves the lowest energy (0.1-4.8 MJ/kg) [135]

[8] https://www.southernaircustoms.com/aircraft-seats/ [Accessed on 16.06.2023]
[9] https://www.airbus.com/sites/g/files/jlcbta136/files/2022-07/GMF-Presentation-2022-2041.pdf [Accessed on 23.05.2023]
[10] https://www.airbus.com/en/newsroom/news/2019-04-a-piece-of-sky-breathing-new-life-into-old-aircraft-parts [Accessed on 16.06.2023]

(b) Thermal: This involves breaking down waste material for the material. Methods such as pyrolysis are the most used in industry today. All products and by-products from the process can be used in high-value fuels and oils, but the quality of fibres is degraded, resulting in lower mechanical properties, and the process releases CO_2, along with consuming 5-10 MJ/kg of energy. [135]

(c) Chemical: This involves dissolving the matrix from the fibres in a reactive medium. Methods such as solvolysis are the most efficient for obtaining good-quality (highest tensile strength) recycled fibres, however, it is not the most environmentally friendly and consumes very high energy (21-91 MJ/kg). [135]

3. **Non-ferrous:** Specific recycling methods are developed for different metal types such as magnesium, titanium or copper. Very high-performance materials like titanium are very energy intensive to manufacture and have limited resources, hence providing a higher benefit in recycling [11].

4. **Other**: Various parts, such as tires, and non-recoverable parts can be repurposed for other uses. Tires can be used as a source of valuable raw materials in different polymeric matrices for the manufacture of low-cost products and a cleaner environment. Rubbers have a role in the sustainable development of the composite and automotive industries [134].

Sustainability Indicators

In order to define and evaluate the sustainability impact of products at the end of life several metrics can be defined. The most relevant criteria for the end-of-life recycling and disposal process are described in the list below:

1. **Waste Generation (WG)**: Waste can be generated in various stages of the disassembly process, when separating for valuable parts and shearing or disassembling the structure, as well as during the recycling process of each material group [136].
2. **Quantity of recycled material (QRM)**: Each recycling process may produce a different amount of material, depending on the quality and energy. This is an important factor and must be traded off against the quality of the obtained material, and the total economic value of the material [136].
3. **Economic value of recycled material** (**EVRM**): This is directly a function of the quality of the recycled material. Higher quality materials, especially if the initial manufacturing process is cost and energy intensive, can result in a higher cost-benefit ratio and be used for high-value applications. The high value of this indicator can incentivise companies to recycle as it reduces economic loss from allocating resources to recycling [136].
4. **Energy Required (ER)**: The energy required in the recycling process can vary widely and can dictate the quantity and quality of the recycled material produced. Additionally, it gives an overview of how beneficial recycling is compared to the production of new materials and allows us to assess if the specific production procedure makes environmental sense [136].
5. **Polluting Impact (PI):** Recycling processes can also result in pollution, especially if the remaining material is scrapped, and produces emissions in any form. This criterion is important to ensure no indirect emissions as a result of the end-of-life process [136].

Wing and Fuselage and Empennage End-Of-Life

In the previous chapters, only the material composition of the wing and fuselage was established. Since the empennage has similar structural responsibilities and is also a critical part, it is likely that it is going to be manufactured from the same materials and face the same sustainability challenges. The three subsystems constitute around 50% of the total weight of the aircraft (excluding the batteries), therefore providing strategies for the end-of-life of those components has a significant impact on the sustainability requirement of 80% reusability at the end of life.

Aerospace-grade aluminium alloys can in principle be fully recycled with only minor changes in fracture properties if appropriate methods are used [137]. At dismantling, the aluminium parts must be pre-sorted, ideally by alloy, but at least by series type - 2xxx and 7xxx. Then, the parts can be shredded, sorted, and remelt to form recycled aluminium [137]. Finally, the material should be cast into ingots and used for new components. If the series sorting was conducted, the material can also be used for non-fracture critical aircraft parts such as flaps [137]. There are already automated shredding and sorting techniques implemented such as laser breakdown spectroscopy [137]. There is, however, a lot of potential for new methods such as digital twin and digital thread that can make it easier for the recycling facility to plan the dismantling and sort the different components by providing easy access to data about the materials used for all the components and component groups [137]. It could even be speculated that AI-driven algorithms could find the optimal dismantling and sorting strategies and offer them as readily available solutions.

The specific aluminum alloy used for ElectriFly - Al7075 was proven to be fully recyclable. The material was first shredded to scraps, sorted out from all the other alloys, and remelt. The mechanical properties remained unchanged in the process [138]. It may be concluded for ElectriFly that the aluminum parts in the wing, fuselage and empennage can

[11] https://www.eib.org/en/stories/titanium-recycling [Accessed on 16.06.2023]

be fully recycled as long as the responsible organization - the aircraft manufacturer or owner does comply with basic requirements for dismantling such as pre-sorting of different materials.

The next material group used for all three ElectriFly parts are composites that are typically considered difficult to recycle [89]. The traditional ways like landfill deposition or pyrolysis are not sustainable as they lead to complete or significant loss of material used [135]. Contrary to usual epoxy and other thermoset composites, thermoplastics offer an opportunity for even 100% recyclability of components without properties and material loss [139]. Yet, the research for effective methods of recycling thermoplastic composites with a high fraction of continuous carbon fibres is still not fully finalised [139].

One of the methods that make it possible to recycle both fibres and resin is mechanical recycling. The parts made of CFRP are milled and shredded and compression moulded into flat panels [140]. The panels can be later used for the creation of new parts. As the process results in creating discontinuous fibres, there is a significant loss in mechanical properties (only 10% of the properties of the original material are achieved in tension) [140]. Hence, the newly recycled carbon fibre would need to find applications in other industries than aerospace or maybe in some non-critical aircraft components. To overcome this problem, new methods are being developed. Aligned Formable Fiber Technology allows for the intentional directional alignment of short fibres which results in recycled carbon fibre composites that keep up to 75% of strength and 85% of stiffness of the original continuous fibre material [12]. With further development of this technology, it would be possible to create recycled carbon fibre that satisfies aerospace-grade structural requirements. It could also provide a path for ElectriFly components end-of-life.

Another possibility of recycling PEEK-based composites could exist with novel methods of fibre-matrix separation. solvolysis could be a promising alternative to pyrolysis, especially if a combination of solvents was found that allows for the regaining of the resin material [13]. For example, sulfuric acid was used to separate the PEEK resin from composites [141], however, the degree of success of using this technique for the specific ElectriFly composites is not fully known. Electrodynamical fragmentation was also proven to be a useful technique for recycling CF/PEEK parts without decreasing their mechanical properties [139]. As the search for carbon fibre recycling techniques and thermoplastic polymer composites continues, it may be expected that in the future, the composite parts of ElectriFly will be (almost) fully recyclable [141].

The last subsystem that is related to the fuselage is the furnishing. As it was previously mentioned, the interior of the fuselage consists largely of aluminium, plastics, and carbon fibre. It does not carry critical structural loads, therefore less strong materials can be chosen such as recycled aluminium. Those materials can be then separated into fractions and recycled - metals and plastics can be remelted to other products. Fabrics can be used in yarn production for carpets [14]. There are specialised facilities that can take care of proper recycling of the interior of the fuselage[15]. Programs are also launched to remove non-recyclable plastic from aircraft interiors [16]. It can be concluded that with appropriate design of the furniture, the majority of it - even up to 100% can be successfully recycled. It could also be recommended that a special budget is assigned by the organization responsible - for instance, the aircraft owner to possibly outsource the recycling of furnishing to appropriate companies.

In conclusion, the total recyclability and reuse potential for the largest structures - wing, empennage and fuselage with its furnishing is very promising. It can certainly meet the required 80% or even more for each of the subsystems. Those subsystems sum up to around 50% recyclability of the total structural mass of the aircraft.

Reusable Structural Components

The second biggest structural group that constitutes almost 30% of the operational empty weight is the engines, landing gear and recharging system. Since those components were not designed in detail and material choices were not made, the end-of-life possibilities of those components can be only briefly discussed. Recommendations are given as to what ElectriFly should do with them at the end of life.

Aircraft engines are an assembly and hence recycling may be a complex procedure, different for a specific engine. Aircraft engines typically consist of metal alloys - titanium, steel and aluminium, all of which can be fully recycled and reused with special techniques appropriate for the specific material [142]. Often engines are sent back to the manufacturer for disassembly and part salvage [131]. It was demonstrated in the PAMELA project that engine manufacturers such as Rolls-Royce can recycle up to 75% of the engines [131]. If at the end-of-life of the aircraft the engines are assessed to be in good condition, they can also be recertified and used on a different aircraft [142]. An additional

[12] https://lineat.co.uk/about/ [Accessed on 19.06.2023]
[13] https://www.compositesworld.com/articles/sustainable-inline-recycling-of-carbon-fiber [Accessed on 19.06.2023]
[14] https://www.aircraftinteriorsinternational.com/features/recycling-aircraft-interiors.html [Accessed on 19.06.2023]
[15] https://www.aira-international.com/recyclingaircraftinteriors/ [Accessed on 19.06.2023]
[16] https://www.aircraftinteriorsinternational.com/features/recycling-aircraft-interiors.html [Accessed on 19.06.2023]

challenge of ElectriFly is that its engines are electric. In many ways the procedure for ElectriFly is similar to a conventional aircraft - the engine has to be dismantled and disassembled and metal alloys in it can be recycled and reused [17]. However, additional components such as magnets are often hard to remove and as a result, it is impossible to recycle them in an economically feasible way [18]. Pilot programs founded by the EU have proven that it is possible to design an easy-to-fully-recycle electric motor [18]. It is hence recommended that during the detailed design and manufacturing of ElectriFly engines, best practices are used to ensure full engine recyclability.

Similarly to the engine, the landing gear can be recycled and reused in more than one way at the end of life. If the part is still in good condition, it may be resold for a favourable price and reused in other aircraft [142]. Otherwise, high-grade steel, titanium and rubber components must be disassembled and processed separately [89]. Steel can be recycled without any loss of mechanical properties by shredding or shearing followed by melting and reshaping [19]. Similarly, titanium is mostly recycled by remelting scraps, however, other techniques such as electrolysis are also investigated [143]. Rubber can have a role in the sustainable development of the composite industry and be used to create different polymeric matrices for the manufacture of low-cost products [134]. For ElectriFly nearly full recyclability of landing gear can be achieved as long as the dismantling and pre-sorting process is conducted correctly.

The recharging system is an additional component, unique to ElectriFly, that also has to be considered for end-of-life. It is possible that this part could be recertified and used for a different aircraft similar to the landing gear and engines. However, if that is not possible, it has to be disassembled into raw materials and those have to be recycled. It is predicted at this design stage that the main materials used are copper (cable), XLPE (insulation), aluminium alloys (retracting system), and nylon (for the cone). The recycling strategies for aluminium alloys were already covered in the previous section, hence it is assumed here that they are fully recyclable. Copper can be fully recycled in a similar way as all the other metals [20]. Nylon can be recycled by means of chemolysis during which it is depolymerised into monomers used for nylon production [144]. Another method for recycling nylon is turning it into Regen, which is not fully sustainable, however, still leads to fewer emissions than landfill [21]. XLPE cannot be reasonably recycled by modern methods. It can be used as a powder filler with other plastic blends or cut in solid phase cut milling recycling process [22]. Novel techniques are investigated to use supercritical de-crosslinking techniques to bring the material back to its thermoplastic stage and remelt similarly to other thermoplastics [145]. The process is not yet economically feasible though [145], it can only offer future recycling possibilities. 27% of the ElectriFly recharging system mass is the XLPE insulation that cannot be properly recycled. Therefore, it must be assumed that for this particular system only around 70% recyclability is possible if it is to be dismantled instead of recertified.

To summarize, the recycling of the engine, landing gear, and recharging system can meet the 80% requirement or even more, except for the recharging cable. This results in around 25% of the total aircraft weight being recyclable based on those subsystems.

Other Aircraft Systems

The remaining 20% of the aircraft weight consists of the various subsystems - avionics, ant-ice, air conditioning, flight controls and electrical casing and wiring. Those systems mostly contain wires with insulation and electrical components such as CPUs, and sensor displays [23]. Air conditioning also contains valves, air systems, compressors, and tubes typically made of metals [24]. Those systems can be therefore treated together in terms of sustainability as electric waste.

The metals from the systems and cable conductors can be pre-sorted during the dismantling process and recycled in a similar way to those described previously for metals [131]. Some of the other subsystems that are still functional can be further certified and sold to use on other aircraft such as some of the structural parts [142]. Depending on the type of electrical insulator - thermoplastics can be easily remelted and formed into new products. Thermosets used for high-temperature applications are not very well recyclable and special methods must be applied. It is recommended that for applications that are not directly related to the propulsion system and battery system, the thermoplastic insulation was chosen and in that way, at least half of the insulation can be recycled.

The recycling of e-waste is a well-known problem to which numerous solutions exist [146]. The recycling process starts with manual separation followed by shredding of the components that cannot be manually disassembled [146]. Then, the mechanical separation of materials by magnets, eddy-currents, and density separators allows the separating of the

[17] https://interbaro.nl/en/producten-metalen/electric-motors-recycling/ [Accessed on 19.06.2023]
[18] https://cordis.europa.eu/article/id/413346-designing-and-recycling-electric-motors [Accessed on 19.06.2023]
[19] https://www.azom.com/article.aspx?ArticleID=7979 [Accessed on 19.06.2023]
[20] https://copperalliance.org/resource/copper-recycling/ [Accessed on 19.06.2023]
[21] https://nordholding.bg/en/news-en/recycling-of-nylon/ [Accessed on 19.06.2023]
[22] https://www.intcorecycling.com/Recycling-Method-Of-Crosslinked-Polyethylene.html [Accessed on 19.06.2023]
[23] https://www.baesystems.com/en-us/definition/what-is-avionics [Accessed on 20.06.2023]
[24] https://www.aircraftsystemstech.com/2017/05/aircraft-air-conditioning-systems.html [Accessed on 20.06.2023]

different materials [146]. Finally, the retrieved materials are purified by means of hydro-, pyro- and bio-metallurgy and can be reused to build new electrical components. In principle, almost all electrical components can be recycled to 80% of their mass. Proper dismantling and end-of-life actions must be ensured, however, by the owner of the aircraft so that the electric waste goes to the appropriate recycling facilities [25].

Summarizing, if handled properly the majority of the subsystems can be recycled. It is not entirely clear if the 80% goal can be achieved for each of the specific subsystems - this analysis is only possible at the detailed design stage of every subsystem. However, with a large degree of confidence, it can be stated that at least half of the scrap from the electronic subsystems can be successfully recycled which sums up to around 10% of the entire aircraft weight.

Summary of the End-of-Life Recyclability

In the previous subsections, the different methods and strategies for the end-of-life of all the aircraft subsystems specified in class II weight estimation were discussed. It was shown that in total, around 85% of the aircraft by weight can be meaningfully recycled in a way that is economically viable as well. Therefore, it is expected that the requirement regarding the sustainability of materials REQ-SUS- can be satisfied by ElectriFly.

17.3. Sustainability of the Battery

The main components of Electric Commuter Aircraft that are different from conventional aircraft are the batteries. Instead of fuel emissions, electric aviation has to deal with battery production, replacement, and end-of-life disposal. Previously, several requirements were identified for the Electric Commuter Aircraft batteries to ensure the solution still stays sustainable. In Section 6.3, it was determined that the aircraft shall use the new technology of solid-state batteries. This section will evaluate the battery design choice with respect to sustainability issues and requirements.

Resource Acquisition and Manufacturing of the Battery

The first stage of development that should be considered is production. In fact, this stage is often the most impactful for batteries [115]. According to the planned sustainability requirements: REQ-SUS-4, the production and material acquisition waste should be minimised and entirely repurposed. Additionally, it has to be compliant with regulations, and sustainability norms and not inflict damage to biodiversity (see: REQ-SUS-5).

Before production, the materials have to be obtained from the natural environment or from recycling. Solid-state batteries use a similar anode-cathode setup as current lithium-ion batteries - which require lithium as well as other rare metals [147]. The current exploitation of lithium, in particular, leads to concerns about material depletion - especially with the growing electric vehicle industry [148]. Therefore, Electric Commuter Aircraft should not use new resources for battery production. As determined in Section 6.3, the battery will consist of a lithium-metal anode, a solid sulfide electrolyte and a lithium nickel manganese cobalt oxide (NMC) cathode. It is known that Recycled lithium provides equally good opportunities and performance in battery production as newly mined lithium [26]. Therefore, it is of vital importance to use lithium that is already used and give it a second-life application. Furthermore, nickel manganese cobalt oxide (NMC) also provides good recyclability options and offers the possibility of separating the various sub-materials without significant loss of performance [149]. Only through implementing the circular economy concept to the solid-state battery's life cycle, will it be possible to acquire enough of the rare materials in a sustainable manner and support large-scale production.

End of Life of the Battery

Due to the growing market of electric vehicles, it is necessary to establish strategies for efficient end-of-life solutions for the batteries they utilise [150]. Currently, only around 5% of lithium-ion batteries are properly reused while it is certainly possible to propose recycling and reuse routes for both lithium-ion and all-solid-state batteries that allow for reusing up to 90% of the battery parts in a cost-efficient way [151] [152]. Previously, four options were presented for the end-of-life solutions for aircraft batteries: restoring, reusing, recycling and disposal. This section will explore the aforementioned solutions with respect to the solid-state battery type that was chosen for the Electric Commuter Aircraft.

The batteries deplete over time becoming unsuitable for heavy applications such as aviation or ground vehicles [150]. However, both lithium-ion and all-solid-state batteries after being used in electric vehicles still offer a promising solution for energy grid power storage [152]. It is also possible to use the batteries for home grid storage that supports solar-power-based energy systems [27]. The biggest challenge of this solution is battery gathering, repackaging and redistribution [150]. To solve it, extended producer reliability policies can be helpful - the aircraft manufacturer could

[25] https://www.conserve-energy-future.com/e-waste-recycling-process.php [Accessed on 20.06.2023]
[26] https://www.scientificamerican.com/article/recycled-lithium-ion-batteries-can-perform-better-than-new-ones/ [Accessed on 22.05.2023]
[27] https://www.hivepower.tech/blog/is-recycling-ev-batteries-for-grid-energy-storage-a-sustainable-plan [Accessed on 23.05.2023]

be responsible for collecting the used batteries and putting them into reuse. In that way, almost 100% of the batteries could be reused before being recycled or disposed of further, as the manufacturer should have data about all cells that were put on aircraft so the company is able to track the batteries.

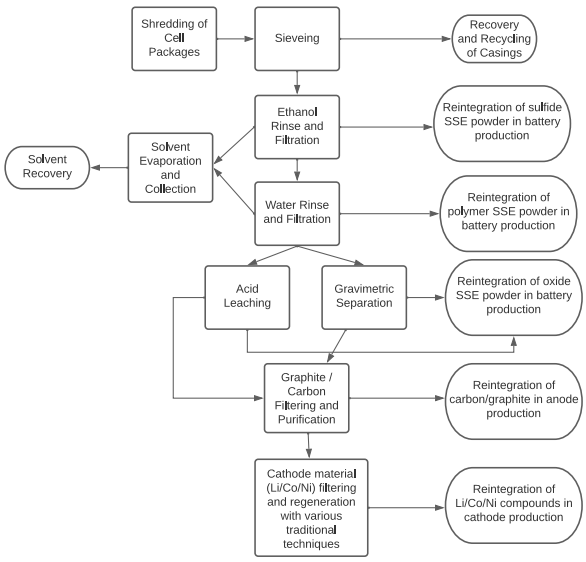

Figure 17.2: *A schematic overview of steps in ideal recycling of solid-state batteries*

Recycling of solid-state batteries is predicted to use similar recycling techniques as the current lithium-ion batteries [151]. By choosing appropriate techniques, both the electrolyte and electrodes can be successfully separated and fully recycled without loss of efficiency of the materials [151]. Currently, Pyrometallurgy, Hydrometallurgy, Hydrothermal Direct Recycling and Dissolution and Precipitation Direct Recycling [151] are used. with the Direct Recycling and Hydrometallurgy being the most promising. Pyrometallurgy is not recommended as typically it only allows for cathode recycling and destroys the remaining battery parts [151]. Hydrometallurgy has the most potential to recover over 90% of the components with low energy cost and gas emissions, yet the process can be complicated and expensive [151]. Direct Recycling offers a cheaper and still environmentally friendly alternative [151]. Figure 17.2 shows a simplified theoretical ideal recycling process for solid-state battery based on a full schema from literature [151].

Novel methods inspired by the steps of the ideal process from Figure 17.2 are also developed for solid-state batteries that reduce the use of toxic chemical compounds, energy and waste in the recycling process [152]. They also allow for an immediate rebuild of the battery from the same materials. It may be therefore expected that, in the future, recycling strategies will be easier and more economically viable than the current trends.

The remaining processes - restoration and disposal - are not recommended for solid state. It is not clear if electrolyte refurbishing is possible for solid-state batteries, but as the batteries offer the largest amount of cycles, the depletion of electrolytes happens further in time and poses less of a challenge than in traditional batteries. However, it may be possible to restore the battery by swapping parts of the battery if they are made up to the same standards and restoring some of the electrodes [152]. Disposal of the components is not recommended as it would create a waste of expensive and often hard-to-obtain metallic resources. It should be avoided at all times and it is possible that with an effective recycling strategy, it will not be necessary.

Summarising, it is entirely possible to satisfy REQ-SUS-BAT-2 and REQ-SUS-BAT-3 and obtain reusability and recyclability rates of over 80%. Nevertheless, to achieve this goal some strategies should already be implemented from the beginning such as an efficient program to collect the used batteries from the aircraft after maintenance. New methods of recycling should also be explored and implemented to offer the best environmental and economic performance.

17.4. Noise Analysis

Impact of Noise on Urban Populations

In 2020, the European Commission published a report that outlined that across 47 European airports that were surveyed, 3.2 million people were exposed to noise levels higher than 45 dB[153]. Furthermore, it addressed that daily, 1 million residents are exposed to more than 50 aircraft noise events at more than 70 dB which equals the sound of a vacuum cleaner[154]. Apart from the fact that this causes annoyance to residents, research shows that it can also have a significant impact on their health [153]. The world health organisation (WHO) revealed that aircraft noise causes hormonal and neural changes, which can significantly affect blood and heart pressure. In line with this, Imperial College London discovered that the chance of being hospitalised due to a stroke or heart attack rose by 10 to 20 % for people living in a high noise zone near airports. Lastly, hypertension and hearing damage are also common complaints as a result of noise[153].

It is clear that the consequences of these noise problems can be fatal and therefore enough attention should be paid to this. As the ElectriFLy is focussed on Urban Air Mobility (UAM) and will mainly be operated between European cities, it is vital to evaluate the noise characteristics of the aircraft and its impact on the local communities around the

airports.

ElectriFly's Noise Expectation

One of the advantages of the ElectriFly in terms of noise is that it has electric motors that generally produce less noise than combustion motors. To analyse the exact noise values of the ElectriFly, measurements would have to be taken with proper equipment during various test flights. Logically, this is not yet possible at the current design stage. Furthermore, there is no specific data available concerning the noise characteristics of the EMRAX208 motor as it's a fairly new model. What can be done to provide some reasonable results is looking at comparable motors and their noise characteristics. Electric motor manufacturer MagniX, which produces a similar kind of electrical axial flux motor, has performed extensive research on noise reduction of electric motors. Figure 17.3 shows the results of an experiment where a conventional combustion engine was replaced with a full electric axial flux motor, and the noise was measured at different flight phases for both propulsion types. The results showed that the modification to electric propulsion significantly reduced the noise effect during all flight phases[28]. Especially during take-off, the electric aircraft induced noise levels of nearly 20.8 dBA lower on average and 24 dBA lower at peak compared to the standard version of the aircraft. These are very favourable results that promise to solve the noise problems to a large extent.

Additionally, the concept of distributed propulsion will probably also have a positive effect on the noise reduction of the ElctriFly. Results of research performed by NASA for their electric X-57 aircraft design showed that by distributing the power over multiple smaller motors, the induced noise is reduced significantly[18]. However, further research should be done to quantify these benefits.

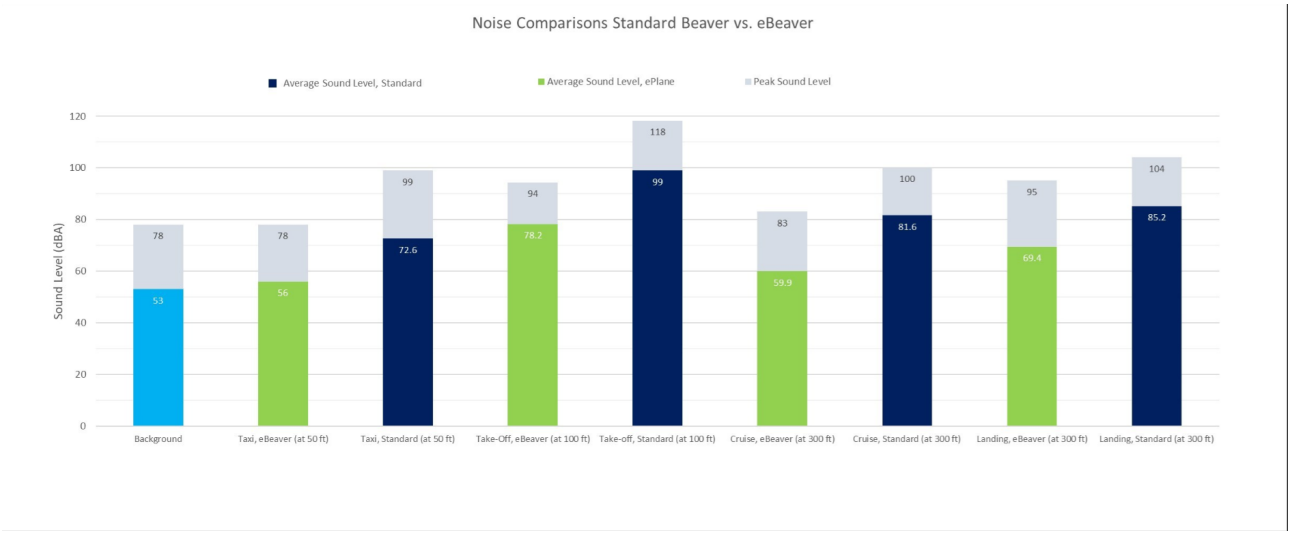

Figure 17.3: *Noise reduction research electric motors by MagniX*[28]

Noise Mitigation Strategies

As the exact noise levels of an aircraft are dependent on multiple factors and therefore often difficult to predict, it is relevant to evaluate various noise mitigation strategies that may be used in case the achieved noise is higher than expected. Figure 17.4 shows a technique that, especially for the ElectriFly, could be interesting. It mainly concerns the application of an increased hence steeper approach angle during the landing phase. This increases the relative distance from the ground and therefore reduces the noise experienced by local residents. Furthermore, it allows for a lower thrust setting required for the same approach speed, which reduces the noise even more[155]. This is an interesting strategy for the ElectriFly as it would also optimise conditions for regenerative braking and therefore more energy would be generated during the landing phase.

28 https://www.prnewswire.com/news-releases/magnix-continued-flight-testing-reveals-electric-aircraft-significantly-reduce-noise-pollution-301264765.html [Accessed on 21.06.2023]

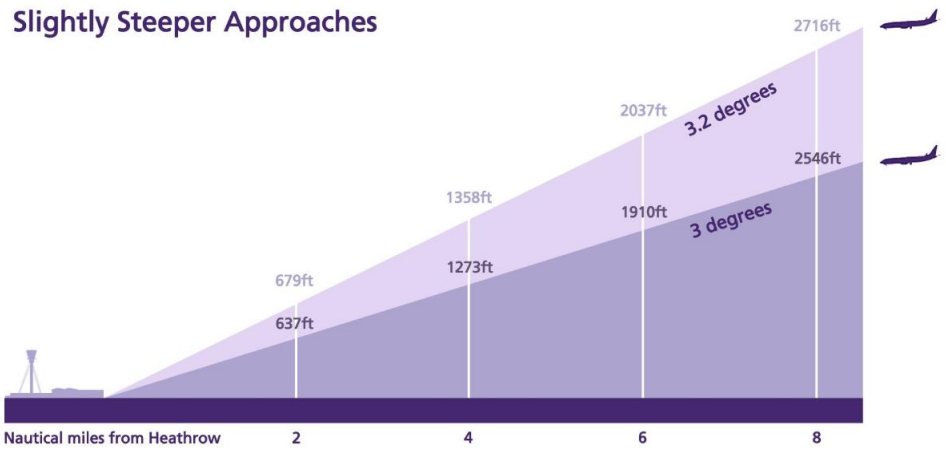

Figure 17.4: *Steep approach technique noise reduction [155]*

Another technique that can be used to decrease noise is by making use of noise-absorbing materials that, as the name suggests, absorb a significant amount of noise by damping it out in the internal structure of the casings. These materials are often used in and around noise-intensive systems. Figure 17.5 shows how the placement of various specific materials around an engine structure can reduce the noise effect. These absorbing materials often have a honeycomb support structure connected to a perforate face sheet [155]. Note that Figure 17.5 shows this technique applied on a combustion engine, but the exact same concept could be applied to an electric engine. Selecting the right materials for this can be done by testing the subsystems and their noise-absorbing materials on the ground and evaluating which material performs best in terms of noise reduction. Subsequently, a trade-off should be made, also taking into account the potential extra weight and costs that come with the new materials.

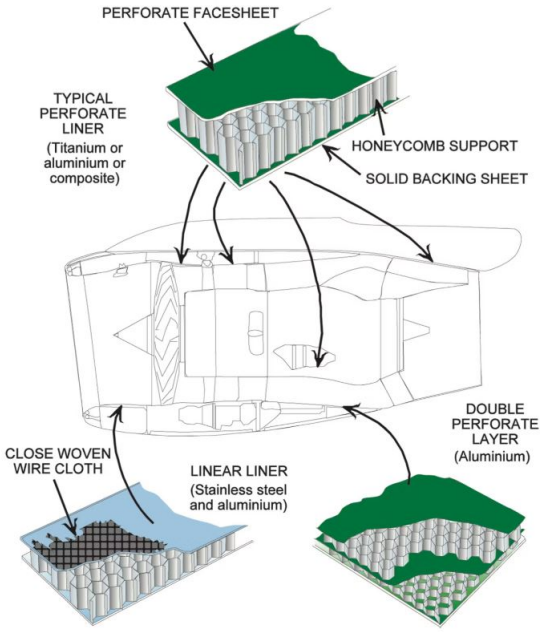

Figure 17.5: *Noise absorbing materials application [155]*

18. Cost Analysis

This chapter will estimate recurring and non-recurring costs, as well as the operational costs of an aircraft. It will up and expand the preliminary findings from the literature by updating by known costs of design choices made. Furthermore, a break-even point will be found, to know the minimal size of the units produced required for a profitable business model and the return of investment.

18.1. Development and Production Costs

Before detailed costs analysis was performed competition was identified. Similarly sized turbo-prop and electrical aircraft costs were specified in Table 18.1 . ElectrtriFly was designed to operate at a cruise speed similar to propeller aircraft speed and therefore significantly significantly lower than that of jet aircraft. For this reason, jet aircraft were not considered in this analysis.

Table 18.1: *Competition Costs*

Model	Aircraft Type	Number of Passengers	Unit Price [M$]	Variable Costs [$ per flight hour]
Beechcraft King Air 350	Twin Propeller	11	4.7	1400
Beechcraft Denali	Single Propeller	7-9	6	3200
SOCATA TBM	Single Propeller	4-6	2.6	1450
EPIC LT	Single Propeller	5	2.8	1230
Epic E1000	Single Propeller	5	4.4	1230
Pilatus PC-12	Single Propeller	6-9	4.9	1378
Aviation Alice	Electric Twin Propeller	9	4	-
Lilium Jet	Electric eVTOL	6	4.5	-

For the development costs analysis Roskam's method was been used. Although constructed in 1970 still applicable after correction factors for inflation rates. The cost estimation assumed production of 400 units and 4 prototypes. To account for the additional difficulty and time cost of fully electrical aircraft design, Ibrahim estimation has been used for engineering-man-hours calculation. In addition, hourly rates for engineering [1], tooling [2] and manufacturing [3] were assumed based on the average hourly wage in the US for each domain in 2023. On top of the standard procedure, the price of the battery was superimposed and multiplied by the number of aircraft produced. Research, Development, Test and Evaluation Costs are described in Table 18.2. Costs calculated exceed preliminary estimation from Cost Budget in Chapter 5. This is caused by an increased number of aircraft planned for production and an increase in the number of prototypes planned from 2 to 4, due to the innovation of the mid-air recharging technology designed.

Table 18.2: *Research and Development, Test and Evaluation Costs*

Type	Costs [$M]
Airframe Engineering and Design	144.7
Development Support and Testing	3.9
Flight Test Aircraft	49.1
Flight Test Operations	0.5
Test and Simulation Facilities	3.0
RDTE Profit	30.2
Financing the RDTE phase	20.1
Total:	251.4

After the calculating Research, Development, Test and Evaluation phase costs, the Manufacturing phase follows. Aircraft production is the biggest fraction, together with other components it can be seen in Table 18.3. The results show that the total production cost per aircraft has been evaluated correctly in Chapter 5 and changed only slightly. Aircraft Production can be described as avionics, engines, battery, interior, material, labour, tooling and quality control costs. In Figure 18.1 representation of components' relative value can be seen, while the cost per aircraft in thousands of US dollars was described in Table 18.4.

[1] https://www.talent.com/salary?job=engineer [Accessed on 18.06.2023]
[2] https://www.zippia.com/tool-technician-jobs/salary/ [Accessed on 18.06.2023]
[3] https://tradingeconomics.com/united-states/wages-in-manufacturing [Accessed on 18.06.2023]

Table 18.3: *Manufacturing Costs*

Type	Costs [$M]	Cost Per Aircraft [M$]
Aircraft Production	1269.5	3.142
Production Flight Test Operations	5.4	0.013
Financing the Manufacturing Program	19.1	0.047
Safety Margin 10%	129.4	0.320
Profit Margin 15%	213.5	0.528
Total:	1636.9	4.052

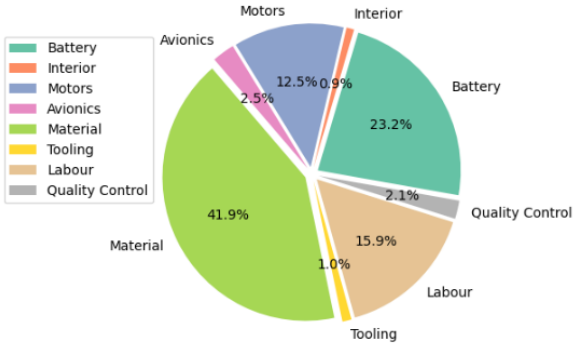

Figure 18.1: *Breakdown of aircraft production costs*

Table 18.4: *Aircraft Production Costs Breakdown*

Aircraft Production Costs [k$]	
Battery	725
Motors	394
Avionics	80
Material	1 323
Labour	500
Tooling	33
Interior	27
Quality Control	65

18.2. Operational Costs

Commercial aircraft operators are mainly interested in Operational costs, thus this category is not lesser in terms of importance. Variable costs per hour of flight will be evaluated separately from fixed costs. For comparison purposes with other aircraft models airport costs were considered together with fixed costs as they highly depend on operational region rather than aircraft model.

Variable Costs per Flight Hour

The major shift between fuel-powered and electric aircraft costs is that fuel price is replaced by electricity price. This contribution differs significantly between the airport and mid-air recharging, therefore the latter will be considered further in the cheaper. To estimate the airport recharge fees, a commercial fee of 0.44 $ per kW/h [4] for the electric car was used[5]. Additionally, it can be expected that electricity fares for electric aircraft, due to carbon-neutrality benefits, can be subsidies by the state and the price decrease, like for electric cars in several cities in the Netherlands [6]. With the required energy of 1172 kWh to charge from 10% to 90%, the airport recharge rate translates to approximately 340$ per flight hour.

Additional cost, which should be considered for electric vehicles is the price of the battery replacement. Considering battery life of 10 000 cycles from Chapter 6 and flight parameters from Chapter 4 it can be approximated that battery replacement will be required every 15 000 flight hours. Furthermore, solid-state battery price approximation ranges from 400-800$/kWh for 2030, therefore by 2035 price of 400 $/kWh is achievable[7], although it can be expected that with time the price will decrease as the technology becomes more commonly used in the industry. With a total energy requirement of 1830 kWh calculated from the Mission Profile, replacement costs contribute 48$ of operational costs per flight hour.

Engine overhaul dictates how often the engine needs to be replaced. These costs can be considered lower compared to fuel-powered vehicles, due to the relative simplicity of the structure. As the price of an electric engine is not easily available in the literature, external source Tine Tomažič Director of Engineering in Pipistrel (electric lightweight aircraft producer) advised engine price approximation of 327$ per kW. It was assumed that 80% of engine costs need to

[4] 0.40€ per kW/h [Conversion rate of 1.10 from 16.06.2023]
[5] https://www.e-flux.io/nl/en/blog/how-much-does-charging-an-electric-car-cost/#:~:text=You%20can%20charge%20your%20electric, to%20the%20present%20price%20influxes. [Accessed on 16.06.2023]
[6] https://www.denhaag.nl/en/in-the-city/nature-and-environment/driving-an-electric-car.htm [Accessed on 16.06.2023]
[7] https://www.dnv.com/to2030/technology/are-solid-state-batteries-the-holy-grail-for-2030.html [Accessed on 16.06.2023]

be replaced every 8 000 hours, approximated by the period of demagnetization. In Chapter 9 distributed propulsion system was chosen with 14 propellers, powered by motors of a peak power of 86kW. Engine overhaul costs can be summarized as 39$ per flight hour.

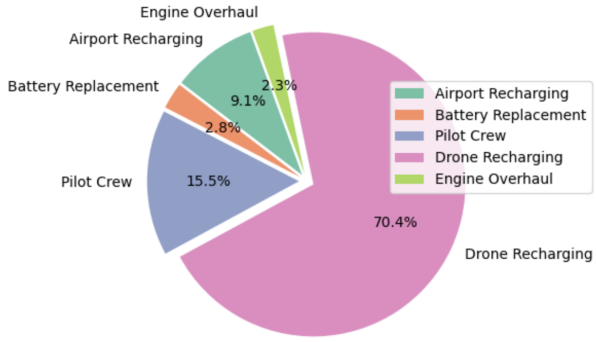

Figure 18.2: *Pie chart with a breakdown of operational costs*

Table 18.5: *Operational Costs Summary*

Operational Cost	short mission [per flight hour]	1300km mission [per flight]
Airport Recharge	$340	$515
Drone Recharge	-	$4000
Cockpit Crew	$268	$880
Battery Replacement	$48	$159
Engine Overhaul	$39	$129
Total:	$696	$5683

Operational costs are based on the flight model of a 1300 km flight, with a full airport recharge and one mid-air recharging procedure. This mission described lasts approximately 3 hours and 20 minutes and describes the distance between Rotterdam and Rome Airport. The rate per in-flight recharge provided by the drone is $4000 [8]. Operational costs per flight settle at $5683. To check the requirements abidance, this value is converted to the cost per hour of flight, leading to $1731. This price does not meet the limitations set by the requirement COS-1 and is slightly higher than the average costs per hour of fuel-based turbo-propeller aircraft. Public opinion studies reveal that almost 60% of people "would pay more for environmentally neutral transport" [156]. Therefore, it can be argued that the price is still competitive.

Fixed and Airport Operation Costs

Maintenance costs and airport operation costs can be considered variable costs, which mainly vary per number of flights. Using Rotterdam Airport, in line with Chapter 3, as a reference hub the following values were established: landing fee of $74 per landing, parking fee $37 per day, service and airport passenger tax $27 per passenger [157]. Maintenance calculated with Raymer's estimation, was additionally adjusted for inflation, as suggested in the book [38], considered at a rate $25 per flight excluding engine overhaul. It is worth noticing that maintenance costs value is conservative, as the costs are expected to decrease due to the innovative application of digital twin, to facilitate and locate possible repairs needed, as described in Chapter 15. On top of that insurance costs of $3500 per year [9] shall be considered. Assuming operations 350 days per year, with 4 flights per day and 8 people on board, summarizing these costs adds up to an additional $377 per flight. In terms of batteries, which need to be replaced after a certain period of time, it should be considered that reselling them to the energy grid can benefit the cost estimation. Although difficult to quantify it can be seen as a negative cost.

18.3. Return of Investment

From previous sections Development stage costs are estimated to be 251.4 million dollars. Recurring (manufacturing) costs of 3.5 M$ were considered by applying an extra 10% safety margin. A unit cost of 4.3 million was chosen, with reference to other competitive models described. The value abides by the cost requirement described in COS-2. With 0.8$ left to cover non-recurring costs, break-even analysis shows 315 units produced are needed to cover the expenses and obtain the return on investment.

On top of the aforementioned analysis, the end-of-life costs have to be considered. These are especially significant for the batteries as they will reach their end-of-life multiple times during the aircraft's operating years. In case they are given a second life in other applications, a negative cost might be applied as a customer will buy it from the operator. This will in turn reduce the cost of battery replacement. On the other hand, recycling will lead to an increase in cost. When it comes to the aircraft itself, the recovery of valuable parts and the re-purposing of material will result in an income cost but recycling will be an extra expense.

[8] *eCarus* DSE Group 10
[9] https://bwifly.com/citation-ii-s550-insurance-cost/ [Accessed on 16.06.2023]

19. Model and Product Verification and Validation

This chapter examines the verification and validation process for the product. With the subsystem verification and validation performed at the subsystem level, the next stage is assumption verification, examined in Section 19.1. Then, to analyse the end-product, product verification and validation are performed in Section 19.2 and Section 19.3.

19.1. Assumption Verification

Throughout the design process, multiple assumptions were introduced to ease the required calculation. Whether the assumption made was valid or not, and how its validity could be improved, is discussed in this section. Most of the used assumptions are validated as such:

ASM-MISS-01: Ideal ISA gives valid calculations, but its sensitivity should be explored in future design phases.
ASM-MISS-02: Scheduled arrival of the drone is implied in the mission requirement of the drone. Moreover, the risk R-04 from Chapter 16 is assessed and given a mitigation strategy, making the assumption valid to use.
ASM-MISS-03: It is reasonable for avionics energy to be related to cruise energy. However, after take-off and landing procedures are defined, more detailed energy consumption ought to be assessed.
ASM-MISS-04: FL150 is not close to optimum for range or endurance as shown in Chapter 11. The mission's cruise condition ought to be changed to a more optimal condition in the following iterations.
ASM-MISS-05: As the ElectriFly is envisioned to fly in 2023, it is safe to assume adequate recharging infrastructure.
ASM-MISS-06: With the use of regenerative braking and by performing gliding flight, no power consumption is valid.
ASM-MISS-07: After closer inspection the climb phase will cover a range close to 50 km. The descent phase can cover a longer range but will be constrained by using regenerative braking.

ASM-BATT-01: A careful regression is in Figure 6.3, and with technology advancing, it is valid to assume.
ASM-BATT-02: Idem as ASM-BATT-02.
ASM-BATT-03: It is already shown that 10000 cycles can be achieved[23]. However, the development of the cycle life has to be monitored as the project progresses.
ASM-BATT-04: The main difference in size between the solid-state and lithium-ion is a negligible casing. This is validated by consulting experts Ir. Lior Zivan and Victor Landgraf.
ASM-BATT-05: The main difference in weight between the solid-state and lithium-ion is the casing that Li cells require. This is validated by consulting experts Ir. Lior Zivan and Victor Landgraf and by NASA's reseach[1].
ASM-BATT-06: The cost expectation for 2026 is estimated to be between 800 \$/kg and 400 \$/kg[2]. However, the development of the cost has to be monitored as the project progresses.

ASM-RECH-01: The drag exerted by the drogue is not significant enough to overcome cable bending stiffness.
ASM-RECH-02: The dimensions and weight of ElectriFly do not exceed those of a KC-46 tanker plane, so it is safe to assume the wake is also smaller.
ASM-RECH-03: With ample space in the rear head of the fuselage, it is safe to assume that it fits. Proper design of the hose and fuel pod ought to be performed in later design phases.
ASM-RECH-04: The expected transformer efficiency of the transformers are validated after consultation with the expert Dr.ir. Pavol Bauer.
ASM-RECH-05: The thrusters are minimally constrained in this design phase, so the available air is sufficient. A detailed assessment is required in detailed design phases.
ASM-RECH-06: The difference in the elasticity between the different materials is not significant with regard to the occurring bending loads.
ASM-RECH-07: The cable's bending characteristics ought to be designed and assessed in more detail for the assumption to be valid.
ASM-RECH-08: As long as the heat is within reasonable bounds, the assumption is safe to be made. However, the heat generation ought to be carefully assessed.
ASM-RECH-09: Since the dimensions of the cable are small with respect to the entire aircraft, the upstream effect will

[1] https://www.nasa.gov/aeroresearch/nasa-solid-state-battery-research-exceeds-initial-goals-draws-interest [Accessed on 14.06.2023]
[2] https://www.prnewswire.com/news-releases/global-automotive-solid-state-battery-market-2019-2030-an-ultra-high-energy-safe-and-low-cost-all-solid-state-rechargeable-battery-for-electric-vehicles-300790807.html [Accessed on 14.06.2023]

be insignificant within the aircraft design.

ASM-AERO-01: The simplification of a trapezoidal wing provides enough accuracy for the current design phase. When cranked or curved planforms will be explored, the effect should be included.
ASM-AERO-02: The blunt body that is the fuselage will stall before the wing does. However, CFD analysis should be used in the future to assess the fuselage's contribution, especially if the fuselage is optimised aerodynamically.
ASM-AERO-03: the main contributor besides the wing is the tail, implying the assumption is valid for aircraft-less-tail.
ASM-AERO-04: Because wing inclination only translates the lift polar horizontally, the induced part is unaffected. A small effect may be present on the wing's zero-lift drag, but its contribution is small.
ASM-AERO-05: The wing drag polar shifts due to its camber, but the effect of wing camber is negligible on the entire aircraft.

ASM-PROP-01: Valid as an initial value[42]. However, the efficiencies of separate components are to be determined.
ASM-PROP-02: The method is correctly extrapolated, but the method ought to be validated against other detailed models, such as the blade element method.
ASM-PROP-03: By including the full wingtip engines, the effect of one extra engine is included. The actual effect is thus expected to be less, but not by a lot.
ASM-PROP-04: The effect has been researched and validated by the consulted expert Ir. Robert Nederlof.
ASM-PROP-05: The effect of turbulence is already small without the use of plasma actuators, so the effect of the actuators will not be significant. However, the use of the actuators should be further explored and researched for detailed design.
ASM-PROP-06: The assumption is invalid when different throttle settings are used for different flight phases. Each phase should be defined in more detail and assessed accordingly.
ASM-PROP-07: The Mach number reaches values of 0.34 for cruise conditions, implying that compressibility effects are occurring. Though the effect is small enough for the current iteration, compressibility corrections should be implemented in further design.

ASM-STRC-01: The skin contribution to the area and moment of inertia for the bending moment and normal stresses is very small.
ASM-STRC-02: In both the wing and fuselage of real aircraft the longitudinal stiffeners are typically responsible for direct loads [70].
ASM-STRC-03: The distance between the centroids of the stiffeners and skin is small, so direct stress is constant through the cross-section [70]
ASM-STRC-04: The battery modules have uniform weight distribution themselves and due to space constraints, it is assumed they are placed along the wing next to each other. In future iterations, the battery placement can be further optimised for the best weight relief.
ASM-STRC-05: The skin thickness is over 1000 times smaller than the diameter.
ASM-STRC-06: The main stresses due to weights and lift bending are larger in larger cross-sections so the design will support enough loads in the cone sections as well.
ASM-STRC-07: Thrust and drag are much smaller than the in-plane loads presented for the wingbox and fuselage. In the wingbox, they also act in the direction in which the wing structure is stronger. *ASM-STRC-08:* The preliminary analysis only included loads that are carried by those elements. More detailed design is needed that considers other failure modes that allow for, for example, rib and frame design.

ASM-PERF-01: Analysis on the NACA 44018 with JavaFoil shows that the difference in Reynolds number does not affect drag within the drag bucket, but has a significant effect on the range of the bucket. For lift coefficients outside the buckets, careful consideration should be taken.
ASM-PERF-02: Since most of the Mach numbers in the flight regime are below the critical Mach, the effect of wave drag is not apparent. Better results could follow from using a compressibility correction factor.
ASM-PERF-03: In reality, the available power is lower for low velocities. However, since the lower power limit only constrains a small part of the flight regime, the difference is safe to neglect.
ASM-PERF-04: In a simplified manner, the thrust provided by the propeller is directly proportional to the air density that is taken in. A complex aerodynamic assessment of the propeller could improve this proportionality in the final design.

ASM-STAB-01: This assumption is true for the steady flight condition that is considered in this project. For other flight conditions in the future, it could be valuable to consider other factors.
ASM-STAB-02, *ASM-STAB-03*, *ASM-STAB-04:* The assumption is based on typical placement from literature data [68].
ASM-STAB-05: The distributed propulsion system allows for the vectored thrust that supports lateral stability and control [78].
ASM-STAB-06: The assumption provides results with appropriate accuracy which was proven in literature [80].

ASM-STAB-07: Many contemporary aircraft utilise this technology, so it is a feasible design decision.
ASM-STAB-08: The T-tail is chosen such that the wake from the wing is minimised and does not influence the speed.

19.2. Product Verification

In order to describe the compliance of ElectriFly's entire aircraft design with the expected requirements described in previous reports, a product verification process is performed. During verification, proof or compliance is shown for each individual requirement, especially the top-level requirements (TLRs)

19.2.1. Verification Methods

This compliance can be proven in 4 different ways:

1. **Inspection (I):** Verification by inspection and performing measurements
2. **Review of Design (RD):** Verification by reviewing design process and documentation
3. **Analysis (A):** Verification by mathematical analysis, including simulation,
4. **Test (T):** Verification by testing the end product in real-life conditions

Here, the product is defined as the design of ElectriFly and not the actual aircraft that can be built. As the real aircraft cannot be produced, this is to distinguish between the verification process of the preliminary design of the aircraft in contrast to the verification itself. Therefore, verification here is performed at a high theoretical level, and not concerning the actual performance of the aircraft.

19.2.2. Compliance Matrix

Table 19.1 presents the compliance matrix, with the updated requirements. The requirements given in **bold** signify the top-level requirements, followed by the verification method and a check column for whether the requirement is met or not. Finally, if the requirement is met, the last column specifies the relevant section in this paper where the requirement is reviewed and analysed. The methods from the previous section are mentioned as acronyms.

Table 19.1: *Compliance Matrix*

No.	ID	Requirement	Method	P/F	Value	Relevant Section
		Operations OPR				
1	OPR-1	**The aircraft shall fly at least 500 km in ideal ISA conditions without recharging**	A, T	✓	630km	Performance
2	OPR-2	**The aircraft shall have a takeoff distance of less than 1000m**	A, T	✓	1000m	Performance
3	OPR-3	**The aircraft shall have a turnaround time of maximum 45 minutes**	A	✓	25 mins	Mission Profile
4	OPR-4	The aircraft shall have a cruising altitude between 15000 and 25000 ft	A	✓	-	Performance
5	OPR-5	The aircraft shall have a maximum stall speed of 180 km/h at sea level at MTOW	A, T	✓	162 km/hr	Performance
6	OPR-6	The aircraft shall have minimum ROC of 200 m/min	A	✓	1020 m/min	Mission Profile
8	OPR-8	The aircraft shall have a landing distance smaller than 1000 m	A, T	✓	1000	Aerodynamics
9	OPR-9	The wingspan of the aircraft shall not be more than 36 m	RD	✓	20.53m	Aerodynamics
10	OPR-10	The aircraft shall have a reference code of 2C aircraft as specified by ICAO	A	✓	-	Operations
12	OPR-12	The aircraft shall adhere to CS23 regulations	A, T	✓	-	
		Structures STR				
13	STR-1	**The cabin shall fit at least 8 passengers**	RD	✓	-	Structures
14	STR-2	A cargo hold shall hold at least 300kg luggage	A	✓	300	Structures
15	STR-3	The structure shall withstand maximum load factors as specified by CS-23	A, T	✓	-	Structures
17	STR-5	The OEW shall be not more than 4300 kg (50 % MTOW)	RD	✓	3300 kg	Structures
18	STR-6	The MTOW shall be not more than 8618 kg [TBC]	RD	✓	7510 kg	Structures

Table 19.1 continued from previous page

19	STR-7	The structure shall withstand pressurization loads of at least 25000 Pa	A	✓	18.42 kPa	Structures
20	STR-8	The aircraft shall have 0-1 lavatories	A	✓	1	Structures
21	STR-9	The aircraft shall have space for a galley serving at least 6-8 passengers	A	✓	-	Structures
22	STR-10	The structure shall provide sufficient space for landing gear integration	D	✓	-	Stability
23	STR-11	The structure shall be able to carry at least 630 kg of passenger payload weight	A	✓	840	Structures
24	STR-12	The aircraft shall be equipped with aircraft and digital twin sensors	RD	✓	-	Digital Twin
		Safety SAF				
24	SAF-1	**The reliability of the individual batteries shall be not less than 99%**	T	✓	-	Battery
25	SAF-2	The EPU shall adhere to Final Special Condition SC E-19	A	✓	-	Propulsion
26	SAF-3	The battery shall not be placed adjacent to any heat sources or hazardous fluids	RD	✓	-	Aircraft Systems
27	SAF-4	The battery compartment shall be equipped with a built-in smoke detection system	RD	✓	-	Battery
28	SAF-5	The battery compartment shall be equipped with ventilation control	RD	✓	-	Battery
29	SAF-6	The battery compartment shall be equipped with a built-in fire suppression system.	RD	✓	-	Battery
30	SAF-7	Any smoke or fire originating in the battery compartment shall not spread to the passenger compartment	A, T	-	-	Aircraft Systems/Risk
31	SAF-8	The aircraft shall be equipped with a deicing system	RD	✓	-	Aircraft Systems
		Battery BAT				
32	BAT-1	**The battery shall supply enough contingency energy for 20 minutes of flight**	A, T	✓	20 mins	Mission Profile
33	BAT-2	The battery shall provide at least enough energy for the entire mission with contingency [TBC]	D	✓	-	Performance
34	BAT-3	The battery shall not be charged above 90%	D	✓	-	Battery
35	BAT-4	The battery shall not be discharged below 10%	D	✓	-	Battery
36	BAT-5	The battery capacity shall not degrade below 80% after 6000 cycles, including recharging cycles.	A, T	✓	10000	Battery
37	BAT-6	The battery container shall have a IP68 rating (water and dust proof)	D	✓	-	Battery
38	BAT-7	The batteries shall operate optimally within a temperature range of 0-26 °C.	A, T	✓	-	Thermal
39	BAT-8	The aircraft shall be equipped with a BMS (battery management system)	RD	✓	-	Aircraft Systems/-Battery
40	BAT-9	The batteries shall be recharged from 25% upto 90% within 45 minutes on ground	A, T	✓	42 mins	Mission Profile/Operations
41	BAT-10	The replacement of the battery shall take not more than 150 manhours	D	✓	-	RAMS
		Recharging RCH				
42	RCH-1	**The aircraft shall be in-flight rechargeable**	A, T	✓	-	Recharging
43	RCH-2	The aircraft shall be recharged for 500 km of cruise flight	D	✓	764 km	Mission Profile
44	RCH-3	The recharge system shall not be able to destabalize the aircraft	D	✓	-	Recharging
45	RCH-4	The aircraft shall provide a flight plan to the recharging system	D	✓	-	Recharging

Table 19.1 continued from previous page

46	RCH-5	The aircraft shall provide an interface for recharging drones	A	✓	-	Recharging
48	RCH-7	The recharging cable shall be stable in cruise conditions	A, T	✓	-	Recharging
49	RCH-8	The recharging cable shall be long enough for the drone to fly without downwash of the aircraft	A, T	✓	-	Recharging
50	RCH-9	The aircraft shall be able to communicate with recharging drones	D	✓	-	Aircraft Systems
51	RCH-8	The recharging cable shall have 15 m of clearance for the plane	A, T	✓		Recharging
52	RCH-9	The interface shall feature a point to equalise 300 kV of static charge between the drone and the plane	A, T	✓		Recharging
53	RCH-10	At full trail the vertical/lateral oscillations should not exceed half the diameter of the drogue canopy. Oscillations should dampen out to 1/3 amplitude after 3 cycles.	A, T	-		Recharging
54	RCH-11	The cable tension/compression should not exceed 6672 N /11 KN value.	A, T	✓	6672N/11kN	Recharging
55	RCH-12	The cable unit shall include a rotation spring and damper to mitigate oscillations between the plane and drone	A, T	✓	-	Recharging
56	RCH-13	The aircraft shall be able to communicate with recharging drones	D	✓	-	Recharging
		Propulsion PRP				
57	PRP-1	The maximum power generated by the engines shall be sufficient for the most power constraining phase	A	✓	-	Propulsion
58	PRP-2	The aircraft shall produce sufficient thrust with one engine inoperative to continue take-off and climb to 10000ft	A	✓	-	Propulsion
		Aerodynamics AER				
59	AER-1	The minimum lift to drag ratio shall be 10	A	✓	26, 21, 15	Aerodynamics
		Stability and Control STC				
60	STC-1	The aircraft shall be able to fly without loss of control with one engine inoperative	A, T	✓	-	Stability
61	STC-2	The aircraft shall have the longitudinal centre of gravity such that it does not tip over during loading on the ground	A	✓	-	Stability
62	STC-3	The aircraft shall satisfy the stability and control criteria as defined in CS-23	A, T	✓	-	Stability
63	STC-4	The aircraft shall provide control of all control surfaces	A, T	✓	-	Stability
		Passengers PAX				
64	PAX-1	The materials used shall not be toxic to passengers	A, T	✓	-	Risk
65	PAX-2	The aircraft shall be pressurised to at least 8000 ft	RD	✓	-	Structures
		Costs COS				
66	COS-1	**Operational cost per hour shall be less than $1400 with mid-air recharging**	A	Fail	1590$/hr	Cost
67	COS-2	Operational cost per hour shall be less than $1400	A	✓	781$/hr	Cost
68	COS-2	Price per Unit shall be lower than $4.5 million	A	✓	$4.3 mil	Cost
69	COS-3	Development costs shall be lower than $700 million	A	✓	$252 mil	Cost
		Schedule SCH				
70	SCH-1	The aircraft shall be produced and certified by 2035	A	✓	-	Battery

Table 19.1 continued from previous page

Sustainability SUS						
71	SUS-1	**At End-of-Life, the aircraft structure shall be not less than 80% reusable**	A	✓	85%	Sustainability
72	SUS-2	**At End-of-Life, the batteries shall be not less than 80% reusable**	A	✓	80%	Sustainability
73	SUS-3	**Emissions shall be fewer than 50% of conventional aircraft**	A	✓	28%	Sustainability
74	SUS-4	The extraction of any materials shall be lawful as defined by the regulations of the UN	A	✓	-	Sustainability
75	SUS-5	The manufacturers for each part shall have measures for sustainable manufacturing and not impact biodiversity according to the OECD	A	✓	-	Sustainability
76	SUS-6	The aircraft shall comply with the noise regulations as defined in ICAO Annex 16	A, T	✓	-	Sustainability

As it can be seen, all assumptions except 4 are met by the design. 3 of them cannot be verified by analysis or review of design, and verification tests shall be described for them in the following subsection. Only 1 top-level requirement is not met: COS-1. This requirement was set to ensure that ticket prices for ElectriFly shall remain competitive by having the operational cost less than 1400$/hr with recharging. However, due to the high cost of mid-air recharging, the cost comes to 1590$/hr, as described in Chapter 18.

19.2.3. Verification Tests

With the final design completed, the compliance matrix reflects the requirements that have been met with the design process. However, some requirements that cannot be analysed or verified through a review of the design need to be tested. Appropriate tests for the requirement that can only be verified through testing are given below:

1. **SAF-1:** The reliability of batteries cannot be analysed directly as they depend on a lot of external factors. Battery tests can be done in various flight concepts for the battery concept described in Chapter 6.
2. **SAF-7:** To ensure that any smoke or fire originating in the battery compartment cannot penetrate the passenger compartments, safety tests according to the regulations must be performed.
3. **RCH-10:** The oscillations caused by the drogue at the full trail and their amplitude should be verified by vibrational testing and wind tunnel testing.

19.3. Product Validation

Following product verification, the product, in this case, the prototype of ElectriFly, should be validated against stakeholder requirements. While verification proves whether 'the product was done right', this validation shall prove whether 'the right product was made'. To achieve this, the products at every level of the system are examined and compared to the stakeholder's expectations. This ensures that the system functions as expected in the intended environment, that the human has been properly integrated into the system and any anomalies are detected and solved before product delivery [3].

This process is conducted in the following stages:

1. **Perform product validation:** To perform product validation, the end product, the validation plan and the baseline stakeholder requirements are required. Then, validation can be performed in four different ways, namely analysis, inspection, demonstration and testing.
2. **Analyze product validation results:** The validation results shall reveal any anomalies, performance variations, deficiencies or non-conformance of the product.
3. **Resolve validation deficiencies:** In case the product reveals any deficiencies, care should be taken that correcting a deficiency or set of deficiencies does not generate a new issue with a part or performance. This can be addressed through regression testing.
4. **Produce Validation results:** Finally, the successfully validated end product is ready for the next production stage or delivery.

19.4. Design Sensitivity Analysis

The sensitivity analysis ought to how the design output reacts under a change of input parameters, and whether the changed design still complies with the requirements. The analysis helps to assess the impact of certain parameters

[3] https://www.nasa.gov/seh/5-4-product-validation [Accessed on 14.06.2023]

that are uncertain and are likely to be altered in future iterations. The analysis is performed for a selection of design choices that are thought to be of interest, being the energy density, cruise altitude, cruise speed, aspect ratio, rate of climb, and tail surfaces. Table 19.2 shows for each change in input parameters, the percentual change in the resultant take-off weight, battery weight, required wing surface area, and required climb power[4].

Table 19.2: *Sensitivity analysis on design*

		Design change [%] for			
Changed Parameter	Changed by [%]	MTOW	W_{bat}	S	$P_{R_{\text{climb}}}$
Energy density	-50	314	551	341	304
Cruise altitude	100	-5	-9	-5	-5
Cruise speed	-27	-10	-14	-10	-9
Aspect ratio	50	8	4	8	6
Rate of climb	33	2	3	2	28
Horizontal tail area	50	1	3	1	2

The sensitivity analysis shows the design's dependency on the discussed parameters. Table 19.2 shows the largest effect for a change in the battery's energy density. Reducing the energy density by 50%, thereby implying the same energy density as for lithium-ion as expected in Figure 6.3, yields more than thrice the original weight. This entails that the energy density of the battery ought to be carefully monitored and designed around throughout the entire project. Other noticeable results consider a change in cruise height or speed. A reduction in speed or an increment in altitude both affect the design's weight, size, and power consumption beneficially.

[4]The effect on required climb power is assessed, as climb becomes the most power consuming flight phase

20. Project Design and Development

This chapter presents the future stages of the project after DSE. The development process is explained and visualised by means of a flowchart and a Gantt chart.

During DSE, a conceptual design of the aircraft was obtained. The next step is to further analyse different domains of the aircraft in order to obtain a more optimized preliminary design. This is done through the use of more extensive methods such as Finite Element Analysis (FEA), Computational Fluid Dynamics (CFD), wind tunnel tests and simulations. Afterwards, comes the final design phase, detailed design. Here, the focus is on obtaining all the final parameters, testing models, developing a flight simulation and setting up the manufacturing stage. Before the aircraft can be operated, it must undergo an extensive certification process and be produced.

The development logic can be seen in Figure 20.1 and the timeline visualised by the means of Gantt Chart in Figure 20.2.

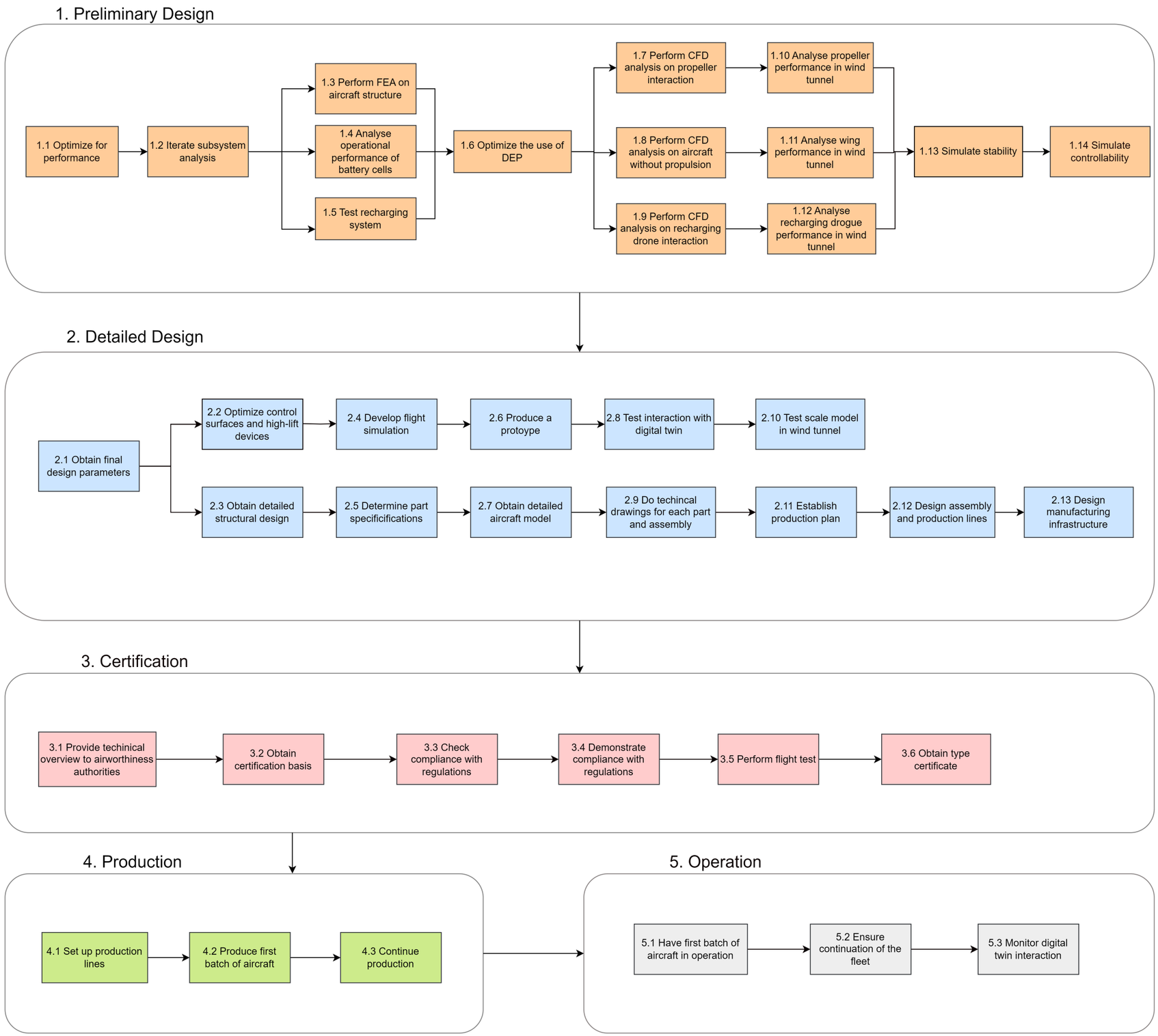

Figure 20.1: *Project Design and Development Flowchart*

ID	WBS	Task Mode	Task Name	Duration	Start	Finish
1	0		Conceptual Design	50 days	Mon 24-4-23	Fri 30-6-23
2	**1**		**Preliminary Design**	**416 days**	**Sat 1-7-23**	**Fri 31-1-25**
3	1.1		Optimize for performance	45 days	Sat 1-7-23	Thu 31-8-23
4	1.2		Iterate subsystem analysis	86 days	Fri 1-9-23	Fri 29-12-23
5	1.3		Perform FEA on aircraft structure	45 days	Mon 1-1-24	Fri 1-3-24
6	1.4		Analyse operational performance of battery cells	45 days	Mon 1-1-24	Fri 1-3-24
7	1.5		Test recharging system	45 days	Mon 1-1-24	Fri 1-3-24
8	1.6		Optimize the use of DEP	85 days	Mon 4-3-24	Fri 28-6-24
9	1.7		Perform CFD analysis on propeller interaction	46 days	Mon 1-7-24	Mon 2-9-24
10	1.8		Perform CFD analysis on aircraft without propulsion	46 days	Mon 1-7-24	Mon 2-9-24
11	1.9		Perform CFD analysis on recharging drone interaction	46 days	Mon 1-7-24	Mon 2-9-24
12	1.10		Analyse propeller performance in wind tunnel	64 days	Tue 3-9-24	Fri 29-11-24
13	1.11		Analyse wing performance in wind tunnel	64 days	Tue 3-9-24	Fri 29-11-24
14	1.12		Analyse recharging drogue performance in wind tunnel	64 days	Tue 3-9-24	Fri 29-11-24
15	1.13		Simulate stability	22 days	Mon 2-12-24	Tue 31-12-24
16	1.14		Simulate controllability	23 days	Wed 1-1-25	Fri 31-1-25
17	**2**		**Detailed Design**	**476 days**	**Mon 3-2-25**	**Mon 30-11-2**
18	2.1		Obtain final design parameters	63 days	Mon 3-2-25	Wed 30-4-25
19	2.2		Optimize control surfaces and high-lift devices	22 days	Thu 1-5-25	Fri 30-5-25
20	2.3		Obtain detailed structural design	43 days	Thu 1-5-25	Mon 30-6-25
21	2.4		Develop flight simulation	87 days	Mon 2-6-25	Tue 30-9-25
22	2.5		Determine part specifications	109 days	Tue 1-7-25	Fri 28-11-25
23	2.6		Produce a prototype	23 days	Wed 1-10-25	Fri 31-10-25
24	2.7		Obtain detailed aircraft model	87 days	Mon 1-12-25	Tue 31-3-26
25	2.8		Test interaction with digital twin	43 days	Mon 3-11-25	Wed 31-12-25
26	2.9		Do technical drawings for each part and assembly	65 days	Wed 1-4-26	Tue 30-6-26
27	2.10		Test scale model in wind tunnel	64 days	Thu 1-1-26	Tue 31-3-26
28	2.11		Establish production plan	22 days	Wed 1-7-26	Thu 30-7-26
29	2.12		Design assembly and production lines	22 days	Fri 31-7-26	Mon 31-8-26
30	2.13		Design manufacturing infrastructure	65 days	Tue 1-9-26	Mon 30-11-26
31	**3**		**Certification**	**2089 days**	**Wed 1-12-27**	**Mon 3-12-35**
32	3.1		Provide technical overview to airworthiness authorities	64 days	Wed 1-12-27	Mon 28-2-28
33	3.2		Obtain certification basis	66 days	Tue 29-2-28	Tue 30-5-28
34	3.3		Check compliance with regulations	109 days	Wed 31-5-28	Mon 30-10-28
35	3.4		Demonstrate compliance with regulations	43 days	Tue 31-10-28	Thu 28-12-28
36	3.5		Perform flight test	24 days	Fri 29-12-28	Wed 31-1-29
37	3.6		Obtain type certificate	87 days	Thu 1-2-29	Fri 1-6-29
38	**4**		**Production**	**6417 days**	**Mon 2-7-29**	**Tue 3-2-54**
39	5.1		Set up production lines	46 days	Mon 2-7-29	Mon 3-9-29
40	5.2		Produce first batch of aircraft	1151 days	Tue 4-9-29	Tue 31-1-34
41	5.3		Continue production	5220 days	Wed 1-2-34	Tue 3-2-54
42	**5**		**Operation**	**7829 days**	**Mon 1-1-35**	**Thu 1-1-65**
43	6.1		Have first batch of aircraft in operation	7829 days	Mon 1-1-35	Thu 1-1-65
44	6.2		Ensure the continuation of the fleet	7829 days	Mon 1-1-35	Thu 1-1-65
45	6.3		Monitor digital twin interaction	7829 days	Mon 1-1-35	Thu 1-1-65

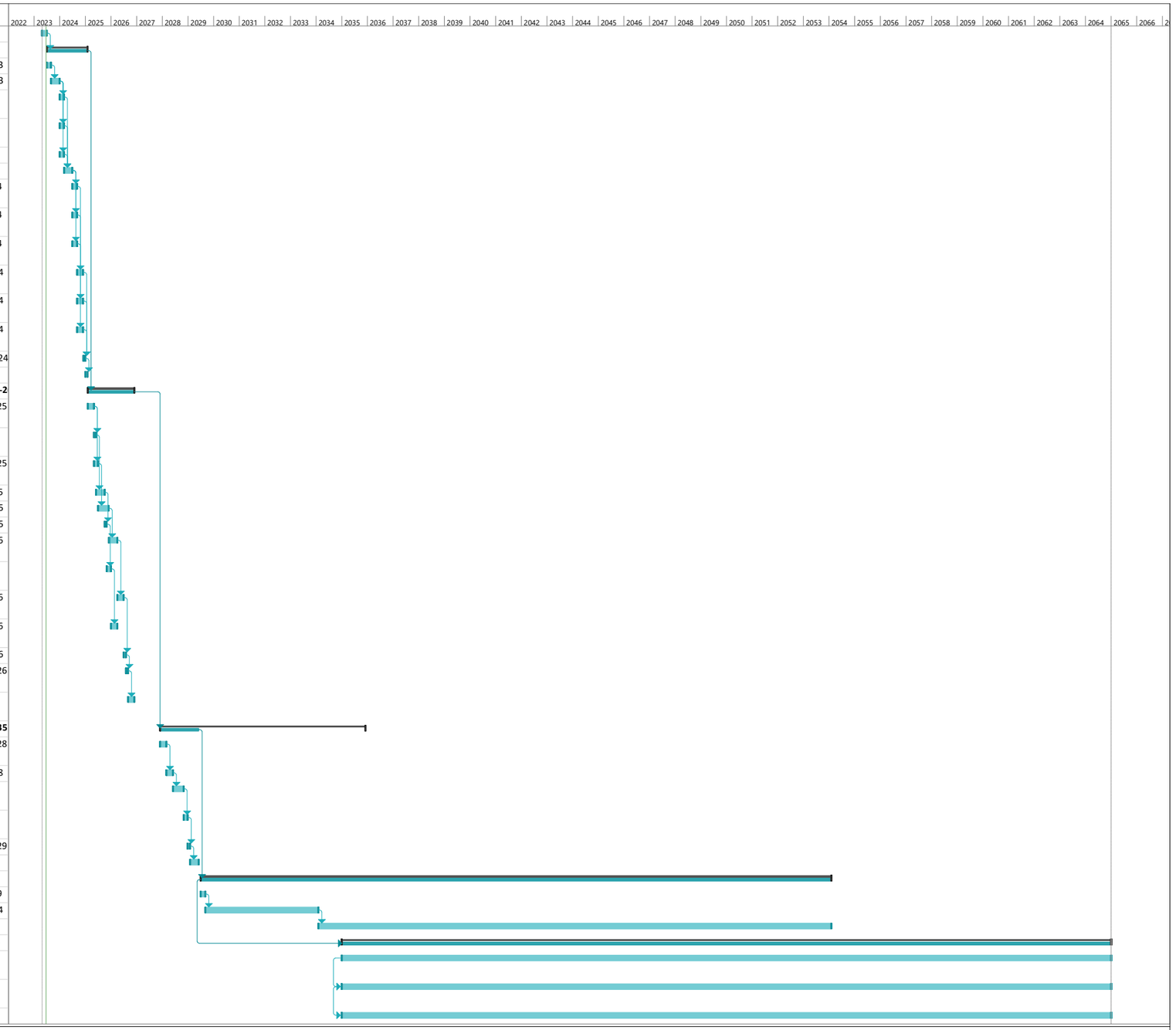

Project: postdsegantt
Date: Tue 20-6-23

Task
Split
Milestone
Summary
Project Summary
Inactive Task
Inactive Milestone
Inactive Summary
Manual Task
Duration-only
Manual Summary Rollup
Manual Summary
Start-only
Finish-only
External Tasks
External Milestone
Deadline
Progress
Manual Progress

Page 1

Figure 20.2: *Project Design and Development Flowchart*

21. Conclusion

This project was undertaken to perform the preliminary design of an all-electric aircraft named ElectriFly, along with a mid-flight recharging system, enabling ElectriFly to extend its range. An in-depth preliminary design was done in the technical aspects of battery, recharging system, aerodynamics, structures and propulsion with an iterative approach to arrive at the final configuration described in Chapter 14. Electrifly can fly 8 passengers over a range of 600 km, and with recharging this range can increase with 764 km. It shall use a solid-state battery with lithium anodes, and feature distributed propulsion along with a regenerative mode in order to regain some energy. Finally, it shall feature a t-tail for stability and shall be integrated with digital twin sensors in order to optimise performance with predictive maintenance. A model of the configuration is presented in Figure 21.1, along with an overview of the characteristics in Figure 21.2.

Figure 21.1: *ElectriFly*

Figure 21.2: *ElectriFly's characteristics*

ElectriFly	
Passengers	8
Range	600 km
Range (Recharged)	764 km
Max Weight	7772 kg
Motors	14

The design process involved the consideration of numerous parameters from various fields such as chemical, electrical, and aerospace. Each of these fields contributed important factors and requirements that needed to be taken into account. However, due to the complexity and vastness of the design space, it was not feasible to delve into the intricate details of every single parameter given the time scope of the project. Therefore, it is acknowledged that the report provides a holistic and valuable overview of the design of an electric aircraft, without delving into every single aspect of the design. These limitations, however, can bring about various optimisation possibilities, which can lead to further innovative improvements in the design.

Recommendations

Based on the design process, several optimisation approaches can be used to increase the robustness of the design. This can be done by fine-tuning existing parameters and obtaining more accurate values for each flight phase. In addition, further optimisation can be conducted for the following areas:

1. Battery placement can be divided into sub-modules and placed more efficiently in the wing, to reduce space needed in the fuselage, leading to a decrease in weight and more wing bending relief.
2. Other airfoils and their influence on wing structure can be analysed to obtain a more optimal airfoil. This can be analysed using computational fluid dynamics (CFD).
3. The interaction of the flow between the propellers, and the turbulence caused by this can be further analysed by more accurate methods, to analyse the benefits and drawbacks of using distributed propulsion.
4. The change (increase) in the sectional lift and drag coefficients, and therefore the overall coefficients shall shift the design point in the loading diagram. This shall resize the wing and shall have an impact on structures, aerodynamics and stability, and shall have a negative snowball effect.
5. For propeller design, an in-depth propeller analysis can be conducted using the blade element method. This can optimise the efficiency of each of the propellers in distributed propulsion.
6. More failure modes, such as vibrations, flutter, buckling, crippling and rivet shear can be analysed. This can be done with a robust finite element analysis (FEM).

A. Acknowledgements

This project would not have been possible without the guidance of numerous external experts, who helped us understand our design and suggest ways to improve the design process in a short time.

Table A.1: *List of external experts approached*

Name	Position	Topic Discussed
Dr.ir. Tomas Sinnige	Assistant professor at the Department of Flight Performance and Propulsion at Delft University of Technology	Expertise in propellers and distribution propulsion aerodynamics
Dr. Tine Tomažič	Pipistrel	General electric aircraft design & Distributed propulsion
Dr. Fabrizio Oliviero	Lecturer at TU Delft, Aircraft Design	Guidance for Class I weight estimation methods for electric aircraft
Dr. Jianning Dong	Assistant Professor of Electromechanics at TU Delft	Aid on electrical configuration. Confirmed that charging and discharging a battery is possible and efficient at the same time.
Dr.ir. Lars Bannenberg	Assistant Professor in the Storage of Electrochemical Energy (SEE) group at Delft University of Technology	Research on specific solid-state battery materials
Dr.ir. Pavol Bauer	Professor with the Department of Electrical Sustainable Energy of Delft University of Technology and head of DC Systems, Energy Conversion and Storage group	Electrical block diagrams & interaction battery-propeller
Dr. Calvin Rans	Associate professor within the Faculty of Aerospace Engineering at Delft University of Technology	Structural design of wingbox and fuselage
Dr. Barış Çağlar	Assistant professor at the Department of Aerospace Manufacturing Technologies at Delft University of Technology	Aerospace composite materials & Recycling
Dr.ir. Maurice Hoogreef	Assistant professor at the department of Flight Performance and Propulsion at Delft University of Technology	Distributed propulsion, boundary layer ingestion, blended wing body aircraft, propeller design
Dr.ir. Reynard de Vries	Researcher at Delft University of Technology	Validation of the distributed propulsion method & propeller design
Dr.ing. Justus Benad	Chief Engineer of the Flying V Team at TU Delft	Consultation about Blended Wing Body design methods and weight estimation methods. Consultation about the three design configuration and their theoretical feasibility and performance.
Ir. Lior Zivan	Former CTO of Eviation Alice, Head of Alice Design Team	Advise on general electric powertrain, electric aircraft design.
Ir. Joris Melkert	Professor at TU Delft, OSCC DSE	Mail contact on certification of electric aircraft.
Ir. Robert Nederlof	PhD candidate in the Department of Flight Performance and Propulsion at Delft University of Technology	Energy-harvesting mode, distributed propulsion.
Ir. Clint Nichols	Engineer for Virgin Atlantic Global Flyer	Guided on twin-boom aircraft, suggests Roskam for the class II weight estimation method.
Victor Landgraf	PhD candidate at Delft University of Technology	Research on solid-state battery
Ir. Pieter-Jan Proesmans	PhD candidate in the department of Flight Performance and Propulsion at Delft University of Technology	Payload-range diagrams.
Ir. Agnes Broer	PhD candidate at the Structural Integrity and Composites Section at the Faculty of Aerospace Engineering of Delft University of Technology	Researches composite aircraft structures. Her research includes works on assessing SHM applications under realistic loading conditions using AI-based multi-sensing approaches.
Robert Darling	Electrochemical researcher at Raytheon Technologies Research Center	Solid-state batteries.
Brandon Litherland	AST, Aerospace Vehicle Design & Mission Analysis at NASA Langley Research Center	Validation on distributed propulsion method & turbulence.
Daan van Dijk	Rotterdam Airport Innovation Department	Infrastructure and costs of airport integration of electric aircraft fleet. The risk factors to consider for short turn-around time missions.

Bibliography

[1] EASA, "Certification Specifications for Normal Category Aeroplanes (CS-23)," , Feb 2023.

[2] Jurgen Janke, W. G. Z., "Challenges in speeding up solid-state battery development," *nature energy*, 2023.

[3] Schmaltz, T., Wicke, T., Weymann, L., Voß, P., Neef, C., and Thielmann, A., "Solid-State Battery Roadmap 2035+," *Solid-State Battery Roadmap*, Fraunhofer Institute for Systems and Innovation Research ISI, 2022.

[4] Agency., E. U. A. S., and Agency., E. E., *European aviation environmental report 2022.*, Publications Office, 2023. doi:10.2822/04357.

[5] Ocko, I. B., and Hamburg, S. P., "Climate consequences of hydrogen emissions," *Atmospheric Chemistry and Physics*, Vol. 22, No. 14, 2022, pp. 9349–9368. doi:10.5194/acp-22-9349-2022.

[6] Precedence Research, "Electric Aircraft Market," , 2023.

[7] Lilium, "Shareholder Letter FY 2022," , 2022.

[8] Bernard, M. R., Tankou, A., Cui, H., and Ragon, P.-L., "CHARGING SOLUTIONS FOR BATTERY-ELECTRIC TRUCKS," 2022.

[9] Ahmad, A., Qin, Z., Wijekoon, T., and Bauer, P., "An Overview on Medium Voltage Grid Integration of Ultra-Fast Charging Stations: Current Status and Future Trends," , 2022. doi:10.1109/OJIES.2022.3179743.

[10] Tabares, D. A., Mora-Camino, F., and Mora-Camino, F., "Aircraft ground handling: Analysis for automation," 2017. doi:10.2514/6.2017-3425Ãŕ.

[11] Förster, P., "Credible Hybrid Electric Aircraft (CHYLA) Deliverable D2.1 Report on Ground Architecture Requirements for the different Solutions," *Clean Sky 2*, 2023.

[12] Santos, B., Morlupo, F., Hoogreef, M., and Steen, M., "Credible Hybrid Electric Aircraft (CHYLA) Deliverable D5.3: Requirements, Certification Specifications and Risk Considerations," *Clean Sky 2*, 2023.

[13] Thalin, P., *Fundamentals of Electric Aircraft*, SEA international, 2019. doi:http://dx.doi.org/10.4271/R-462.

[14] Hamann, J. R., van Tooren, L. J. M., "Systems Engineering And Technical Management Techniques Part I," Delft University of Technology, Lecture Notes, 2006.

[15] *Certification Specifications for Normal-Category Aeroplanes (CS-23) and Acceptable Means of Compliance and Guidance Material to the Certification Specifications for Normal-Category Aeroplanes (AMC & GM to CS-23)*, EASA, 2023.

[16] Ibrahim, R., "Market and Cost Analysis of Hybrid-Electric Aircraft," , 2018.

[17] Cervone, A., Zandbergen, C. T. B., Klein, R. and Claes, J., "AE2230-II: Propulsion & Power Electrical Power Systems for Aerospace Vehicles," Delft University of Technology, Course Reader, 2017.

[18] Adu-Gyamfi, B. A., "Electric aviation: A review of concepts and enabling technologies," 2022.

[19] Gould, J., and Fitzgerald, D., "NASA's Solid-State Battery Research Exceeds Initial Goals, Draws Interest," 2022.

[20] Blain, L., "CATL launches ultra-high density 500-Wh/kg "condensed battery"," 2023.

[21] del Grano, M., "Optimal Approach to the Preliminary Sizing of Hydrogen-Driven Transport Aircraft," 2021.

[22] Dean, M., "The Future of Battery Technology," 2021.

[23] Cheng, Z., "Achieving long cycle life for all-solid-state rechargeable Li-I2 battery by a confined dissolution strategy," 2022.

[24] Dalot, F., "Global Solid State Battery Market - Industry Trends and Forecast to 2029," 2022.

[25] Dalot, F., "Recycling for All-Solid-State Lithium-Ion Batteries," 2022.

[26] Benveniste, G., Rallo, H., Canals Casals, L., Merino, A., and Amante, B., "Comparison of the state of Lithium-Sulphur and lithium-ion batteries applied to electromobility," *Journal of Environmental Management*, Vol. 226, 2018, pp. 1–12. doi:https://doi.org/10.1016/j.jenvman.2018.08.008.

[27] Patoux, S., Daniel, L., Bourbon, C., Lignier, H., Pagano, C., Le Cras, F., Jouanneau, S., and Martinet, S., "High voltage spinel oxides for Li-ion batteries: From the material research to the application," *Journal of Power Sources*, Vol. 189, No. 1, 2009, pp. 344–352. doi:https://doi.org/10.1016/j.jpowsour.2008.08.043, selected Papers presented at the 14th INTERNATIONAL MEETING ON LITHIUM BATTERIES (IMLB-2008).

[28] Ilango, P. R., Modigunta, J. K. R., Parameswaran, A. K., Sofer, Z., Murali, G., and In, I., "Novel Design Aspects of All-Solid-State Batteries," *Solid State Batteries*, Springer International Publishing, 2022, pp. 157–191. doi:10.1007/978-3-031-12470-9_6.

[29] Boer, B., Cahigas, C., Beckers, J., Elskamp, J., Oerlemans, L., Dumont, P., Schoots, P., Demian, S., Blackmore, S. and Tan Zing, S., "Final Report: Design Synthesis Exercise Group 10 Mid-flight Aircraft Recharging System," , 2023. Baseline Report.

[30] Mark S. Jurkovich, C. J. H., "Understanding the Flowfield Behind a Tanker Aircraft," , 2018.

[31] Materials, A., "Crosslinked Polyethylene - XLPE," , 2001.

[32] S. Butterworth, F. E. S., "Eddy-Current Losses in Cylindrical, with Special Applications to the Alternating Current Resistances of Short Coils." , 1921.

[33] Enig, E. N., and Enig, J. W., "Hose-and-drogue in-flight refueling system," United States Patent Application Publication, 2006.

[34] Ro, K., Basaran, E., and Kamman, J. W., "Aerodynamic Characteristics of Paradrogue Assembly in an Aerial Refueling System," 2007. doi:10.2514/1.26489.

[35] Mendez, M. A., Nardo, M. D., and Benocci, C., "Running FineOpen43 Simulations at VKI: A tutorial and a collection of scripts," 2017. doi:10.13140/RG.2.2.19214.31041.

[36] Nita, M., and Sholz, D., "Estimating the Oswald factor from basic aircraft geometrical parameters," *Deutscher Luft- und Raumfahrtkongress*, 2012.

[37] Roskam, J., *Airplane Design Part II: Preliminary Configuration Design and Integration of the Propulsion System*, DARcorporation, 2017.

[38] Raymer, D. P., *Aircraft Design: A Conceptual Approach*, AIAA Education Series, 1999.

[39] Finck, R. D., *USAF (United States Air Force) Stability and Control DATCOM (Data Compendium)*, Defence Technical Information Center, 1987.

[40] Oliviero, F., "Lift & Drag Estimation," , 2022. Presentation slides.

[41] Oliviero, F., "Design for AC longitudinal stability," , 2022. Presentation slides.

[42] Hepperle, M., "Electric Flight – Potential and Limitations," *NATO*, 2012.

[43] Riboldi C.E.D., G. F., "An integrated approach to the preliminary weight sizing ofsmallelectricaircraft," *Aerospace Science and Technology*, 2016.

[44] EASA, "Final Special Condition SC E-19 - Electric / Hybrid Propulsion System," , 2021.

[45] Michael D. Patterson, B. J. G., "Simplified Aerodynamics Model to Predict the Effects of Upstream Propellers on Wing Lift," 2015.

[46] de Vries, R., Brown, M., and Vos, R., "Preliminary Sizing Method for Hybrid-Electric Distributed-Propulsion Aircraft," Vol. 65(6), 2019.

[47] Patterson, M. D., "Conceptual Design of High-lift Propeller System for Small Electric Aircraft," Master's thesis, 2016.

[48] Nederlof, R., Kooij, R., Veldhuis, L. L. M., and Sinnige, T., "Contribution of Swirl Recovery to the Induced Drag of a Propeller-Wing System – A Parametric Study," 2023.

[49] Koutsoukos, P. A., "Aerodynamic and Aeroacoustic Interaction Effects of a Distributed-Propeller Configuration in Forward Flight," Master's thesis, 2022.

[50] Wang1, Y., Al-Dujaly, H., Yan, Y., Zhao, N., and Liu, C., "Physics of multiple level hairpin vortex structures in turbulence," *Science China*, Vol. 59, 2016.

[51] Fujii, K., "High-performance computing-based exploration of flow control with micro devices," *Philosophical Transactions of the Royal Society A: Mathematical, Physical and Engineering Sciences*, Vol. 372, 2014. doi:10.1098/rsta.2013.0326.

[52] Chen, F.F., *Introduction to Plasma Physics and Controlled Fusion*, Plenum Press., 2016.

[53] Choi, K.-S., Jukes, T., and Whalley, R., "Turbulent boundary-layer control with plasma actuators," *Philosophical Transactions of the Royal Society*, Vol. 369, 2011, pp. 1443–1458.

[54] Go, D. B., Garimella, S. V., Fisher, T., and Mongi, R. K., "Ionic Winds for Locally Enhanced Cooling," *Journal of Applied Physics*, Vol. 102, 2007.

[55] Erfani, R., Zare-Behtash, H., and Kontis, K., "Plasma actuator: Influence of dielectric surface temperature," *Experimental Thermal and Fluid Science*, Vol. 42, 2012, pp. 258–264. doi:https://doi.org/10.1016/j.expthermflusci.2012.04.023.

[56] Lilley, A. J., Roy, S., Michels, L., and Roy, S., "Performance recovery of plasma actuators in wet conditions," *Journal of Physics D: Applied Physics*, Vol. 55, No. 15, 2022, p. 155201. doi:10.1088/1361-6463/ac472d.

[57] Aversa, A., Do Cao, K., Hadzhiyski, E., Karaca, C., Oortwijn, M., van Oostrum, I., Platenburg, J., Ruijten, N., de Vries, J., and Welters, S., "Aerodynamic Performance of a Propeller in Propulsive and Regenerative Regimes,"

, 2022. Final report.

[58] van Neerven, J., "Design of a Variable Pitch, Energy-Harvesting Propeller for In-Flight Power Recuperation on Electric Aircraft," Master's thesis, 2020.

[59] Gudmundsson, S., *General Aviation Aircraft Design*, Elsevier, 2022. doi:10.1016/c2018-0-03861-x.

[60] Lawless, A., Lewis, G., Norton, B., Hrehov, D., Arney, S., Minor, J., Kidman, D., Moulder, C., and Stevens, C., *Flight Test Engineering Reference Handbook*, McDonnell Douglas/Boeing, 2013.

[61] Wang, J., and Feng, L., *Plasma Actuator*, Cambridge Aerospace Series, Cambridge University Press, 2018, p. 206–245. doi:10.1017/9781316676448.010.

[62] Oliviero, F., "Weight estimation and iterations in a/c design," , 2022. Presentation slides.

[63] Alderliesten, C.R., *Introduction to Aerospace Structures and Materials*, Delft University of Technology, 2021.

[64] Ashby, M. F., *Materials selection in mechanical design*, Butterworth-Heinemann, 1999.

[65] Van de Velde, K., and Kiekens, P., "Thermoplastic polymers: overview of several properties and their consequences in flax fibre reinforced composites," *Polymer Testing*, Vol. 20, No. 8, 2001, pp. 885–893. doi:https://doi.org/10.1016/S0142-9418(01)00017-4.

[66] Ashby, M., Shercliff, H. and Cebon, D., *Materials Enginnering, Science, Processing and Design*, 4th ed., Butterworth-Heinemann, 2019.

[67] Dixit, C. A., Achutha, V. M., and Sridhara, K. B., *materialstoday: Proceedings*, Vol. 43, 2021, pp. 1253–1257. doi:https://doi.org/10.1016/j.matpr.2020.08.766.

[68] Vos, R., Hoogreef, M., and Zandbergen, B., *AE1222-II Aerospace Design and Systems Engineering Elements I*, TU Delft, 2021.

[69] Sen, I., "Aircraft Fuselage Design Study: parametric modelling, structural analysis, material evaluation, and optimization for aircraft fuselage." , 2010.

[70] Megson, T. H. G., *Aircraft structures for engineering students*, Elsevier Ltd., 2017.

[71] Hibbeler, C. R., *Mechanics of Materials*, 10th ed., Pearson, 2018.

[72] Hibbeler, C. R., *Statics*, 14th ed., Pearson, 2016.

[73] Sadraey, M. H., *Aircraft design : a systems engineering approach*, John Wiley & Sons, Ltd, 2013.

[74] *AE1222-II Aerospace Design & Systems Engineering Elements I Lecture 7: Empennage and gear design*, Delft University of Technology, 2022.

[75] Fabrizio, N., Danilo, C., Pierluigi, V., Salvatore, C., and Vincenzo, C., "A comprehensive review of vertical tail design," 2016. doi:10.13140/RG.2.2.12606.69448.

[76] Torenbeek, E., *Synthesis of Subsonic Airplane Design*, Delft University Press, 1982.

[77] Obert, E., *Aerodynamic Design of Transport Aircraft*, IOS Pres, 2009.

[78] E. Nguyen Van, P. P., D. Alazard C. Doll, "Co-design of aircraft vertical tail and control laws using distributed electric propulsion," *Automatic Control in Aerospace*, Vol. 21, 2019. doi:https://doi.org/10.1016/j.ifacol.2019.11.295.

[79] *AE3211-I Systems Engineering and Aerospace Design. Lecture 9: Lateral and Ground design*, Delft University of Technology, 2023.

[80] Mulder, J., van Staveren, W., van der Vaart, J., de Weerdt, E., de Visser, C., in 't Veld, A., and Mooij, E., "AE3212-I Flight Dynamics Lecture Notes," Tech. rep., TUDelft, 2013.

[81] *AE3211-I Systems Engineering and Aerospace Design. Lecture 7: Requirement Analysis and Design principles for A/C stability & control (Part 1)*, Delft University of Technology, 2023.

[82] Gudmundsson, S., "Chapter 11 - The Anatomy of the Tail," *General Aviation Aircraft Design (Second Edition)*, edited by S. Gudmundsson, Butterworth-Heinemann, 2022, second edition ed., pp. 481–516. doi:https://doi.org/10.1016/B978-0-12-818465-3.00011-2.

[83] Yahyaoui, M., "A new method for the prediction of the downwash angle gradient," *International Journal of Aviation, Aeronautics, and Aerospace*, Vol. 6, 2019. doi:10.15394/ijaaa.2019.1336.

[84] *AE3211-I Systems Engineering and Aerospace Design. Lecture 6: Requirement Analysis and Design Principles for A/C Stability and Control (Part II)*, Delft University of Technology, 2023.

[85] "Michelin aircraft tire: Engineering Data," , #MAT-DB-01 Rev.A.

[86] Eskue, N., "Digital Thread Roadmap for Manufacturing and Health Monitoring the Life Cycle of Composite Aerospace Components," *Aerospace*, Vol. 10, 2023. doi:10.3390/aerospace10020146.

[87] Singh, V., and Willcox, E. K., "Engineering Design with Digital Thread," *AIAA Journal*, Vol. 56, 2018. doi:https://doi.org/10.2514/1.J057255.

[88] Azadivar, F., and Wang, J., "Facility layout optimization using simulation and genetic algorithms," *International Journal of Production Research*, Vol. 38, No. 17, 2000, pp. 4369–4383. doi:10.1080/00207540050205154.

[89] Mouritz, P. A., *Introduction to Aerospace Materials*, 1st ed., Woodhead Publishing, 2021.

[90] Rana, S., and Fangueiro, R., *Fibrous and Textile Materials for Composite Applications*, 1st ed., Springer, 2016.

[91] Sinke, J., "Production of Aerospace Systems," Delft University of Technology, 2023.

[92] Hiken, A., and Dekoulis, G., *Aerospace Engineering*, Intech Open, 2019.

[93] Dai, J.-N., Kou, S.-Q., Yang, H.-Y., Xu, Z.-B., Shu, S.-L., Qiu, F., Jiang, Q.-C., and Zhang, L.-C., "High-content continuous carbon fibers reinforced PEEK matrix composite with ultra-high mechanical and wear performance at elevated temperature," *Composite Structures*, Vol. 295, 2022, p. 115837. doi:https://doi.org/10.1016/j.compstruct.2022.115837.

[94] Ahmadi, Z., Ghaffarianl, S., and Amiri, D., "Continuous Melt Impregnation Process : Materials Parameters," *Iranian Polymer Journal (English Edition)*, Vol. 9, 2000.

[95] Parandoush, P., Tucker, L., Zhou, C., and Lin, D., "Laser assisted additive manufacturing of continuous fiber reinforced thermoplastic composites," *Materials & Design*, Vol. 131, 2017, pp. 186–195. doi:https://doi.org/10.1016/j.matdes.2017.06.013.

[96] Liu, G., Xiong, Y., and Zhou, L., "Additive manufacturing of continuous fiber reinforced polymer composites: Design opportunities and novel applications," *Composites Communications*, Vol. 27, 2021, p. 100907. doi:https://doi.org/10.1016/j.coco.2021.100907.

[97] Omairey, S. L., Sampethai, S., Hans, L., Worrall, C., Lewis, S., Negro, D., Sattar, T., Ferrera, E., Blanco, E., Wighton, J., Muijs, L., Veldman, S. L., Doldersum, M., Tonnaer, R., Jayasree, N., and Kazilas, M., "Development of innovative automated solutions for the assembly of multifunctional thermoplastic composite fuselage," *The International Journal of Advanced Manufacturing Technology*, Vol. 117, No. 5, 2021, pp. 1721–1738. doi:10.1007/s00170-021-07829-2.

[98] Iyer, S., and Drzal, L., "Manufacture of Powder-Impregnated Thermoplastic Composites," *Journal of Thermoplastic Composite Materials*, Vol. 3, 1990, pp. 325–355. doi:10.1177/089270579000300404.

[99] Texier, A., Davis, R., Lyon, K., Gungor, A., McGrath, J., Marand, H., and Riffle, J., "Fabrication of PEEK/carbon fibre composites by aqueous suspension prepregging," *Polymer*, Vol. 34, No. 4, 1993, pp. 896–906. doi:https://doi.org/10.1016/0032-3861(93)90378-N.

[100] Crosky, A., Grant, C., Kelly, D., Legrand, X., and Pearce, G., "4 - Fibre placement processes for composites manufacture," *Advances in Composites Manufacturing and Process Design*, edited by P. Boisse, Woodhead Publishing, 2015, pp. 79–92. doi:https://doi.org/10.1016/B978-1-78242-307-2.00004-X.

[101] Minchenkov, K., Vedernikov, A., Safonov, A., and Akhatov, I., "Thermoplastic Pultrusion: A Review," *Polymers*, Vol. 13, 2021, p. 180. doi:10.3390/polym13020180.

[102] Barış Vatandaş, B., Uşun, A., Yıldız, N., Şimşek, C., Ömer Necati Cora, Aslan, M., and Gümrük, R., "Additive manufacturing of PEEK-based continuous fiber reinforced thermoplastic composites with high mechanical properties," *Composites Part A: Applied Science and Manufacturing*, Vol. 167, 2023, p. 107434. doi:https://doi.org/10.1016/j.compositesa.2023.107434.

[103] Veldman, S., Kortbeek, P., Wölcken, P., Herrmann, R., Kos, J., and Villegas, I., "Development of a Multifunctional Fuselage Demonstrator," 2020.

[104] Meister, S., Wermes, M., Stüve, J., and Groves, R. M., "Investigations on Explainable Artificial Intelligence methods for the deep learning classification of fibre layup defect in the automated composite manufacturing," *Composites Part B: Engineering*, Vol. 224, 2021, p. 109160. doi:https://doi.org/10.1016/j.compositesb.2021.109160.

[105] Boyang, Q., Mou, L., Wu, L., Xiao, Z., Hu, T., and Jiang, J., "A Direction-Sensitive Microwave Sensor for Metal Crack Detection," *Applied Sciences*, Vol. 12, 2022, p. 9045. doi:10.3390/app12189045.

[106] Iyer, S., and Drzal, L., "Manufacture of Powder-Impregnated Thermoplastic Composites," *Journal of Thermoplastic Composite Materials*, Vol. 3, 1990, pp. 325–355. doi:10.1177/089270579000300404.

[107] Texier, A., Davis, R., Lyon, K., Gungor, A., McGrath, J., Marand, H., and Riffle, J., "Fabrication of PEEK/carbon fibre composites by aqueous suspension prepregging," *Polymer*, Vol. 34, No. 4, 1993, pp. 896–906. doi:https://doi.org/10.1016/0032-3861(93)90378-N.

[108] Schmidt, C., Denkena, B., Völtzer, K., and Hocke, T., "Thermal Image-based Monitoring for the Automated Fiber Placement Process," *Procedia CIRP*, Vol. 62, 2017, pp. 27–32. doi:https://doi.org/10.1016/j.procir.2016.06.058, 10th CIRP Conference on Intelligent Computation in Manufacturing Engineering - CIRP ICME '16. [Edited by: Roberto Teti, Manager Editor: Doriana M. D'Addona].

[109] Kralovec, C., and Schagerl, M., "Review of Structural Health Monitoring Methods Regarding a Multi-Sensor Approach for Damage Assessment of Metal and Composite Structures," *Sensors*, Vol. 20, No. 3, 2020. doi:

10.3390/s20030826.

[110] Mandal, N. R., *Welding Parameters*, Springer Singapore, Singapore, 2017, pp. 159–174. doi:10.1007/978-981-10-2955-4_14.

[111] Brüning, J., Denkena, B., Dittrich, M.-A., and Hocke, T., "Machine Learning Approach for Optimization of Automated Fiber Placement Processes," *Procedia CIRP*, Vol. 66, 2017, pp. 74–78. doi:10.1016/j.procir.2017.03.295.

[112] Zambal, S., Eitzinger, C., Clarke, M., Klintworth, J., and Mechin, P.-Y., "A digital twin for composite parts manufacturing: Effects of defects analysis based on manufacturing data," *2018 IEEE 16th International Conference on Industrial Informatics (INDIN)*, 2018, pp. 803–808. doi:10.1109/INDIN.2018.8472014.

[113] Seon, G., Nikishkov, Y., Makeev, A., and Ferguson, L., "Towards a digital twin for mitigating void formation during debulking of autoclave composite parts," *Engineering Fracture Mechanics*, Vol. 225, 2020, p. 106792. doi:https://doi.org/10.1016/j.engfracmech.2019.106792.

[114] Arinez, J. F., "Artificial intelligence in advanced manufacturing," *Journal of manufacturing science*, 2019.

[115] Troy, S., Schreiber, A., Reppert, T., Gehrke, G. H., Finsterbusch, M., Uhlenbruck, S. and Stenzel, P., "Life Cycle Assessment and resource analysis of all-solid-state batteries," *Applied Energy*, Vol. 169, 2016, pp. 757–767.

[116] TE Connectivity, "Smarter Solutions Start with the Connectivity Sensors," , 2016.

[117] Connectivity, T., "rotary+linear-potentiometers-selection-guide," 2023.

[118] "Aerospace-grade surface mounted optical fibre strain sensor for structural health monitoring on composite structures evaluated against in-flight conditions," *Smart Materials and Structures*, Vol. 28, 2019. doi:10.1088/1361-665X/ab1458.

[119] Lawrence, C. M., Nelson, D. V., Udd, E., and Bennett, T., "A Fiber Optic Sensor for Transverse Strain Measurement," *Experimental Mechanics*, Vol. 39, No. 3, 1999, pp. 202–209. doi:10.1007/BF02323553.

[120] Putra, B., Chen, R., Kramer, J. V., Machado, I., Polak, T., and Vousten, M., "Mechanical Analysis of a Morphing Leading Edge Concept," 2022.

[121] Vepdz, "Strain Gages," , 2023.

[122] Tang, H. Y., Winkelmann, C., Lestari, W., and Saponara, V. L., "Composite structural health monitoring through use of embedded PZT sensors," *Journal of Intelligent Material Systems and Structures*, Vol. 22, 2011, pp. 739–755. doi:10.1177/1045389X11406303.

[123] Pinsard, L., "02 Design & Construction (2019) text," 2019.

[124] Zhu, W., Ye, H., Zou, X., Yang, Y., and Dong, H., "Analysis and optimization for chemical absorption of H2S/CO2 system: Applied in a multiple gas feeds sweetening process," *Separation and Purification Technology*, Vol. 276, 2021. doi:10.1016/j.seppur.2021.119301.

[125] Hilt, A., Jaro, G., and Bakos, I., "Availability Prediction of Telecommunication Application Servers Deployed on Cloud," *Periodica Polytechnica, Electrical Engineering*, Vol. 60, 2016, pp. 72–81. doi:10.3311/PPee.9051.

[126] EMRAX, "Technical Data and Manual for EMRAX Motors / Generators User's Manual for Advanced Axial Flux Synchronous Motors and Generators," , 2018.

[127] Shu, X., Yang, W., Guo, Y., Wei, K., Qin, B., and Zhu, G., "A reliability study of electric vehicle battery from the perspective of power supply system," *Journal of Power Sources*, Vol. 451, 2020, p. 227805. doi:10.1016/j.jpowsour.2020.227805.

[128] Lindsey, R., "Climate Change: Atmospheric Carbon Dioxide," *Climate.gov*, 2023.

[129] Asmatulu, E., Twomey, J., and Overcash, M., "Evaluation of recycling efforts of aircraft companies in Wichita," *Resources, Conservation and Recycling*, Vol. 80, 2013, pp. 36–45. doi:https://doi.org/10.1016/j.resconrec.2013.08.002.

[130] Kuchariková, L., Tillová, E., and Bokuvka, O., "Recycling and properties of recycled aluminium alloys used in the transportation industry," *Transport Problems*, Vol. 11, 2016, pp. 117–122. doi:10.20858/tp.2016.11.2.11.

[131] Asmatulu, E., Overcash, M., and Twomey, J., "Recycling of Aircraft: State of the Art in 2011," *Journal of Industrial Engineering*, Vol. 2013, 2013, pp. 1–8. doi:10.1155/2013/960581.

[132] Keivanpour, S., Kadi, D. A., and Mascle, C., "End-of-life aircraft treatment in the context of sustainable development, lean management, and global business," *International Journal of Sustainable Transportation*, Vol. 11, 2017. doi:10.1080/15568318.2016.1256455.

[133] Das, S. K., Green, J. A. S., Kaufman, J. G., Emadi, D., and Mahfoud, M., "Aluminum recycling—An integrated, industrywide approach," *JOM*, Vol. 62, No. 2, 2010, pp. 23–26. doi:10.1007/s11837-010-0026-6.

[134] Zhao, D., Guo, Z., and Xue, J., "Research on Scrap Recycling of Retired Civil Aircraft," *IOP Conference Series: Earth and Environmental Science*, Vol. 657, No. 1, 2021, p. 012062. doi:10.1088/1755-1315/657/1/012062.

[135] Krauklis, A. E., Karl, C. W., Gagani, A. I., and Jørgensen, J. K., "Composite Material Recycling Technology—State-

of-the-Art and Sustainable Development for the 2020s," *Journal of Composites Science*, Vol. 5, No. 1, 2021, p. 28. doi:10.3390/jcs5010028.

[136] Sabaghi, M., Cai, Y., Mascle, C., and Baptiste, P., "Sustainability assessment of dismantling strategies for end-of-life aircraft recycling," *Resources, Conservation and Recycling*, Vol. 102, 2015, pp. 163–169. doi:https://doi.org/10.1016/j.resconrec.2015.08.005.

[137] Das, S. K., "Recycling Aluminum Aerospace Alloys," *Advanced Materials & Processes*, Vol. 166, 2008, pp. 34–35.

[138] Zhou, B., Liu, B., Zhang, S., Lin, R., Jiang, Y., and Lan, X., "Microstructure evolution of recycled 7075 aluminum alloy and its mechanical and corrosion properties," *Journal of Alloys and Compounds*, Vol. 879, 2021, p. 160407. doi:https://doi.org/10.1016/j.jallcom.2021.160407.

[139] Roux, M., Dransfeld, C., Eguémann, N., and Giger, L., "Processing and recycling of thermoplastic composite fibre/PEEK aerospace part," *16th European Conference on Composite Materials, ECCM 2014*, 2014, pp. 1–8.

[140] Li, H., and Englund, K., "Recycling of carbon fiber-reinforced thermoplastic composite wastes from the aerospace industry," *Journal of Composite Materials*, Vol. 51, No. 9, 2017, pp. 1265–1273. doi:10.1177/0021998316671796.

[141] McLauchlin, A., Ghita, O., and Savage, L., "Studies on the reprocessability of poly(ether ether ketone) (PEEK)," *Journal of Materials Processing Technology*, Vol. 214, No. 1, 2014, pp. 75–80. doi:https://doi.org/10.1016/j.jmatprotec.2013.07.010.

[142] Zhao, X., Verhagen, W. J., and Curran, R., "Disposal and Recycle Economic Assessment for Aircraft and Engine End of Life Solution Evaluation," *Applied Sciences*, Vol. 10, No. 2, 2020. doi:10.3390/app10020522.

[143] Jiao, H., Song, W.-L., Chen, H., Wang, M., Jiao, S., and Fang, D., "Sustainable recycling of titanium scraps and purity titanium production via molten salt electrolysis," *Journal of Cleaner Production*, Vol. 261, 2020, p. 121314. doi:https://doi.org/10.1016/j.jclepro.2020.121314.

[144] Achilias, D., Andriotis, L., Koutsidis, I., Louka, D., Nianias, N., Siafaka, P., Tsagkalias, I., and Tsintzou, G., *Recent Advances in the Chemical Recycling of Polymers (PP, PS, LDPE, HDPE, PVC, PC, Nylon, PMMA)*, InTech, 2012, Chap. 1, pp. 3–55. doi:10.5772/33457.

[145] Bawareth, M., Xu, W., Ravichandran, D., Zhu, Y., Jambhulkar, S., Fonseca, N., Miquelard, G., Camille, V., Matthew, L., Campbell, W., and Song, K., "Crosslinked Polyethylene (XLPE) Recycling via Foams," *Polymers*, Vol. 14, 2022. doi:10.3390/polym14132589.

[146] Kumar, A., Holuszko, M., and Espinosa, D. C. R., "E-waste: An overview on generation, collection, legislation and recycling practices," *Resources, Conservation and Recycling*, Vol. 122, 2017, pp. 32–42. doi:https://doi.org/10.1016/j.resconrec.2017.01.018.

[147] Chen, R., Nolan, M. A., Lu, J., Wang, J., Yu, X., Mo, Y., Chen, L., Huang, X. and Hong, L., "The Thermal Stability of Lithium Solid Electrolytes with Metallic Lithium," *Joule*, Vol. 4, 2020, pp. 812–821.

[148] McManus, C. M., "Environmental consequences of the use of batteries in low carbon systems: The impact of battery production," *Applied Energy*, Vol. 93, 2012, pp. 288–295.

[149] Akhmetov, N., "Li-Ion Battery Cathode Recycling, An Emerging Response to Growing Metal Demand and Accumulating Battery Waste," *electronics*, 2020.

[150] Agency, I. E., "Global Supply Chains of Electrical Vehicles," *International Energy Agency*, 2019.

[151] Azhari, L., Bong, S., Ma, X. and Wang, Y., "Recycling for All Solid-State Lithium-Ion Batteries," *Matter*, Vol. 3, 2020, pp. 1845–1861.

[152] Tan, S. H. D., Xu, P., Yang, H., Kim, M., Nguyen, H., Wu, A. E., Doux, JM., Banerjee, A. Meng, S.Y., and Chen, Z., "Sustainable design of fully recyclable all solid-state batteries," *MRS Energy & Sustainability*, Vol. 7, 2020. doi:https://doi.org/10.1557/mre.2020.25.

[153] Gallagher, T., "Noise pollution: How are airports and airlines addressing the issue?" *euronews.next*, 2021.

[154] lichtbeeldengeluid, "Table with Noise levels," , 2018.

[155] MAAZ, M. A., "The Main Sources Of Aircraft Noise & The Steps Taken To Reduce Them," *Simple Flying*, 2022.

[156] Steele, J., "The Role of 'Fully Electric Aircraft' for Sustainable Aviation," *Master Economic Geography*, 2022.

[157] Rotterdam Airport The Hague, "Airport Charges Regulation April 2022 Summary," , 2022.